Nanostructured Mesoporous Materials via Electrospinning

Principle concepts in the preparation of oxide nanofibers from different building blocks

Dissertation

by

Dipl.-Chem. Claas Wessel

born 21. Mai 1982 in Buchholz i. d. N.

for the degree of

"Doctor rerum naturalium"

- Dr. rer. Nat. -

submitted to the

Faculty of Biology and Chemistry

Justus-Liebig University Gießen, Germany

Gießen, December 2015

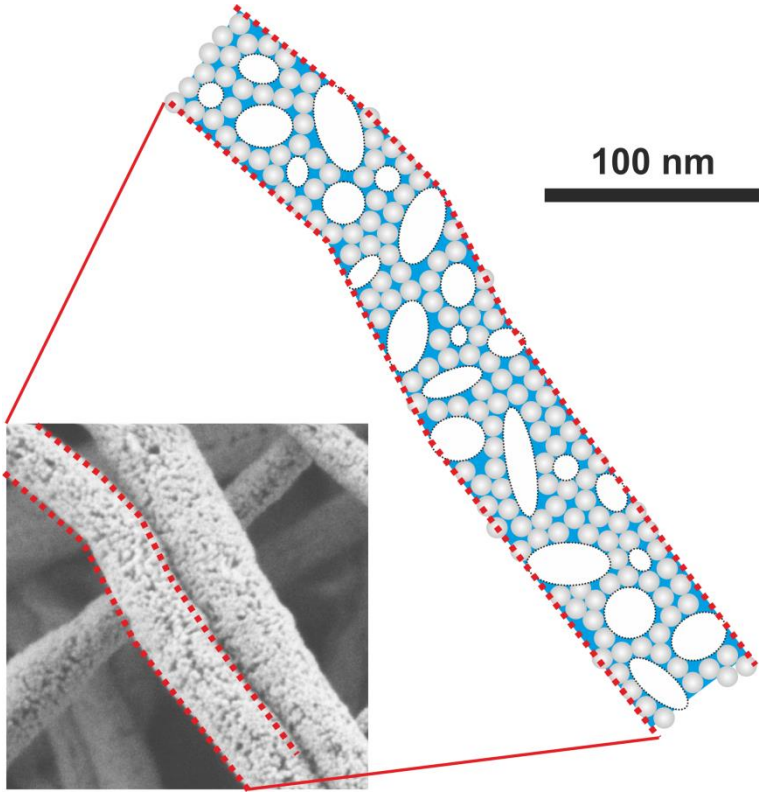

Mesoporous, electrospun fibers:
Straightforwardly prepared from preformed nanoparticles

Es war ein langer, langer Weg

B. O., 1992

Dean	Prof. Dr. V. Wissemann
1st Reviewer	Prof. Dr. B. M. Smarsly
2nd Reviewer	Prof. Dr. H. Over
submitted	11. December 2015

The present thesis was prepared in the period of 16.02.2009 – 11.12.2015 at the Institute of Physical Chemistry of the Justus-Liebig-University Giessen under the supervision and guidance of Prof. Dr. Bernd Michael Smarsly.

I declare:

The present thesis was prepared by myself and without illicit help from others. Any citations being included literally, by adaptation from literature or personal communications have been marked appropriately. The principles of best practice in academia, as documented in the respective charter of the Justus-Liebig-University have been applied in all investigations constituting this thesis.

Die vorliegende Arbeit wurde in der Zeit vom 16.02.2009 – 11.12.2015 am Physikalisch-Chemischen Institut der Justus-Liebig-Universität Gießen bei Prof. Dr. Bernd Michael Smarsly durchgeführt.

Ich erkläre:

Ich habe die vorgelegte Dissertation selbständig und ohne unerlaubte fremde Hilfe und nur mit den Hilfen angefertigt, die ich in der Dissertation angegeben habe. Alle Textstellen, die wörtlich oder sinngemäß aus veröffentlichten Schriften entnommen sind, und alle Angaben, die auf mündlichen Auskünften beruhen, sind als solche kenntlich gemacht. Bei den von mir durchgeführten und in der Dissertation erwähnten Untersuchungen habe ich die Grundsätze guter wissenschaftlicher Praxis, wie sie in der „Satzung der Justus-Liebig-Universität Gießen zur Sicherung guter wissenschaftlicher Praxis“ niedergelegt sind, eingehalten.

Gießen, der 11. Dezember 2015

(Claas Wessel)

Abstract

Over the last decade electrospinning has gained considerable scientific interest as a method for the preparation of nanostructured inorganic materials. Electrospun metal oxide fiber mats are under investigation for applications as e. g. electrode materials in electrochemical devices, as heterogeneous catalysts or as active material in sensing devices. The efficiency of such devices is strongly influenced and controlled by the material´s porosity and pore structure.

While the preparation of metal oxide fibers from sol-gel precursors is already widely used for oxides of numerous elements, the synthesis of such fibers using preformed, dispersed nanoparticles is less exploited and understood. Simultaneously, it was observed, that titania fibers prepared from preformed nanoparticles feature improved porosities compared to sol-gel-based fibers.[1]

This thesis investigates the fundamentals of the preparation of oxide nanofibers from different building blocks, namely sol-gel precursors, preformed nanoparticles or a combination of both in order to establish a basic concept concerning electrospinning of inorganic materials. This concept focuses on the origin of mesoporosity which is frequently observed, when electrospun fibers are prepared from preformed nanoparticles, but which has not been understood so far.

Nitrogen physisorption as a straightforward method to characterize mesoporosity was investigated concerning its applicability to electrospun fibers and the assessment of pore sizes and pore volumes in such fibers. Therefore, electrospun silica model materials were prepared from commercial Ludox nanoparticle dispersions and analyzed by nitrogen physisorption in detail. By means of these basic investigations a specific density functional theory (DFT) analysis method was selected as a standard method to analyze electrospun fibers and afterwards applied to fibers of several metal oxides. Using this methodology it was possible to compare the mesoporosity of electrospun fibers of several metal oxides for the first time.

Zusammenfassung

Elektrospinnen als Methode zur Herstellung nanostrukturierter anorganischer Materialien hat im letzten Jahrzehnt starkes wissenschaftliches Interesse hervorgerufen. Elektrogesponnene Metalloxid Fasermatten werden derzeit u. a. im Hinblick auf Anwendungen auf den Gebieten der heterogenen Katalyse oder Sensorik oder als Elektrodenmaterial in elektrochemischen Zellen untersucht. Die Effektivität der Materialien in derartigen Anwendungen wird maßgeblich durch deren Porosität und Porenstruktur beeinflusst und gesteuert.

Während die Herstellung von elektrogesponnenen Fasern aus Sol-Gel-Vorläuferverbindungen für Metalloxide bereits weit verbreitet ist und für Oxide zahlreicher Elemente angewandt wird, ist die Synthese von solchen Fasern ausgehend von vorgeformten, dispergierten Nanopartikeln deutlich weniger erforscht und verstanden. Gleichzeitig wurde festgestellt, dass aus vorgeformten Nanopartikel hergestellte Titandioxid-Fasern über eine erhöhte Porosität im Vergleich zum Sol-Gel-Fasern verfügen.[1]

Diese Dissertation untersucht die Synthese von Oxidnanofasern ausgehend von verschiedenen Bausteinen, nämlich Sol-Gel-Vorläuferverbindungen, vorgeformten Nanopartikeln oder einer Kombination aus beiden, um ein grundlegendes Konzept zur Synthese elektrogesponnener anorganischer Materialien zu entwickeln. Dieses Konzept konzentriert sich auf die Analyse und Erklärung von Strukturbildungsprozessen, die zu Mesoporosität führen, welche häufig beobachtet wird, wenn elektrogesponnene Fasern aus vorgeformten Nanopartikel hergestellt werden.

Um die auftretende Mesoporosität in elektrogesponnenen Oxidfasern einfach und schnell charakterisieren zu können, wurde die Stickstoffphysisorption als Analysemethode grundlegend hinsichtlich ihrer Anwendbarkeit auf elektrogesponnene Fasern und der Bewertung derer Porengrößen und Porenvolumina untersucht. Für diese methodischen Studien wurden elektrogesponnene Siliziumdioxid Modellmaterialien aus kommerziellen Ludox Nanopartikel-Dispersionen hergestellt und analysiert. Durch diese Grundlagenuntersuchungen wurde ein spezifisches Dichtefunktionaltheorie (DFT)-Analyseverfahren als Standardmethode ausgewählt, um elektrogesponnene Fasern zu analysieren und anschließend auf unterschiedliche Fasermaterialien angewendet. Mit dieser Methodik war es erstmals möglich, die Mesoporosität von elektrogesponnenen Fasern mehrerer Metalloxide zu vergleichen.

1 Introduction

1.1 Motivation

Electrospinning has gained considerable scientific interest as a method to synthesize nanostructured inorganic materials over the last decade. Furthermore, hierarchically porous materials are of considerable scientific interest for diverse applications, such as electrochemical devices, heterogeneous catalysis or sensing which are all based on surface reactions. Electrospun fiber mats, which intrinsically exhibit large inter-fiber void spaces representing macropores, are an adequate candidate to prepare hierarchically porous materials by introducing additional meso- and/or microporosity into the fibers.

In this context the present thesis will focus on the preparation of mesoporous electrospun fibers of several oxide materials and fundamental investigations concerning the origin of mesoporosity in such materials. While the preparation of oxide fibers from sol-gel precursors is well-established and already applied to oxides of numerous elements, an alternative approach using preformed, dispersible nanoparticles as building blocks is much less exploited and consequently barely understood from a physico-chemical point of view. Moreover, also combining sol-gel precursors and preformed nanoparticles in a so-called “brick and mortar” (B+M) approach is a viable but rarely[2] applied way to prepare inorganic fibers. This approach will also be investigated in this thesis.

Preliminary studies revealed that electrospun fibers prepared from preformed nanoparticles can exhibit significantly increased mesoporosity in comparison to sol-gel-derived fibers[1] motivating more detailed investigations concerning the origin of such mesoporosity. However, the characterization of mesoporosity in electrospun fibers is challenging, because the structure of electrospun fiber mats is very different from the structure of other porous materials like powders or thin-films. Nitrogen physisorption as one powerful and widely applied, sophisticated analytic method to characterize mesoporous materials is selected to study electrospun fibers within this thesis, although there are several open questions concerning the applicability of this method to electrospun materials. It remains to be evaluated which pore sizes and volumes of mesoporous electrospun fibers can be extracted from nitrogen physisorption analysis and how precise and reliable such data are. Consequently, initial experiments and analyses will be conducted to investigate the applicability of nitrogen physisorption and its limitations concerning mesoporous fibers in order to establish a reliable analytic method.

Subsequently, systematic studies on several oxide materials will be performed in order to establish a fundamental concept for electrospinning of inorganic materials explaining the occurrence of mesoporosity in fibers prepared from different building blocks (i. e. sol-gel precursors and/or preformed nanoparticles). Such a concept would facilitate the directed synthesis of mesoporous fibers and thus would represent considerable scientific progress.

1.2 Overview

The fields of action are composed and implemented in the course of this thesis in the following manner:

In the theoretical section the mechanistic models of spinodal decomposition (SD) and diffusion-limited cluster aggregation (DLCA) are introduced after a brief overview of general concepts for the preparation of porous nanostructures in order to be able to explain the formation of mesoporosity during electrospinning. Furthermore, some basic considerations concerning nitrogen physisorption analyses on electrospun fibers are discussed.

Subsequently, silica nanofibers were prepared using commercial Ludox dispersions to serve as model material elucidating the validity and limitations of nitrogen physisorption analyses on electrospun fibers in chapter 3.2.3. After these methodological investigations a systematic study of numerous silica materials was conducted in order to gain insight into the origin of mesoporosity, which is frequently observed in electrospun fibers prepared from preformed, dispersed nanoparticles. Therefore, comparative investigations on sol-gel- and nanoparticle-derived electrospun fibers and comparable bulk reference samples will be conducted (see chapter 3.2.4). From these experiments a first mechanistic concept for the preparation of mesoporous electrospun inorganic fibers will be established.

In the subsequent chapters 3.3 - 3.5 other metal oxides, namely zirconia, ceria and tin oxide, will be investigated in a similar manner in order to gain further evidence of the previously established conceptual understanding concerning electrospinning of inorganic materials in general. Additionally, these chapters will investigate additional features in the preparation of electrospun oxide fibers expanding this general concept. While the experiments on zirconia materials examine the influence of different nanoparticles on the structure of the resultant electrospun fibers, tin oxide experiments study the “brick and mortar” concept for the synthesis of oxide fibers exemplarily. Moreover, several important parameters like the used solvent(s) and their composition influencing the spinning experiments are discussed in these chapters.

In the concluding chapter 3.6 all the former results are restated and analyzed with special emphasis on the general mechanistic features determining the porosity and surface structure of electrospun fibers irrespective of the material under investigation. These comparative analyses on several materials result in a pivotal concept explaining the generally increased mesoporosity of nanoparticle-derived electrospun fibers.

2 Theoretical background

Hierarchically porous materials are of considerable interest in the scientific field of advanced functional materials.[3] Electrospun nonwoven fiber mats intrinsically exhibit macroporous inter-fiber void space which allows for enhanced mass transport through the material.[4] Combining this intrinsic macroporosity with distinct mesoporosity would result in a hierarchically porous material with a pore structure which hardly can be prepared by other methods. This thesis introduces a new concept for the preparation of mesoporous nanostructured materials via the electrospinning method which allows for a simple and straightforward preparation of such nanoarchitectures.

In this context the preparation of nanostructures in general (see chapter 2.1) and porous nanostructures in particular (see chapter 2.2) will be shortly introduced in order to outline the scientific field of this thesis. Background discussions concerning concepts for the preparation of porous materials (see chapter 2.3) as well as illustrations of the electrospinning method (see chapter 2.4) and its application for the preparation of porous materials (see chapter 2.5) will be given to allow the reader to understand and value the results of this thesis. Finally, the evaluation of nitrogen physisorption experiments with respect to electrospun fibers is considered in chapter 2.6 permitting to interpret such experiments correctly.

2.1 Nanostructured materials

The size range of 1-100 nm - or in a less rigorous definition the size range of 1 nm-1 µm – defines the nanoscale to which nanostructured materials refer.[5] Electrospun fibers are a representative of so-called 1D-nanostructures like nanorods, nanotubes or other fibrous materials which all exhibit only one dimension beyond the nanoscale. In line with such classification of nanostructures there are also 0D-, 2D- or 3D-nanostructures which possess 0, 2, or 3 dimensions beyond the nanoscale respectively (see figure 2-1): Nanoparticles are typical examples of 0D-nanostructures while thin-films are a representative in the group of 2D-nanostructures. Finally, 3D nanostructures are macroscopic structures which exceed the nanoscale in all three dimensions, but which are structured internally on the nanoscale. Typical examples of such 3D-nanostructures are monolithic materials or meso- or macroscopic aggregates of nanoparticles.

Besides the classification of nanostructured materials by its dimensionality, also the porosity of nanostructures is an important feature which needs consideration. While some nanostructured materials like zeolites or mesoporous silica materials (e. g. SBA-15, MCM-41, KIT-6 etc.) are intrinsically porous nanostructures,[6] thin-films or fiber materials may be prepared as dense or porous structures. An exhaustive presentation of all classes of nanostructured materials is excrescent and will not be presented here as this thesis focuses on the subclass of 1D-nanostructures only, to which mesoporous electrospun fibers belong. For a detailed overview of different classes of nanostructured materials the reader is referred to the literature,[7] while a short excursion with special respect to porous nanostructures is given below in order to argue why electrospun nanostructures stand out from other structures (see chapter 2.2.1). Therefore, it also needs some general consideration of the electrospinning method and the properties and benefits of electrospun fibers (see chapter 2.4).

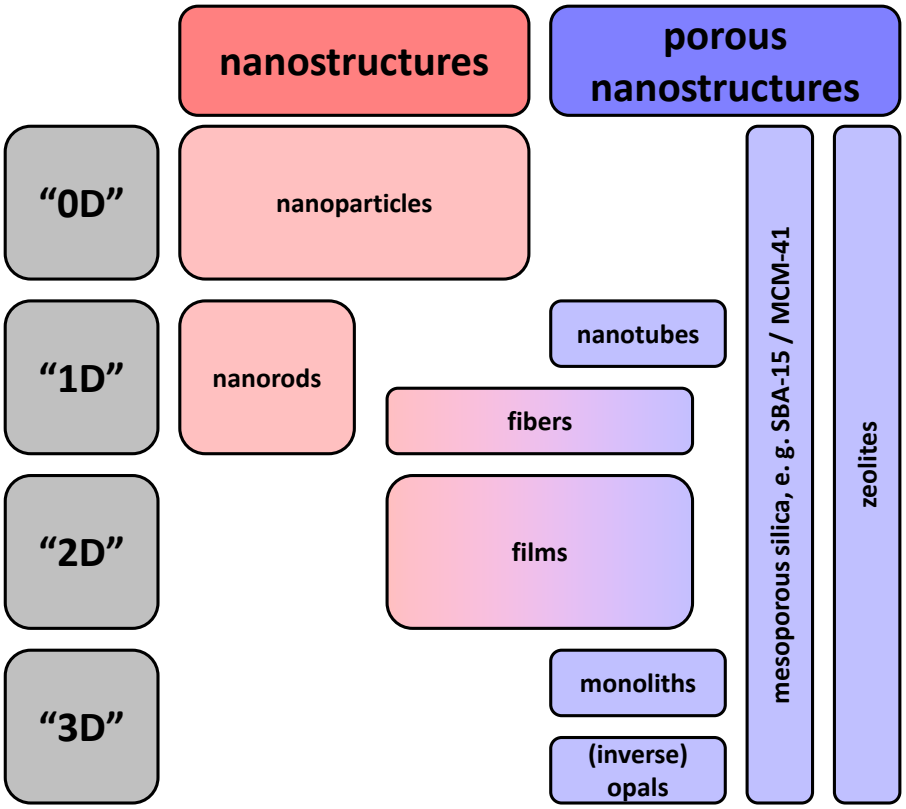

Figure 2-1: Rough classification of nanostructures with respect to their morphological structure and representative examples.

From the experimenters point of view the preparation of nanostructured materials can be distinguished into "bottom-up" and "top-down" approaches.[5] In a "top-down" approach larger micro- or macrostructures are transferred or modified to structures with domain sizes in the nanoscale. Typical "top-down" approaches are etching or lithographic processes like nanoimprint lithography[8–12] which are basically sophisticated physico-chemical processing techniques. In contrast, "bottom-up" processes are based on the aggregation of molecular precursors or nanoparticles typical for (wet-) chemical synthetic approaches. Such aggregation can be done via diverse routes including methods that are based on self-aggregation phenomena. One example of self-aggregation, which is well studied and often applied in the preparation of thin-films or powders, is the evaporation-induced self-assembly (EISA) process.[13–15] Also the electrospinning technique is usually considered as "bottom-up" method because molecular species and/or nanoparticles are confined into a nanostructured fiber. Otherwise, the thinning of the fibrous structure from several microns at the Taylor cone down to several nanometers can also be considered as a "top-down" process. For more details of the electrospinning process see chapter 2.4.

2.2 Porous nanostructures

Porous structures can be generated with different pore diameters *d* which are classified in micropores ($d < 2$ nm), mesopores ($d = 2–50$ nm) and macropores ($d > 50$ nm) according to IUPAC definition.[16] There are numerous concepts and preparative approaches to prepare porous materials with a wide variety of pore sizes which will be summarized in the following. This overview will not be exhaustive but it rather will illustrate how the porosity of a material can be addressed and controlled in a sophisticated synthetic protocol in order to result in a specific porous structure. Structure-property-relationships determining which porous structure is best suited for a designated application will be discussed in order to motivate why hierarchically porous materials are of considerable interest (see chapter 2.2.1.2). Afterwards (see chapter 2.5), it will be discussed why it is still a scientific challenge to synthesize mesoporous electrospun fibers, which belong to the class of hierarchically porous nanostructures. Within this field, this thesis especially addresses the class of inorganic materials prepared via electrospinning.

2.2.1 Preparative concepts and processes for the generation of porous materials

Porous nanostructures are an active field of scientific research with a wide variety of preparative approaches. In order to obtain porous nanostructures straightforwardly fundamental synthetic concepts are required addressing the nanostructure as well as their porosity simultaneously. Concepts to prepare porous materials are so manifold that book volumes concerning this topic are available.[17] Although basic concepts to prepare porous materials are often the same for macroscopic as well as nanostructured porous materials the following discussion will omit macroscopic porous structures like foamed polymers (e. g. expanded polystyrene (EPS/styropor) or expanded polypropylene (EPP)) or aerated concrete (e. g. Ytong) as they are not relevant in the context of this thesis.

However, surveying the preparative processes resulting in porous nanostructures reveals that almost any synthetic approach refers to the two opposing basic concepts of decomposition or templating (see figure 2-2). Decomposition processes introduce heterogeneity into an emerging structure by phase separation which may result in a porous structure directly if one of the phases is gaseous or liquid and the other one solid in the end of the process. Otherwise, a phase-separated structure can be transferred into a porous material, if one of the two phases is selectively removed in a subsequent step.[17] Decomposition processes can further be differentiated into spinodal decomposition (SD) (see chapter 2.3.1) or nucleation and growth (i.e. binodal decomposition), neglecting some cases of transient situations in which both concepts need to be considered (for details see chapter 2.3.1).

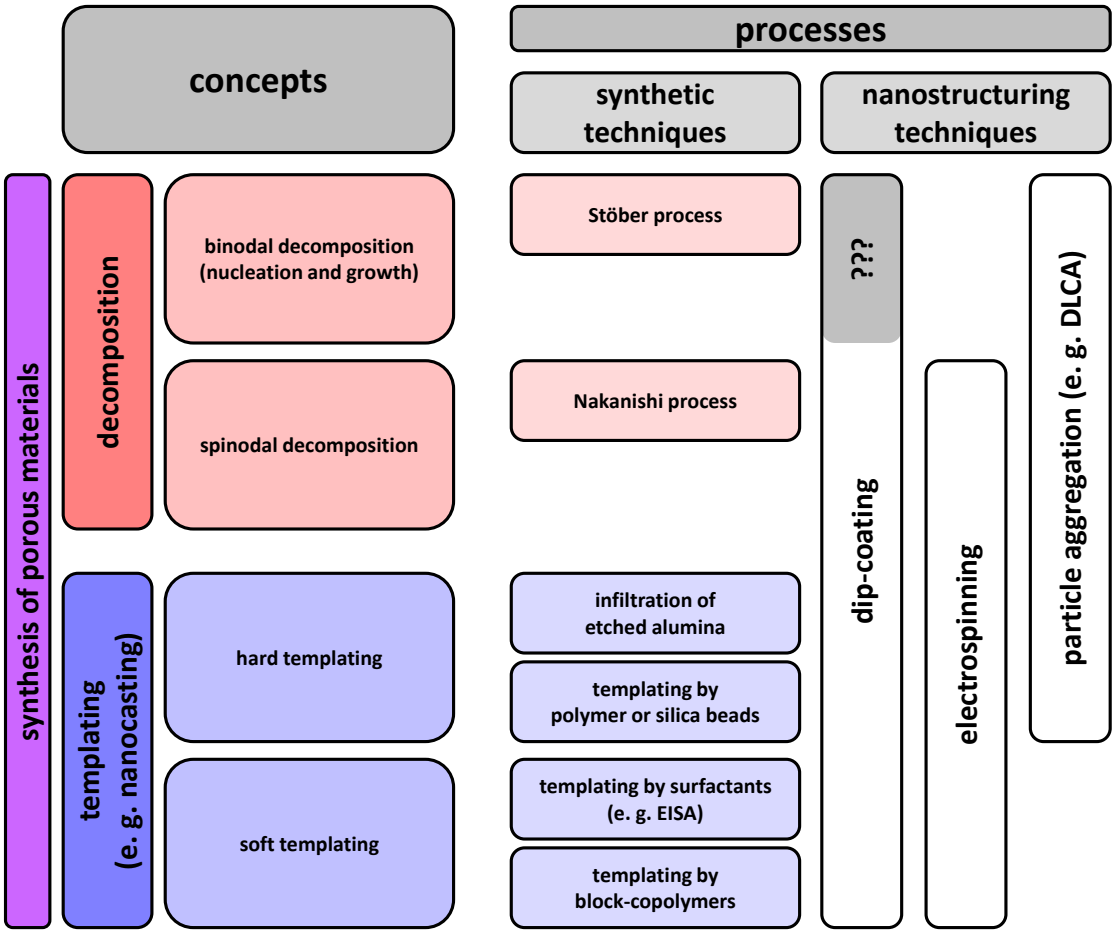

Figure 2-2: Preparative concepts and exemplary processes for the generation of porous materials.

The Nakanishi process, a well-studied example of SD processes, will be presented in chapter 2.3.1.1 because the detailed understanding of the Nakanishi process allows for a pivotal understand of the spatiotemporal evolution during SD, which is also relevant in the context of electrospinning (see chapter 2.5.4). A well-studied example of binodal decomposition which often is considered as an contrary process to SD is the so-called Stöber process.[18]

Templating concepts comprise the two approaches of soft or hard templating. Hard templating summarizes all preparative methods using any “solid” material as template including templates for macrostructured materials. If only nanostructured materials are addressed nanocasting is a templating process contrasted to cooperative assembly processes.[19] Otherwise, in case of soft templating a strict differentiation between templating and cooperative processes is a question of details (see below). Typical templates in nanocasting are zeolites, anodically etched alumina membranes or (ordered) mesoporous silica or carbon materials.[19] Such template materials are mostly porous materials themselves which also need to be prepared e. g. by soft templating (like mesoporous silica or carbon materials) or decomposition processes (like zeolites[20] or anodically etched alumina membranes[21]).

In soft templating syntheses “soft” (i. e. mostly liquid) matter is used as template. Typical soft-templates are surfactants (surface active agents, which are differentiated in cationic, anionic or non-ionic ones)[6] or amphiphilic block-copolymers like KLE, Pluronic P123 or F127 polymers.[6,22] Such templates are able to form micelles or other lyotropic mesophases leading to heterogeneous structures which result into porous structures upon removal of the template. Depending on the mechanism of mesophase formation soft templating may proceed via “true” liquid crystal templating or via cooperative self-assembly.[6] The difference between these two processes is sometimes subtle as they may merge. In the first case micelles are formed before the surrounding phase condenses while in the latter case micelle formation and condensation of the other phase take place simultaneously. The most prominent representative of cooperative self-assembly processes is the evaporation-induced self-assembly (EISA) which is often applied in the synthesis of mesoporous oxide powders or thin-films via sol-gel chemistry.[13–15]

Diffusion-limited cluster-aggregation (DLCA) is an alternative concept explaining structure formation starting from preformed particles which cannot be pegged to one of the above mentioned concepts. It focusses on the properties of the starting material rather than on the classification of the structure ripening process itself (see chapter 2.3.2).

Turning to the preparation of porous nanostructures via electrospinning the origin of (intra-fiber) porosity is mostly ascribed to a templating effect of a component in the spinning solution or it is believed to arise from a SD process during the spinning process. In chapter 2.5 this state-of-the-art in the understanding of electrospinning will be discussed revealing some lack of knowledge concerning the conceptual understanding of pore formation in this field. In chapter 2.5.4 the relevance of SD to electrospinning is illustrated in detail pointing to the limits of this concept. Otherwise, electrospinning using preformed nanoparticles can also be discussed and understood in terms of the DLCA concept, although this has not been done before. To the best of my knowledge the application of the DLCA concept to electrospinning will be presented for the first time in this thesis (see chapter 2.5.5).

2.2.1.1 Syntheses of porous materials with defined pore sizes

One important property of porous materials is their pore size. Most syntheses of porous matter result in materials with relatively narrow pore size distributions, although hierarchically porous systems with different pore sizes are of even larger interest concerning application (see chapter 2.2.1.2). Before hierarchically porous materials can be addressed, a very brief overview of materials with defined pore sizes is given in order to get an idea how hierarchically porous materials might be synthesized by combining different approaches resulting in unequal but monomodal pore size distribution.

Porous silica materials are intensively studied and serve as model materials in the class of porous inorganic matters. Most syntheses of such materials are soft templating approaches starting from sol-gel precursors like tetraethyl orthosilicate (TEOS) or tetramethyl orthosilicate (TMOS) resulting in structures exhibiting pores of a defined size with a narrow size distribution as a result of the physico-chemical mechanisms involved in their synthesis.[23] Other oxidic materials are accessible via the same approach under similar synthetic conditions if the sol-gel precursor is changed. For the synthesis of porous metal oxide materials metal alkoxides and/or metal halides are typical precursors.

However, there are several classes of porous silica based materials like zeolites, SBA, KIT or M41S materials including the most prominent representatives of these material classes like MCM-41, MCM-48, SBA-15 or KIT-6. All these materials exhibit pore structures of narrow, monomodal pore size distribution but differ in their size, shape and symmetry.

A detailed presentation of these structures and the principle mechanisms involved in their synthesis is well documented elsewhere[6,23] and will not be repeated at this point. Here it only should be noted that the structure of all these materials is determined by molecular interactions between the template and the sol-gel species. These interactions normally result in monomodal pore sizes with narrow size distribution because the structure formation process is driven by thermodynamics which force the templates to form homogeneously sized structures in order to minimize the interfacial energy in the system. Consequently, the pore size of such mesoporous silica materials is determined by properties of the applied template. While surfactants like cetyltrimethylammonium bromide (CTAB) are used as templates for small mesopores, block-copolymers have to be utilized if pores with diameters exceeding 5 nm are desired, because surfactants are not able to template such large structures due to their limited size. In contrast, block-copolymers like KLE, Pluronic P123 or F127 polymers are able to form much larger micelles whose size correlates to their molecular weight.[6,22] Nevertheless, also block-copolymer templating is limited to produce pores not larger than approximately 20 nm because the preparation of soluble block-copolymers with large block lengths is a scientific challenge itself. Hence, block-copolymers which are able to template pores exceeding 20 nm are not (or at least no longer) commercially available.[22] Consequently, materials exhibiting large mesopores or macropores have to be prepared differently. For the preparation of macroporous materials an often applied method is hard-templating with polymer beads.[24,25]

Besides the pore size also other parameters like pore connectivity or symmetry of the porous structure are of considerable impact on the properties of the materials. These structural features can be addressed by the synthetic conditions and are important differences between the above mentioned classes of mesoporous silica materials. For example, the MC41S materials are generally prepared under basic conditions while SBA or KIT materials are obtained from acidic precursor solutions. If the pores in the silica material are aligned in an ordered or disordered manner, if the pores are obtained from spherical micelles or cylindrical micelles or if a three dimensional porous network is obtained also depends on the synthetic conditions. In this respect the template concentration, its hydrophilic/hydrophobic contrast and the synthesis temperature are of considerable importance.[6,23]

2.2.1.2 Hierarchically porous materials

Porous materials are relevant for numerous applications involving surface processes, such as heterogeneous catalysis, separation, electrochemical applications, sensing devices etc. Basically porous materials with defined pore sizes (see chapter 2.2.1.1) are already beneficially for such applications because they exhibit increased specific surface areas compared to imporous nanostructures. However, materials with a narrow pore size distribution are only optimal for specific applications like e. g. separation applications in which the pore size has to match the size of a specific target molecule. For example, in molecular sieves, which can be used for the drying of organic solvents, the pore size should match the size of water molecules which is the reason why zeolites are used for this purpose.

Nevertheless, for other applications - e. g. as heterogeneous catalyst or as electrode material in electrochemical devices - hierarchically pore structures are often better suited because they combine the advantages of different pore sizes. While micro- and mesopores increase the specific surface area of a material significantly and exhibit sizes which affect the selectivity and efficiency in the host-guest interaction between the active sites of the porous material (host) and the reactants/substrates (guest), they suffer from deficient diffusion and convection paths within the material. Diffusion and convection paths enhancing the accessibility of the surface for guest molecules can be granted by macroporous structures. Consequently, hierarchically porous structures exhibiting pore sizes on different length scales are most adequate to meet the demands in such applications.

The practical requirement of hierarchically porous structures motivates the scientists´ search for straightforward methods to prepare hierarchically porous materials. One possibility is to “simply” combine templates of different size which were introduced in the previous chapter 2.2.1.1. Although this concept is realized indeed, the preparative realization of this approach is not as simple as it seems at first glance. Without going into the physico-chemical details explained elsewhere[3,22,26,27] the challenge of this concept consists in finding adequate conditions which allow all different templates to coexist without interacting with each other in a manner which disturbs their template properties. Qualitatively, a certain polarity contrast between template and templated material (e. g. a sol-gel material in the preparation of oxide materials) is required in order to ensure that a phase separation between these two species is enabled. Reversely, this means that different templates are necessarily similar concerning their polarity facilitating some interactions which need to be avoided. This preparative dilemma prevents the combination of different templates to be realized more often in order to prepare hierarchically porous materials. Finding adequate synthetic conditions like pH-value, temperature and composition of the reaction-solution is very elaborate for this synthetic approach and presumably hardly possible for a wide variety of materials.

Another method to prepare hierarchically porous materials is the Nakanishi process which will be discussed in detail in chapter 2.3.1.1. However, the Nakanishi process is limited to the preparation of monolithic materials. Other methods for the preparation of hierarchically porous materials on similar length scales including macroporosity are rare and often highly specialized to specific materials and/or structures[3] leading to the conclusion that further concepts and preparative methods are required which are universally applicable to synthesize different

materials with hierarchical pore structure. The preparation of electrospun fibers is a very straightforward and elegant approach to prepare such hierarchically porous structures featuring intrinsic macroporosity (see chapter 2.5).

2.3 SD and DLCA: Understanding the process of structure evolution during the preparation of porous nanostructures

Concerning the generation of mesoporosity in electrospun fibers two concepts are of particular interest and need to be introduced because they are relevant for the explanation of the pore formation mechanisms during the spinning experiments (see chapter 2.5). Hence, the two concepts of spinodal decomposition (SD) and diffusion-limited cluster aggregation (DLCA) are surveyed in the following chapters 2.3.1 and 2.3.2.

2.3.1 Spinodal decomposition (SD)

The model of SD describes a process starting from a monophasic system which is rapidly quenched into an unstable region of the corresponding phase diagram fast enough to traverse the metastable region of the phase diagram without triggering nucleation and growth mechanisms (i. e. binodal decomposition). The first theoretical investigations describing SD were presented by Cahn and Hilliard for a fluid, bicomponent system which separates into the pure substances A and B.[28,29] These investigations resulted in the well-established Cahn-Hilliard equation which is the basis of more detailed models developed in recent years and resulting in an advanced understanding of SD nowadays. In a simple bicomponent system consisting of e. g. a solvent (substance A) and a solute (substance B) quenching usually takes place via a rapid change in temperature (T) to T_0 (path I in figure 2-3) or a change in composition (expressed in terms of substance amount fraction χ for example) often triggered by solvent evaporation (path II in figure 2-3). In more complex systems, also other changes like chemical reactions destabilizing the monophasic system may cause SD as is the case in the Nakanishi process (see chapter 2.3.1.1). However, in any case the model of SD describes the spatiotemporal evolution of such a destabilized system from the initial state (with $\chi_0(i)_{non\text{-}eq.}(T_0)$; i: substance A or B respectively) at the temperature T_0 towards a (new) thermodynamically stable situation in which two phases 1 and 2 (with $\chi_1(i)_{eq.}(T_0)$ and $\chi_2(i)_{eq.}(T_0)$ respectively) coexist at the considered temperature T_0.

The new equilibrium phases are enriched in component A in the one phase and in component B in the other phase. The compositions of the phases 1 and 2 have to meet the condition

$$n_i(\chi_{i0,\,non-eq.}) = n_i(\chi_{i1,\,eq.}) + n_i(\chi_{i2,\,eq.}) \qquad (2\text{-}1)$$

with

n_i = substance amount of *i* in the considered phase.

due to the conservation of mass. It has to be noted, that none of the two phases necessarily has to consist of pure A or pure B.

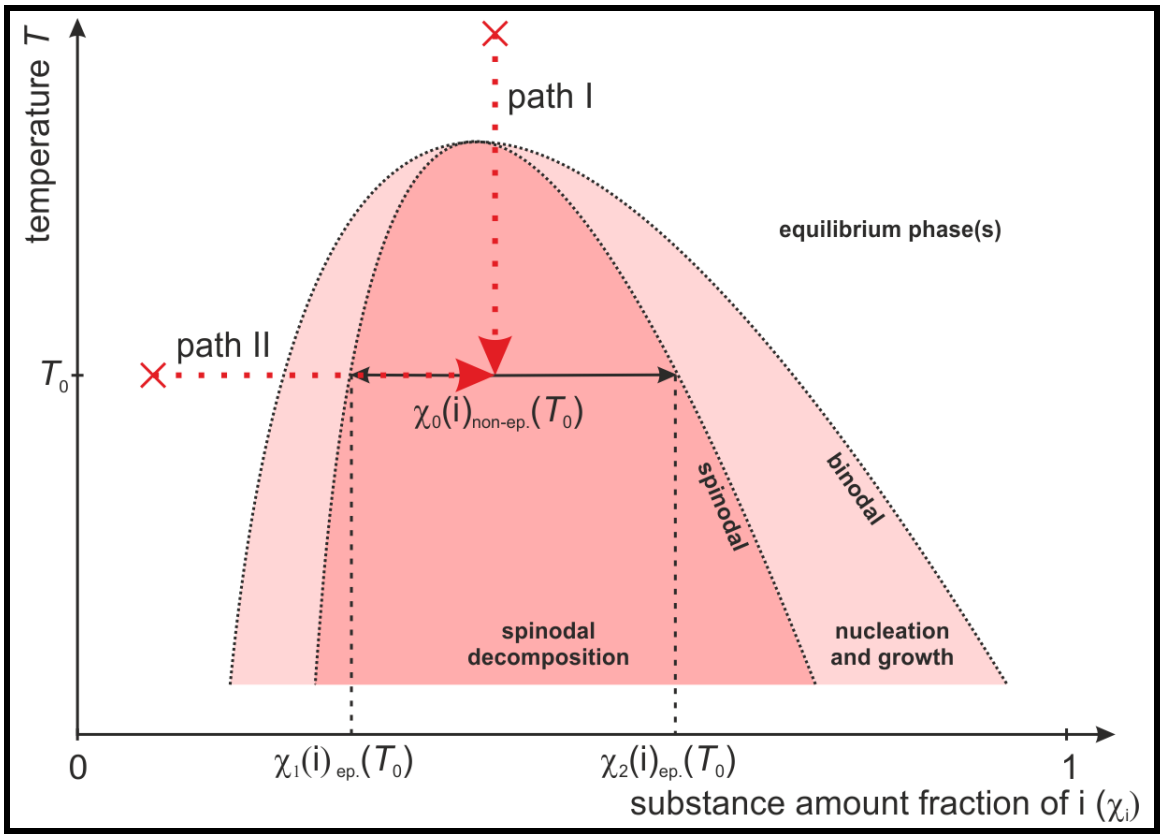

Figure 2-3: Schematic phase diagram illustrating the spatiotemporal evolution of phases in the SD process starting from an initial quenching step. The shown diagram exhibits an upper critical solution temperature (UCST) as it is typical for e. g. polymer/solvent systems, though in other cases also a lower critical solution temperature (LCST) may occur. However, this fact does not alter any principle step of the SD process. A detailed description of the process is given in the text.

The spatiotemporal structure evolution of the quenched unstable system starts with infinitesimal concentration fluctuations around $\chi_0(i)_{non\text{-}eq.}(T_0)$ which develop towards a biphasic, separated system with space and time. There are plenty of theoretical investigations calculating the spatiotemporal evolution of SD[30–37] which are backed by experimental results.[38–41] In the theoretical studies initial concentration fluctuations are modeled by a wavelength *l* which is a dimensionless parameter representing the dimension of space. This wavelength is characteristic of the SD process at any place in the considered system at a given time t_i irrespective of the fact that the characteristic wavelength l_c is a statistic dimension which may be subjected to some local fluctuations (see figure 2-4). The initial concentration fluctuations in SD (spinodal concentrations) are generally different from the equilibrium concentrations (i. e. $\chi_1(i)_{eq.}(T_0)$ and $\chi_2(i)_{eq.}(T_0)$). With elapsing time *t* the initial concentration fluctuations at t_0 converge towards the equilibrium concentrations reached at t_∞ via the transient situations at t_1 and t_2 (see figure 2-4). Simultaneously with the ripening of the concentrations, the initially diffuse phase boundaries sharpen during the time interval between t_0 and t_∞ until two distinctive phases with the compositions $\chi_1(i)_{eq.}(T_0)$ and $\chi_2(i)_{eq.}(T_0)$ are formed. Theory as well as experimental results proved the resulting biphasic structure to be co-continuous as a result of the concentration ripening in SD.

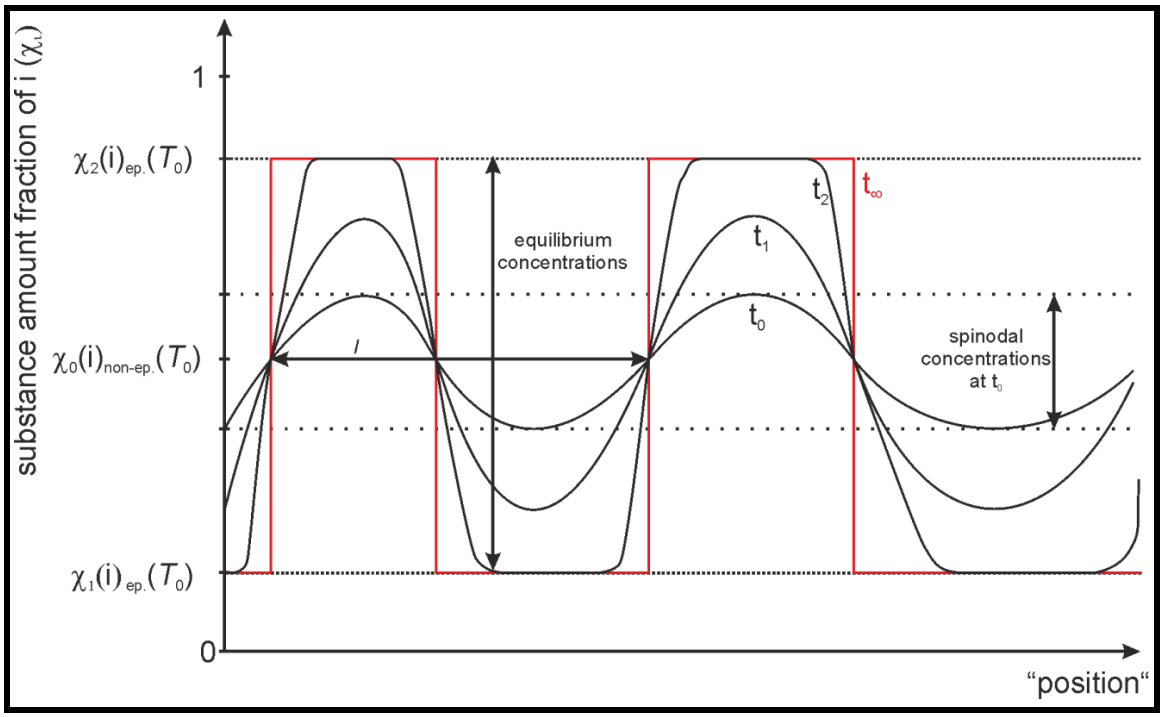

Figure 2-4: Evolution of concentration fluctuations in SD with time. Note that domain size growth is neglected in this picture for clearance, although it may take place simultaneously in later stages of the process (see text and figure 2-5).

However, SD does not only proceed via concentration ripening with time; also the domain size is subjected to a temporal evolution driven by the minimization of surface energy. The growth of domain sizes which is equivalent to an increase of l_c is observed experimentally in polymer blends by time-resolved light scattering in laser scanning confocal microscopy.[40–42] Theoretical simulations on the basis of a time-dependent Ginzburg-Landau equation are able to model the observed growth of domains in polymer blends.[41] It was proven that domain size growth proceeds self-similarly, meaning that the form of the biphasic separated structure stays statistically identical and hence co-continuous while the size of the domains grows. This self-similar growth may proceed over several orders of magnitude but is dependent on the initial composition of the bicomponent system (i. e. $\chi_0(i)_{non\text{-}eq.}(T_0)$, see figure 2-5). In case of an initial composition which is far from being equivolumetric (points A and C in figure 2-5) the domain size ripening may ultimately lead to isolated "islands" of one phase in the continuous other phase. In such case, the resulting structure is indistinguishable from structures typical for nucleation and growth (i. e. binodal) decomposition.

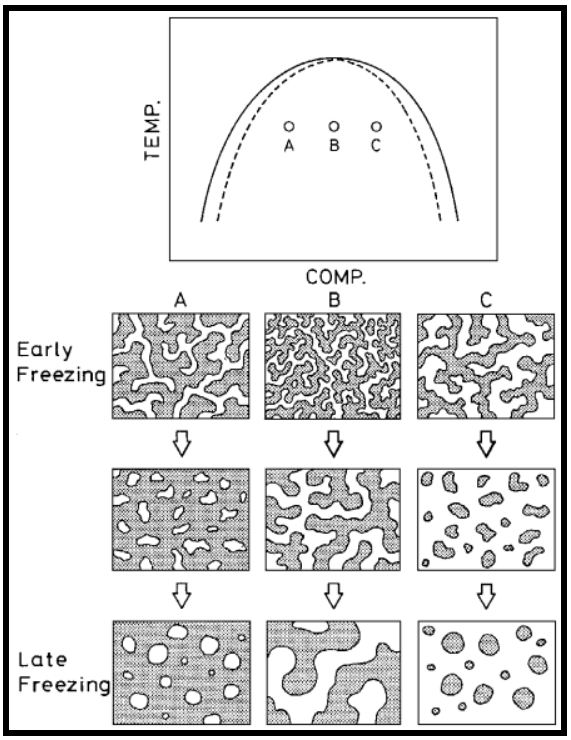

Figure 2-5: Schematic illustration of structures resulting from SD in dependence of the initial unstable composition $\chi_0(i)_{non\text{-}eq.}(T_0)$ (points A, B, C) and moment of observation (i. e. early vs. late freezing).[43]

Fundamentally, the chronological evolution of SD is the same in all cases: In the initial stage (the so-called early stage) solely concentration ripening occurs as illustrated in figure 2-4 while domain size growth does not take place. In the late stage of SD only domain size growth is observed while no concentration ripening proceeds in this phase because the equilibrium concentrations in the two separated phases with $\chi_1(i)_{eq.}(T_0)$ and $\chi_2(i)_{eq.}(T_0)$ are already reached. In the intermediate stage of SD (i. e. after the early and before the late stage) both processes (i. e. concentration ripening and domain size growth) take place simultaneously.

However, not all of the above described spatiotemporal evolutions which can be described within the model of SD do necessarily take place in real experimental systems, because the decomposition process may be stopped at an intermediate state. Consequently, the resulting separated structure in such case is a “frozen” intermediate which is not the thermodynamic equilibrium structure but kinetically stabilized. At which stage a SD process is stopped strongly depends on properties of the experimental system determining the point of solidification of the system which universally occurs at a specific instant of time preventing the decomposition to proceed further. Basically, solvent evaporation or other chemical changes can be the reasons for solidification and interruption of a SD process. In the preparation of porous inorganic materials from sol-gel precursors for example, gelation of a sol represents a chemical change in the system. The Nakanishi process (see chapter 2.3.1.1) or dip-coating experiments starting from sol-gel precursors are examples of SD processes in which solidification occurs due to gelation of a sol.

Though SD can basically be modeled by theoretical calculations at any of the above mentioned stages one fundamental problem is still unsolved: There is no universal theoretical model which is able to capture SD throughout all stage. Instead, there are several models which are only able to describe the individual stages introduced above. Consequently, it is not possible to model the whole process from initial infinitesimal concentration fluctuations up to the completely phase-separated thermodynamic equilibrium structure. The available theoretic models are not able to predict at which point of SD structure freezing occurs since solidification is often also a time-consuming process rather than a spontaneous event which may start at the very beginning but finishes in a later stage of SD. The moment of structure freezing needs to be evidenced experimentally for each investigated chemical system and it is so far not possible to model the process of structure freezing in conjunction with the spatiotemporal evolution of a SD process. In practice, the freezing point can be influenced by several experimental parameters which are consequently adequate to tune material properties in a desired manner during their synthesis. Such “structure-tuning” is well-investigated for syntheses via the Nakanishi process which will be introduced in chapter 2.3.1.1 including a discussion of possibilities to influence the freezing point of SD experimentally.

2.3.1.1 The Nakanishi process: An example of SD processes

Several fundamentals of the SD process were investigated in the context of the Nakanishi process which is a method to prepare monolithic porous materials with bimodal pore structure. The monolithic material is typically prepared from silica sol-gel precursors although there are some reports in which the synthetic concept of the Nakanishi process is transferred to other metal oxide sol-gel precursors[44] or the preparation of silica based materials from water glass.[45] However, the bimodal pore structure of such monoliths is generated by two preparation steps. While the macroporous structure of the monolith is formed in a first step as a consequence of SD between a sol-gel-rich phase and an organic, polymer-rich phase, the mesoporous structure is generated in a subsequent “aging” step. In the initial step the sol-gel precursor reacts until a space spanning gel is formed. The second step consists of a successive heat treatment step in which the gel-network is partly re-dissolved by in situ decomposition of urea: The decomposition of urea produces ammonia which increases the local pH-value partly re-dissolving the macroporous silica network on the surface. This re-dissolution triggers rearrangement of the silica material forming mesopores in the previously solidified co-continuous macroporous network. This second “aging” step of the Nakanishi takes place under basic conditions, on the timescale of a few hours and at temperatures of around 100 °C.[46–48]

However, the first step of the Nakanishi process is the part of the process which will be discussed in detail here in order to explain how SD can be used to “tailor” the structure of porous materials by influencing the moment of structure freezing during the SD process.

In a typical synthesis tetramethyl orthosilicate (TMOS) is reacted in an aqueous acetic acid solution (0.01 M) under addition of polyethylene glycol (PEG, M_w = 10,000 g*mol^{-1}) and urea at typically 25 °C for several hours.[46] Initially, this mixture is a stable and monophasic solution because all components are hydrophilic. When the TMOS reacts under the acidic conditions a sol of silica oligomers is formed which becomes increasingly hydrophobic with proceeding reaction. As soon as the hydrophilic/hydrophobic contrast is large enough a SD process between a hydrophilic PEG-rich and a hydrophobic silica-rich phase is triggered. In physico-chemical terms, the destabilization of the initially monophasic reaction solution can also be explained as follows: The condensation of TMOS precursors generates a polymeric structure and hence decreases the entropy ΔS in the system which can be understood in terms of the Flory-Huggins theory.[46]

Consequently, the Gibbs energy ΔG in the system increases due to

$$\Delta G = \Delta H - T \cdot \Delta S \tag{2-2}$$

giving a further argument why the system gets unstable and SD is triggered as soon as

$$\Delta G > 0 \leftrightarrow \Delta H > T \cdot \Delta S \tag{2-3}$$

In other words, the ongoing sol-gel reaction represents the quenching step of the SD process and PEG acts as porogen (pore forming agent) because it becomes incompatible to the growing silica clusters with proceeding reaction time.

The spatiotemporal evolution of the porous structure in the above mentioned quenched system is dependent on two processes which take place simultaneously: One process is the condensation of the silica oligomers which proceeds until the whole system freezes as soon as the gelation point of the reaction is reached and no further movement/diffusion of silica species is any longer possible. The other process is the phase separation between the continuously reacting silica phase and the PEG-rich phase in the destabilized system which tries to reach its thermodynamic equilibrium by SD. Hence, the whole structure formation process has to take place in the time interval between the first moment when the growing silica oligomers get incompatible to the PEG and the gelation point. This structure formation process can generally be influenced by several parameters like the pH-value, the reaction temperature, the molecular weight of the PEG, the polarity of the solvent or the relative composition of TMOS to PEG. All these parameters influence either the hydrophilic/hydrophobic contrast of the two separating phases or the time interval in which the SD is allowed to proceed. For example, more acidic conditions lead to a faster sol-gel reaction, an earlier gelation of the silica network and hence decrease the time interval of the SD process. A shorter time interval of SD again results in a macroporous silica network exhibiting smaller pore sizes because the self-similar growth of the SD process is interrupted earlier.

For a more detailed description of the Nakanishi process and a more detailed discussion of the underlying physico-chemical principles the reader is referred to the literature.[43,46–48] With respect to the topic of this thesis it is sufficient to highlight that the SD in the Nakanishi process leads to a macroporous (silica) network because a reacting TMOS-phase separates from a polymer-rich phase. This process is allowed to take place over several hours so that self-similar growth during the SD may proceed until the silica network exhibits domain sizes in the range of several hundred nanometers to a few microns.[46,48] This finding needs to be discussed when SD decomposition is consulted to explain the generation of mesoporosity in electrospun fibers because such mesoporous structures are roughly two orders of magnitude smaller. Why SD may lead to such significantly smaller structures in electrospinning experiments will be considered in chapter 2.5.4.

2.3.2 Diffusion-limited cluster aggregation (DLCA)

Diffusion-limited cluster aggregation (DLCA) represents a mechanistic theory explaining the structure formation from particles as building blocks. In this theory diffusion and aggregation of dispersed particles constitute the main concept determining the final structure of aggregates. This model starts from the assumption of initially isotropic distributed individual particles diffusing through a finite space. In the simplest model the diffusing particles stick together irreversibly upon collision. Theoretical calculations predicted irreversible collisions to result in open, fractal structures which may be space spanning representing porous materials.[49] If the aggregation of diffusing particles is partly reversible or if thermally activated rearrangement is enabled, the fractal structures may ripen to more dense aggregates which are not system spanning. The compactness of aggregates is expressed in the fractal dimension d_f which is three for a closest packed three-dimensional aggregate while a three-dimensional complete open fractal structure exhibits the lowest possible $d_f = 1.78 \pm 0.05$.[50] The fractal dimension correlates the radius of gyration r_g of an aggregate to its mass m which is proportional to the number of particles n composing the fractal cluster:

$$n \sim m \sim {r_g}^{d_f} \tag{2-4}$$

From correlation (2-4) it is obvious that growing cluster aggregates diffuse slower, the larger they grow, because the self-diffusion coefficient D is proportional to $m^{-0.5}$:[51]

$$D = \frac{{k_B}^{1.5}}{\pi^{0.5}} \cdot \frac{1}{\sigma} \cdot \frac{1}{m^{0.5}} \cdot \frac{1}{p} \cdot T^{1.5} \tag{2-5}$$

with:

- k_B = Boltzmann constant;
- σ = collision cross section of the particle/aggregate;
- p = pressure;
- T = absolute temperature in Kelvin.

Furthermore, it can be concluded that an open fractal structure which necessarily exhibits a larger collision cross section diffuses slower than a dense structure of the same mass.

Whether DLCA leads to open fractals or close packed structures depends on basically two general parameters: the interaction strength between the particles and the time in which the particles are able to diffuse. The time interval in which diffusion is allowed depends on experimental conditions and may vary strongly. For example, solvent evaporation leading to solidification of the considered dispersion ultimately prevents particle diffusion and depending on the evaporation speed solidification may take several hours to days (e. g. for aqueous bulk dispersions at room temperature) or just (split) seconds as in the case of electrospinning experiments (see chapter 2.5.5).

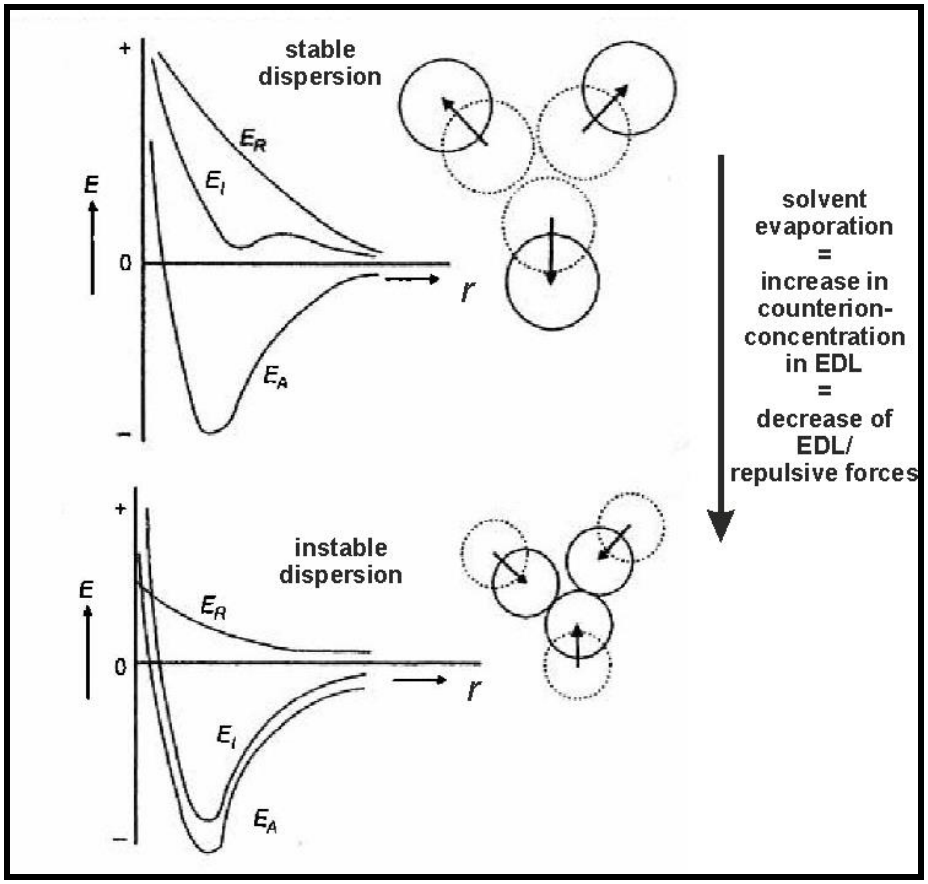

Figure 2-6: Illustration of potential energies E_I resulting from the DLVO theory versus the particle-particle distance *r* obtained by balancing attractive (E_A) and repulsive (E_R) forces ($E_I = E_R+E_A$). Upper part: stable dispersion; lower part: unstable dispersion. Decreasing the thickness of the electrochemical double-layer (EDL) (i. e. a decrease of E_R) by e. g. solvent evaporation leads to a destabilization of the dispersion and triggers coagulation of particles (adapted from[52]).

The other important parameter, the interaction of dispersed colloidal particles is basically described by the DLVO-theory (named after their inventors **D**erjagin, **L**andau, **V**erwey and **O**verbeek). Similarly as the Lenard-Jones potential balances attractive and repulsive forces for uncharged, molecular species, the DLVO theory balances attractive and repulsive forces of colloidal particles stabilized by surface charges. Attractive forces E_A between dispersed particles are predominantly Van-der-Waals forces and repulsive forces E_R are mainly electrostatic repulsions of the charged particle surfaces. While the attractive Van-der-Waals forces are assumed to scale with r^{-6} (r: distance between two particles) the repulsive forces typically scale with r^{-12} resulting in interaction energy-distance plots similar to plots of the Lenard-Jones potential (see figure 2-6). However, there is a fundamental difference: In contrast to the Lenard-Jones potential the repulsive forces in the DLVO theory are strongly dependent on the chemical surrounding of the particles due to the electrochemical double layer (EDL) which stabilizes the particles. The EDL again can be influenced by changes in the pH-value of the dispersion and/or the addition of salts.[52] Consequently, the potential curve which results from the DLVO theory may exhibit different energy minima due to differences in the EDL. In case of a negative energetic minimum, coagulation of particles occurs if they approach each other to the appropriate distance (see figure 2-6, lower part). If the energetic minimum is positive, the dispersion is stable and the mean particle-particle distance will be the distance at which the minimum is seated (see figure 2-6, upper part).

The DLVO-theory is able to explain, why coagulation can occur if solvent evaporates from initially stable dispersions: An initially stable dispersion refers to a situation illustrated in the upper part of figure 2-6, whereas solvent evaporating from the solution changes the situation to that one illustrated in the lower part of figure 2-6. Solvent evaporation necessarily leads to an increase in counterion concentration of the EDL decreasing its thickness and the strength of the repulsive forces which finally may result in coagulation as solvent evaporation proceeds.

Exactly such ongoing solvent evaporation is taking place during electrospinning so that the DLVO-theory explains why solutions in colloidal electrospinning[53] experiments (i. e. electrospinning of solutions containing dispersed nanoparticles) experience destabilization. Consequently, aggregation of particles in a destabilizing colloidal electrospinning solution may be discussed in terms of the DLCA theory which will be introduced in chapter 2.5.5.

2.4 Electrospinning

2.4.1 History and overview

The concept of the first electrospinning apparatus was presented by A. Formhals and subsequently patented as early as 1929.[54,55] His idea was based on a device for the electric dispersion of fluids patented by J. F. Cooley in 1899.[56] However, these inventions did not result in widespread usage of the method neither in a scientific nor in an industrial application directly, because analytic methods to investigate electrospun fibers were not available to that time so that the benefits of this method were not realized. Two specific events were necessary to establish electrospinning in the scientific community: First, several research results of G. Taylor in the 1960s were necessary to gain a first understanding of the physics involved in the electrospinning process.[57–59] Secondly, the availability of methods to investigate nanostructures was indispensable. Electrospun fibers with sub-micron diameters can hardly be investigated by conventional light microscopes due to their intrinsic resolution limit. Hence, a detailed investigation of electrospun fibers depends on the technical development of microscopic methods that are able to analyze structures smaller than the wavelength of the visible light (i. e. some hundreds of nanometers). Among other technologies like atomic force microscopy (AFM) etc., it was especially the omnipresent availability of the scanning electron microscopy (SEM) which promoted the research on the electrospinning method. Consequently, electrospinning did not attract considerable attention in the scientific community before the 1990s. In this decade primarily the work groups around D. H. Reneker and A. L. Yarin contributed numerous results to this new research field.[60–62] Their investigations were mainly focused on the electrospinning of polymer solutions and further theoretical knowledge derived from such fibers. In the following years other research groups, among them the groups around D. Li and Y. Xia[63] or A. Greiner and J. H. Wendorff[64] followed and established electrospinning as a discrete scientific research field. After polymer nanofibers having been investigated widely and the electrospinning process itself was understood in its physical fundamentals, the technique was extended and transferred to other materials. One recent focus of research interest in the area of electrospinning is the preparation of inorganic nanofibers, which was established by first experiments based on the electrospinning of different sol-gel precursors with the beginning of the new millennium.[65] Applications of such electrospun materials are manifold. Basically electrospun fibers representing 1D-nanostructures are interesting for any application in which surface processes are involved because their intrinsically large surface-to-volume ratio is highly accessible to guest molecules (see chapter 2.2.1.2). Consequently, electrospun inorganic fibers are investigated as sensors (e. g. tin oxide fibers, see chapter 3.5.1.1), catalysts (e. g. ceria fibers, see chapter 3.4.1.1), electrode materials and many more.

2.4.2 Electrospinning setup

The basic electrospinning setup shown in figure 2-7 will only be outlined and provided shortly in the following section in order to ensure that the consecutive chapters can be understood. For more detailed information the interested reader is referred to the literature.[66]

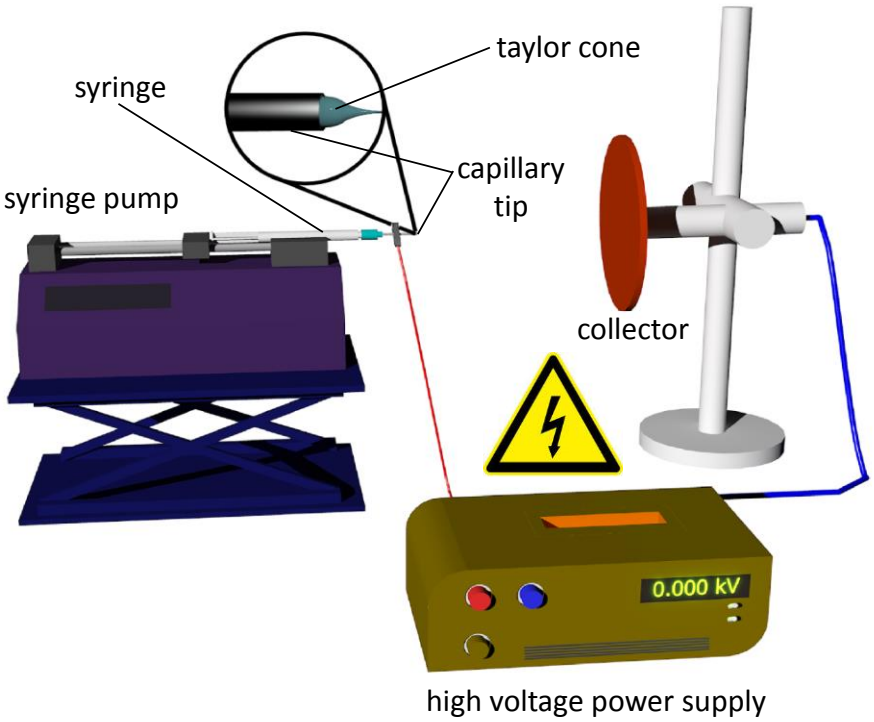

Figure 2-7: Scheme of the general electrospinning setup.

The principle of electrospinning is based on the stretching of a viscous liquid by electric forces. Generally the liquid may be a solution or a melt though the latter is by far not as frequently used so that it will be omitted in the following discussion.

In a typical setup the viscous solution is pumped through a capillary tip (diameter typically some tenth of a millimeter) connected to a high voltage potential (see figure 2-7). This potential is increased until the surface tension of the ejected solution is overcome by the repulsive electric forces resulting in the so-called Taylor cone and a spinning jet is ejected. The jet accelerates towards a collector, e. g. a grounded metal plate in the simplest case, which is placed in a typical distance of approximately 10-30 cm from the needle. The so-called bending and axisymmetrical instabilities, which originate from the charge on the jet lead to further stretching and thinning of the emerging nanofiber while the jet is traveling towards the collector. This is accompanied by the evaporation of the solvent so that a solid fiber is deposit on the collector. These processes are explained in detail in the corresponding literature.[63,64,66–68]

As-spun fibers can be modified by different post-treatments. For example, metal oxide fibers can be obtained if as-spun fibers containing some source of the metal oxide are calcined at elevated temperature removing the spinning polymer by combustion (see chapter 2.4.6).

For the electrospinning experiments of this thesis two hand-crafted setups using some commercially available components were used. One setup consists of the required components illustrated in figure 2-7 with a spinning chamber constructed from acrylic glass. The second setup includes a climate control device that allows the control of temperature (in the range of ± 1 °C) and humidity (in the range of ± 5% relative humidity) in the electrospinning chamber (see figure 2-8 C-E, for further information see chapter 6.2.2.3).

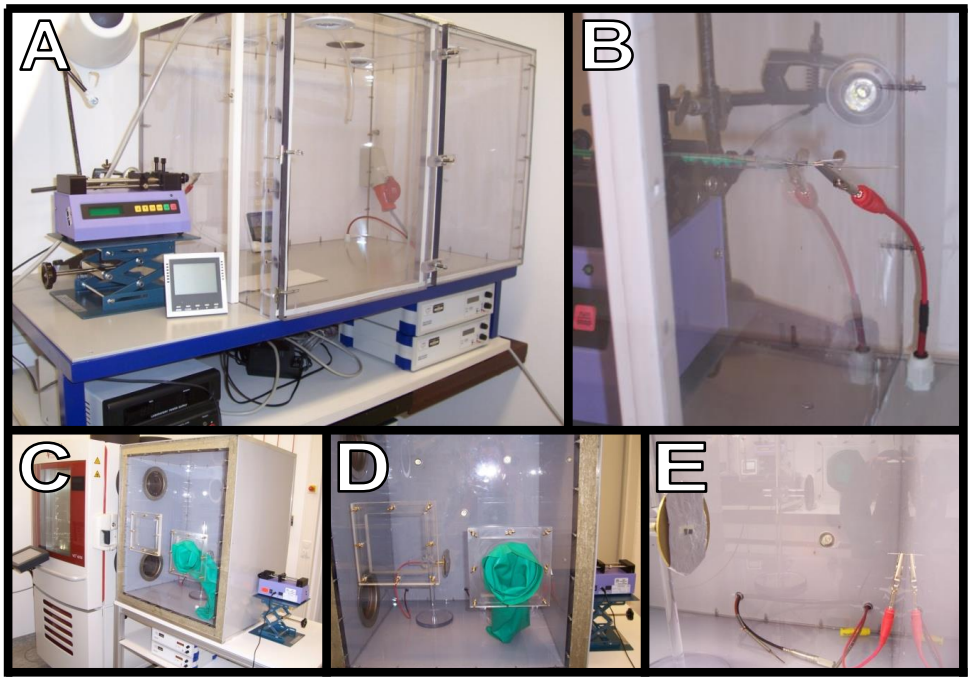

Figure 2-8: Self-constructed electrospinning setup. A, B: standard setup; C-E: setup with climate control.

2.4.3 Experimental requirements for electrospinning

Electrospinning is a method that enables the production of "endless" fibers with diameters in the range of several tens of nanometers up to some micrometers. Nearly all kinds of material can be electrospun and even living species like bacteria can be electrospun as demonstrated earlier.[69] Although there are only few limitations on the materials side there are some basic requirements of the electrospinning method which need to be considered and narrow its applicability slightly. Thus, these requirements which can be roughly summarized with the three keywords viscosity, conductivity and homogeneity are shortly outlined below.

2.4.3.1 Viscosity

The first basic requirement for electrospinning is a colloidally stable, homogeneous solution, dispersion or melts with a viscosity that is adequate for spinning. Viscosities that are adequate for electrospinning are in the range of 0.1-2 Pa·s which can roughly be compared to the viscosity of honey.[62,70] The viscosity can be adjusted by selecting a mostly organic, soluble polymer with a high molecular weight and optimizing its concentration in the spinning solution. The exact value of the viscosity allowing for a stable spinning process is further affected by solvent parameters like e. g. its vapor pressure or surface tension. Also the temperature during the spinning experiment affects the viscosity albeit in practice electrospinning is barely conducted at other temperatures than room temperature.

2.4.3.2 Conductivity

During electrospinning the surface of the solution is charged by applying a high voltage potential at the capillary tip of a syringe (see figure 2-7 and figure 2-8 B). If the ionic conductivity of the solution is too low, the charge may not be distributed homogeneously on the surface resulting in the formation of mostly undesired beads, i. e. droplet-like thickenings on the nanofibers. To suppress bead formation a conducting salt may be added to the solution. For the preparation of inorganic fibers it has to be considered that these salts are contaminants which have to be removed after spinning. For polar solutions the usage of ammonium carbonate as conducting salt is an elegant choice because this salt decomposes completely into gaseous products (ammonia, water and carbon dioxide) upon mild heat treatment. In order to obtain pure inorganic fibers, a subsequent heating step after spinning is necessary in most cases anyway to remove the spinning polymer and condense and/or crystallize the inorganic matter. Other salts such as sodium chloride are not volatile and would stay in the fiber after calcination.

On the other hand, the conductivity of the spinning solution should also not be too high. Otherwise short circuits between the capillary tip and the collector may occur which would prevent a constant jet formation and therefore a stable spinning process. This is a common synthetic problem for the preparation of inorganic fibers from sol-gel precursors, especially if the precursor is ionic and dissociates in the spinning solution.

Nevertheless, it is possible to optimize the composition of the spinning solution in most cases to a conductivity that is adequate for spinning. Consequently, the “conductivity problem” does not significantly limit the preparative possibilities of electrospinning. In practice, the optimum level of conductivity is usually found by “trial and error” and the experience of the experimenter rather than it is measured and set to a distinct value.

2.4.3.3 Homogeneity

The spinning solution or dispersion may basically contain many kinds of different substances: polymers, organic and/or inorganic reagents, nanoparticles or even biomolecules or bacteria. There is only one requirement concerning the composition: The different substances that shall be combined have to be compatible with each other, meaning that the mixture has to stay monophasic or at least metastable as long as the electrospinning experiment is conducted. The precipitation of any component in the spinning solution has to be avoided before spinning. This may be a problem, for instance, when polar and nonpolar substances have to be combined.

The homogeneity of the spinning solution is a major preparative challenge concerning the preparation of inorganic fibers from nanoparticles (see chapter 2.4.6). Dispersions of inorganic nanoparticles can only be stabilized in specific solvents and only up to a limited concentration.[71–74] Sometimes this substantially limits the choice of solvents which may be used for the electrospinning experiment and hence finding a spinning polymer that is compatible with such dispersions in an adequate concentration range represents a major synthetic task: First, there is the necessity to dissolve sufficient polymer to achieve a viscosity of the solution high enough for spinning. Secondly, the overall concentration of nanoparticles should not be too low, because otherwise the amount of nanoparticles will not be sufficient to form an inorganic fiber after combustion of the polymer. As a rule of thumb the nanoparticle mass concentration in the

spinning solution should be roughly the same as the polymer concentration or at least one third of the polymer concentration to prevent disintegration of the fiber morphology during calcination.

2.4.4 Properties of electrospun fibers: advantages and challenges

Properties of electrospun fibers depend on both the material and the structure of the fiber mat. The morphological shape of electrospun fibers determines some essential properties elucidated below which are a direct consequence of their 1D-nanostructure. To be straightforward the following discussion will be focused on metal oxide fibers which constitute an important subclass of inorganic materials and which are investigated within this thesis.

Electrospun fibers normally obtained as nonwoven mats with a random orientation on the collector exhibit a 1D-nanostructure which leads to an intrinsically huge void space between individual fibers resulting in a macroporous inter-fiber structure (see figure 2-9). Such fiber mats generally possess a tremendous overall porosity which is significantly higher than it could be obtained for other nanoarchitectures like dip-coated thin-films even if these are prepared with the help of macropore templates.[24,27] Simultaneously, the nanoscale diameter of electrospun fibers results in large specific surface areas typically in the range of approximately 30 - 200 m^2/g for oxide nanofibers (see chapter 3) which is roughly comparable to the specific surface areas of dip-coated thin-films (i. e. a 2D-nanostructure).[1]

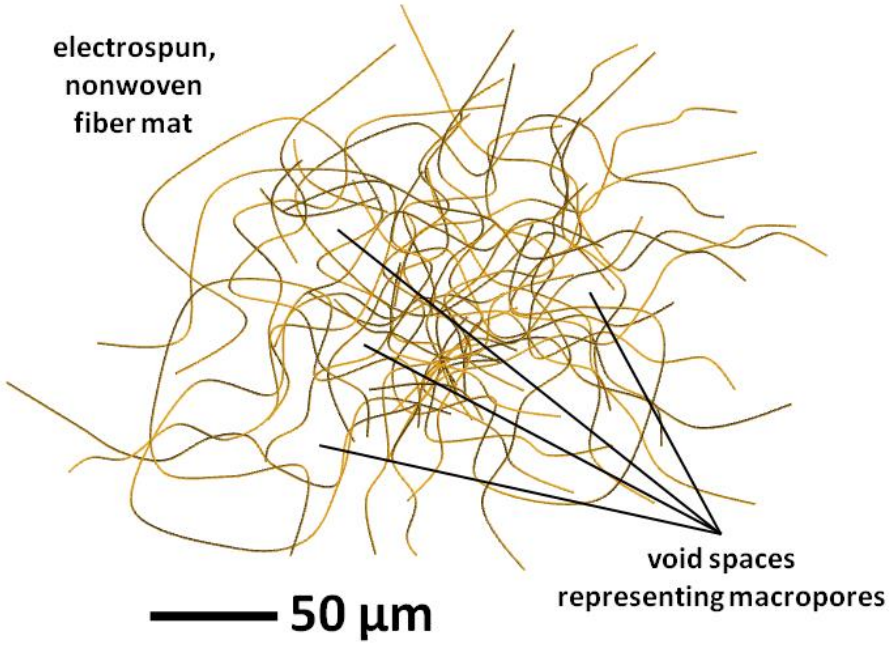

Figure 2-9: Electrospun nonwoven fiber mat: Void spaces between individual fibers represent macropores (adapted with permission from[75], Copyright 2011 American Chemical Society).

[1] It has to be noted that the density of the oxide (in the dimension $[g \cdot cm^{-1}]$) has a strong impact on these values (see chapter 2.6.3). Nevertheless, a rough mathematical estimation of the specific surface area of nanofibers compared to particles is presented below (see chapter 2.4.5).

Compared to nanoparticles (i. e. a 0D-nanostructure) the surface of fibers can be calculated to be as large as two third of the specific surface area of spherical particles with the same radius *r*.[2,[76]] Hence, in case the focus lies only on the maximization of specific surface areas spherical particles are the favorable structure. Otherwise, the 1D-nanostructure of fibers exhibits advantages which may compensate the slightly lower specific surface area. For instance, in applications like semiconducting sensing devices electronic conductance is required because the sensing reaction on the active material generates an electronic signal which needs to be promoted to a drain in order to be able to construct a working sensor.[77,78] In this respect particle-based systems suffer from grain boundaries which are an intrinsic barrier for conduction paths because they may interrupt the percolation path from the active site to the drain.[79] In contrast, the "endless" axis of electrospun fibers may function as percolation path as long as no intra-fiber grain boundaries or fiber-cracks are present interrupting the percolation path.[80]

As already mentioned (see chapter 2.2.1.2), the inter-fiber macroporosity of electrospun nonwoven mats enhances mass transport of guest molecules to the surface of the fibers. If fibers with additional intra-fiber mesoporosity can be prepared this further improves the accessible surface area not only for small molecules like nitrogen gas but also for larger substrates that even may be as large as biomolecules. Such hierarchically meso-/macroporous fibers are interesting candidates for applications in which surface reactions are pivotally involved as for example in heterogeneous catalysis: Electrospun fibers may be used as (solid, "stationary" phase) catalyst for processes with the reactants in a liquid or gaseous, "mobile" phase. Superior catalytic performance of electrospun fibers was demonstrated for some applications,[81–83] which can be ascribed to the above mentioned beneficial morphology of the nanofibers.

Recently, the morphology of nanofiber catalysts revealed some further benefit: Electrospun fibers can be used as sophisticated model catalyst to monitor degradation of catalysts under reaction conditions. If an active material experiences any structural degradation during catalysis, such degradation can be observed by simple electron microscopy on fibrous nanostructures. In contrast, such morphological transformations cannot be detected in a similar simple manner on catalysts consisting of packed nanoparticle. Hence, electrospun model catalysts can be successfully employed to study catalytic activities in correlation to structural and morphological rearrangements.[84,85]

Apart from the above mentioned advantages, electrospun materials also exhibit some basic challenges which need to be considered: First, up-scaling is a challenge if nanofibers shall be produced in industrial dimensions via electrospinning. Although some industrial electrospinning setups are already commercially available so far,[86,87] the dimensions of nonwoven mats that can be produced are limited to some square meters. Furthermore, such fiber mats usually feature thicker fiber diameters than fibers from typical scientific lab setups as a consequence of the slightly altered technique used in industrial setups necessary to circumvent the "batchwise" use of syringes as reservoir for the spinning solution.[88] Additionally, such a setup may cause some problems if air-sensitive spinning solutions should be spun which is especially problematic if inorganic nanofibers are prepared via sol-gel chemistry: Highly reactive sol-gel precursors may

[2] In this comparison the top and bottom surfaces of the cylinder are neglected.

react and condense in the reservoir before they can be spun to fibers. Thus, especially for up-scaling purposes and industrial production of inorganic nanofibers it is essential to develop an electrospinning technique for inorganic fibers not based on sol-gel chemistry. Therefore, electrospinning of dispersible inorganic nanoparticles is a very promising approach (see chapter 2.4.6).

A second challenge concerning electrospun fibers of oxide materials arises from their mechanical properties. Metal oxides are generally hard and brittle materials. If such materials are spun to fibers with just some hundreds of nanometers in diameter the fiber mats are prone to crack when handling them destroying the beneficial "endless" 1D-nanoarchitecture (see above). Furthermore, the preparation of inorganic nanofibers using organic polymers as spinning auxiliary (see chapter 2.4.6) suffers from huge mechanical stress within the fiber mats during the calcination process also provoking cracks. During the removal of the polymer mechanical stress arises from the shrinkage of the fibers that accompanies this process. Attaching electrospun fiber to substrates may help to overcome such difficulties. But in contrast to dip-coated thin-films, which are generally fixed to a substrate, the attachment of electrospun fibers to a mechanical support is much more complicated because the contact area between fibers and substrate is much smaller. So far investigations on fiber anchorage on substrates did not lead to satisfying results for a broad variety of materials.[89]

Finally, safety and health issues of nanostructures like particles or fibers are still a matter of research since the consequences of the invasion of nanostructures in the human organism for instance via inhalation are unclear.[90] In this context electrospun nanofibers have the huge advantage of forming nonwoven mats of "endless" fibers which are much less prone to be released as respirable dust than individual nanoparticles. Nevertheless, the release of small, cracked fiber sections which may be generated upon mechanical stress of nonwoven mats needs to be effectively prevented because it is expected that especially inorganic fibrous materials may cause similar reactions of the human body as e. g. silica based materials in the asbestosis disease.

2.4.5 Rough estimation for the specific surface area of nanofibers

As the specific surface area is a pivotal property of nanoarchitectures, it is helpful to roughly estimate an expected specific surface area of electrospun fibers for oxide materials investigated in the course of this thesis. A comparison of electrospun fibers to nanoparticles with the same radius *r* was already presented elsewhere[76] and will not be repeated here. As already mentioned in chapter 2.4.4, these former calculations resulted in a 1.5-fold specific surface area for nanoparticles compared to fibers with the same radius *r*.[3]

[3] In this comparison the top and bottom surfaces of the cylinder are neglected.

However, starting from the assumption that a mass of 4 mg material with a density of 4 g·cm^{-3} is considered the volume of this material will be 1 mm^3.[4] As a bulk material this volume could exist in a cubic shape with an edge length of one millimeter (see figure 2-10 A) possessing a specific surface area of 1.5·10^{-3} m^2*g^{-1}.

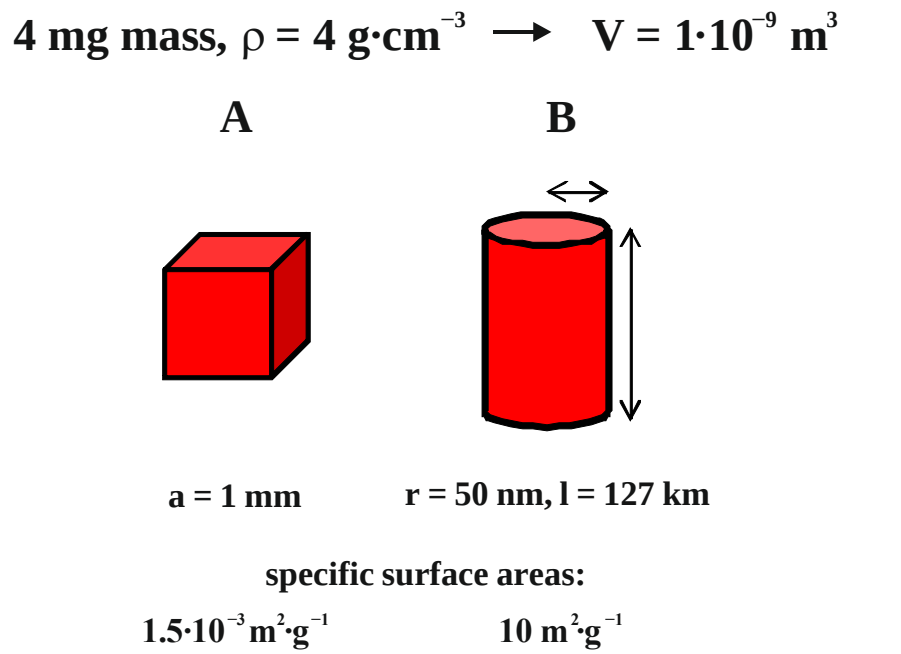

Figure 2-10: Comparison of "shape model materials" with identical volume. A: bulk material with cubic shape; B: (electrospun) nanofiber with ideal cylindrical shape.

In electrospun fibers the same volume would possess the form of a cylinder with an exemplary radius of 50 nm which is a typical value for electrospun nanofibers. This cylinder has a length of approximately 127 km resulting in the assumed volume of one cubic millimeter (see figure 2-10 B and table 2-1).

Table 2-1: Calculation of specific surface areas of the "shape model materials" with identical volume presented in figure 2-10.

sample morphology	specific surface area (absolute values)	relative surface ratio
bulk	$\frac{6 \cdot a^2[\mathrm{m}^2]}{4 \cdot 10^{-3}\mathrm{g}} = 1.5 \cdot 10^{-3} \frac{\mathrm{m}^2}{\mathrm{g}}$	:= 1
nanofiber[1)]	$\frac{2 \cdot \pi \cdot r \cdot l[\mathrm{m}^2]}{4 \cdot 10^{-3}\mathrm{g}} = 10 \frac{\mathrm{m}^2}{\mathrm{g}}$	6667

[1)]: The areas of the bottom- and top-surfaces of the cylinder are neglected in the calculation.

[4] A density of 4 g·cm^{-3} is a typical value for inorganic oxides like e. g. titania as representative example.

According to this estimation the nanofibers have a specific surface area of approximately 10 $m^2 \cdot g^{-1}$ which is roughly the 7000-fold value compared to the bulk material. Furthermore, electrospun fibers, especially inorganic ones, are normally not as smooth as an idealized cylinder. This will certainly lead to an increase in the specific surface area of real nanofibers. Considering that the diameter of nanofibers strongly influences the specific surface area of the material it is worth calculating how the specific surface area of nanofibers is affected by their diameter: Reducing the fiber diameter of a cylinder by a factor of ten results in a 100-fold increase of its length if the volume is kept constant. This causes an increase of the specific surface area by a factor of 10. In other words, assuming a constant volume the surface area and the diameter of a cylinder are inverse proportional to each other.

To conclude the preceding estimations lead to an expected surface area of oxide nanofibers around 10 $m^2 \cdot g^{-1}$ which seems to be in accordance with measured values presented in chapter 3: It should be noted, that the measured values presented there refer to fibers which exhibit additional mesoporosity which is not considered in the above calculations tending to result in an even higher specific surface area. This effect is partly counteracted by slightly larger fiber diameters evidenced by electron microscopy.

2.4.6 Synthetic concepts: Different approaches towards metal oxide nanofibers

Metal oxide nanofibers can be synthesized by electrospinning via different synthetic routes (see figure 2-11). These different synthetic concepts exhibit some specific benefits and drawbacks which have to be considered when inorganic fibers shall be prepared. However, not all pathway-specific particularities are known so far and it is a matter of this thesis to gain further insight in this context.

The first synthetic approach towards electrospun metal oxide fibers is to add an inorganic precursor, typically a metal halide or a metal alkoxide, to a spinable polymer solution (see figure 2-11 A and figure 2-11 B). Via sol-gel reactions these precursors can then be chemically transformed to the corresponding metal oxide. Such sol-gel reactions may already start during the spinning process and are usually completed by thermal treatment of the electrospun composite fibers. The thermal treatment is also necessary to remove the spinning polymer by combustion and is usually adjusted for the specific metal oxide. The sol-gel approach is already widely used for the synthesis of a variety of metal oxide fibers and consequently the most investigated approach.[65]

Basically, it is also possible to electrospin a sol-gel solution without the addition of any organic polymer, because sol-gel solutions may become very viscous during gelation of the precursors. When the sol-gel precursors react, a network of metal-oxygen bonds is established resulting in the formation of a gel that can be considered as an inorganic, cross-linked polymer featuring a high viscosity in solution. Depending on the degree of condensation of the precursors the viscosity of sol-gel solutions changes during the reaction. This, however, can be problematic as spinning of sol-gel solutions suffers from increasing viscosity with ongoing sol-gel transition which in turn affects the electrospinning process and finally prevents it.

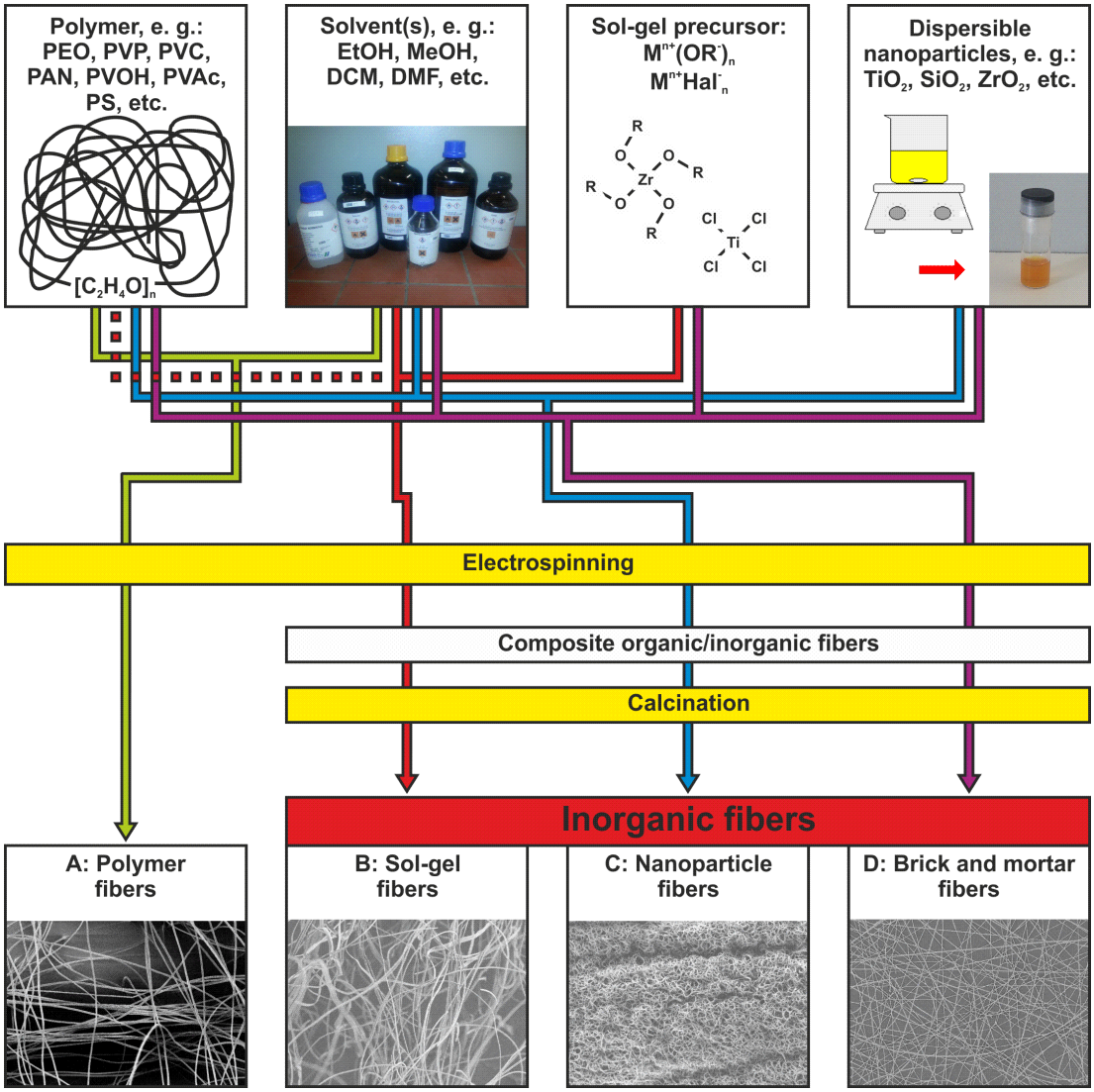

Figure 2-11: Synthetic concepts for the preparation of electrospun fibers: A: preparation of polymeric fibers; B: preparation of inorganic fibers via the sol-gel route (with or without the addition of organic polymers); C: preparation of inorganic fibers via the nanoparticle approach; D: preparation of inorganic fibers via the "brick and mortar" approach.

To avoid such problems an alternative concept is to use preformed inorganic nanoparticles instead of sol-gel precursors (see figure 2-11 C).[75,91] In this strategy a viscous solution of an organic polymer is combined with a dispersion of inorganic nanoparticles (NPs). As inorganic nanoparticles are chemically more or less unreactive compared to sol-gel precursors the spinning solution is chemically stable as long as precipitation of any component and side reactions is suppressed. The bottlenecks of this synthesis route are the availability of dispersible inorganic nanoparticles and the preparation of inorganic dispersions with a certain "threshold" concentration of nanoparticles sufficient to form an inorganic fiber after polymer removal. This nanoparticle-approach (NP-approach) is much less investigated than the sol-gel approach and the preparation process is much less understood on its physico-chemical basis. The NP-approach can be considered as part of the more general colloidal electrospinning concept.[53] Colloidal electrospinning is mostly used to prepare composite fibers of different compounds so that the

spinning polymer is only rarely removed after the spinning experiment. Another important advantage of the NP-approach is that materials are accessible, which cannot be prepared via sol-gel chemistry. One example is a report on titania in the TiO_2(B) modification,[92] a metastable crystalline phase of titania, which is not accessible via simple sol-gel chemistry. Hence, electrospun fibers of this material can only be prepared if dispersible TiO_2(B) nanoparticles are spun to nanoparticle-derived fibers (NP-fibers). In this report the synthesis of TiO_2(B) nanoparticles was succeeded in a specific mixed solution of ionic liquids which cannot be used to prepare a spinning solution using the sol-gel approach.

In some cases it is difficult to sinter the nanoparticles during the combustion of the organic polymer, resulting in the loss of the fibrous morphology. In this case a synthetic concept, which uses a spinning solution containing nanoparticles and a small amount of sol-gel precursor as "molecular glue", can be applied (see figure 2-11, D). This recipe was first reported by Szeifert et al. for the preparation of thin-films via dip-coating and is known as the "brick and mortar" concept.[2] The "brick and mortar" concept (B+M-approach) is barely applied for electrospinning syntheses up to now. To the best of my knowledge the only report on all-inorganic electrospun "brick and mortar"-fibers (B+M-fibers) are composite metal oxide/silica fibers prepared by combining silica nanoparticles with metal oxide sol-gel precursors.[93] There are no reports on single metal oxide B+M-fibers so far. Consequently, fundamentals of this approach still need to be studied in detail. Within this thesis the B+M-approach is investigated and compared to fibers prepared by the sol-gel and NP-approach on the example of tin oxide fibers. Such investigations can reveal specific synergetic features of B+M-fibers compared to pure sol-gel-derived or NP-fibers. The corresponding results are discussed in the chapters 3.5.4 and 3.5.5.

2.5 Formation of mesoporous electrospun fibers

2.5.1 Porous electrospun fibers

Electrospun nonwoven fiber mats intrinsically exhibit significant macroporosity in form of inter-fiber void spaces. Consequently, only micro- and mesoporosity have to be implemented by an adequate synthesis of electrospun fibers in order to obtain hierarchically porous nanostructures in a straightforward manner. While the macropore void spaces represent inter-fiber porosity, micro- and mesoporosity have to arise mainly from intra-fiber porosity (see figure 2-12). This thesis focusses on the characterization of the mesoporosity in electrospun nanofibers though some commentary on microporosity will be given where it is helpful in the overall context. For a detailed investigation of microporosity the method of argon physisorption should be applied while macroporosity can be characterized by mercury intrusion porosimetry. However, such investigations are beyond the scope of this thesis and are a task for future projects. Consequently, this section will focus on the theoretical background concerning mesoporosity of electrospun nanofibers and former experimental results in this context to illustrate the state of the art concerning mesoporous electrospun fibers.

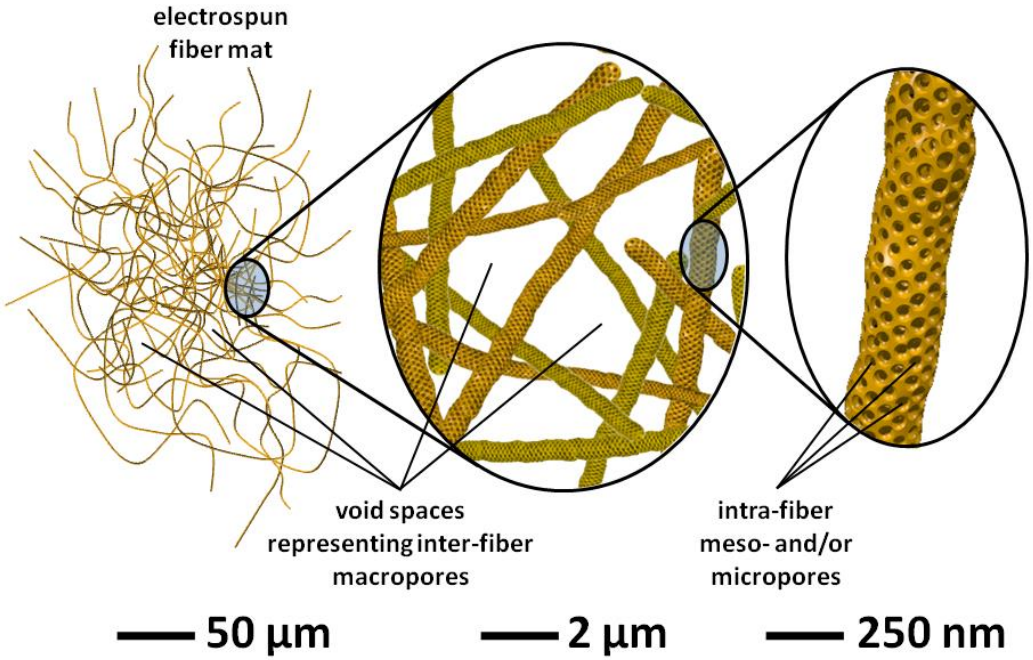

Figure 2-12: Electrospun nonwoven fiber mat: Void spaces between individual fibers represent inter-fiber macropores. Meso- and/or microporosity predominantly have to arise from intra-fiber porosity (adapted with permission from[75], Copyright 2011 American Chemical Society).

Theoretical studies predicted that porous or hollow polymer fibers may occur under adequate conditions due to phase separation phenomena, mass transport and fluctuations taking place within the electrospinning jet as a consequence of solvent evaporation.[94–96] Several experimental results back these theoretical predictions and also the structure of some inorganic electrospun fibers seem to be in accordance with such theory.[97,98]

Mesoporous electrospun fibers can be prepared by different techniques: Soft templating by micelle-generating block-copolymers is an adequate approach to introduce mesopores into polymeric or inorganic nanofibers analogously to the preparation of dip-coated thin-films.[81,99–102] Alternatively, the combination of two polymers in the electrospinning process and a subsequent selective removal of one of them afterwards can also result in porous electrospun fibers even when none of the polymers is a micelle-forming block-copolymer.[103]

Yet, more elegant ways to generate mesoporosity within electrospun fibers exist, which do not require the addition of a template or a second polymer which first have to be synthesized or purchased and removed in a subsequent step afterwards. Such synthetic concepts are known as self-assembly processes. Also in the field of electrospinning several studies give evidence that self-assembly processes may occur during the experiments resulting in the formation of mesopores in polymer fibers. In these investigations parameters like humidity in the spinning chamber,[104,105] temperature,[106,107] molecular weight of the spinning polymer[105] or solvent vapor pressure[107,108] were found to influence the self-assembly process and hence the mesoporosity. In all cases basically the same explanation for the occurrence of mesoporosity is given: The change of the parameters always influences a phase separation process during the spinning process which leads to the generation of mesoporosity as a consequence.

However, such results cannot be simply transferred and adapted to inorganic fibers, because the electrospinning solutions used to prepare inorganic fibers are much more complex. In most cases the inorganic material or its precursor are combined with an organic spinning polymer to achieve an adequate viscosity of the solution for electrospinning (see chapter 2.4.6). Hence, interactions between the inorganic material (i. e. sol-gel precursors and/or preformed nanoparticles) and the spinning polymer have to be considered. Furthermore, it has to be taken into account that the spinning polymer may also act as pore forming agent (porogen) complicating the cause study concerning the origin of mesoporosity. Fortunately, solutions for the preparation of dip-coated thin-films are similar to electrospinning solutions in many aspects, so that knowledge from this scientific field may help with the understanding of pore forming processes in electrospinning of inorganic materials (see chapter 2.5).

If the literature on porous electrospun inorganic fibers is surveyed, another point of criticism is uncovered: In a lot of cases porosity of electrospun fibers is only investigated qualitatively, mainly by electron microscopy examining whether pores can be found at all or not. In the electrospinning community, analysis via physisorption experiments is not very common. Such analyses on fibers are presented only rarely and the data are often superficially evaluated: Physisorption is predominantly performed to estimate the specific surface areas of selected fiber samples within some studies. Detailed analyses of porosity and pore size distributions are rare. This is probably a consequence of ambiguities concerning the evaluation of physisorption data of electrospun fibers. Investigations on the mesoporosity via physisorption analysis generally require some preliminary information on structural features like the pore geometry in the sample. For electrospun fibers it is unclear which evaluation method of the physisorption data is best suited to analyze their porosity because pore geometries are not known (for details see chapter 2.6.2). Furthermore, the inter-fiber void spaces may have significant but presumably unpredictable influence on the sorption behavior of electrospun fiber mats, especially in the upper relative pressure range of the physisorption isotherms (i. e. $p/p_0 > 0.9$), which correlates to large mesopores. Hence, such fundamental questions have to be investigated before any sophisticated study on the porosity of electrospun fibers can be conducted as it will be presented in chapter 3.2.3 for some representative samples.

2.5.2 Preliminary investigations on electrospun titania fibers

Preliminary investigations on the formation of mesoporous inorganic fibers from preformed oxide nanoparticles were conducted on titania fibers[1,75] giving first insights into mesopore-generating processes in such electrospinning systems. Several experiments within this thesis, especially regarding the synthesis of zirconia fibers (see chapter 3.3), were performed in analogy to the previous titania experiments. The knowledge obtained from the preceding study may help to understand general conclusions of this thesis concerning mesopore-generating processes. Furthermore, the results on different metal oxides will be compared to each other to elucidate general similarities in the formation of mesopores in electrospun metal oxide fibers irrespective of the material (see chapter 3.6). For a more general consideration the result on the titania fibers will be incorporated in such comparison.

Table 2-2: Overview of all synthesized titania samples and composition of the corresponding solutions that were used for the syntheses.

sample no.	sample category	polymer	TiO_2	weight ratio TiO_2/polymer	solvent	wt.-% solvents
1	sol-gel fibers	4.9 wt.-% PVP	15 wt.-% $Ti(OiPr)_4$ (≙ 3.2 wt.-% TiO_2)	0.65/1	EtOH	60.3
2	pure particles	none	"crystalline" WCS-NPs	---	MeOH	96.0
3	NP-fibers	2.0 wt.-% PEO	1.0 wt.-% TiO_2 [1)]	0.5/1	$CHCl_3$/MeOH	48.5/48.5
4	NP-fibers	2.0 wt.-% PEO	1.0 wt.-% TiO_2 [1)]	0.5/1	CH_2Cl_2/MeOH	48.5/48.5

[1)]: **"crystalline", wet chemically synthesized nanoparticles (WCS-NPs)**

Table 2-3: Physisorption results on electrospun titania nanofibers: BET[1)], CPV[2)], TPV[3)] and relative porosity[4)] values. For the calculation of the different data see chapter 2.6.

sample no.	sample category	TiO_2 source	solvent(s)	BET[1)] [$m^2 \cdot g^{-1}$]	CPV[2)] [$cm^3 \cdot g^{-1}$]	TPV[3)] [$cm^3 \cdot g^{-1}$]	relative porosity[4)] [%]
1	sol-gel fibers	sol-gel TiO_2 i. e. $Ti(OiPr)_4$	EtOH	68	0.082	0.090	25.9
2	pure particles	"crystalline" WCS-NPs	MeOH	73	0.120	0.126	32.9
3	NP-fibers	"crystalline" WCS-NPs	$CHCl_3$/MeOH	164	0.335	0.366	58.8
4	NP-fibers	"crystalline" WCS-NPs	CH_2Cl_2/MeOH	111	0.285	0.334	56.6

[1)]: **specific surface area calculated by the BET method;**
[2)]: **cumulative pore volume calculated by the DFT method; this is the pore volume of the last data point in the CPV plot;**
[3)]: **total pore volume calculated by the Gurvich rule (see equation (2-11));**
[4)]: **calculated from the TPV values (for explanation of the data reduction see chapter 2.6.3.1).**

The compositions of some titania samples investigated in the former study are presented in table 2-2 and the corresponding physisorption results are listed in table 2-3. All data are presented analogously to the data of the materials studied within this thesis.

In the former study dispersible titania nanoparticles were prepared in two states of low and high crystallinity.[5] These particles were inaccurately distinguished as “amorphous” or “crystalline” ones, respectively. Here, only the fibers obtained from the more “crystalline” titania nanoparticles are selected for comparison, because they were calcined at the same temperature as the other materials (i. e. 550 °C), while the fibers from “amorphous” titania nanoparticles were calcined at slightly lower temperature (i. e. 500 °C). To complete the selection of samples needed for the comparisons of the different metal oxides a sample of pure “crystalline” titania nanoparticles and titania sol-gel fibers prepared according to a literature synthesis[109] are considered.

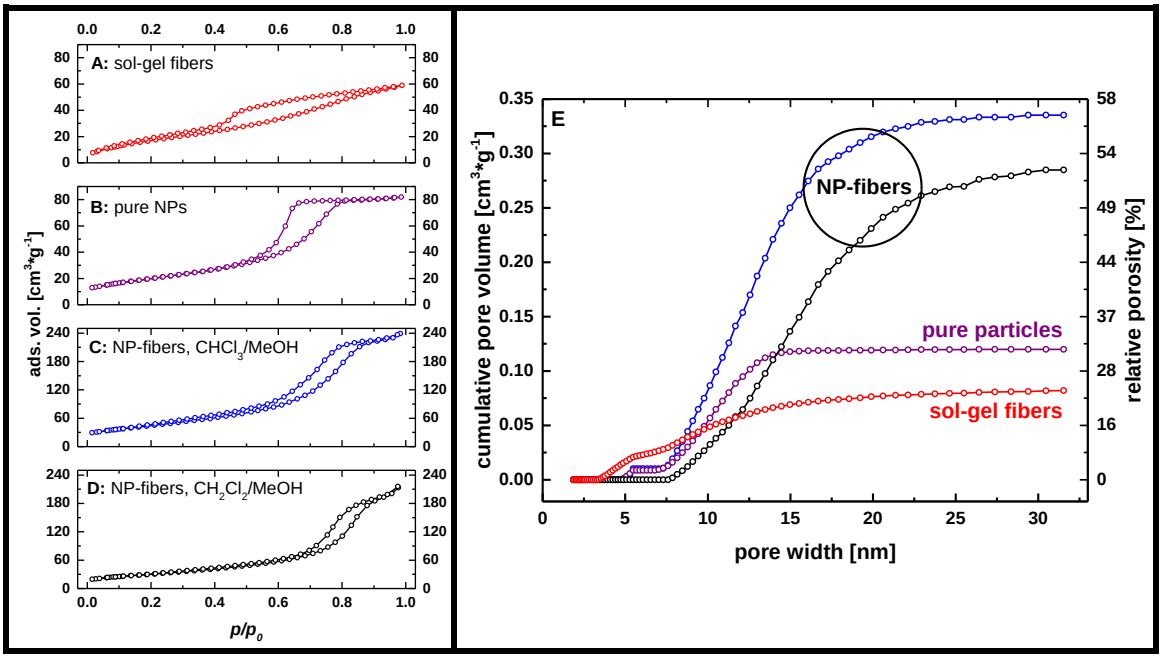

Figure 2-13: N_2-Physisorption isotherms (A-D) and CPV plots from DFT (E) of different titania fibers and of pure titania NPs. For the DFT analysis the “spherical adsorption” model is used in analogy to the investigations on other materials in this thesis (see chapter 3.2.3). Magnifications of the isotherms can be found in the appendices (see figure 6-5–figure 6-8). Color coding: red: sol-gel fibers spun with 4.9 wt.-% PVP (see table 2-2, sample 1); purple: pure, calcined titania NPs (see table 2-2, sample 2); blue: fibers prepared from titania NPs spun from mixed $CHCl_3$/MeOH as solvent with 2.0 wt.-% PEO (see table 2-2, sample 3); black: fibers prepared from titania NPs spun from mixed CH_2Cl_2/MeOH as solvent with 2.0 wt.-% PEO (see table 2-2, sample 4).

[5] The crystallinity of the titania particles was adjusted in the synthesis of the nanoparticle dispersions by temperature during and duration of the synthesis. Experimental details and characterization of the particles are presented elsewhere.[75]

The following conclusions are results of the previous titania study and are only shortly restated and illustrated here: First, nanoparticle-derived titania fibers showed an increased total mesoporosity compared to sol-gel fibers (see figure 2-13). It was concluded that the mesoporosity was generated by a SD process during electrospinning and was not a replication of a porous structure of pure polymer fibers consisting of the spinning polymer. Comparative investigations revealed that the formation of such mesoporous titania fibers depends on parameters like crystallinity of the nanoparticles, solvent composition, molecular weight of the polymer and humidity during spinning. It was explained that the "crystalline" particles are more prone to precipitate from the spinning solution due to their inferior dispersibility compared to the "amorphous" particles: The starting composition of the spinning solution containing the "crystalline" particles is closer to a phase boundary than the starting composition of the spinning solution containing the "amorphous" particles facilitating the initial quenching step of SD (see figure 2-14).

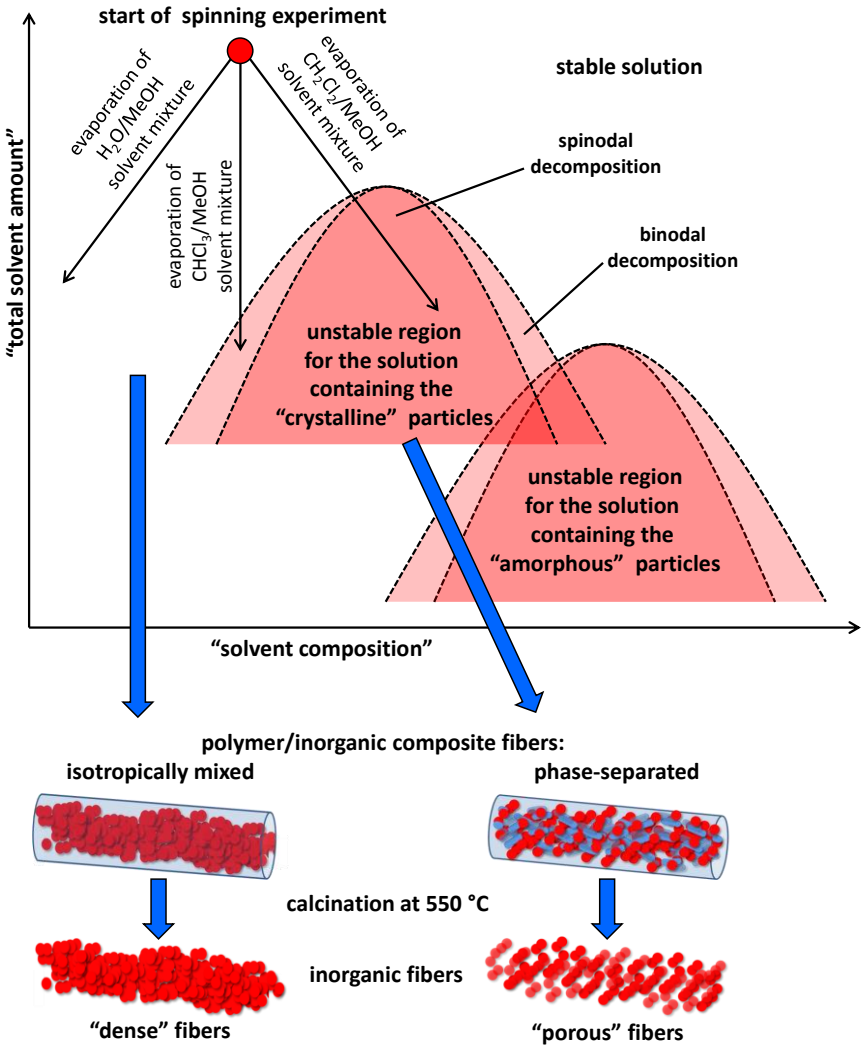

Figure 2-14: Schematic illustration of the decomposition process producing mesoporous electrospun fibers. The differently composed spinning solutions containing PEO, titania nanoparticles, and different solvents evolve in different directions with respect to the instable region in which decomposition occurs. Consequently, fibers with different mesoporosity can be obtained (adapted with permission from[75], Copyright 2011 American Chemical Society).

The assumed influence of the solvent composition is illustrated in figure 2-15 and figure 2-14: In the previous study different spinning solutions were prepared and investigated. The spinning solutions were obtained by combining a dispersion of titania nanoparticles in methanol with a solution of poly(ethylene oxide) (PEO) in chloroform, dichloromethane or water respectively. In all cases both solvents were used in the same weight percentage. The solvent evaporation during electrospinning causes a change in the solvent composition because the three solvents used to dissolve the PEO possess different boiling points (T_b). For instance, dichloromethane (T_b = 40 °C) evaporates faster than methanol (T_b = 65 °C) resulting in an increase of the ratio of methanol in this solvent mixture during spinning. Likewise, the portion of methanol decreases, when water (T_b = 100 °C) is used as co-solvent. Thus, the different solvent mixtures traverse different pathways with respect to the phase boundary beyond which decomposition is initiated (see figure 2-14). It was concluded that the solvent mixture containing dichloromethane as co-solvent is most likely to undergo SD: Basically, the decomposition is a consequence of the interaction between a good and a poor solvent (see figure 2-15): While methanol is a precipitant for PEO, chloroform and dichloromethane are poor solvents for the titania nanoparticles. In contrast, water is a good solvent for PEO and the titania particles. The solution containing dichloromethane thus facilitates the separation of PEO (see figure 2-15 A) due to the increasing portion of the precipitant methanol in the solution during evaporation. Contrariwise, phase separation is impeded with water as co-solvent (see figure 2-15 C), because the portion of the good solvent water for the particles and the polymer increases during evaporation. In case of chloroform (T_b = 61 °C) being co-solvent, the solvent composition stays constant in first approximation, because both solvents evaporate more or less simultaneously. Consequently, segregation of PEO and/or titania particles may occur, but the phase boundary at which decomposition takes place is not reached as fast as if dichloromethane is used as co-solvent (see figure 2-14). In summary, the interactions of the spinning polymer, the titania particles and the solvent(s) determine if an initially stable solution is quenched by traversing a phase boundary triggering a SD process within the instable region of the phase diagram.

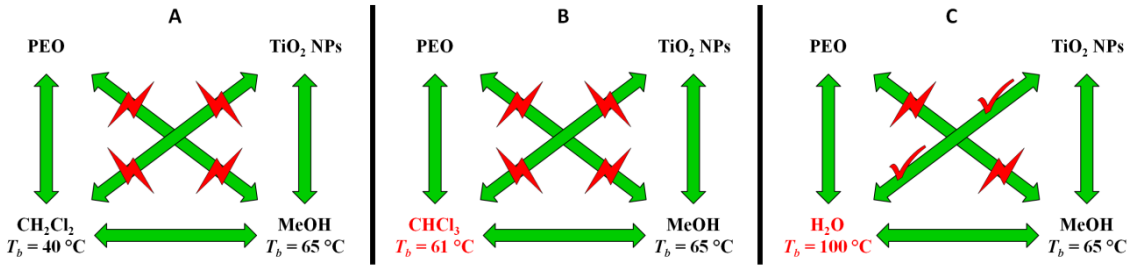

Figure 2-15: Schematic illustration of compatibility and interactions of the different solvents with the spinning polymer PEO and the titania nanoparticles in the spinning solutions (adapted with permission from[75], Copyright 2011 American Chemical Society).

As a consequence of the variable behavior of the spinning solutions with different co-solvents, the resulting titania fibers exhibit distinctive internal mesoporosities (see table 2-3 and figure 2-13). SEM pictures of the fibers can be found in the literature.[75] While titania sol-gel fibers have a specific surface area of 68 $m^2 \cdot g^{-1}$ and a total pore volume of 0.090 $cm^3 \cdot g^{-1}$, the NP-fibers obtained from the "crystalline" titania particles exhibit much larger specific surface areas of

111 $m^2 \cdot g^{-1}$ if dichloromethane is used as co-solvent and 164 $m^2 \cdot g^{-1}$ if chloroform is used as co-solvent. Furthermore, the total pore volume (TPV) of the NP-fibers is significantly increased to 0.366 $cm^3 \cdot g^{-1}$ (with chloroform as co-solvent) and 0.334 $cm^3 \cdot g^{-1}$ (with dichloromethane as co-solvent). This increased porosity is not a simple replication of the properties of the titania nanoparticles, which exhibit a specific surface area of 73 $m^2 \cdot g^{-1}$ and a TPV of 0.126 $cm^3 \cdot g^{-1}$ if the pure dispersions are dried and calcined at 550 °C. Accordingly, the increased mesoporosity of the NP-fibers versus the pure particles has to arise from a decomposition process as discussed above. It was assumed, that such decomposition does not emerge during the synthesis of sol-gel fibers because sol-gel precursors are typically highly soluble in several solvents.[6]

Another result of the physisorption analyses requires explanation: Although it was deduced that the spinning solution containing dichloromethane as co-solvent is most likely to undergo phase separation, the fibers obtained from the solution with chloroform as co-solvent exhibits a higher porosity (see figure 2-13 E). Ergo, the above discussed pathway for the generation of mesoporosity in the fibers seems to be incorrect or at least incomplete. This inconsistency will be discussed and analyzed in detail in conjunction with the results on zirconia fibers in chapter 3.3.5. Possibly, an explanation can be found in differences of the spatiotemporal evolution which follow upon the initial quenching step of SD (see chapter 2.3.1). However, this discussion is postponed at this point.

2.5.3 Challenges in studying pore forming processes in electrospinning

The conclusions in the former titania study were all drawn from analyses (i. e. SEM and nitrogen physisorption analyses) conducted on the as-prepared and/or calcined electrospun fibers. Similarly, the formation of porous structures by processes like vapor induced phase separation (VIPS)[110] or thermally induced phase separation (TIPS)[111] explaining the generation of porosity during thin-film preparation were deduced from post-synthesis analyses resulting in the conclusion that SD has taken place during these syntheses. However, an improved in-depth understanding of such processes would require in situ observations of the evolving structures allowing for monitoring the formation processes time-resolved.

Concerning the electrospinning of titania fibers the origin of mesoporosity was ascribed to a SD process because it is a justified general belief that decomposition during electrospinning necessarily has to be spinodal rather than binodal due to the very fast solvent evaporation. Nevertheless, SD basically includes a spatiotemporal structure evolution like introduced before (see chapter 2.3.1). Such spatiotemporal evolution was neither discussed in detail nor was it possible to give any evidence that the evolution is in accordance with SD theory because it is generally not possible to give such prove doubtlessly without in situ observations. This is consequently also a point of criticism concerning other pore processes like VIPS or TIPS.

[6] For example some alkoxide precursors like $Zr(OiPr)_4$ can be purchased in 80 wt.-% concentration in isopropanol proving the very high solubility of this precursor in isopropanol.

How in situ methods can be used to analyze spatiotemporal structure formation processes in order to develop a theoretical model of a structure forming process is best illustrated on the example of in situ investigations on dip-coating experiments. In situ methods are mainly scattering techniques such as in situ wide-angle X-ray scattering (WAXS), small-angle X-ray scattering (SAXS) or grazing-incidence small-angel scattering (GISAS) which are able to monitor the structure evolution in an emerging thin-film immediately after it is withdrawn from the dip-coating solution. Such scattering techniques are especially suitable as in situ method because it is possible to acquire structural information in short periods of time which may be as short as some milliseconds.[112,113] These in situ experiments during dip-coating helped to develop and prove important structure formation processes as for example the EISA process:[113] The EISA concept explains the occurrence of porous structures in inorganic materials by self-assembly of organic template micelles in an inorganic continuous phase. The self-assembly of the micelles is induced by the evaporation of solvent during the synthesis.[13,14] In consequence, the application of this concept enables a systematic preparation of inorganic materials with highly crystalline and/or ordered structures.[15,114,115]

Dip-coating experiments are conducted with starting solutions which are very similar to electrospinning solutions consisting of an organic polymer dissolved in an adequate solvent. In order to obtain inorganic nanostructures sol-gel precursors or dispersed nanoparticles may be added in concentrations similar to those used in electrospinning solutions. The main difference in the starting solutions is the lower viscosity of dip-coating solutions compared to electrospinning experiments achieved by a lower concentration and/or molecular weight of the polymer. Consequently, the initial situation in electrospinning and dip-coating solutions is comparable from a physico-chemical point of view allowing a discussion of structure formation processes in a similar manner. Besides the different viscosity of the starting solutions there is mainly one other relevant disparity which needs to be considered: While solvent evaporation and solidification of the resulting material takes several seconds to minutes in dip-coating experiments,[13] an even shorter period of time of only split-seconds[94,108,116] is required for solvent evaporation in electrospinning experiments. Thus, the time scale available for structure formation processes before solidification occurs is significantly shorter in electrospinning syntheses, so that decomposition processes have to be rather a spinodal than a binodal process in almost any case.[108] In contrast, binodal phase separation also needs to be considered as relevant structure formation process in dip-coating experiments due to the slower solvent evaporation. Furthermore, considering cases in which amphiphilic, micelle-forming templates are added to dip-coating or spinning solutions, self-assembly processes enabling the formation of ordered structures via EISA or similar processes in dip-coating syntheses also have to proceed much faster in electrospinning experiments. Consequently, the formation of ordered pore systems in electrospun fibers seems to be implausible due to the fast solvent evaporation making the occurrence of disordered structures more likely. Hence, it has to be doubted if structure formation processes like EISA can be transferred to the electrospinning technique and for a sophisticated discussion of structure formation in electrospinning syntheses experimental in situ evidences would be of great benefit. Without such evidences a comparison to dip-coating syntheses stays ambiguous.

Unfortunately, in situ analyses in electrospinning experiments are not performed so far and it has to be questioned if such analyses are possible at all. For two reasons structure formation processes taking place during the flight of the jet from the capillary tip to the collector can hardly be observed by in situ methods: First, the observation of a bending jet by e. g. scattering techniques would not generate evaluable signals: The fast movement of the jet in space equalizes any detectable inhomogeneities. The local observation of only one position in the jet is not possible due to the movement of the jet and the insufficient local resolution of typical in situ scattering setups. In contrast, the observation area in dip-coating (i. e. the whole film surface of several square centimeters) is much bigger and can be observed on a fixed position immediately after the film is withdrawn from the coating solution. Secondly, the structure formation during electrospinning taking place within split seconds is probably too fast to be monitored by typical in situ methods: It would be necessary that the in situ analysis method is able to acquire the analytic data within a time interval which is orders of magnitude smaller than split seconds so that transient situations of the structure formation can be captured. Hence, it would be necessary to acquire scattering profiles (e. g. SAXS, GISAS etc.) within less than a millisecond which is not possible so far. Consequently, these practical challenges seem to preclude in situ observations of electrospinning experiments generally.

However, the analysis of processes generating porous structures within electrospun fibers represents one main scientific challenge of this thesis. Hence, at least sophisticated thought experiments and reasonable argumentations are indispensable if direct in situ observations are not possible. For this reason, the two pivotal concepts of SD and DLCA which were introduced in the chapters 2.3.1 and 2.3.2 will be considered theoretically concerning electrospinning in the following chapters 2.5.4 and 2.5.5 including an overview of investigations and theoretical calculations already presented within this context. Afterwards, the plausibility of these thought experiments and the mechanistic picture of the structure formation processes conceptualized with their help need to be evidenced by post-synthesis analyses of the prepared electrospun fibers in chapter 3.

2.5.4 SD with respect to electrospinning

The structure formation process leading to mesoporous titania fibers from preformed nanoparticles is believed to be basically SD of a polymer-rich phase and a phase containing the nanoparticles. Solvent evaporation during electrospinning is so fast, that the spatiotemporal evolution of the decomposition is fundamentally believed not to be able to proceed via nucleation and growth (i. e. binodal decomposition)[75] as also mentioned in several other former theoretical[94–96,117] and experimental[94,103,107,108] publications investigating the formation of porosity within electrospun fibers. Mathematical models describing decomposition during electrospinning are based on algorithms which are in accordance with the spatiotemporal evolution of SD. However, most of the former investigations and calculations are restricted to the synthesis of pure polymer fibers without any other additives (see chapter 2.5.4.1). Considerations concerning spinning systems containing inorganic additives which are in the focus of this thesis are presented in chapter 2.5.4.2.

2.5.4.1 Electrospinning of polymer solutions without additives

Several publications dealing with the synthesis of electrospun polymer fiber exhibiting intra-fiber (meso-)porosity attribute the structure formation to SD.[94,103,107,108] In this context there are some theoretical investigations concerning SD in confined geometries in general[31,32,118,119] and also with special respect to the confinement in electrospinning experiments using polymer solutions (without further additives) undergoing a separation into a polymer-rich and a solvent-rich phase.[94–96,117]

Confined geometries (i.e. spatial confinement) basically may influence a SD processes by interactions with the surrounding (i. e. "surface effects") leading to enrichment or depletion of one of the separated phases at the interface while the internal structure may be different.[118,120] Surface effects are of relevance in the special case of the formation of hollow electrospun fibers[96] but concerning fibers which are porous throughout their whole cross section such surface effects are negligible. Rather, confinement in electrospinning is dominated by the large surface to volume ratio leading to very fast solvent evaporation and consequently to a strong confinement in time (additional to the confinement in space). The very fast solvent evaporation rate not only accounts for a rapid quenching of the system (as illustrated in figure 2-3, path II[7]) but also restricts the time interval available for the subsequent steps of SD to only some milliseconds[94,116] until solidification freezes the separating structure. Thus, the time interval for the ripening steps of SD is significantly shorter than in other preparation methods like dip-coating (some seconds)[13] or the Nakanishi process (some hours).[46,47] Consequently, SD is interrupted much earlier in electrospinning processes so that the late stage of SD in which self-similar domain size growth takes place can be assumed to be of minor relevance in electrospinning experiments. Rather, SD in electrospinning is supposed to be restricted to the quenching step and the subsequent early stage of structure ripening in which the evolution of concentration fluctuations takes place. This results in solidified structures exhibiting domain sizes probably being not very much larger than the characteristic wavelength of the initial concentration fluctuations. Such restriction is also necessary because self-similar growth in the confined space of electrospun fibers would prevent the formation of continuous fibers as soon as the domain size reaches dimensions as large as typical fiber diameters (i. e. in the range of approximately 10^{-7} m) leading to fiber fractures at positions of solvent rich domains. In turn, this argumentation also implies that the size of the (solvent-rich) domains resulting in the intra-fiber pores is necessarily limited to the mesopore size region.

Theoretical calculations simulating electrospinning experiments and aiming to explain how mesoporous polymer fibers are formed via SD provided evidence that solvent volatility and the phase diagram of the polymer-solvent mixture are of decisive influence on the resulting structures.[94,117] It was predicted that the pore size decreases as the solvent evaporation rate increases by calculating concentration sweeps in the jet at different temperatures below the critical temperature beyond which no phase separation occurs. Higher temperatures are equivalent to a faster solvent evaporation in these calculations but they also enhance other

[7] Note that fast solvent evaporation generally also involves cooling of the residual solution (path I in Figure 2-3). Thus, this evaporative cooling does not alter the decomposition process qualitatively so that it can be neglected for the sake of simplicity in the discussion.

kinetic processes like diffusion. Interestingly, these calculations did not result in larger pore sizes with increased temperature as it can be expected if diffusion contributes significantly to coarsening of the separating structure. This finding apparently confirms the solvent evaporation speed being so fast that structure coarsening by diffusion/self-similar growth is effectively suppressed before the structure solidifies.

2.5.4.2 Electrospinning of polymer solutions with (inorganic) additives

Electrospinning with inorganic additives can be performed with different substances, for example with sol-gel precursors and/or preformed nanoparticles (NPs) (see figure 2-11). In how far sol-gel precursors or preformed NPs behave differently concerning structure evolution during electrospinning needs special consideration (see below) but for the moment the discussion will focus the fact that inorganic additives generally are of significant impact on the phase behavior of spinning solution.

Whether a spinning solution undergoes spinodal phase separation is dependent on the phase diagram and the evolution of the spinning solution under the exact experimental conditions. For example, the substitution of the spinning polymer (e.g. PEO with a molecular weight M_w of 300,000 g·mol^{-1}) by the same mass of the same polymer but with a different molecular weight (e. g. PEO with M_w = 1,000,000 g·mol^{-1}) may be sufficient to influence the phase separation process substantially, because the molecular weight of a polymer changes its solubility considerably. Similarly, the phase behavior of spinning solutions with inorganic additives and hence the resulting structure of electrospun fibers is also strongly dependent on properties of the deployed inorganic substances (i. e. sol-gel precursors and/or preformed nanoparticles). Parameters like the solubility of sol-gel precursors and their reactivity or the dispersibility of nanoparticles - which changes with properties like their size, crystallinity, chemical surface modification, etc. - are all relevant if the phase behavior of such complex solutions needs to be considered. Furthermore, the starting concentration of each component in the solution including polymer and solvent concentrations as well as the time interval available for a phase separation process play a crucial role. Finally, atmospheric conditions like temperature and humidity are important parameters influencing the volatilization of solvents and hence the phase behavior of a drying solution.[104–107]

Accounting for all above mentioned parameters of influence a system with at least eight parameters is present (i. e. three starting concentrations, molecular weight of the polymer, particle/precursor properties, time, temperature, humidity, etc.) resulting in a phase diagram (or better: map) that is at least eight-dimensional. Consequently, the estimation of the complete phase map and thus the predictability of the phase behavior of complex spinning solutions are practically unachievable. In order to get insight into the phase behavior of such systems the practical approach is to conduct several series of systematic experiments in which only one parameter per series is varied in order to understand the influence of individual parameters on the whole system. Unfortunately, it is very difficult to vary only one single parameter at once and thus obtain coherent and distinctive conclusions because it is often impossible to vary parameters of influence independently from each. For example, changing the concentration of one component consequently also changes the concentration of at least one other component. Furthermore, the reliability of predictions based on such systematic investigations strongly

depends on the total number of experiments conducted to "scan" the whole parameter matrix. Accordingly, it is not trivial to conduct such a study and the estimation of phase maps of multi-component systems stays scientifically challenging. For complex spinning solutions like the investigated ones, a single PhD thesis is by far not sufficient to understand all details of such extensive phase maps. Nevertheless, systematic investigations were performed within the former titania study[75] and will also be conducted and discussed concerning other materials in this thesis in order to gain at least partial insight in - and understanding of - the phase diagrams of multi-component spinning solutions.

Basically, it is unclear which the components of two separating phases are if inorganic substances are added to a simple polymer/solvent spinning solution. While phase separation in pure polymer/solvent spinning solution necessarily has to result in one polymer-rich and one solvent-rich phase, the situation with inorganic additives allows different scenarios: Possibly, a solvent-rich phase separates from a nanoparticle- and polymer-rich phase. Otherwise, also the separation of a polymer-rich phase from a nanoparticle-rich phase may occur. In the preliminary work on titania fibers evidences suggesting the second possibility to be more reasonable were found, since porous polymer fibers were expected, but not obtained, if the inorganic additives were left out from the spinning solutions: Keeping the polymer/solvent composition the same as with the additives, no porous fibers were found ruling out the separation of a solvent-rich phase from a polymer- (and nanoparticle-) rich phase in such case.[75] This finding suggests that the evolution of the spinning system with inorganic additives proceeds via a separation of an inorganic (nanoparticle-rich) phase from a polymer-rich phase if mesoporous inorganic fibers are obtained (after combustion of the spinning polymer at 550 °C).

However, mesoporous titania fibers were only obtained if preformed nanoparticles were used while fibers obtained from sol-gel precursors exhibit nearly no mesoporosity. It will be shown that this trend is not only valid concerning titania fibers but also generally for all materials investigated within this thesis. The fundamentally different porosities of sol-gel and nanoparticle-derived inorganic fibers could not be expected and their origin has to be found in a pivotally different behavior of the respective spinning solutions:

A simple and reasonable argument to explain this finding is that sol-gel precursors usually exhibit a high solubility in typically applied solvents.[8] In contrast, nanoparticle dispersions like they were used are much closer to their stability limit essentially facilitating phase separation compared to sol-gel systems. Apparently, phase separation between a sol-gel-species-rich phase and a polymer-rich phase seems to be effectively prevented in all investigated cases. Alternatively, it could be argued that the calcination at 550 °C led to the collapse of a possibly formed separated structure in the sol-gel systems while the calcination temperature was not sufficient to destroy the separated/porous structure if preformed NPs were used.

[8] For example some alkoxide precursors like $Zr(OiPr)_4$ can be purchased in 80 wt.-% concentration in isopropanol proving the very high solubility of this precursor in isopropanol.

In order to gain a better understanding of the differences between sol-gel- and nanoparticle-based spinning systems some basics need to be recapitulated: It is a matter of fact and part of the fundamentals creating the field of colloid science that (inorganic) NPs basically behave different than their molecular counterparts (i. e. sol-gel precursors). For instance, sol-gel precursors are reactive species whose properties (e. g. their solubility) alter with proceeding reaction during electrospinning which again may influence the spatiotemporal phase evolution within the jet/emerging fiber. Furthermore, it was not taken into account so far that the concept of SD based on the spatiotemporal evolution of concentration gradients can hardly be modeled and followed for electrospinning of nanoparticle containing solutions: The confinement existing in form of the jet decreases the space of the SD process to such extent, that the concentration of nanoparticles is "digitalized" (see figure 2-16) because the confined space of an emerging fiber (i. e. a slightly conical cylinder with a diameter of some hundreds of nanometers) is too small to allow for an estimation of concentration fluctuations with respect to nanoparticles having diameters in the range of typically 10 nm.

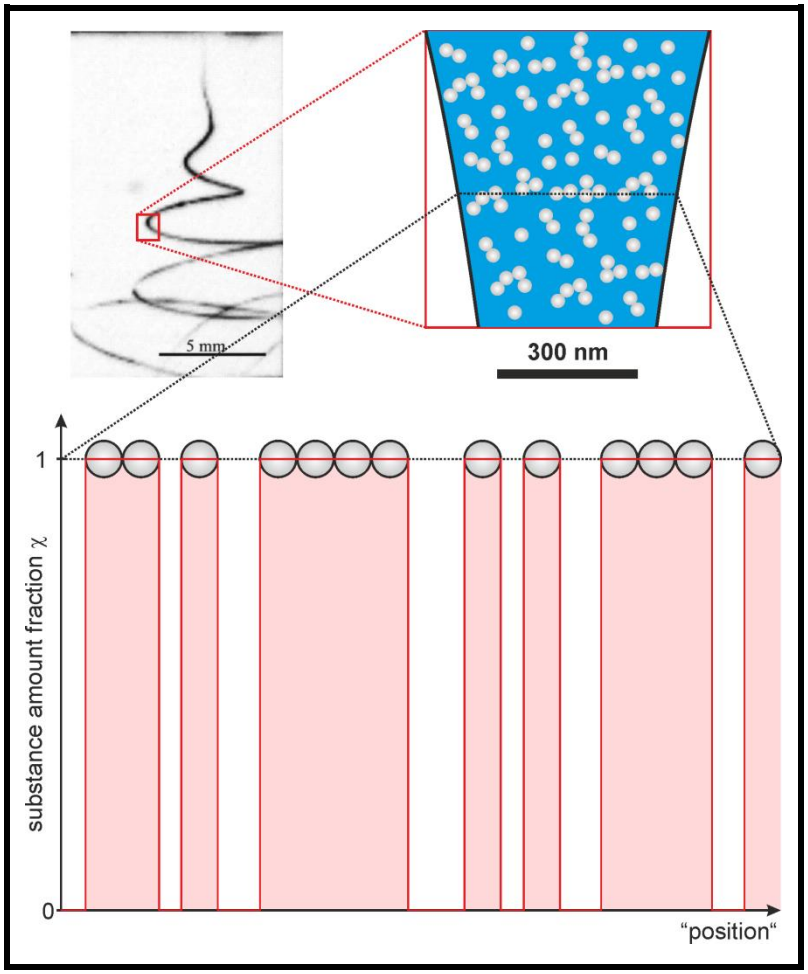

Figure 2-16: Concentration profile across the diameter of an electrospinning jet consisting of a spinning solution containing NPs: The concentration (in terms of substance amount fractions χ) of NPs in the jet has to be considered as "digitalized" because it is either "0" or "1". This complicates the discussion of structure evolution in terms of SD (compare figure 2-4; see text for more details).

In first approximation such particles can be considered as hard spheres with a sharp interface. In the confined space of an electrospun fiber their concentration profile across the fiber diameter is “digitalized” because there are only two possibilities: Either a particle is found at a specific position and the molar fraction of the particle is unity or no particle is present and the molar fraction is consequently zero (see figure 2-16, lower part). In other words, the difference between the jet diameter and the particle diameter is too small to estimate local particle concentrations because the “compartment” for which reasonable local particle concentrations could be calculated would be at least as large as the jet is thick. Otherwise, in case the compartment is selected significantly smaller than the jet diameter the initial concentration values are already the final ones (i. e. “0” or “1” in molar fractions, respectively). This “order of magnitude dilemma” consequently prevents the calculation of spatiotemporal evolutions of concentration fluctuations which is strongly different to systems in which molecular species are used. Molecules like sol-gel precursors with a size of typically some hundreds of picometers are approximately two orders of magnitude smaller allowing the estimation of concentration profiles within small structures (compare lower part of figure 2-16 and figure 2-4).

Hence, the discussion of structure formation in the sense of SD in electrospinning jets with preformed NPs becomes ambiguous if the spatiotemporal evolution of concentrations cannot be modeled. Using NPs for electrospinning the only steps left from the whole SD process are the fast initial quenching step and a very short period of time afterwards in which the particles may move for small distances within the confined space. However, another physico-chemical model exists which may be more adequate to understand structure formation processes with special respect to particles as building blocks. This model is not mandatorily in contradiction to SD but it elucidates structure formation from another point of view. This model, the diffusion-limited cluster aggregation (DLCA), basically introduced in chapter 2.3.2 is discussed with respect to electrospinning in the following chapter 2.5.5.

2.5.5 DLCA in electrospinning: Evaporation-induced cluster aggregation (EICA)

Colloidal electrospinning[53] using initially stable NP dispersions may also be discussed in terms of the diffusion limited cluster aggregation (DLCA) model like it was shortly introduced in chapter 2.3.2: The basic idea of the DLCA model is that a structure consisting of small nanoparticles is formed by agglomeration of individual particles which collide and stick together. Collision of particles in this model is driven by their diffusion. Hence, this model is basically applicable to the movement of nanoparticles in the confined space of an electrospinning jet in which particles may diffuse for a short period of time before solvent evaporation and solidification freeze the emerging structure. During electrospinning the evaporation of solvent from the jet forces the particles to approach each other until they may experience a net attraction and stick together (see figure 2-6). If the energetic sink is deep, this process can be considered to be irreversible while a less deep energetic sink would result in a reversible process allowing the particles to rearrange by cooperative gyration or transient detachment. However, even if the sticking of particles is basically reversible from the thermodynamic point of view, it could be suppressed in electrospinning due to the very fast solvent evaporation restricting the time interval for rearrangement of particles strongly so that it might be generally insufficient.

Solvent evaporation from an electrospinning jet of nanoparticle containing solutions triggers several simultaneous processes which exhibit important impact on the structure formation (see figure 2-17): First, solvent evaporation increases the viscosity which again slows down the diffusion of the particles in the solution until it is effectively suppressed; latest when the emerging fiber solidifies. Secondly, solvent evaporation reduces the volume of the jet gradually forcing the nanoparticles to approach each other while the jet diameter decreases from several microns at the Taylor cone down to hundreds of nanometers at the collector. This increase in "confinement" is attended by an increase in both particle and counter-ion concentration which in turn reduces the thickness of the electrochemical double-layer so that the nanoparticle dispersion is destabilized enabling aggregation. The above mentioned conditions during electrospinning presumably lead to a random aggregation of the nanoparticles in the jet, because there is no time to generate any kind of ordered structures. Such random packing is equivalent with a fractal structure only achievable under kinetically controlled conditions.

Consequently, the cluster aggregation during electrospinning is probably not diffusion limited but "viscosity/time-limited". As the whole process is induced by solvent evaporation, the above discussed structure formation process illustrated in figure 2-17 may be called an "Evaporation-induced cluster aggregation" (EICA) process.

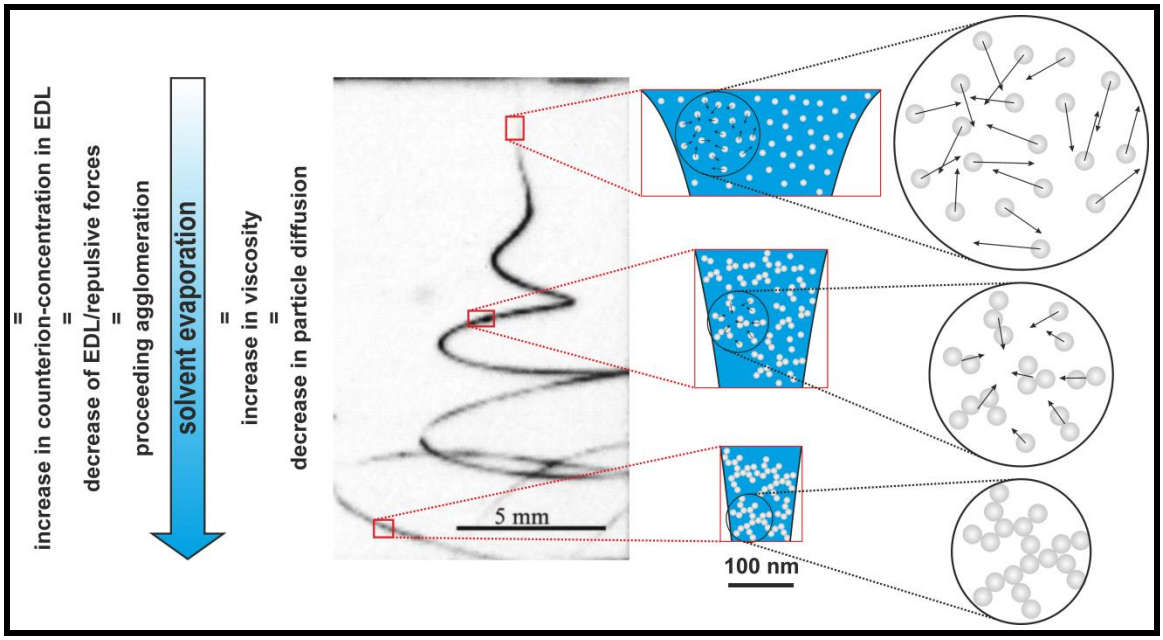

Figure 2-17: Evolution of a nanoparticle containing electrospinning solution in course of the spinning jet: Top: Initial state near the Taylor cone: Isotropic solution with relatively small particle concentration and solution viscosity. Individual particle are able to diffuse relatively fast. Middle: Intermediate state: Particle concentration increases, first agglomerates form, and the increasing viscosity of the solution impedes diffusion. Bottom: Late stage near the collector: Solvent evaporation leads to solidification of the jet and the particles stick together in a fractal arrangement because diffusion is effectively suppressed so that a thermodynamically preferable dense packing of the particles cannot be realized.

When such an EICA process generates a fractal arrangement of inorganic particles in the as-synthesized electrospun fibers, the preservation of this arrangement throughout the calcination step would lead to highly mesoporous fiber obtained from the inorganic NPs (see figure 2-18). However, from the thermodynamic point of view such random, fractal arrangement of particles is unfavorable and a thermally activated rearrangement of the particles should always lead to a densification and loss of the porous structure.

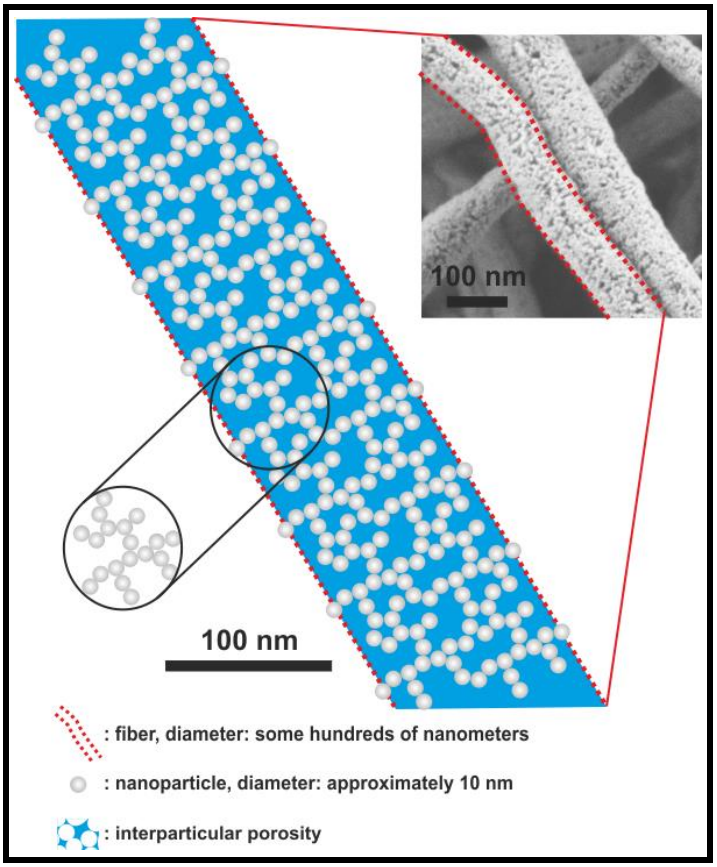

Figure 2-18: Fractal arrangement of NPs constituting the structure of a mesoporous electrospun fiber.

In case porous fibers are indeed obtained after calcination at e. g. 550 °C the thermal energy E_{kin}

$$E_{kin} = \frac{3}{2} \cdot k_B \cdot T \tag{2-6}$$

with:

k_B = Boltzmann constant;

T = absolute temperature in Kelvin.

during calcination is obviously not sufficient to induce significant rearrangement. Accordingly, the sticking of the particles in the as-spun fibers is stronger than E_{kin} or further chemical reactions of the stuck particles strengthen the porous structure sufficiently so that rearrangement during calcination is effectively suppressed. Possibly, condensation of particle surface groups (e. g. hydroxyl-groups) fortifies the as-prepared structure before rearrangement may occur. Using increasingly high calcination temperatures may lead to a collapse of the porous

structure due to rearrangement (i. e. thermally induced diffusion) within the fibers like it was demonstrated in the former titania study after calcination at 750 °C.[75] Hence, investigating the structure of the fibers in dependence of the calcination temperature would allow for conclusions concerning the bound strength between the nanoparticles in the fibers and the thermodynamic stability of the porous structures. Such study should be envisioned for the future in order to continue the effort of this thesis.

2.5.6 Concluding remarks: Comparison of SD and EICA with respect to electrospinning

In the preceding chapters the experimental conditions under which structure formation processes during electrospinning take place were introduced. It was discussed that up to now SD is mostly used to explain the occurrence of mesoporosity in electrospun fibers. Nevertheless, some arguments were found doubting that SD is the only concept which allows understanding the formation of mesopores in electrospun fibers. Especially in the field of colloidal electrospinning the formation of porous fibers from preformed nanoparticles may be better comprehended on the basis of the DLVO theory which is incorporated in the fundamental DLCA concept. From this theoretical background a new structure formation process respecting the experimental conditions of electrospinning was conceptualized which can be understood as an evaporation-induced cluster aggregation (EICA) process.

In comparison, SD and EICA are two processes which both may help to explain the occurrence of mesoporosity in electrospun fibers. While SD was often applied coherently to explain the occurrence of mesoporosity when molecular precursors were employed as starting materials, the concept of SD faces some problems if electrospinning solutions containing preformed nanoparticles are considered. In such case the EICA concept may be more reasonable. However, whether and in which case EICA is actually able to explain the experimental results of this thesis has to be discussed in chapter 3. At this point, it only shall be emphasized that these two models are not contradictory but they focus on different aspects of structure formation. Structure formation via SD is predominantly driven and explained by thermodynamics. SD ultimately leads to thermodynamic equilibrium structures as long as the process is not “frozen” at a certain stage before. In contrast, EICA is a model focusing the kinetics of the process in which the thermodynamics are of minor importance. Consequently, it is a question of the balance between thermodynamics and kinetics and the interpretative emphasis which of both concepts is preferably used to explain structure formation in electrospinning jets. Furthermore, the interactions of the components in the spinning solutions are differently emphasized in the alternative concepts: In the SD concept the initial phase separation leading to a co-continuous inorganic/polymer fiber is triggered by a solubility limit of either of the two components - the polymer or the inorganic material. In contrast, the influence of the polymer on the structure formation process is neglected in the concepts of DLCA or EICA: In first instance, the polymer is part of the matrix in which a mesoporous structure is formed by a process mainly governed by electrostatic interactions between the particles in the matrix consisting of polymer and solvent(s).

2.6 Characterization of porous materials by nitrogen physisorption

A standard method to characterize porous materials is nitrogen physisorption especially suited to analyze mesoporosity. In contrast, argon physisorption is preferably used for the analysis of microporosity[121] and mercury porosimetry is the method of choice for the investigation of macroporosity. However, the characterization of porous materials in this thesis focuses on mesoporosity and its in-depth analysis. Thus, this chapter will give some relevant background information on nitrogen physisorption and its application to the characterization of mesoporous electrospun fibers. For basic information on this analytic method the reader is referred to the literature.[122] The information provided in this section are restricted to special aspects which need to be introduced and discussed concerning the analyses performed within this thesis (see chapter 3).

2.6.1 Correlation between specific surface area and pore size

Before the characterization of porous materials by nitrogen physisorption is discussed, the fundamental correlation between specific surface areas and the size of mesopores will be calculated. Nitrogen physisorption data can give information on both but as the correlation of pore size and specific surface area is dependent the overall porosity of the material some preliminary considerations are required. Thus, the influence of the pore size on the specific surface area is illustrated and discussed under the assumption that the total pore volume (TPV) is kept constant. Furthermore, it is assumed that the surface area of mesoporous materials is dominated by the surface area of the pores so that the outer surface of the material can be neglected.

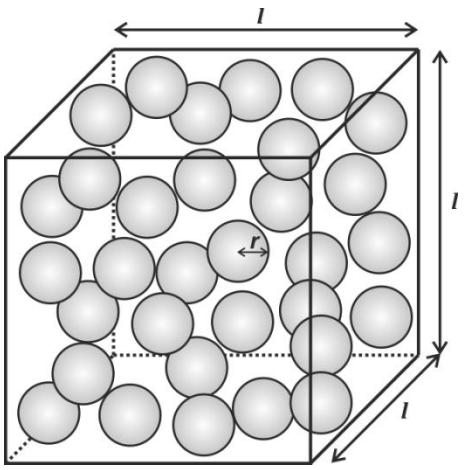

Figure 2-19: Illustration of a (meso-) porous material of cubic shape with the edge length *l* and a pore radius *r*. It can be shown that the specific surface area of such a material is reciprocal to the pore radius *r* if the outer surface of the cube is neglected and the total pore volume is kept constant (see discussion below).

For a simple calculation of the correlation between pore size and specific surface area, a cubic sample volume V_{total} with an edge length *l* and a porosity of 50% can be assumed (see figure 2-19), so that the total volume of all pores $V_{allpores}$ has to sum up to:

$$V_{\text{allpores}} = \frac{V_{\text{total}}}{2} = \frac{l^3}{2} \tag{2-7}$$

For spherical pores with the radius *r* the surface area of one individual pore S_{pore} is given by $4 \cdot \pi \cdot r^2$. When a quantity of *n* pores is present in the sample, the total surface area of all pores S_{total} is:

$$S_{\text{total}} = n \cdot 4 \cdot \pi \cdot r^2 \tag{2-8}$$

The quantity *n* can be expressed by the ratio of $V_{allpores}$ and the pore volume of one individual pore V_{pore}:

$$n = \frac{0.5 \cdot V_{\text{total}}}{V_{\text{pore}}} = \frac{0.5 \cdot l^3}{\pi \cdot r^3} \tag{2-9}$$

Insertion of (2-9) in (2-8) leads to:

$$S_{\text{total}} = \frac{0.5 \cdot l^3}{\pi \cdot r^3} \cdot 4 \cdot \pi \cdot r^2 = 2 \cdot l^3 \cdot r^{-1} \tag{2-10}$$

Formula (2-10) states that the specific surface area is inverse proportional to the radius *r* of the pores in the sample as long as the porosity (i. e. the TPV) stays the same. The absolute value of the overall porosity does not influence this basic finding, because it only changes the constant factor in the equations (2-7) and (2-10).

2.6.2 Physisorption analysis on mesoporous electrospun fibers

Although nitrogen physisorption is a standard method to characterize mesoporous materials there are fundamental restrictions of this method which have to be considered. Mesoporous electrospun fibers feature some peculiarities in their topography and pore structure: As mentioned before (see chapter 2.4.4), nonwoven mesoporous fiber mats are hierarchically porous systems with intra-fiber mesoporosity and inter-fiber void spaces representing macropores (see figure 2-20). Concerning intra-fiber porosity, it was discussed that mesoporosity in electrospun fibers usually exhibits a disordered pore structures (see chapter 2.5) with undefined, random pore geometries featuring manifold shapes, sizes and different connectivity (see figure 2-20 B).

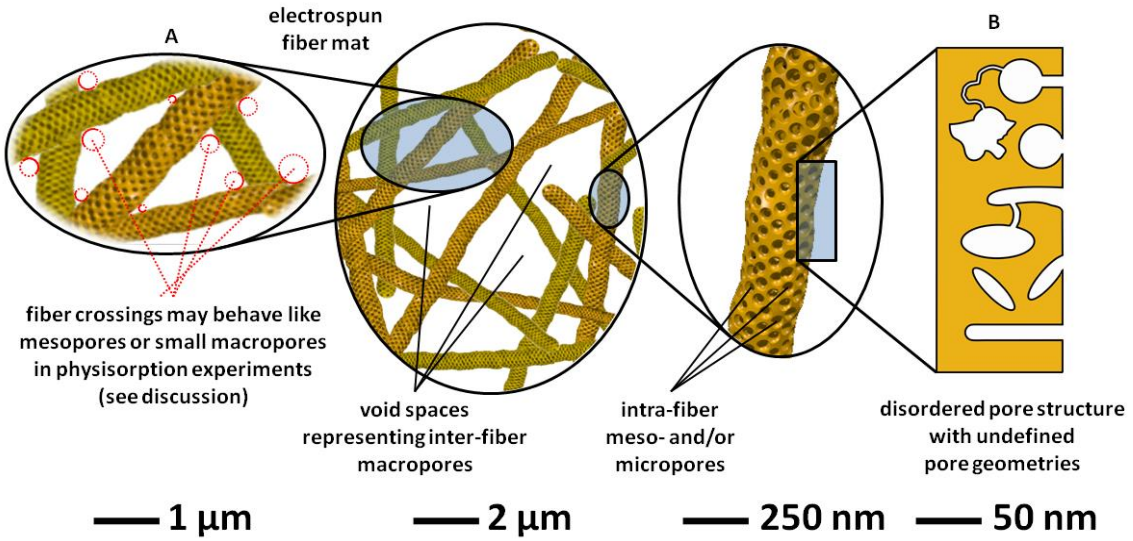

Figure 2-20: Scheme of an electrospun fiber mat with disordered pore structure including an illustration of structural features which have to be considered in pore size analysis from nitrogen physisorption data. Left magnification A: Fiber crossings may influence the sorption behavior of the fiber mat. Red circles: Fiber crossings exhibit surface curvatures which may be in the mesopore size range. Right scheme B: Intra-fiber mesoporosity can be assumed to be of disordered structure with undefined pore geometries. For more details see discussion (partly adapted with permission from[75], Copyright 2011 American Chemical Society).

While the calculation of specific surface areas for samples with different pore structures is relatively unproblematic, the calculation of pore volumes and corresponding pore sizes strongly depend on topographic features of the material. If such structural information is unknown, pore size calculations might lead to unreasonable values. Thus, structural data like pore geometries and sizes should be gathered and confirmed by other analytic methods like scanning electron microscopy (SEM), transmission electron microscopy (TEM), small-angle X-ray scattering (SAXS), small-angle neutron scattering (SANS), grazing incidence small-angel scattering (GISAS) or confocal microscopy techniques. However, such analyses on electrospun fibers are challenging: While electron microscopy only acquires two-dimensional information of individual sections on the surface of a sample, the application of scattering techniques for the analysis of strongly disordered porous materials is very elaborate if discrete structural information shall be extracted. Consequently, scattering techniques can hardly be used to analyze disordered structures routinely. Also the analysis of cord length distributions[123] or electron tomography,[124] an advanced TEM method, which can be used to gather three-dimensional information on mesoporous disordered materials are not adequate as standard method to analyze a large number of samples. Electron tomography requires the availability of a high-resolution TEM and only small samples can be analyzed in a very time consuming, elaborate study which can only be evaluated by few experts.

Due to the lack of alternative simple analysis techniques, it was decided to study the porosity of electrospun fibers only by nitrogen physisorption. A special theoretical consideration of issues concerning the pore structure analysis of electrospun fibers by nitrogen physisorption is presented in the following:

First, physisorption of adsorbate depends on the surface curvature of the samples due to the fundamental underlying physical interactions.[122] Basically, a rough, curved surface exhibits similar behavior like a pore with the same radius. Fiber crossings mimic such a "curved surface" in the knee of the crossing with a radius depending on the angle of the fiber crossing (see figure 2-20 A). Consequently, it is expected that fiber crossings may behave like pores with different radii in physisorption experiments. These radii might be somewhere in the range of larger mesopores or small macropores resulting in merging of intra-fiber mesoporosity and inter-fiber porosity in physisorption analyses. As a consequence such experiments are not adequate to distinguish between intra-fiber and inter-fiber porosity. Inter-fiber porosity probably leads to the absence of a plateau in the physisorption isotherm at high relative pressures, so that the assessment of an overall porosity is challenging. Nevertheless, the comparison of "total porosity volumes" of different samples should be possible with some constraints (see chapter 2.6.2.1).

Concerning intra-fiber mesoporosity the various different shapes of the pores in electrospun fibers are a further analytic challenge: Mesopore size analysis from nitrogen physisorption fundamentally assumes well-defined cylindrical and/or spherical pore geometries (see chapters 2.6.2.1 and 2.6.2.2) which are not representative for the structure expected in electrospun fibers. Thus, pore size analysis of such samples is problematic due to unknown pore geometries. Nevertheless, physisorption analyses are able to characterize the porosity of electrospun fibers in some important aspects irrespective of missing structural information:

There are two suitable analytic methods selected to characterize the porosity of physisorption samples in this thesis. On the one hand porosity can be calculated from a single data point in the isotherm under the assumption of bulk properties of the adsorbate nitrogen (see chapter 2.6.2.1). On the other hand the porosity can be analyzed by the density functional theory (DFT) method, which is a microscopic approach for the characterization of porosity (see chapter 2.6.2.2). These two approaches are not directly comparable, because the data evaluation processes are fundamentally different resulting in different information. Nevertheless, a correlation of both methods may help to interpret porosity data correctly, so that analytic uncertainties arising from missing structural information might be bypassed. Therefore, it is necessary to have a closer look on the underlying physical and mathematical background of both data reduction processes (see chapters 2.6.2.1 and 2.6.2.2).

2.6.2.1 The "deBoer"-method

The "deBoer" method uses only one individual data point of a measured isotherm consisting of a relative pressure value and a corresponding amount of adsorbate to deduce the porosity of the sample. The calculation of the total pore volume and the corresponding pore size from the isotherm data are explained in the manual of the "AS1win" analysis software:[125]

Assuming bulk properties of the adsorbate, the total pore volume (TPV) of a sample can be calculated from the volume of the gaseous adsorbate V_{ads} according to the so-called Gurvich rule.[126] The TPV is equal to the volume of the liquid adsorbate V_{liq}, which normally is nitrogen. V_{ads} is taken from the measured physisorption isotherm under assumption of ambient conditions. Hence, V_{liq} can be calculated from V_{ads} by using the ideal gas law:

$$V_{\mathrm{liq}} = \frac{p^{\theta} \cdot V_{\mathrm{ads}} \cdot V_m}{R \cdot T^{\theta}} \qquad (2\text{-}11)$$

with:

p^{θ} = standard ambient pressure = $1.013 \cdot 10^5$ Pa;
V_m = molar volume of the liquid adsorbate = 34.7 $cm^3 \cdot mol^{-1}$ for nitrogen;
R = ideal gas constant = 8.314 $J \cdot K^{-1} \cdot mol^{-1}$;
T^{θ} = standard ambient temperature = 273.15 K.

The corresponding pore size is calculated by using the "de Boer" approach, which is basically a corrected Kelvin equation. This calculation has two important intrinsic limitations: First, the usage of the incorporated Kelvin equation generally assumes cylindrical pore geometry. Secondly, the calculated pore size is the maximum pore size filled with adsorbate at the relative pressure considered. As far as larger pores are present in the investigated sample, these large pores are not filled completely at this relative pressure, but possess a surface layer of adsorbate.

The Kelvin equation correlates the Kelvin radius r_K to the relative pressure $(\frac{p}{p_0})$ in the physisorption experiment:

$$r_K = \frac{-2 \cdot \gamma \cdot V_m}{R \cdot T_{b,N_2} \cdot \ln(\frac{p}{p_0})} \qquad (2\text{-}12)$$

with:

γ = surface tension of nitrogen at its boiling point = $8.85 \cdot 10^{-7}$ $J \cdot cm^{-2}$ at 77 K;
V_m = molar volume of liquid nitrogen = 34.7 $cm^3 \cdot mol^{-1}$ for nitrogen;
R = ideal gas constant = 8.314 $J \cdot K^{-1} \cdot mol^{-1}$;
T_{b,N_2} = boiling temperature of nitrogen = 77 K.

Inserting the characteristic values of nitrogen in (2-12) the Kelvin equation is simplified to formula (2-13), giving the maximum pore size r_K filled at a given relative pressure:[125]

$$r_K[nm] = \frac{-0.415}{\log(\frac{p}{p_0})} \qquad (2\text{-}13)$$

This so-called Kelvin radius r_K represents a pore radius smaller than the real pore radius, because the nitrogen already adsorbed at the considered relative pressure on the pore walls shrinks the empty space of the pore to r_K (see figure 2-21).

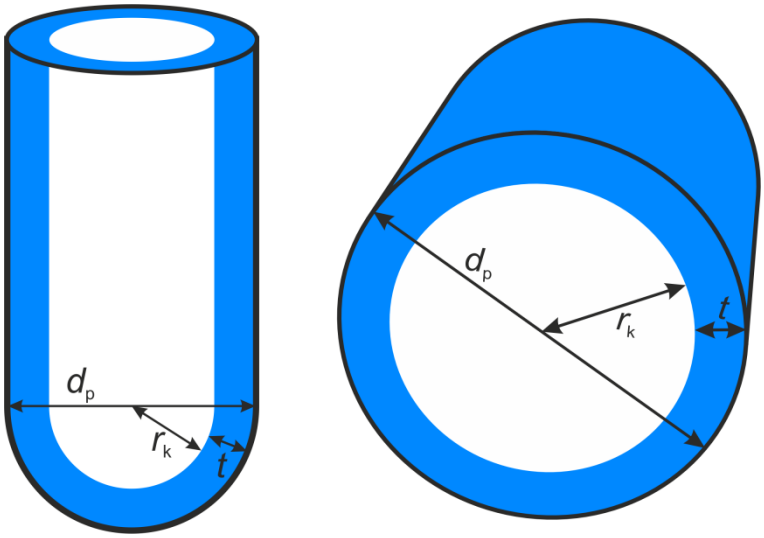

Figure 2-21: Illustration of a partly filled cylindrical pore which is assumed in the "de Boer" approach using the Kelvin equation: Side view (left) and top view (right) of a cylindrical pore. d_p: pore diameter, r_k: Kelvin radius, t: thickness of an adsorbate surface layer.

The thickness t of the adsorbed nitrogen layer can be calculated by formula (2-14).[125]

$$t[nm] = 0.1 \cdot \left(\frac{13.99}{-\log\left(\frac{p}{p_0}\right) + 0.034} \right)^{\frac{1}{2}} \tag{2-14}$$

Finally, the pore diameter d_p can be calculated by the addition of the adsorbate layer thickness t to the Kelvin radius r_k:

$$d_p = 2 \cdot (r_K + t) \tag{2-15}$$

When data points of the isotherms with relative pressures near unity are used to calculate the TPV, the corresponding pore diameters calculated by formula (2-15) are in the range of approximately 100 nm. In other words, this TPV values include large mesopores and small macropores in the calculation. It has to be noted, that the pore volume, calculated by this method is quite reliable for data points close to unity of the relative pressure, because the assumption of bulk properties for the nitrogen adsorbate is reasonable in this pressure range (see equation (2-11)). In contrast, the corresponding calculated pore sizes have to be considered with caution and represent only a rough estimation, because pore sizes calculated from equation (2-15) are increasingly imprecise the larger the relative pressure is as a consequence of the exponential correlation of pore size and relative pressure (see equations (2-13) and (2-14). Under the assumption that the relative pressure can be measured with a precision of ± 0.005 an experimental error for the assessment of the pore size can be calculated. As an example a measured relative pressure of p/p_0 = 0.9750 ± 0.005 leads to a calculated pore size in the range of 66.2−98.2 nm. This experimental error will be respected and discussed in chapter 3.2.3.2.

The calculation of a total pore volume by equation (2-11) does not include macroporosity in a size range beyond the upper limit of approximately 100 nm (see equation (2-15)). Consequently, inter-fiber void spaces are only partly captured by physisorption experiments because they cannot be filled with adsorbate completely. Nevertheless, the data of different samples can be compared to each other, if the TPV data are calculated from data points at similar relative pressures (see chapter 3.2.3.2) though for the assessment of the effective overall porosity including the complete macroporosity, mercury porosimetry measurements are indispensable. Unfortunately, such analyses could not be performed within this thesis, because the large sample amounts necessary for mercury porosimetry could not be prepared with the available experimental setup.

The TPV calculations can basically be done for every data point of a measured isotherm resulting in a plot of the TPV versus the pore size giving a kind of "cumulative total pore volume plot" similar to the cumulative pore volume plot obtained from DFT calculations (see chapter 3.2.3.2). Since the data of the adsorption branch of a measured isotherm do not represent the thermodynamic equilibrium, but the Kelvin equation is only valid at the thermodynamic equilibrium, the analyses using the "deBoer" method should be applied to the desorption branch of the isotherm which is assumed to represent the thermodynamic equilibrium concerning the adsorbate-adsorbent interactions. Only if pore blocking occurs on the desorption branch, the evaluation of the adsorption branch may be considered alternatively.

2.6.2.2 DFT analysis methods

There are several DFT approaches for the analysis of physisorption data of porous materials. These different approaches account for special properties and interactions of adsorbate and adsorbent.[125] While the quenched-solid DFT (QSDFT) is best suited for the characterization of microporous carbons, mesoporous oxides are mostly analyzed by the non-local DFT (NLDFT) approach.[127] Hence, the NLDFT approach is the DFT method of choice for the materials investigated within this thesis. As only the NLDFT method is used in this thesis, is will be shortly referred to as DFT method from now on.

Pore size distributions and the plots of the cumulative pore volume can be calculated by using the so-called DFT kernels that contain reference data obtained from well-characterized samples.[122] The most important limitation of the DFT method is that it is always necessary to choose the proper DFT kernel for analyzing a sample. If the pore sizes and their size distribution have to be analyzed, it is essential to choose a DFT kernel that uses reference data with similar pore geometries, because the pore geometry is a fundamental feature determining the sorption behavior of a material. It would lead to inaccurate results if a sample was analyzed by an inappropriate kernel which misfits to the pore geometries of the investigated material. Consequently, DFT analyses on samples with unknown pore geometries, as it is the fact for mesoporous electrospun fibers, cannot be guaranteed to result in accurate pore sizes. The validity of such results is restricted and its limitations have to be taken into account. In this context it is helpful to compare the available DFT kernels in order to identify the best suited DFT kernel before samples with unknown pore geometry are analyzed. Thus, the differences among the available DFT kernels will be closely examined and demonstrated exemplarily on silica sample in chapter 3.2.3.1.

For metal oxide samples DFT reference data are available in form of silica model materials with different pore geometries. Metal oxides are similar to silica materials concerning physisorption physics, so that silica is the reference material of choice for all inorganic oxides. Silica materials can be synthesized in manifold different micro- and mesoporous structures (see chapter 2.2.1.1), so that more silica reference materials are available than for any other metal oxide justifying its use as model material. Based on these reference data there are three DFT kernels available to analyze porous oxide materials:[125]

- The “cylindrical equilibrium” model using the desorption branch of the isotherm under the assumption of cylindrical pore geometry;
- The “cylindrical adsorption” model using the adsorption branch of the isotherm under the assumption of cylindrical pore geometry;
- The “spherical adsorption” model using the adsorption branch of the isotherm under the assumption of spherical pore geometry for pores with diameters larger than 5 nm. However, also this model assumes cylindrical pore geometry for pores with diameters below 5 nm.

For a material with defined, cylindrical or spherical pore geometry the choice of a DFT kernel is straightforward, but concerning fibrous or especially electrospun materials with undefined pore geometries there is a general lack of reference materials, because such materials are not common in the community of physisorption science. Which DFT kernel is suitable to analyze electrospun fibers is one of the challenging tasks covered by this thesis (see chapter 3.2.3). Within this context also a general comparison of the TPV and the cumulative pore volume (CPV) from DFT calculation will be discussed.

Another peculiarity of mesoporous electrospun fibers is that these fibers are expected to show very irregular pore geometries (see figure 2-22) for which the definition of a distinctive pore size is a fundamental problem. Ignoring all other structural features, a pore size of spherical geometry may be estimated resulting in a value within a specific range between a reasonable minimum and maximum (see red circles in figure 2-22). Furthermore, large irregular mesopores might be captured as several smaller mesopores in DFT analysis (see blue circles in figure 2-22) because the wall curvature in the corresponding section of the irregular pore is the same as the curvature of smaller “model mesopores”. Such analytic problems are a consequence of the fact that the wall curvature in porous materials is a decisive physical parameter determining the sorption behavior towards nitrogen adsorbate. Hence, these method-intrinsic predicaments give further rise for uncertainties concerning the validity of estimated pore sizes in mesoporous electrospun fibers. Nevertheless, the comparability of DFT analyses of several electrospun fiber samples should not be affected strongly by such method-intrinsic problems, because they lead to the same deficiencies in the analyses of all samples.

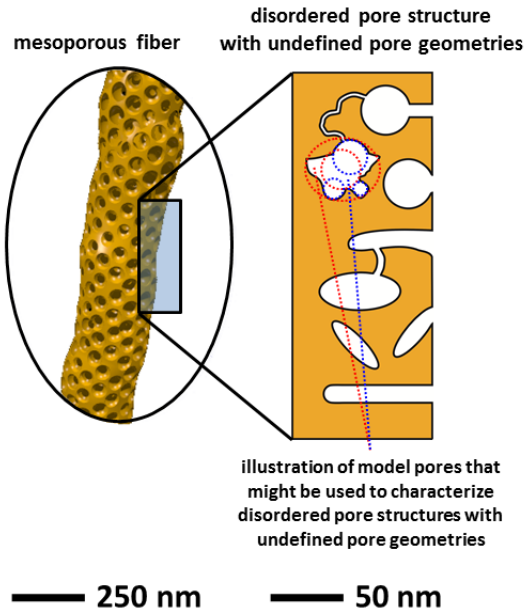

Figure 2-22: Illustration of intra-fiber mesoporosity with disordered pore structure and undefined pore geometries. Red circles: Illustration of a minimum and a maximum pore size which might be calculated for such irregular pore geometries; blue circles: If irregular pores exhibit a certain size, they may be captured as several smaller mesopores in DFT analysis. For more details see discussion (partly adapted with permission from[75], Copyright 2011 American Chemical Society).

In summary, DFT analyses on mesoporous electrospun fibers do not allow for the exact assessment of pore sizes but only for the estimation of a porosity of the samples and the trend of its accumulation with increasing pore size. This constraint concerning the validity of DFT analyses on electrospun fibers is still a matter of ongoing discussion treated within this thesis (see chapter 3.2.3).

2.6.3 Comparison of different materials

If physisorption data of different materials should be compared their unequal physical properties need to be accounted for. First of all, the adsorption potentials on the surfaces of materials with different chemical identity are not the same resulting in slightly imprecise analysis results if silica reference data are used for other materials.[122] This problem affects the comparability only to a small extent and can be neglected as long as metal oxides are considered, because metal oxides generally exhibit similar adsorption potentials to silica.[122] Secondly, results of physisorption data like the specific surface area or the specific pore volume are usually referred to the mass of the sample which is inadequate if materials with different densities should be compared. For example, nonporous silica has a density of 2.2 $cm^3 \cdot g^{-1}$,[128] while nonporous ceria has nearly a threefold density of 7.2 $cm^3 \cdot g^{-1}$ (JCPDS card number 00-034-0394). Consequently, the physisorption data of different oxides should be converted to other physical quantities which are better comparable in a meaningful discussion. Helpful physical quantities for such comparisons are introduced in the following.

2.6.3.1 Comparison of porosity data

One possibility to compare different oxides is to refer the physisorption data to the volume of the nonporous material resulting in data which are comparable irrespective of the density of the materials. These data have to be calculated by the following procedure because such "relative porosity values" are not implemented in the physisorption analysis software:

The porosity referred to the sample mass p_m can be converted to a "porosity per volume" of the nonporous material p_v by multiplication with the density of the nonporous material ρ:

$$p_v \left[\frac{\mathrm{cm}^3_{\text{pore volume}}}{\mathrm{cm}^3_{\text{nonporous material}}}\right] = p_m \left[\frac{\mathrm{cm}^3_{\text{pore volume}}}{\mathrm{g}}\right] \cdot \rho \left[\frac{\mathrm{g}}{\mathrm{cm}^3_{\text{nonporous material}}}\right] \qquad (2\text{-}16)$$

Although this "volume porosity" p_v is a dimensionless physical index variable it is helpful to keep the dimensions with its indices because the volume dimensions in p_m and ρ have different meanings. Using p_v values porosities of materials with different densities can be compared quantitatively. However, this p_v is not very demonstrative and it is beneficial to calculate a more comprehensive quantity. From the p_v values a "relative porosity" p_{rel} specifying how much of the total sample volume consists of pore volume can be calculated. p_v represents the pore volume in a sample per one cubic centimeter of nonporous material and consequently p_{rel} can be calculated from p_v by the following equation:

$$p_{\text{rel}} = \frac{p_v}{p_v + 1} = \frac{p_m \cdot \rho}{p_m \cdot \rho + 1} \qquad (2\text{-}17)$$

p_{rel} is the pore volume of a porous material in percentage terms referred to the total sample volume and is independent of the material density. A value of $p_{\text{rel}} = 0.4$ means that 40% of the sample volume consists of pore volume and consequently 60% of the sample volume consists of non-porous (metal oxide) material.

In general, the relative porosity value can be calculated from the CPV or the TPV data. Within this thesis, tabulated relative porosity data were calculated on the basis of the TPV values and thus include pore volumes of pores up to a diameter of approximately 100 nm. Otherwise, comparative discussions, especially in chapter 3.6, will be done on the basis of DFT-derived CPV plots, in which relative porosity values are calculated from the CPV values. It has to be taken into account that the relative porosities derived from the CPV values neglect all porosity generated by pores larger than approximately 32 nm, which is the upper pore size limit accessible by DFT calculations using the "spherical adsorption" model (see chapter 3.2.3).

Relative porosity values in this thesis are calculated and illustrated in all tables and figures in addition to the "traditional" mass referred data so that the reader is always able to compare the data of different materials with each other. Especially in chapter 3.6 such relative porosity values will be used for the discussion and evaluation of the physisorption data, when the different materials are explicitly compared to each other. Within the other chapters, in which only one material is considered at a time, the mass referred data are preferably used in the discussions.

2.6.3.2 Comparison of specific surface areas

Similarly as the porosity of different materials, also the specific surface areas of different materials may be better comparable, if they are not referred to the sample mass. Unfortunately, it is not possible to calculate a physical index quantity for the specific surface area which is comparable for different materials analogously as the relative porosity values. In principle, a measured surface area can be referred to

a. the sample´s mass *m*,
b. the sample´s volume *v* or
c. the sample´s molar amount of substance *n*

resulting in specific surface area values of the following dimensions:

a. the "weight normalized" specific surface area S_m [$m^2 \cdot g^{-1}$];
b. the "volume normalized" specific surface area S_v [$m^2 \cdot cm^{-3}$] or
c. the "molar normalized" specific surface area S_n [$m^2 \cdot mol^{-1}$].[9]

From the physisorption analysis software[125] specific surface areas derived via the BET method are usually given as S_m value, but with the help of the density of the materials ρ or its molar mass M these data can be converted to S_v or S_n values.

Indeed, all these three specific surface areas are not dimensionless index quantities and which of them is most adequate to compare specific surface areas of different materials needs to be investigated in dependence of the actual scientific problem (see chapter 3.6.2).

[9] Such S_n values were already propose earlier.[129]

3 Synthesis of metal oxide nanofibers

3.1 Goals and syntheses overview

Inorganic nanofibers of different oxides, namely silica (see chapter 3.2), zirconia (see chapter 3.3), ceria (see chapter 3.4) and tin oxide (see chapter 3.5), were prepared with the focus on the preparation of inorganic fibers from polymer solutions containing nanoparticle dispersions. Syntheses of oxide fibers starting from polymer solutions containing sol-gel precursors are already known from literature,[65,109,130–132] and were prepared mainly for the purpose of comparison. Advantages of the approach starting from nanoparticles as well as challenges which had to be overcome were discussed in chapter 2.4.6 (see figure 2-11): First, it was necessary to prepare nanoparticle dispersions that are compatible with a spinning polymer and which could be combined with a spinning solution of sufficiently high concentrated polymer as well as nanoparticles. It was investigated whether nanoparticle-derived fibers (NP-fibers) exhibit pivotally different properties than sol-gel-derived fibers as it could be assumed on the basis of the preliminary titania study.[75] Afterwards, the morphological properties of the prepared NP-fibers were characterized by electron microscopy (SEM) and physisorption and compared to the properties of "conventional" sol-gel fibers. These comparative analyses will be discussed concerning general conceptual differences in the preparation of electrospun fibers from different building blocks, namely nanoparticles or sol-gel precursors.

The chapters 3.2−3.5 each present the results for one of the investigated oxides. In chapter 3.6 all these individual results are summarized including results of the former study on titania fibers (see chapter 2.5.2)[75] in order to deduce general trends that can be found for all materials and that originate from the preparation method.

3.2 Silica fibers

3.2.1 Introduction and sample overview

Electrospun polymer/silica composite nanofibers were first prepared by Shao et al. from poly(vinyl alcohol) (PVA) and tetraethyl orthosilicate (TEOS) sol-gel precursor as silica source in 2003.[133] In the same year Choi et al. electrospun a pure, aged TEOS-sol without the addition of any organic polymer to obtain pure silica nanofibers.[134] Various publications dealing with silica-based nanofibers used sol-gel precursors as silica source for electrospinning in the following years.[135–138] In 2006 Lim et al. were the first to use aqueous suspensions of preformed silica nanoparticles instead of sol-gel precursors for electrospinning.[139] Although there are some other publications on nanoparticle-derived silica fibers,[91,93,140,141] there is a lack of detailed investigations on the morphological properties of these fibers that go beyond the characterization by electron microscopy. Furthermore it is unclear, if there are any characteristic differences between sol-gel- and nanoparticle-derived silica fibers. Hence, differences between these two approaches are explored and characterized in this chapter. Therefore various silica nanofibers were produced via different synthetic approaches using tetramethyl orthosilicate (TMOS) as sol-gel precursor on the one hand and different commercial nanoparticle dispersions (known as so-called "Ludox"-dispersions) on the other hand.

Table 3-1 gives a survey of the synthesized samples that were further examined by nitrogen physisorption (see chapter 3.2.4).

Table 3-1: Overview of all synthesized silica samples and composition of the corresponding solutions that were used for the syntheses.

sample no.	sample category	polymer	SiO_2	weight ratio SiO_2/polymer	solvent
1	sol-gel fibers	5 wt.-% PVP	15 wt.-% TMOS (≙ 6 wt.-% SiO_2)	1.18/1	MeOH/H_2O
2	sol-gel fibers	8 wt.-% PVP	15 wt.-% TMOS (≙ 6 wt.-% SiO_2)	0.74/1	MeOH/H_2O
3	pure particles	none	Ludox "AS" NPs	---	H_2O
4	pure particles	none	Ludox "HS" NPs	---	H_2O
5	pure particles	none	Ludox "SM" NPs	---	H_2O
6	NP-fibers	2 wt.-% PEO	0.45 wt.-% SiO_2 (Ludox "AS" NPs)	0.23/1	H_2O
7	NP-fibers	2 wt.-% PEO	0.45 wt.-% SiO_2 (Ludox "HS" NPs)	0.23/1	H_2O
8	NP-fibers	2 wt.-% PEO	0.45 wt.-% SiO_2 (Ludox "SM" NPs)	0.23/1	H_2O
9	dried spinning solution	2 wt.-% PEO	0.45 wt.-% SiO_2 (Ludox "AS" NPs)	0.23/1	H_2O
10	dried spinning solution	2 wt.-% PEO	0.45 wt.-% SiO_2 (Ludox "HS" NPs)	0.23/1	H_2O
11	dried spinning solution	2 wt.-% PEO	0.45 wt.-% SiO_2 (Ludox "SM" NPs)	0.23/1	H_2O
12	NP-fibers	2.3 wt.-% PEO	1.2 wt.-% SiO_2 (Ludox "AS" NPs)	0.50/1	H_2O
13	NP-fibers	2.3 wt.-% PEO	1.7 wt.-% SiO_2 (Ludox "AS" NPs)	0.75/1	H_2O
14	NP-fibers	2.3 wt.-% PEO	2.3 wt.-% SiO_2 (Ludox "AS" NPs)	1.00/1	H_2O
15	NP-fibers	2.3 wt.-% PEO	2.8 wt.-% SiO_2 (Ludox "AS" NPs)	1.25/1	H_2O
16	NP-fibers	2.3 wt.-% PEO	2.8 wt.-% SiO_2 (Ludox "AS" NPs)	1.25/1	H_2O
17	NP-fibers	2.3 wt.-% PEO	3.3 wt.-% SiO_2 (Ludox "AS" NPs)	1.50/1	H_2O

Sol-gel fibers were produced from methanolic solutions containing TMOS as precursor and electrospun with poly(vinylpyrrolidone) (PVP) as spinning polymer similarly as already published elsewhere.[142] Two different samples were prepared: One sample was prepared from a solution containing 5 wt.-% PVP[10] in the spinning solution, another contained 8 wt.-% PVP. In both cases the concentration of the TMOS precursor was 15 wt.-% equivalent to 6 wt.-% of SiO_2. Also all other experimental parameters were kept constant in order to investigate the influence of the polymer concentration.

[10] The wt.-% of different components in the spinning solutions are calculated as mass of the component per total mass of the electrospinning solution.

Nanoparticle-based electrospun fibers were spun from Ludox dispersions with poly(ethylene oxide) (PEO) as spinning polymer and water as solvent. In the experiments the type of Ludox dispersion – namely "AS 30", "HS 30" or "SM 30" dispersion[143] – was changed in the spinning solutions while the PEO concentration was kept constant at 2.0 wt.-% and the weight ratio of SiO_2 particles to PEO was fixed to 0.23/1. The particles in the Ludox dispersions had diameters in the range of 10 nm in all cases. The differences between the Ludox dispersion are mainly their different stabilizations which are specified by the acronyms "AS", "HS", or "SM".[143] In order to compare these fiber materials with the properties of the bare particles, the pure Ludox dispersions were dried and calcined at the same temperature as the fibers, which was 550 °C.[11]

Further experiments were conducted to elucidate the interaction between the polymer PEO and the Ludox particles. It was found that Ludox "AS 30" dispersions are best suited for electrospinning because other dispersions such as Ludox "HS 30" or Ludox "SM 30" produce a less stable jet during electrospinning, when they are used in high concentrations. In the experiments with the Ludox "AS 30" particles, the amount of Ludox dispersion in the spinning solutions was varied, while the PEO concentration was kept constant at 2.3 wt.-%. The weight ratio of SiO_2 particles to PEO was varied in the range of 0.5/1 to 1.5/1. Except for the Ludox concentrations all other experimental conditions were the same in these investigations. The concentration of the Ludox "AS 30" dispersions in the spinning solutions of the above mentioned experiments was more than twice as high (i. e. in the range of 1.2−3.3 wt.-%) as in the other set of experiments, in which the different kinds of Ludox dispersions are studied. Nevertheless, these experiments are comparable, because all other experimental conditions were the same.

Besides SEM investigations (see chapter 3.2.2), detailed analyses by nitrogen physisorption were conducted on all above mentioned fiber samples in order to characterize their porosities comparatively (see chapter 3.2.4). A similar study has already been performed on electrospun titania nanofibers[1,75] and these published results will be cited in case it helps to discuss the results on silica fibers.

One difficulty in the study on titania nanofibers was the limited availability of titania nanoparticle dispersions. The titania dispersions had to be self-synthesized and their limited laboratory batch size required a multiple synthesis of new dispersions. It was not possible to synthesize "self-made" particle dispersions on a lab scale large enough to conduct all electrospinning experiments from one batch, so that such self-synthesized particle dispersions may suffer from slight variations in their properties like particle size, their size distribution or the dispersion concentration etc. In contrast, aqueous SiO_2 nanoparticle dispersions are commercially available[143,144] in typical batch sizes of one liter (e. g. from Sigma-Aldrich) preventing problems of reproducibility concerning the synthesis of the particle dispersions. This amount is sufficient to conduct a lot of electrospinning experiments from only one batch, so that the dispersion properties are the same for all experiments.

[11] The Ludox dispersions used are all aqueous based dispersions with the same particle concentrations. They only differ in properties like the stabilization of the particles (ammonia vs. sodium stabilized).[143] This may have influence on surface properties of the particles and will be investigated in chapter 3.2.4.

For this reason the following experiments on nanoparticle-derived electrospun silica fibers can be considered as reliable model experiments for nanoparticle-derived electrospun fibers of other materials (see chapters 3.3−3.5) facilitating to study general questions on the electrospinning of nanoparticles by using Ludox dispersion. The results obtained for other oxides (see chapters 3.3 - 3.5) will be compared with the results on silica fibers in chapter 3.6 so that a more general conceptual understanding may be deduced by combining the results of all materials.

3.2.2 SEM analyses on silica fibers

Generally, SEM investigations were performed on all synthesized fiber samples listed in table 3-1, so that there is proof of a successful electrospinning process for all of them. Nevertheless, only representative SEM analyses are presented in this section, because samples prepared from very similar solutions showed no significant differences in the SEM pictures. For example, the samples 12−17 from table 3-1 were prepared from the same solution apart from a different content of Ludox particles. Only four out of these six samples are presented in figure 3-3, because the two missing samples had a content of Ludox particles lying in between the concentrations of the samples shown, with no significant differences concerning the SEM results.

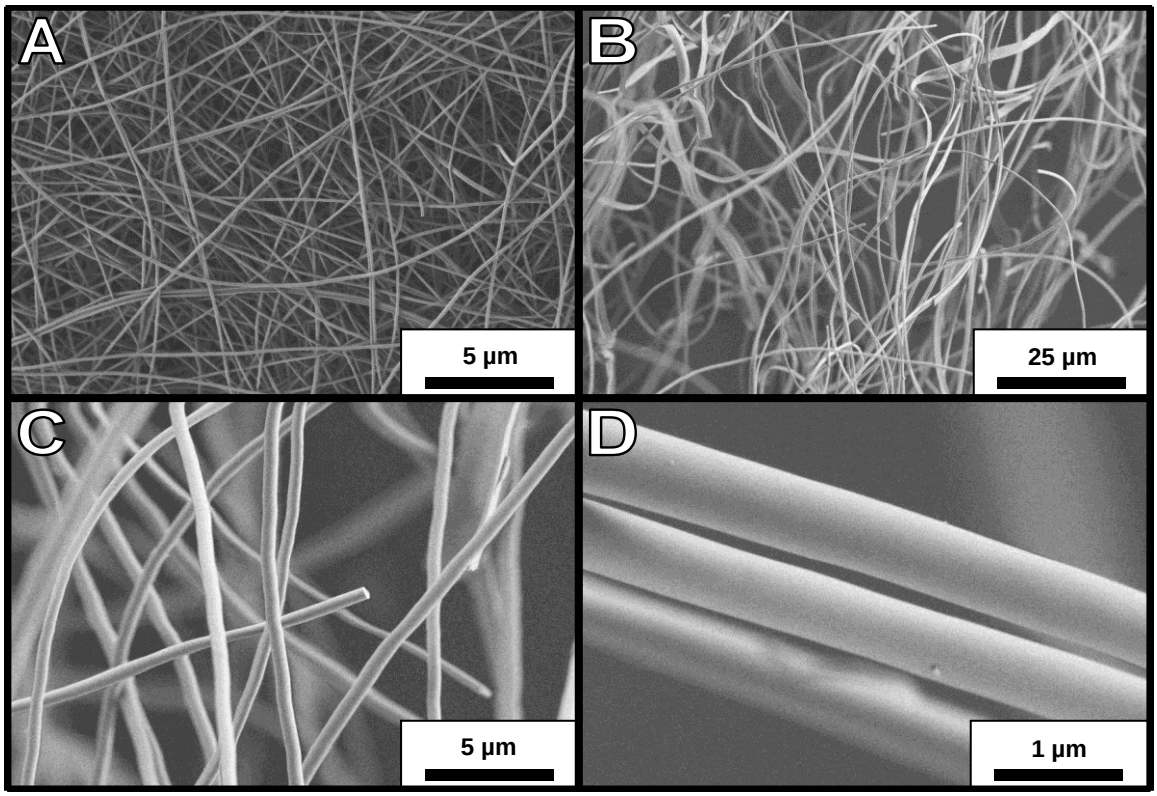

Figure 3-1: SEM pictures of silica fibers obtained from TMOS as sol-gel precursor and electrospun with PVP after calcination at 550 °C; A: Spun with 5 wt.-% PVP (see table 3-1, sample 1); B–D: Spun with 8 wt.-% PVP (see table 3-1, sample 2).

The silica sol-gel fibers electrospun with 8 wt.-% PVP (sample 2 in table 3-1) had typical diameters around 500 nm with optically smooth surfaces (see figure 3-1 B–D). Fibers electrospun with 5 wt.-% PVP had typical diameters around 150 nm and are thinner due to the lower viscosity of the spinning solution and the resulting stronger stretching of the jet (see figure 3-1 A; sample 1 in table 3-1) as expected. The distributions of the fiber diameters were found to be within a narrow range of not more than approximately ± 20 % around the above mentioned mean diameters for both samples. These homogeneous fiber diameters are a consequence of constant and well-controlled electrospinning conditions concerning parameters like viscosity of or charge density on the jet. Such constant spinning cannot be generally expected for sol-gel-derived fibers, because the ongoing sol-gel reactions during the spinning process often cause alteration in fiber diameters. Except for the fiber diameters there are no other considerable differences obvious from the SEM investigations that arise from the different PVP content in the respective spinning solutions. Furthermore, the calcined silica fiber mats had almost no cracks in contrast to all other oxide fibers prepared within this thesis. This is a consequence of the also macroscopically observable mechanical flexibility of these fibers. The silica fiber mats from sol-gel precursors can be bent like polymer fiber mats suggesting an untypically high elastic modulus for an inorganic material. None of the other electrospun fiber samples showed similar mechanic properties, irrespective of either the material (TiO_2, ZrO_2, CeO_2, etc.) or the starting material (sol-gel precursors or nanoparticles). Also the nanoparticle-derived silica fibers were much more brittle which may be a consequence of an incomplete sintering of the particles resulting in predetermined breaking points. Furthermore, such brittleness is generally expected for the other investigated metal oxides, because they are typical ceramic materials which are intrinsically brittle.

Silica fibers obtained from different Ludox nanoparticles were electrospun with 2.0 wt.-% PEO and 0.45 wt.-% Ludox particles in each experiment. It was possible to obtain silica fibers from all three silica dispersions (Ludox “AS-30”, “HS-30” or “SM-30”, respectively; see table 3-1, samples 6-8) after calcination at 550 °C. The SEM investigations revealed very similar results for all three types of Ludox particles (see figure 3-2). They all had typical diameters with a narrow distribution in the range of 150 nm to 300 nm. Furthermore, no significant amount of beads was found in any of the samples and they had only sporadic cracks on the macroscopic length scale. The Ludox fibers are all collected in a wounded manner that is significantly different to the sol-gel fibers (see figure 3-1). The second mentionable difference to the sol-gel fibers is the optically rough surface structure of the Ludox fibers (compare figure 3-2 E and figure 3-1 D). Such rough surface structures were observed for all nanoparticle-based fibers. This finding is the first hint at an increased porosity of nanoparticle-based fibers compared to sol-gel fibers which will be further investigated in chapter 3.2.4.

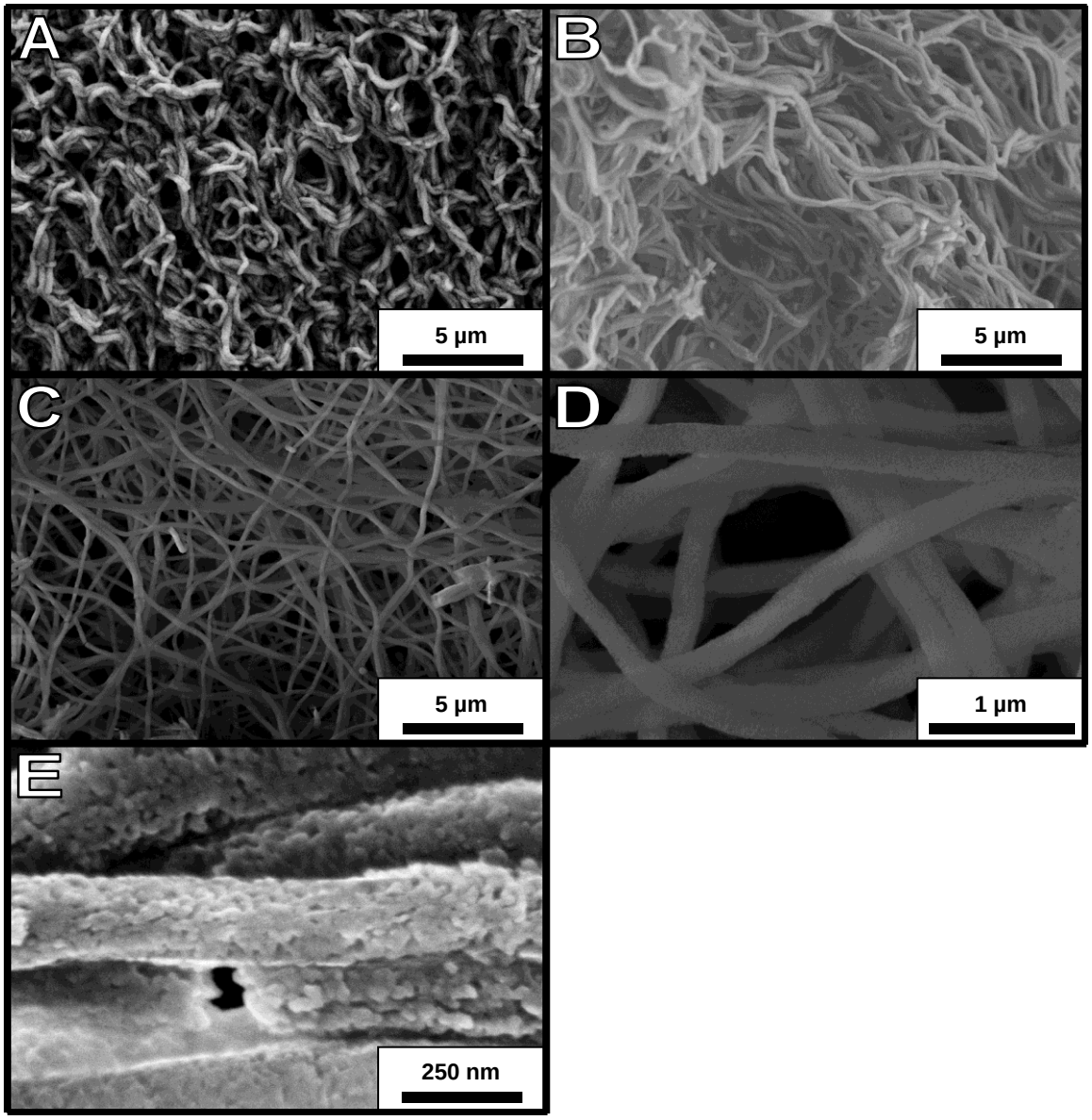

Figure 3-2: SEM pictures of silica fibers obtained from different Ludox particles and electrospun with 2.0 wt.-% PEO after calcination at 550 °C. Each spinning solution contained 0.45 wt.-% of Ludox particles; A: Fibers from a Ludox "AS-30" dispersion (see table 3-1, sample 6); B: Fibers from a Ludox "HS-30" dispersion (see table 3-1, sample 7); C–E: Fibers from a Ludox "SM-30" dispersion (see table 3-1, sample 8).

When Ludox "AS 30" dispersions were electrospun with a varying amount of particles in the range of 1.2 wt.-% to 3.3 wt.-% and with 2.3 wt.-% of PEO in the spinning solution (see table 3-1, samples 12−17) the optical shape of the fibers changed with the employed amount of silica particles (see figure 3-3). This is a consequence of the changing properties of the spinning solution: Particularly the electric conductivity of the spinning solution increases with higher Ludox particle content, because the Ludox "AS" particles are ionically stabilized by ammonium ions. This argument also explains why a PEO concentration as high as 2.3 wt.-% is necessary to spin the above mentioned Ludox containing solutions (see table 3-1, samples 12−17).

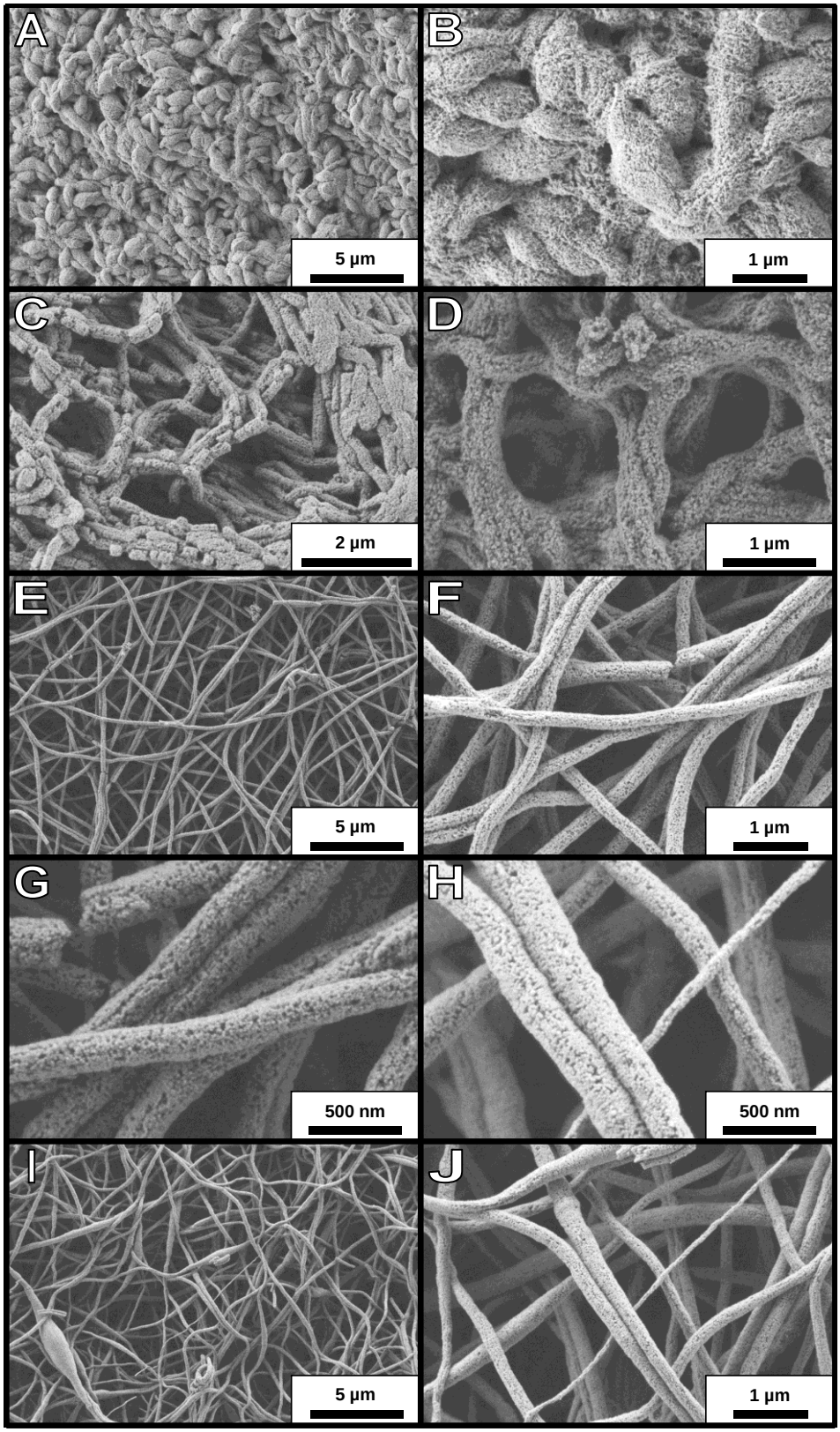

Figure 3-3: SEM pictures of several silica fibers obtained from Ludox AS particles electrospun with 2.3 wt.-% PEO after calcination at 550 °C; The concentrations of Ludox particles in the spinning solutions was varied: A, B: 1.2 wt.-% (see table 3-1, sample 12); C, D: 1.7 wt.-% (see table 3-1, sample 13); E–G: 2.3 wt.-% (see table 3-1, sample 14); H–J: 3.3 wt.-% (see table 3-1, sample 17).

Without any Ludox particles electrospinning of PEO (used with a molecular weight (M_w) of 1,000,000 g·mol^{-1} in all these experiments) would not be possible in such a high concentration; the solution would be far too viscous. However, if Ludox particles are added, the high viscosity of the spinning solution is counteracted by the ionic conductivity of the ionically stabilized particles. In case only 0.45 wt.-% Ludox particles are added to the spinning solution (see samples 6-8), the concentration of PEO had to be reduced to 2.0 wt.-% in order to achieve a stable spinning process due to the lower conductivity of the solution. As a fundamental trend the stretching and thinning of the jet is promoted by a higher ionic conductivity of the spinning solution due to the higher concentration of charge carriers within the jet. Concerning the Ludox particle-derived silica fibers the variation of the charge carrier density within the jet leads to the following results evidenced by SEM pictures (see figure 3-3): With low silica particle content (see table 3-1, sample 12; figure 3-3 A, B) the SEM figures show a material whose fibrous morphology could hardly be identified. The figures show mainly large beads in a seemingly random site. Only on closer inspection is it possible to see the pearl–necklace-like connectivity of these beads. Due to the low Ludox content of only 1.2 wt.-% in the spinning solution and the resulting low conductivity, the electrospinning process produces only strongly beaded fibers.[12] When the Ludox content in the spinning solution is increased to 1.7 wt.-% or 2.3 wt.-% respectively (see figure 3-3 C, D and E–G), the increased conductivity within the solution leads to fibers that are more or less devoid of beads and exhibit narrower distributions in the fiber diameters. When the Ludox content is further increased up to 3.3 wt.-% (see figure 3-3 H–J) the fiber diameters are more inhomogeneous and some elongated beads occur. This might be explained by "agglomeration effects": When the Ludox particle concentration within the solution becomes too high, small fluctuations in their distribution may lead to such altering diameters of the fibers after spinning. In conclusion, a Ludox concentration in the range of approximately 1.5 wt.-% to 3.0 wt.-% seems to be optimal to spin homogenously thick fibers with aqueous 2.3 wt.-% PEO solutions. When lower Ludox concentrations are to be spun, also the PEO concentration has to be reduced (see table 3-1, samples 6–8). In other words, the concentration of the Ludox particles should be in the same range as the polymer concentration. This phenomenon can be observed in many electrospinning experiments and can be considered as an empirical rule of thumb for the preparation of inorganic fibers from nanoparticle dispersions.

A further observation is that all nanoparticle-derived silica fibers are brittle after calcination at 550 °C. Depending on the location of the SEM picture on the sample, there are areas featuring numerous cracks on the macroscopic length scale (see e. g. figure 3-3 C). Furthermore, all fibers in figure 3-3 seem to have a porous surface structure which can be observed easily in the high magnification images G and H. The SEM pictures indicate that all these fibers possess small pores with diameters of some nanometers. This porosity will be investigated in detail by nitrogen physisorption in chapter 3.2.4.

[12] A slightly lower PEO concentration would probably lead to less beaded fibers, as can be evidenced by the samples in Figure 3-2: The PEO concentration in these experiments had to be reduced to obtain spinable solutions because the Ludox concentrations in these experiments was much lower (0.45 wt.-%).

3.2.3 Physisorption: General investigations concerning electrospun fibers

3.2.3.1 Choice of the DFT model

Surface and porosity characteristics of electrospun fibers are analyzed by nitrogen physisorption in this thesis. The materials investigated are predominantly mesoporous, and microporosity is absent in most of the samples so that only nitrogen physisorption was performed to analyze the mesoporous materials. Only particular samples exhibit some microporosity which could be analyzed in more detail by argon physisorption but this was beyond the scope of this thesis.

Before the porosity of mesoporous electrospun fibers can be analyzed in detail (see chapter 3.2.4), it has to be figured out which DFT kernel is best suited to analyze such materials. Therefore the different DFT kernels are compared exemplarily on several representative silica samples[13] (see table 3-1, samples 3, 6, 9, 11, 14 and figure 3-4–figure 3-6).[14]

There are three kernels for the DFT method available to analyze silica materials with nitrogen as adsorbate:

1. One kernel is for a silica adsorbent with cylindrical pore geometry in which the non-linear density functional theory (NLDFT) is applied to the adsorption branch of the measured isotherm. This model will be entitled as “cylindrical adsorption” model in the following discussion. In figure 3-4–figure 3-8 the data from this model are illustrated in black.
2. The second kernel is for a silica adsorbent with cylindrical pore geometry in which the NLDFT is applied to the desorption branch of the measured isotherm. This model will be entitled as “cylindrical equilibrium” model in the following discussion. In figure 3-4–figure 3-8 the data from this model are illustrated in blue.
3. The third kernel is for a silica adsorbent with cylindrical pore geometry for pores smaller than 5 nm in diameter and spherical pore geometry for pores larger than 5 nm in diameter in which the NLDFT is applied to the adsorption branch of the measured isotherm. This model will be entitled as “spherical adsorption” model in the following discussion. In figure 3-4–figure 3-8 the data from this model are illustrated in red.

The comparison of the measured isotherm with the calculated ones obtained from the three different DFT models are all in good accordance with each other (see figure 3-4 B–D). Measured and calculated isotherms are in such good agreement that they can hardly be distinguished. The magnifications for small relative pressures (see figure 3-4 C) reveal that the cylindrical adsorption model slightly overestimates small mesopores, so that the calculated isotherm is shifted to slightly higher adsorbed volumes from the measured isotherm. The magnifications for large relative pressures (see figure 3-4 D) illustrate that the two adsorption models continue along the adsorption branch and the equilibrium model follows the desorption branch of the

[13] At this point only the general methodological analysis results shall be discussed, so that no details and interpretations concerning the representative samples are given here. The detailed discussion of the data will be given later in chapter 3.2.4.

[14] Please note that all deductions that will be drawn within this section are also valid for all other electrospun samples. The following analyses were repeated on different further samples with the same results, so that the general validity was proven. The presentation of these analyses is omitted, because it would not reveal any new results.

measured isotherm precisely. The staged trend of the calculated isotherms for large relative pressure values is a consequence of the limited number of implemented reference data for large pore sizes in the kernels.

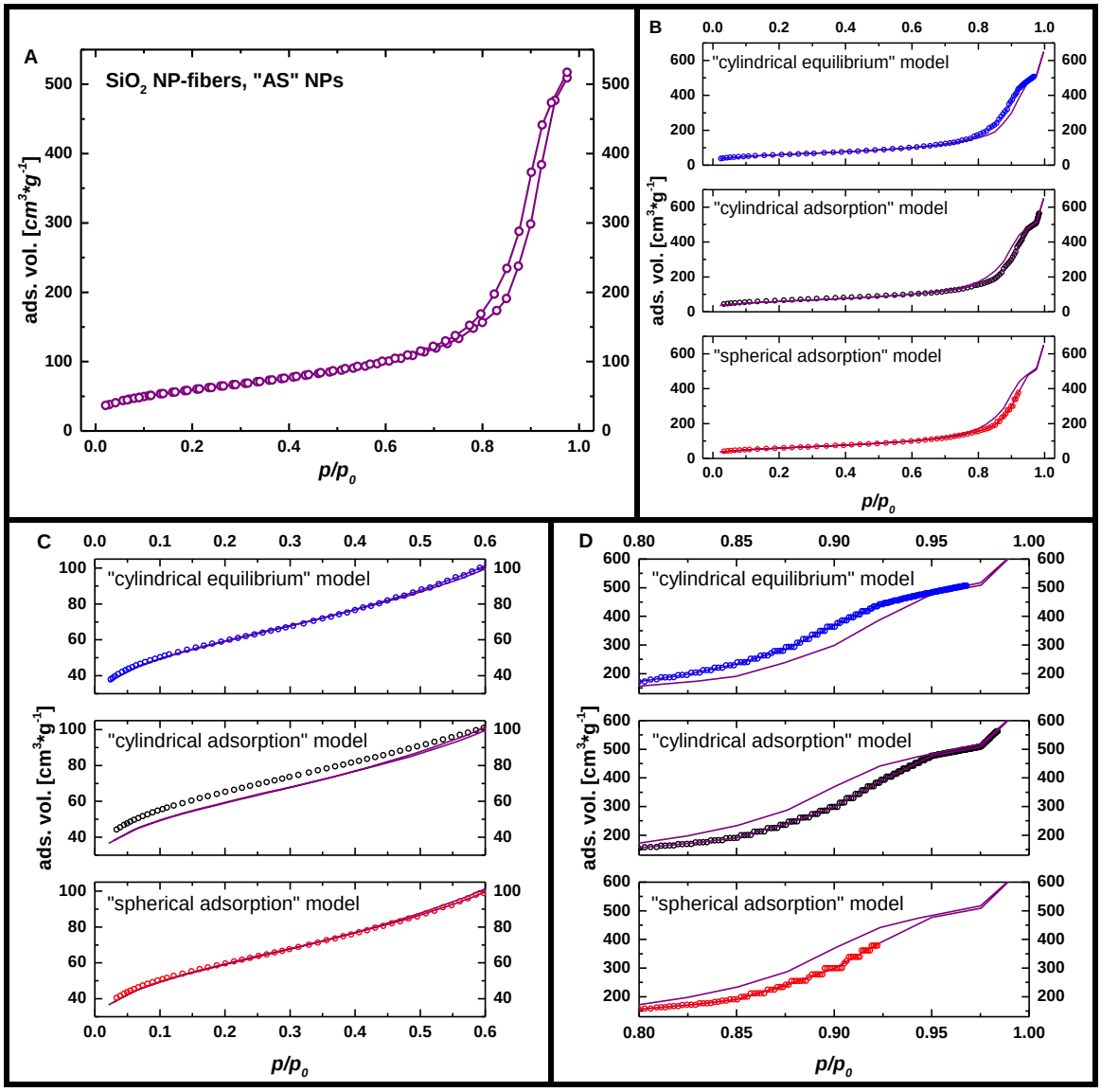

Figure 3-4: A: Measured isotherm of silica NP-fibers obtained from Ludox "AS" NPs (see table 3-1, sample 6); B–D: Comparison of the measured isotherm illustrated in A with isotherms calculated by DFT; B: overview of the complete p/p_0 range ($0 \le p/p_0 \le 1$); C: magnification of the low relative pressure range ($0 \le p/p_0 \le 0.6$); D: magnification of the high relative pressure range ($0.8 \le p/p_0 \le 1.0$). Color coding: purple: measured isotherm; black: data calculated by the "cylindrical adsorption" model; blue: data calculated by the "cylindrical equilibrium" model; red: data calculated by the "spherical adsorption" model.

Since all three models are in good accordance with the measured data, the comparison of measured and calculated isotherms does not help to figure out the optimum DFT model for the analysis of electrospun fibers. Hence, more profound considerations are necessary to assess which model should be applied for electrospun fibers. Consulting the user manual of the "AS1win" data analysis Software,[125] there are some hints to the differences between the DFT models:

The cylindrical equilibrium model is well suited to characterize samples with a type H1 hysteresis loop typical of samples with a well-defined pore size and structure.[16] However, electrospun fibers were found to mostly exhibit type H2 or H3 hysteresis loops (see chapter 3.2.4) which are typical of disordered pore structures with a wide pore size distribution. Since the electrospinning synthesis is not expected to produce well-ordered pore structures with a narrow pore size distribution and the SEM analyses also back this assumption (see chapter 3.2.2), the cylindrical equilibrium model does not seem to be optimal to analyze these samples. In contrast, the cylindrical adsorption model is assumed to give reliable results for samples with H2 hysteresis loops,[125] though this model overestimates the small mesopores (see above and figure 3-4 C) in electrospun fibers. Hence, this model also seems not to be the optimal one. The remaining spherical adsorption model assumes spherical pore geometry for pores larger than 5 nm in diameter. The SEM figures support the hypothesis that the mesopores that can be observed especially within the nanoparticle-derived fibers, have a more or less spherical shape, rather than a cylindrical one (see e. g. figure 3-3 G and H). Consequently, the DFT analyses of all samples of this thesis will be performed using this kernel. It has to be noted that the spherical pore geometry of the samples cannot be verified by SEM analyses doubtlessly, because SEM pictures only give a two- but not three-dimensional image of a sample. Hence, the decision to use the spherical adsorption model remains an arbitrary decision with considerable consequences on the data analyses:

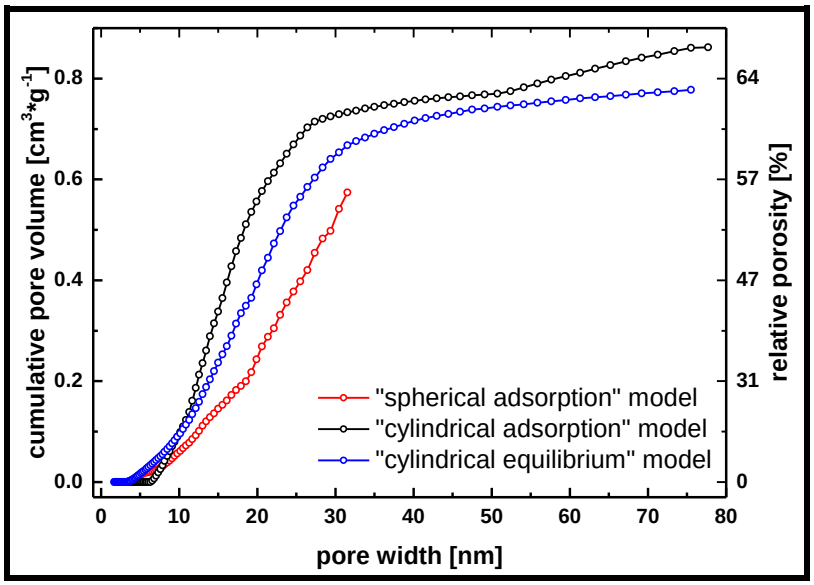

Figure 3-5: Comparison of the CPV plots of silica NP-fibers obtained from Ludox AS NPs (see table 3-1, sample 6) calculated by the three different DFT approaches. Color coding: black: calculated data from "cylindrical adsorption" model; blue: calculated data from "cylindrical equilibrium" model; red: calculated data from "spherical adsorption" model.

These consequences become obvious when the results from the different DFT kernels are compared (see figure 3-5): Although all three DFT kernels are able to reproduce the measured isotherm quite precisely, there are significant differences between the models concerning the calculated pore size distributions. When the cumulative pore size distribution is calculated for one and the same sample with all three DFT kernels, these significant differences can be seen

(see figure 3-5). Generally, all three “cumulative pore volume” (CPV) plots show a similar linear trend for pore sizes in the range of approximately 5−30 nm which will be interpreted later (see chapter 3.2.4). Qualitatively, the main difference in the three plots is an offset in the pore sizes. For a given cumulative pore volume of e. g. 0.5 $cm^3 \cdot g^{-1}$ the corresponding maximum pore sizes that contribute to this porosity change in a range between approximately 20 nm (“cylindrical adsorption” model) up to approximately 30 nm (“spherical adsorption” model). In other words, irrespective of the fact that all three models are in good agreement with the measured isotherm, the calculated pore sizes differ over a range as wide as 10 nm in this example. The “spherical adsorption” model gives pore sizes that are up to 50% larger than the pore sizes obtained from the “cylindrical adsorption” model. This finding is a consequence of the different pore geometries assumed with the different kernels. Interpreting figure 3-5 the other way round, it also can be stated that the three different DFT models give different porosities, if a specific upper pore size limit is considered. From this point of view, the “spherical adsorption” model always gives the lowest porosity of all three models as was expected due to the assumed pore geometries: If the same pore diameters are considered, a spherical pore always has a lower volume than a cylindrical pore which is a general trend valid for all investigated samples (see figure 3-6).

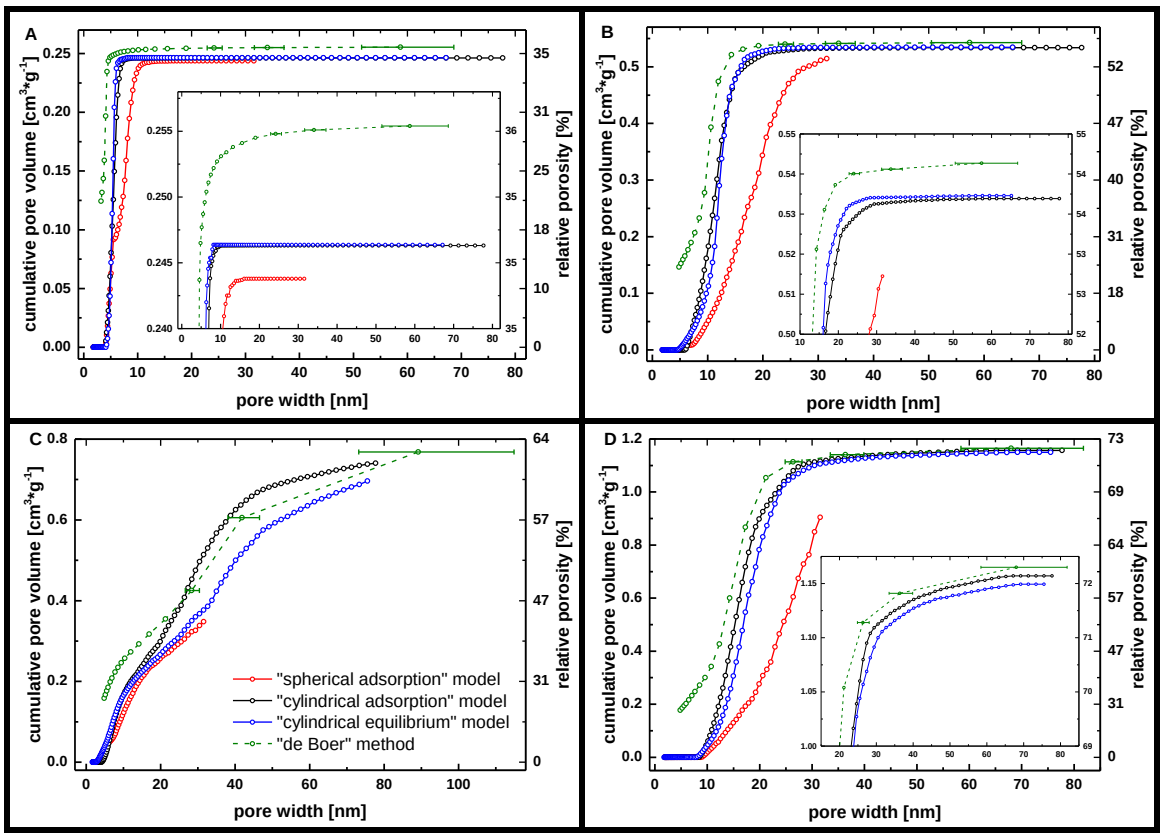

Figure 3-6: Comparison of the CPV plots of several representative silica samples (see table 3-1, A: samples 3, B: sample 9, C: sample 14 and D: sample 11) calculated by the three different DFT approaches. Additionally, data calculated by the “de Boer” method are implemented (see chapter 3.2.3.2). The corresponding isotherms of the illustrated samples can be found in the appendices (see figure 6-5–figure 6-8). Color coding: black: calculated data from “cylindrical adsorption” model; blue: calculated data from “cylindrical equilibrium” model; red: calculated data from “spherical adsorption” model; green: data calculated by the “de Boer” method with error bars in the high relative pressure range representing the reliability of the calculated pore sizes at the considered pressure.

Furthermore, the two other models, i. e. the “cylindrical adsorption” and the “cylindrical equilibrium” model both result in similar porosities for a given upper pore size limit.

As a consequence of the above considerations, only the trend of the CPV plots can be interpreted when electrospun fibers are investigated. The absolute pore size values have to be considered with great caution and it has to be taken into account that these values may deviate considerably from the real pore sizes as long as they are not verified by other analytic methods. Unfortunately, the disordered pore structure of the electrospun fibers prevents additional analyses by methods like e. g. small-angle X-ray scattering (SAXS), which is a standard alternative method used to estimate pore sizes in ordered mesoporous samples.[145,146]

Fortunately, the most important point in the physisorption analyses performed within this thesis is the relative and qualitative comparison of different samples concerning their porosity. Therefore an exact determination of pore size is not necessary. As long as only one DFT model is used for the analyses of all samples, they can be directly compared and the qualitative interpretation of these analyses is not affected by uncertainties in the calculation of precise pore sizes. If several samples exhibit specific differences in their porous characteristics and the accumulation of the pore volume with increasing pore size, the DFT analyses reveal such differences anyway (see figure 3-7). It has to be noted, that some DFT analyses exhibit a slight kink of the CPV plot at a pore size of 5 nm (see e. g. figure 3-7, plot in green). This kink is supposed to be an artifact of the analysis, because the “spherical adsorption” model switches from assumed cylindrical pore geometry to spherical pore geometry at this pore size which is probably not consistent with the structure of the sample. If a DFT kernel assuming solely cylindrical pore geometry is used for the analysis, no kink can be found in the corresponding CPV plot proving the kink to be an artifact originating from the change of assumed pore geometry in the former DFT model.

As long as the spherical adsorption model is used, it can be stated that calculated pore sizes can be understood as an upper limit, because this model provides larger pore sizes compared to the other DFT kernels. In the event that the assumed spherical pore geometry within the fiber samples is not correct and the physisorption behavior of such samples is more similar to a material with cylindrical pores, the real pore sizes would be smaller than calculated with the “spherical adsorption” model.

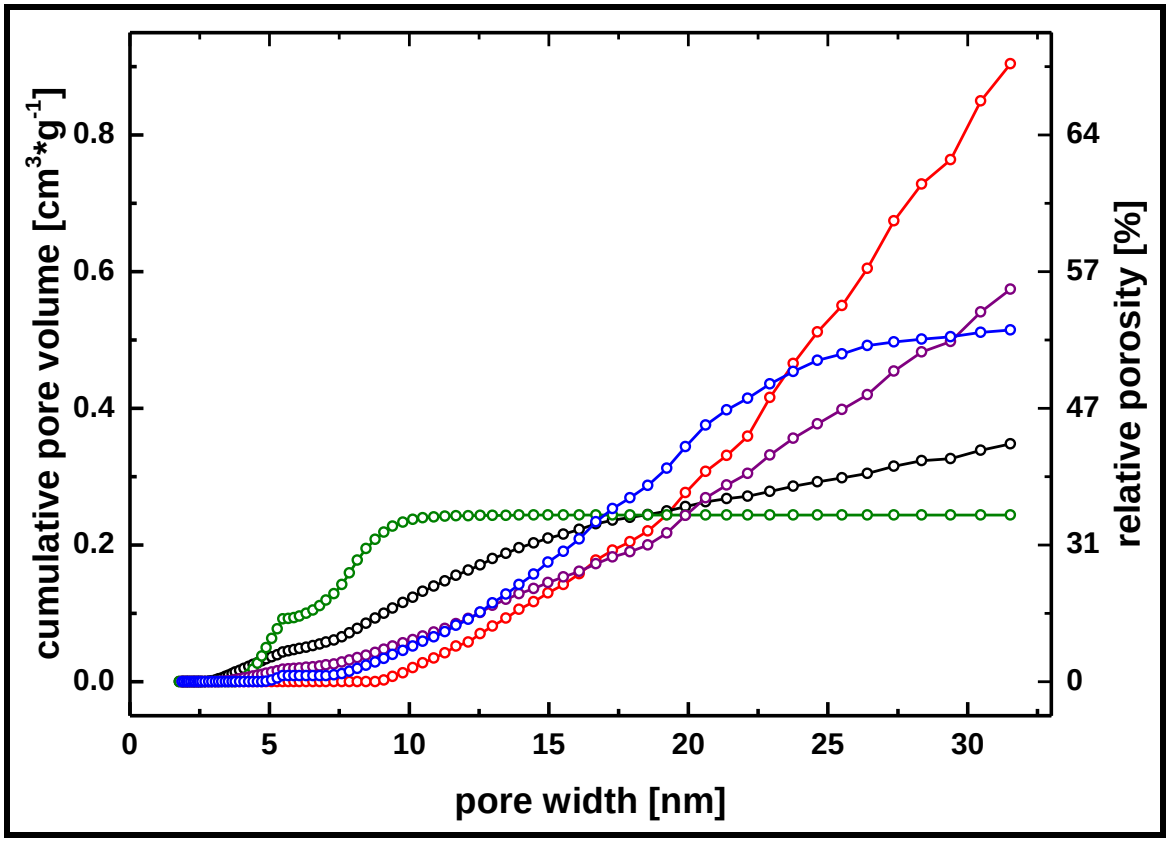

Figure 3-7: Comparison of CPV plots derived from the "spherical adsorption" DFT-model for several representative silica samples. The DFT analyses reveal differences in the porous characteristics of the samples irrespective of the uncertainties which are intrinsically present due to the unknown structural features of the investigated samples (see discussions). The detailed discussion of the physisorption results is presented in chapter 3.2.4. Color coding for the samples (see table 3-1): green: sample 3; purple: sample 6; blue: sample 9; red: sample 11; black: sample 14.

It has to be taken into account that only pore sizes up to approximately 32 nm in diameter can be analyzed using the "spherical adsorption" model, because there are no reference data in this kernel that refer to larger pore sizes. The other two models do have reference data for pores of up to 100 nm width, so that the CPV plots also present data in the range of 32−100 nm pore size width. Yet, these data have to be considered with caution: As can be seen from the Kelvin equation (2-13), the relative pressure and the pore size are in an exponential dependence. Although the exact mathematical background in the DFT model is much more complicated, this exponential relation is also roughly valid for DFT calculations. In order to illustrate the problem that accompanies any analysis concerning macro- or large mesopores by DFT the Kelvin equation is quite helpful: Using the Kelvin equation (2-13), pores of 40 nm or 100 nm in diameter correspond to a relative pressure of $p/p_0(r_k = 20\ nm) = 0.953$ or $p/p_0(r_k = 50\ nm) = 0.981$, respectively. In other words data beyond a pore diameter of 40 nm refer to data above a relative pressure of 0.95. In this range only very few measured data points can be acquired, so that the DFT analyses in this pore size region are based on only few experimental data and hence the results are vague. Thus, it is necessary to limit the DFT analyses to pore sizes in the mesoporous region to ensure the results to be reliable. For the analysis of macropores other methods like e. g. the mercury porosimetry should be used that are more adequate for such pore sizes.

3.2.3.2 Correlation of the DFT-derived cumulative pore volume and the total pore volume

In chapter 2.6.2 it was suggested that a "cumulative total pore volume plot" (TPV plot) could be constructed from the "de Boer method by using equations (2-13)–(2-15). When such a plot is constructed from the desorption data of the measured isotherm it can be compared with the CPV plots obtained from the different DFT kernels (see figure 3-8).

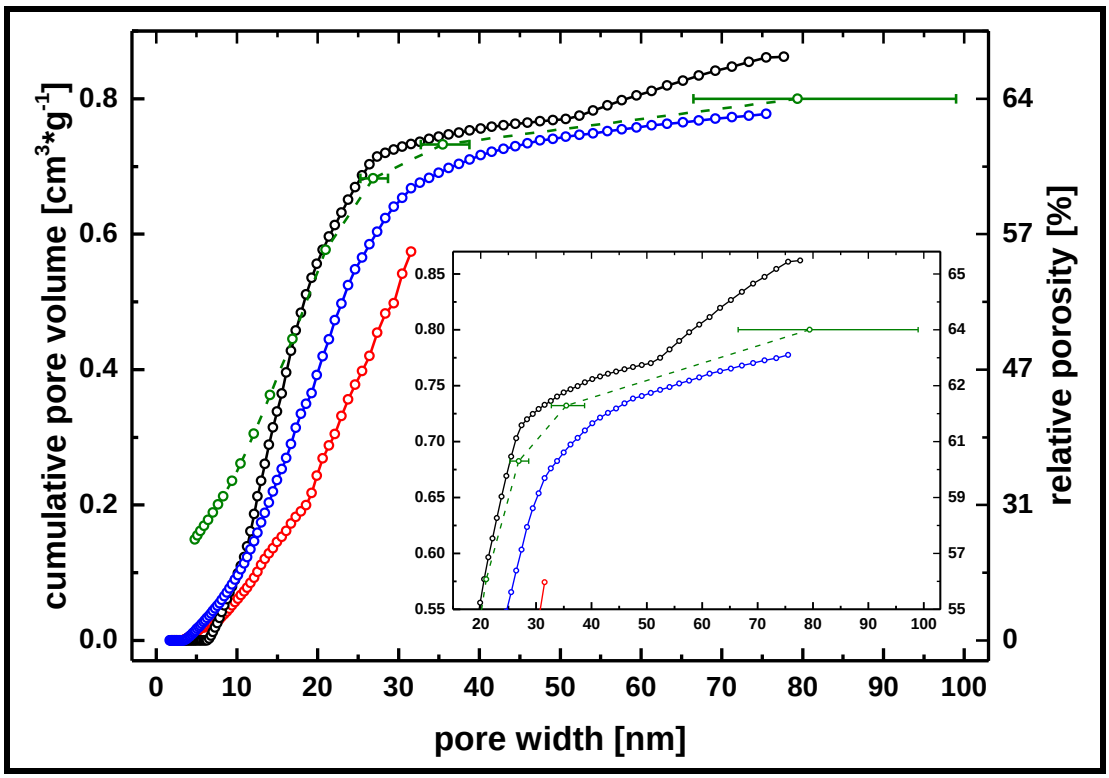

Figure 3-8: Comparison of the "cumulative total pore volume" plot obtained from the desorption data of the measured isotherm (silica NP-fibers obtained from Ludox AS NPs, see table 3-1, sample 6) by the "de Boer" approach (green, see equation (2-15)) with CPV plots calculated by different DFT models. Color coding for the DFT models: black: cylindrical adsorption model; blue: cylindrical equilibrium model; red: spherical adsorption model.

As already mentioned, the calculation of pore sizes from the "de Boer" method should only be considered as a rough estimation. As long as the pore geometry in a sample is known, the DFT analysis should lead to more reliable pore widths. Otherwise, the determination of the total porosity via DFT calculations is not reliable, because the influence of macropores cannot be calculated definitively (see chapter 3.2.3.1). In contrast, the TPV includes the influence of macropores more accurately as long as they can be filled with adsorbate during the physisorption experiment.[15] Hence, the overall porosity of different samples should preferably be compared by using the TPV data instead of the CPV data obtained from DFT. However, the comparison of DFT-derived data and TPV data allows further insight into the reliability of the data reduction procedures and its results:

[15] At relative pressures very close to unity condensation of adsorbate in the measurement cell may occur. Consequently, the last reliably measureable point of an isotherm lies in the range of approximately $p/p_0 = 0.99$. Applying equation (2-15), this corresponds to a pore diameter around 100 nm. Hence, larger macropores cannot be filled in a physisorption experiment.

Generally, the TPV plot obtained by the "de Boer" method lies within the same range as the CPV values derived by the two DFT models assuming cylindrical pore geometries (see figure 3-8 and figure 3-6). This finding is a simple consequence of the fact that cylindrical pore geometries are assumed in all above mentioned cases. Significant differences between the TPV plot and the CPV plot can only be found in the range of small mesopores below approximately 15 nm, where the TPV plot tends to give higher porosities than the CPV plots. This finding illustrates the limits of the "de Boer" method: At such small pore sizes, corresponding to low relative pressures in the measured isotherm, the assumption of bulk properties for the nitrogen adsorbate fails to yield reasonable results. On the other hand, the TPV plot and the CPV plots are in good accordance with each other in the range of pore sizes beyond approximately 40 nm, which is the range that normally has to be considered with caution concerning the CPV data derived from the DFT calculations. This finding can be interpreted as proof of the reliability of the DFT data: It is generally accepted that the Gurvich rule (see equation (2-11)) produces reliable values for the total pore volume in this pore size range. Hence, the TPV plots only suffer from uncertainties concerning the estimated pore sizes via the "de Boer" method (see equations (2-13)−(2-15). The error bars for the uncertainties in the pore sizes were calculated for the last three data points of the plots, where the errors are large and hence of eminent significance.[16] Nevertheless, the large error bars do not exhibit strong influence on the general trend of the TPV plot because the trend in the TPV plot is flat in this pore size range. Considering not only the sample illustrated in figure 3-8 but also the samples in figure 3-6 it becomes obvious that the TPV data are adequate to expand the interpretation of sample porosities for pore sizes up to approximately 100 nm. Especially the sample in figure 3-6 C is adequate to explain such a conclusion: This sample (see table 3-1 and table 3-2, sample 14) exhibits a very large discrepancy between its TPV of 0.768 $cm^3 \cdot g^{-1}$ (for pores up to approximately 100 nm width) and its cumulative pore volume of 0.348 $cm^3 \cdot g^{-1}$ (for pores up to approximately 32 nm width) derived from DFT calculations by using the "spherical adsorption" model. This discrepancy proves that this sample possesses significant porosity in the size range of 32-100 nm width. Even in case of this sample, the TPV plot and the CPV plots for the "cylindrical adsorption" and the "cylindrical equilibrium" DFT-model are very close to each other with similar trends. The error bars of the TPV plot roughly overlap the trends of the CPV plots. Hence, the TPV data provide proof of the general validity of the CPV data trends irrespective of slight uncertainties in this pore size range. However, the validity of such data is not achieved by the precision of the underlying calculations. It is more a consequence of self-consistency. In the considered pore size range of approximately 32−100 nm, the presence of only some pores increases the overall porosity of a sample significantly. Hence, the presence of steep slopes in the CPV or TPV plots in this pore size range is intrinsically implausible. Steep slopes in this range would lead to tremendous overall porosities which are not expected for the materials investigated in this thesis. Consequently, the slopes of the CPV and TPV plots are always relatively flat in this region and thus intrinsically similar to each other, because such plots have to continue strictly increasing.

[16] The error bars were calculated by adding and subtracting an assumed error of ± 0.005 to the measured relative pressure for each data point (see chapter 2.6.2.1), respectively. Afterwards the so obtained relative pressure range was converted to a corresponding pore size range by using equation (2-15).

However, the above mentioned deductions lead to the following fundamental basics concerning discussions of porosities in the following chapters 3.2.4−3.6:

As discussed in the last chapter, it was decided to analyze all samples within this thesis with the “spherical adsorption” model. This model only allows for the detailed analysis of pore sizes up to approximately 32 nm width. Otherwise it was explained that TPV values obtained by the Gurvich rule are adequate to characterize the porosity of samples for pore sizes up to approximately 100 nm width. Hence, the comparison of DFT-derived CPV data and the TPV values allows the estimation of sample porosities in the range of 32−100 nm. Furthermore, such comparison helps to distinguish between different sample classes. In some cases the CPV results in similar overall porosities as the TPV (“class a” samples, e. g. samples 3 and 9 in table 3-2). In other cases the TPV gives significantly higher porosities than the CPV data (class b” samples, e. g. samples 6, 11 and 14 in table 3-2). Such deviation is a consequence of the presence of larger mesopores that are filled by the nitrogen adsorbate at high relative pressures as already explained. These pores cannot be captured by DFT, but they do contribute to the TPV. Hence, CPV plots of “class a” samples typically run into "saturation” for larger mesopores. In these samples no significant amounts of large mesopores are present, so that the overall CPV converges towards a constant value beyond a critical pore size. This behavior is exemplified by the samples in figure 3-6 A and B (samples 3 and 9 in table 3-1 and table 3-2). The CPV plots of “class b” samples do not run into "saturation” for larger mesopores. In these samples larger mesopores contribute significantly to the overall CPV. This behavior is exemplified by the samples in figure 3-8 and in figure 3-6 C and D (samples 6, 11 and 14 in table 3-1 and table 3-2).

Especially for these “class b” samples investigation of the porosity by mercury porosimetry would be interesting, because this method is better suited to investigate such larger pore sizes. Unfortunately, it is quite difficult to synthesize enough electrospun fibers for this analysis method with the lab equipment that was available for the experiments. Hence, it was not possible to conduct such analyses within this thesis. However, mercury porosimetry on electrospun fibers is strongly recommended as an investigation method to characterize porous electrospun fibers more precisely in future projects: Mercury porosimetry would be able to validate nitrogen physisorption analyses beyond the doubtlessly reliable pore sizes range which ends at pore sizes of approximately 30 nm.

3.2.4 Physisorption: comparative analyses on silica fibers

After theoretical background issues were presented and discussed in the previous chapters 2.6 and 3.2.3 a detailed interpretation of the physisorption experiments on silica samples will be presented in this section. Therefore, physisorption results on electrospun fibers obtained from sol-gel precursors (sol-gel fibers) or Ludox nanoparticles (NP-fibers) will be compared with results on bulk reference samples. These comparative investigations have the objective to reach a more detailed understanding of the structure generating processes during the electrospinning synthesis of silica fibers. Whether these results can be generalized for other inorganic materials will be discussed in chapter 3.6.

3.2.4.1 Experimental results: detailed discussion of specific surface areas and porosities

Silica sol-gel fibers spun with 5 wt.-% PVP exhibit a surface area of 178 $m^2 \cdot g^{-1}$ and a TPV of 0.13 $cm^3 \cdot g^{-1}$ after calcination at 550 °C. The other sol-gel fibers spun with 8 wt.-% PVP have a slightly higher TPV of 0.14 $cm^3 \cdot g^{-1}$ and a specific surface area of 235 $m^2 \cdot g^{-1}$ (see table 3-2). The porosity of both samples arises mainly from micropores and the larger surface area of the second sample originates from the increased microporosity. This can be clearly concluded from the isotherms and the plots of the DFT-derived CPV (see figure 3-9): Both isotherms exhibit a nearly negligible hysteresis proving the presence of only a very limited amount of mesopores. This results in two CPV plots that are both nearly horizontal and parallel to each other. The absence of significant mesoporosity in the silica sol-gel fibers proves that fiber crossings in electrospun fiber mats do not behave like mesopores in physisorption experiments as suggested in chapter 2.6.2 (at least concerning the analyzed pore size range of 2–32 nm).

The only difference between the two sol-gel-derived silica fiber samples is a shift in the pore volume of approximately 0.01 $cm^3 \cdot g^{-1}$ arising from the increased microporosity of the sample spun with 8 wt.-% PVP which concomitantly results in an increased surface area. The origin of such microporosity in the silica sol-gel fibers may be a consequence of a templating effect of the spinning polymer PVP. It is known that ionic liquids like 1-Hexadecyl-3-methylimidazolium chloride (C_{16}MImCl) can act as a template for small pores in the size range of micro- and small mesopores.[26] Similarly, polymer chains may also act as a template for such small pores.[147–149] Probably the PVP chains from the spinning polymer generate micropores in between the silica sol-gel material.

In summary, the different concentrations of the PVP spinning polymer seem to have only a small impact on the properties of the calcined silica fibers. The higher PVP content in the spinning solution increases the surface area by approximately one third although the fibers spun with 5 wt.-% PVP had smaller fiber diameters (see chapter 3.2.2, figure 3-1). Obviously, the microporosity of both samples exceeds the influence of the fiber diameter leading to the unexpected result that the thinner fibers exhibit the smaller specific surface area. In addition, no other differences were found by SEM or physisorption analysis, so that the amount of the spinning polymer does not affect the porous structure and morphology of the resulting sol-gel-derived silica fibers.

Table 3-2: Physisorption results on electrospun silica nanofibers: BET[1)], CPV[2)], TPV[3)] and relative porosity[4)] values.

sample no.	sample category	weight ratio SiO_2/polymer	SiO_2 source	BET[1)] [$m^2 \cdot g^{-1}$]	CPV[2)] [$cm^3 \cdot g^{-1}$]	TPV[3)] [$cm^3 \cdot g^{-1}$]	relative porosity[4)] [%]
1	sol-gel fibers	1.18	sol-gel SiO_2 from TMOS	178.3	0.113	0.132	22.5
2	sol-gel fibers	0.74	sol-gel SiO_2 from TMOS	234.6	0.133	0.144	24.1
3	pure particles	---	Ludox “AS” NPs	215.3	0.244	0.255	36.0
4	pure particles	---	Ludox “HS” NPs	156.3	0.206	0.216	32.2
5	pure particles	---	Ludox “SM” NPs	132.3	0.265	0.276	37.8
6	NP-fibers	0.23	Ludox “AS” NPs	213.9	0.574	0.800	63.8
7	NP-fibers	0.23	Ludox “HS” NPs	187.5	0.520	0.788	63.4
8	NP-fibers	0.23	Ludox “SM” NPs	237.6	0.727	0.887	66.1
9	dried spinning solution	0.23	Ludox “AS” NPs	201.4	0.514	0.543	54.4
10	dried spinning solution	0.23	Ludox “HS” NPs	184.0	0.577	0.780	63.2
11	dried spinning solution	0.23	Ludox “SM” NPs	254.4	0.905	1.17	71.9
12	NP-fibers	0.50	Ludox “AS” NPs	201.0	0.512	0.596	56.7
13	NP-fibers	0.75	Ludox “AS” NPs	203.0	0.494	0.640	58.5
14	NP-fibers	1.00	Ludox “AS” NPs	206.9	0.348	0.768	62.8
15	NP-fibers	1.25	Ludox “AS” NPs	192.8	0.470	0.588	56.4
16	NP-fibers	1.25	Ludox “AS” NPs	209.5	0.496	0.629	58.1
17	NP-fibers	1.50	Ludox “AS” NPs	207.5	0.468	0.542	54.4

[1)]: specific surface area calculated by the BET method;
[2)]: cumulative pore volume calculated by the DFT method; this is the pore volume of the last data point in the CPV plot;
[3)]: total pore volume calculated by using the Gurvich rule (see equation (2-11));
[4)]: calculated from the TPV values (for explanation of the data reduction see chapter 2.6.3.1).

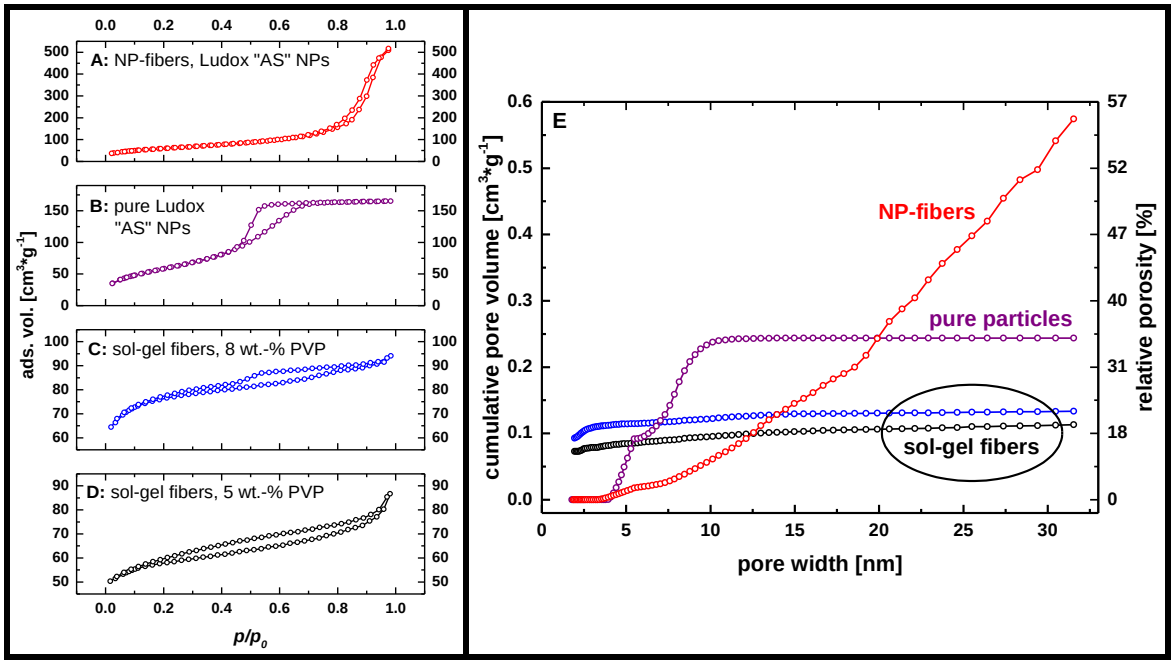

Figure 3-9: N_2-Physisorption isotherms (A-D) and CPV plots from DFT (E) of silica sol-gel fibers, pure Ludox "AS" particles and silica fibers obtained from Ludox "AS" particles. Magnifications of the isotherms can be found in the appendices (see figure 6-9–figure 6-11 and figure 6-14). Color coding: black: sol-gel fibers spun with 5 wt.-% PVP (see table 3-2, sample 1); blue: sol-gel fibers spun with 8 wt.-% PVP (see table 3-2, sample 2); purple: pure, calcined Ludox "AS" particles (see table 3-2, sample 3); red: electrospun fibers from Ludox "AS" particles (see table 3-2, sample 6).

The isotherms of two further, representative samples are depicted in figure 3-9 for comparison: First, electrospun fibers prepared from commercially available Ludox "AS" nanoparticles exhibiting a surface area of 214 $m^2 \cdot g^{-1}$ and a TPV of 0.80 $cm^3 \cdot g^{-1}$ are shown. These fibers were electrospun with the help of PEO being removed by calcination at 550 °C after the spinning process. The spinning solution contained 0.45 wt.-% of SiO_2 and 2 wt.-% of PEO in aqueous solution. Furthermore, the pure Ludox "AS" NP dispersion was dried and also calcined at 550 °C resulting in a bulk material with nearly the identical specific surface area of 215 $m^2 \cdot g^{-1}$ and a TPV of 0.26 $cm^3 \cdot g^{-1}$. These two samples illustrate that the NP-derived fibers possess a significantly improved mesoporosity compared to the sol-gel fibers. Also the bulk sample features a higher mesoporosity than the sol-gel fibers and the pore structures of all three kinds of samples are completely different. These findings will be investigated and discussed in more detail below.

One point that was ignored in the last passage is that the sol-gel fibers are not really directly comparable to the NP-fibers. There are two important differences between the samples that may influence the porous characteristics of the fibers: First, the spinning polymer is PVP in one case and PEO in the other case. As polymers may act as porogen in syntheses of inorganic materials, PEO might act so while PVP does not.[114,150,151] Unfortunately, the sol-gel precursors are not compatible with PEO, because PEO and SiO_2 precursors are not soluble in the same solvents. Otherwise, the Ludox dispersions are aqueous and not compatible with the water-insoluble PVP. Consequently, it was not possible to produce sol-gel fibers and NP-fibers with the help of the same spinning polymer in the case of silica fibers because this "solubility dilemma" could not be circumvented. Hence, the influence of the different chemical nature of the spinning

polymers could not be investigated in this way. Fortunately, it was possible to prepare electrospun tin oxide fibers from both (i. e. sol-gel precursors and nanoparticles) by using the same spinning polymer poly(methyl methacrylate) (PMMA) so that the comparability of sol-gel fibers and NP-fibers will be investigated and discussed exemplarily on tin oxide in detail (see chapter 3.5.4).

The second difference between the silica sol-gel fibers and NP-fibers is the composition of the spinning solution: The weight ratio of SiO_2 to spinning polymer is approximately 1/1 in the two sol-gel solutions and only 1/4 in the afore-mentioned nanoparticle containing spinning solution. In other words, in the case of the NP-fibers 80 wt.-% of the fibers are removed when the polymer is combusted during calcination. Possibly, this large loss of polymer mass may generate mesoporosity within the silica NP-fibers while the lower mass lost during calcination of the sol-gel fibers does not allow for the formation of significant mesoporosity.

An experimental series with a varying amount of Ludox "AS" particles but a constant amount of PEO in the spinning solution was conducted (see table 3-2, samples 12−17) in order to elucidate the influence of the weight (or volume) ratio of SiO_2 to polymer on the mesoporosity of the electrospun fibers after calcination. The corresponding isotherms and CPV plots in figure 3-10 show very similar sorption behavior for all these samples. The physisorption isotherms of all samples showed a type-IV-like trend typical for a mesoporous material.[16] The CPV plots revealed a very broad pore size distribution giving evidence that all analyzable pore sizes (up to approximately 30 nm diameter) contribute equally to the TPV attendant on a linear trend of this plot. The specific surface areas of all six samples lie within the range of 192−210 $m^2 \cdot g^{-1}$, which is within the experimental error of approximately ± 10%. Additionally, the porosities also lie within a narrow range of 0.54−0.77 $cm^3 \cdot g^{-1}$ for the TPV. The main conclusion to be drawn from these data is that the structure of all these silica NP-fibers is not influenced by the weight ratio of nanoparticles to polymer in the spinning solution, at least within the investigated range (weight ratio of SiO_2/PEO in the range of 0.5/1−1.5/1). It seems that the small differences between the samples are only a consequence of experimental errors in both the electrospinning experiments and the physisorption analyses. This assumption can be justified with the result on the two samples 15 and 16 (see table 3-2): Both samples were obtained from two spinning solutions with identical composition and a weight ratio of SiO_2/PEO of 1.25/1. However, the specific surface areas are 192 $m^2 \cdot g^{-1}$ and 210 $m^2 \cdot g^{-1}$, respectively: These two samples have the highest and the lowest surface area within the above mentioned series, although the spinning solutions were identical within the experimental error. Hence, the differences also have to be attributed to experimental errors.

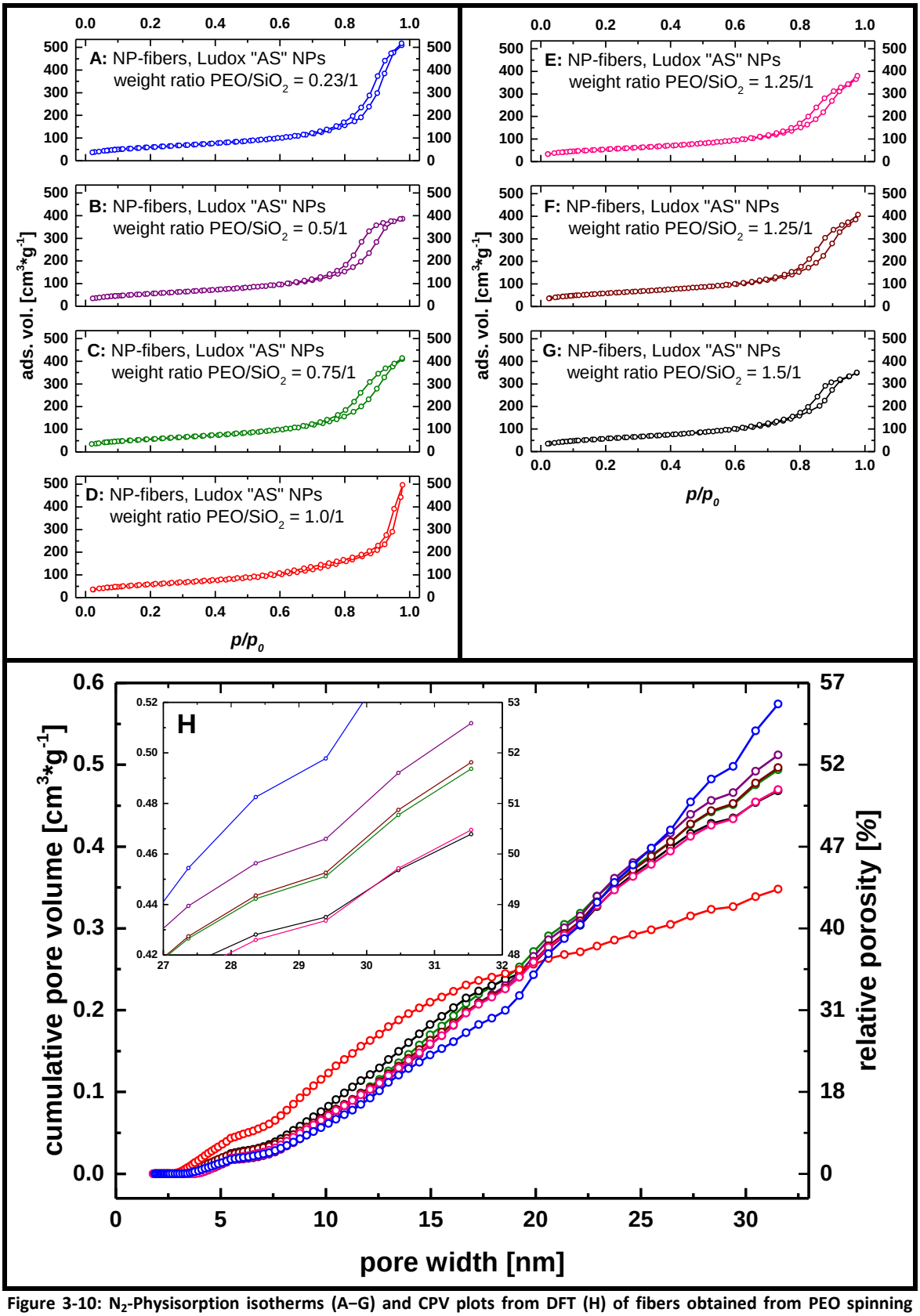

Figure 3-10: N_2-Physisorption isotherms (A–G) and CPV plots from DFT (H) of fibers obtained from PEO spinning solutions with different amounts of Ludox "AS" particles. Inset in H: magnification of the CPV plot for large pore sizes. Magnifications of the isotherms can be found in the appendices (see figure 6-20–figure 6-25 and figure 6-14). Color coding for the weight ratio of SiO_2/PEO in the spinning solution (see table 3-2): blue: 0.23/1 (sample 6); purple: 0.5/1 (sample 13); green: 0.75/1 (sample 12); red: 1.0/1 (sample 14); pink: 1.25/1 (sample 15); brown: 1.25/1 (sample 16); black: 1.5/1 (sample 17).

The following points can be regarded as the main experimental errors:

- When the spinning solutions were mixed from PEO, Ludox particles and water as solvent, the accuracy of the balance results in a small error concerning the composition of the spinning solutions. With a typical minimum batch size for a spinning solution of one gram and an accuracy of five milligram for each component, this error is below 0.5 wt.-% for each component.
- When the physisorption experiments were conducted, the mass of each sample was at least 15 mg and this was estimated with an accuracy of 0.1 mg resulting in an error below 0.7 wt.-%.
- Although it was tried to conduct all electrospinning experiments under identical conditions, some small differences could not be excluded absolutely. Especially small deviations in the room temperature (in the range of ± 1 °C) and humidity (in the range of ± 5% relative humidity) have to be considered, which also could not be excluded by using our electrospinning setup with climate control. These influences cannot be put into numbers, because their influence is not clear. Nevertheless, the uncertainties in temperature and humidity during the electrospinning experiments are probably the most prominent experimental errors, because the relative deviations in these parameters are higher than the above mentioned weighing inaccuracies.

All these experimental errors lead to slight deviations in the results. The samples 15 and 16 justify that the specific surface areas of all six samples within this experimental series can be averaged to 204 $m^2 \cdot g^{-1}$ with a standard deviation of 6.8 $m^2 \cdot g^{-1}$, because all other samples of this series are within the experimental error that is proven by these two samples. Similarly, also the TPV can be averaged to $5.97 \cdot 10^{-1} \pm 5.5 \cdot 10^{-2}$ $cm^3 \cdot g^{-1}$, although the highest and lowest TPV were measured for the samples 14 (weight ratio SiO_2/PEO = 1.0/1) and 17 (weight ratio SiO_2/PEO = 1.5/1), respectively. Here the averaging is justified because there is no clear trend within the data: The TPV values seem not to correlate with the weight ratio of SiO_2/PEO. They rather seem to alternate statistically around a mean value.

Although sample 6 was electrospun with a slightly lower amount of 2 wt.-% PEO (see table 3-1) it is worth comparing the physisorption results with the six samples electrospun with 2.3 wt.-% PEO. While the TPV of sample 6 with a value of 0.80 $cm^3 \cdot g^{-1}$ is somewhat higher than for the other six samples, the specific surface area of 214 $m^2 \cdot g^{-1}$ is nearly identical to the other six samples though the weight ratio of SiO_2/PEO is as low as 0.225/1 in this sample. Nevertheless, the specific surface area also stays constant at this ratio and the TPV increases only to a small extent.

The CPV plots in figure 3-10 H are very similar to each other, so that they can hardly be distinguished. Only the plot of sample 14 (weight ratio SiO_2/PEO = 1.0/1) shows a noticeably different trend that is not completely linear. The origin of this slightly different pore size distribution is unclear. Hence, the data of this sample have to be considered with caution. Possibly, this sample provides proof of the extent of experimental errors, but otherwise this sample also might show a slightly different sorption behavior due to other problems which were not recognized during the synthesis.

If the mesoporosity of the NP-based electrospun fibers is not dependent on the weight (or volume) ratio of SiO_2 to polymer their mesoporous structure has to be explained by other reasons.

In this context the influence of particle properties has to be investigated: Different Ludox dispersions (namely Ludox "AS", "HS" or "SM" dispersions, see table 3-2) were used for the syntheses of electrospun fibers. All three Ludox dispersions were electrospun in the same concentration with the help of PEO as spinning polymer to result in NP-fibers after calcination at 550 °C. For comparison all three kinds of pure Ludox particle dispersions were also dried and calcined at 550 °C. The measured nitrogen physisorption data of all these samples are illustrated comparatively in figure 3-11.

The physisorption isotherms of all samples showed a type-IV-like behavior typical for mesoporous materials,[16] but with some differences in their trends. The bulk samples consisting of pure, calcined particles had different specific surface areas in the range of 130 – 220 $m^2 \cdot g^{-1}$. Concerning the overall porosity these samples were all similar with a total pore volume (TPV) in the range of 0.22 – 0.28 $cm^3 \cdot g^{-1}$. The electrospun fibers exhibit specific surface areas in the range of 180 – 240 $m^2 \cdot g^{-1}$ and TPVs in the range of 0.79–0.89 $cm^3 \cdot g^{-1}$ (see table 3-2).

Although the physisorption data differ slightly with the different particles used, it can be stated that neither the surface area nor the TPV is dominated by intrinsic properties of the Ludox particles. This conclusion is valid for the electrospun fibers as well as for the bulk samples obtained from the pure particle dispersions. This becomes clear when the results from the fibers and the pure particles are compared: There is no obvious trend in the specific surface area values such that one kind of particles produces the samples with the lowest surface areas and another kind of particles produces the samples with the highest specific surface areas. The differences rather seem to be statistically within a narrow range that is a bit more distinctive for the bulk samples consisting of pure, calcined particles.

The common features of the samples are most obvious in the CPV plots that reveal similar characteristics for all fiber samples as well as similar characteristics for all bulk samples. On the other side, there is a significant disparity between these two sample groups (see figure 3-11 G): The CPV plots revealed a very broad pore size distribution for all analyzable pore sizes (up to approximately 30 nm diameter) for all fiber samples, while the particle samples possess mainly small mesopores. None of the pure particle samples exhibits mentionable amounts of pores larger than approximately 13 nm in diameter. Interestingly, these bulk samples generally possess a higher cumulative pore volume in the pore size range below approximately 15 nm than the electrospun fibers prepared from these particles. This finding will be discussed in detail in chapter 3.2.4.2.

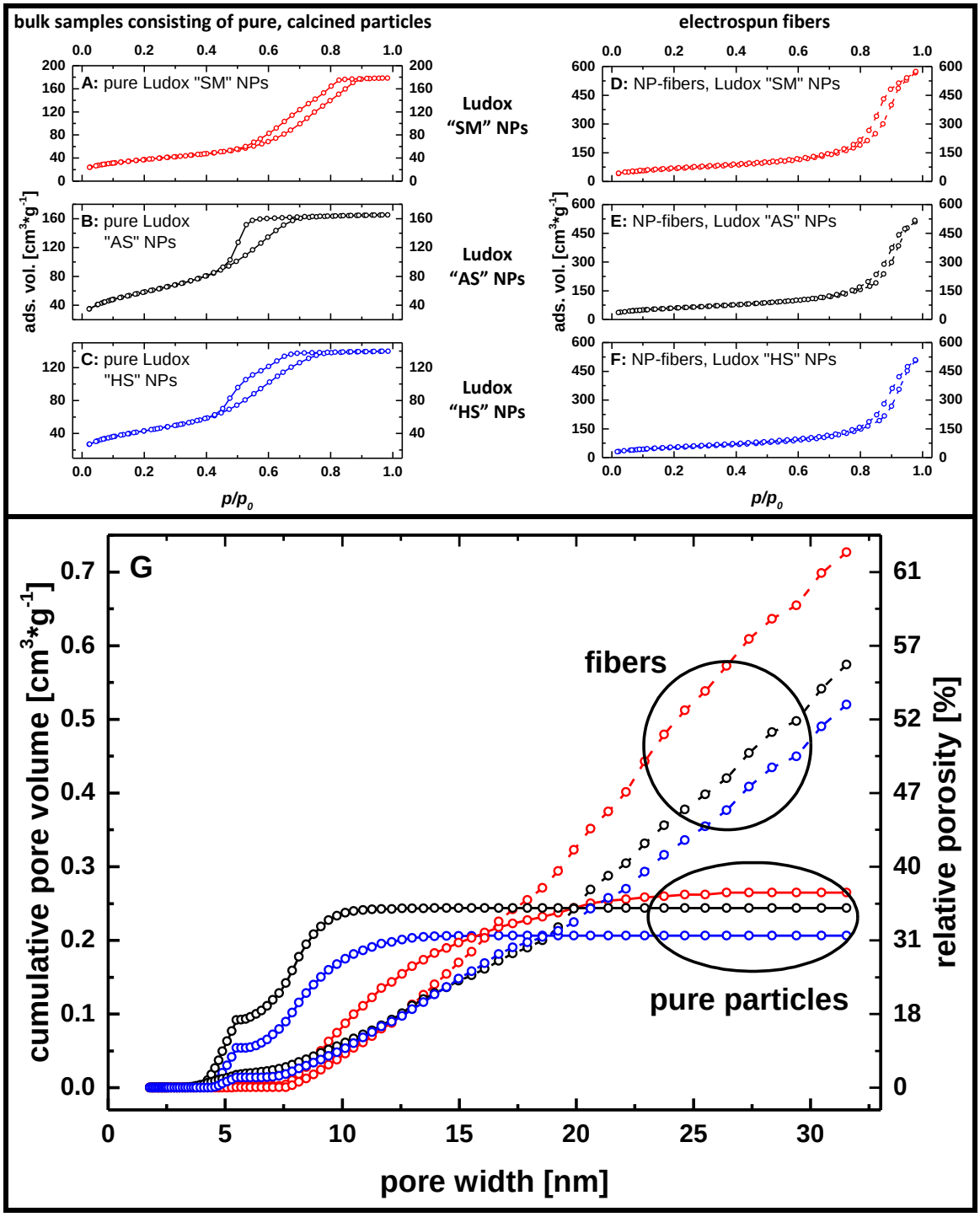

Figure 3-11: N_2-Physisorption isotherms (A–F) and CPV plots from DFT (G) of pure, calcined Ludox particles (solid lines) and electrospun fibers obtained from these Ludox particles (dashed lines). Magnifications of the isotherms can be found in the appendices (see figure 6-11–figure 6-16). Color coding: black: samples from Ludox "AS" particles (see table 3-2, samples 3 and 6); blue: samples from Ludox "HS" particles (see table 3-2, samples 4 and 7); red: samples from Ludox "SM" particles (see table 3-2, samples 5 and 8).

The physisorption data seem to prove that the electrospun fibers do not exhibit significantly enlarged specific surface areas compared to the bulk samples, while the TPV of the fibers is increased by a factor of three or four at the same time. At first glance, it seems implausible that this huge increase of the TPV does not go along with a noticeable increase in the specific surface area. It was already discussed in chapter 2.6.1 that the specific surface area of a sample decreases, if the pore size in the sample increases, as long as the TPV is kept constant. Furthermore, the TPV is intrinsically dominated by the volume of larger pores while the specific surface areas are governed by the presence of smaller pores. Consequently, the presence of larger mesopores in electrospun fibers predominantly affects the TPV but not the specific surface areas. This general statement can easily be understood by the cumulative surface area plots which can be derived via DFT calculations similarly as the CPV plots (see figure 3-12): The trends in the plots are comparable to the corresponding trends of the CPV plots (see figure 3-11 G) because the plots are generated from the same underlying pore size distribution calculated via the "spherical adsorption" model. The only qualitative difference between figure 3-11 G and figure 3-12 is the much steeper slope of the cumulative surface area plots for the bulk samples consisting of pure, dried and calcined particles in the range of small pore sizes up to approximately 10 nm. As a consequence, the total cumulative surface areas of these samples reach the same order of magnitude as those of the fiber samples, if all pore sizes up to a size of 32 nm are considered though they exhibit strongly different porosities.

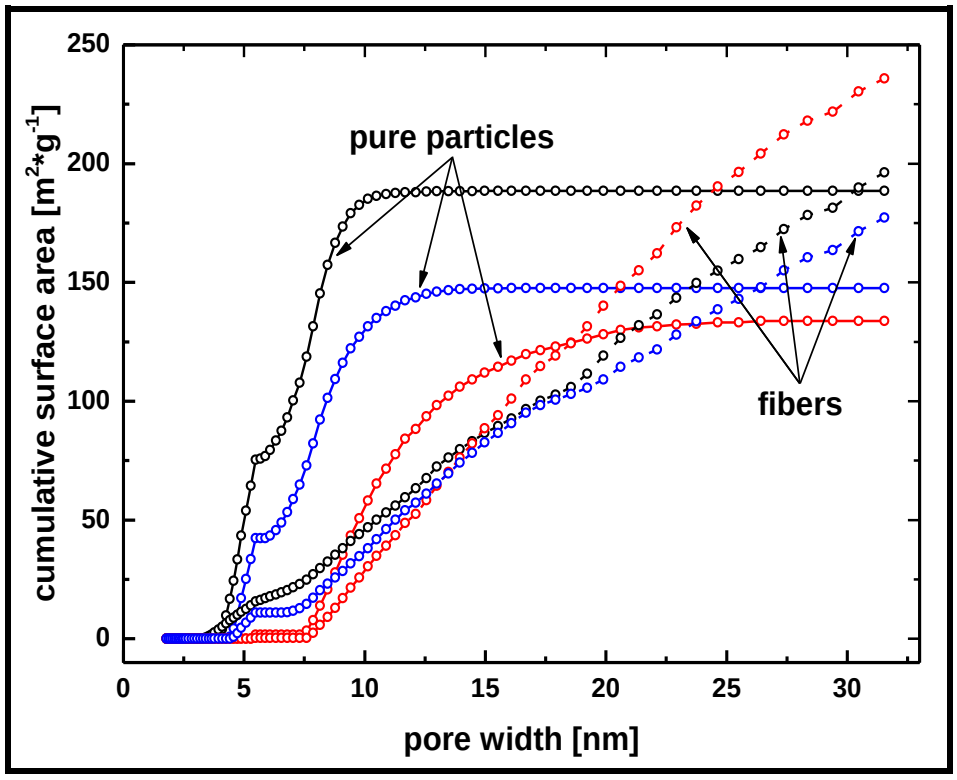

Figure 3-12: Cumulative surface area plots derived by DFT calculations using the "spherical adsorption" model for the samples illustrated in figure 3-11. Samples: pure, calcined Ludox particles (solid lines) and electrospun fibers obtained from these Ludox particles (dashed lines). Color coding: black: samples from Ludox "AS" particles (see table 3-2, samples 3 and 6); blue: samples from Ludox "HS" particles (see table 3-2, samples 4 and 7); red: samples from Ludox "SM" particles (see table 3-2, samples 5 and 8).

It remains to be investigated why the electrospun fibers exhibit significantly improved TPVs compared to the bulk samples consisting of the pure, calcined particles. Possibly, the increased TPVs of the fiber samples arise from some kind of templating effect of the spinning polymer PEO or another effect of the electrospinning process. In order to investigate this question, the spinning solutions were dried and calcined in identical composition to the solutions used for the preparation of the fibers but without spinning them. The physisorption characteristics of these bulk materials were compared to the corresponding data of the electrospun fibers and of the pure, calcined particles, respectively (see figure 3-13).

The bulk samples prepared from unspun spinning solutions had different specific surface areas in the range of 180 – 255 $m^2 \cdot g^{-1}$. The TPVs of these samples were in the range of 0.54 - 1.17 $cm^3 \cdot g^{-1}$ (see table 3-2). Compared to the electrospun fibers and the pure particles, the following findings can be put on record:

- The specific surface areas of the bulk samples are in the same range as those of the fiber samples and therefore only slightly higher than those of the pure particles.
- The isotherms of the bulk samples exhibit mesoporous characteristics with a trend that accords more to the fiber samples rather than to the pure particle samples.
- Consequently, the TPVs of the unspun samples are also comparable to the fiber samples and are significantly increased versus the TPVs of the pure particles.
- The TPVs of the unspun samples differ much more from each other than the corresponding TPVs of the fiber samples among each other.

From these findings it can be concluded that the electrospinning process itself is not the decisive incident generating the mesoporosity of the fibers. Obviously, similar mesoporosity can also be achieved, if the spinning solutions are only dried and calcined without electrospinning them. At first glance, the spinning polymer PEO seems to play a crucial role in the process ending up with the formation of significant mesoporosity in the resulting silica materials after calcination. The interactions of the particles with the polymer seem to add an increased mesoporosity to all these samples, so that especially mesopores with diameters larger than approximately 10−15 nm are generated. This finding may be understood as a “templating effect” of the polymer discussed in more detail in chapter 3.2.4.2.

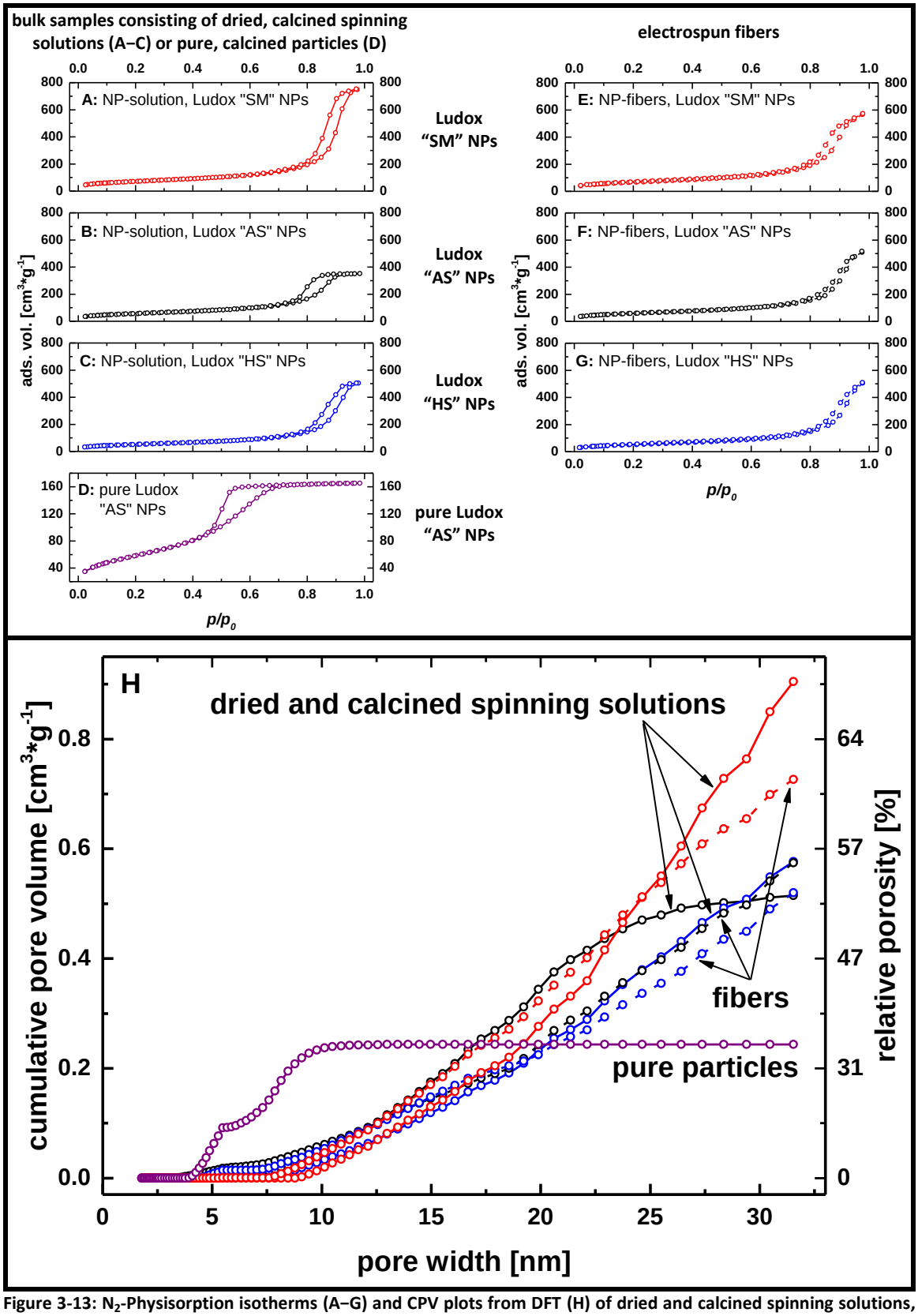

Figure 3-13: N_2-Physisorption isotherms (A–G) and CPV plots from DFT (H) of dried and calcined spinning solutions, pure Ludox particles (solid lines), and electrospun fibers obtained from these solutions (dashed lines). Magnifications of the isotherms can be found in the appendices (see figure 6-14–figure 6-19 and figure 6-11). Color coding: black: from Ludox "AS" particles (see table 3-2, samples 6 and 9); blue: from Ludox "HS" particles (see table 3-2, samples 7 and 10); red: from Ludox "SM" particles (see table 3-2, samples 8 and 11); purple: pure, dried and calcined Ludox "AS" particles (see table 3-2, sample 3).

3.2.4.2 Interpretation of trends in the results regarding principles of structure formation

The physisorption experiments presented in chapter 3.2.4.1 gave insight into the origins of mesoporosity in the different silica materials. In this chapter general trends in the results will be compared and interpreted in order to develop a fundamental mechanistic understanding concerning the formation of porous structures in such materials.

Starting with the physisorption results on bulk samples consisting of pure, dried and calcined Ludox particles, only low TPVs for all different kinds of particles (i. e . Ludox “AS”, “HS”, “SM” particles) were found. These TPVs are generated by pores not larger than approximately 10 nm and beyond this pore size no appreciable mesoporosity could be found (see figure 3-11). Furthermore, no microporosity was found in these samples proving the structure of the Ludox particles to be dense and non-porous (at least after calcination). The small mesoporous with diameters in the size range of approximately 4-10 nm in theses samples have to be generated by inter-particle void spaces which are intrinsically present if such particles are packed accidentally in a bulk material (see figure 3-14 B). These pores are too big to be intra-particle pores since the (Ludox) particles themselves exhibit a diameter of approximately 10 nm.[143]

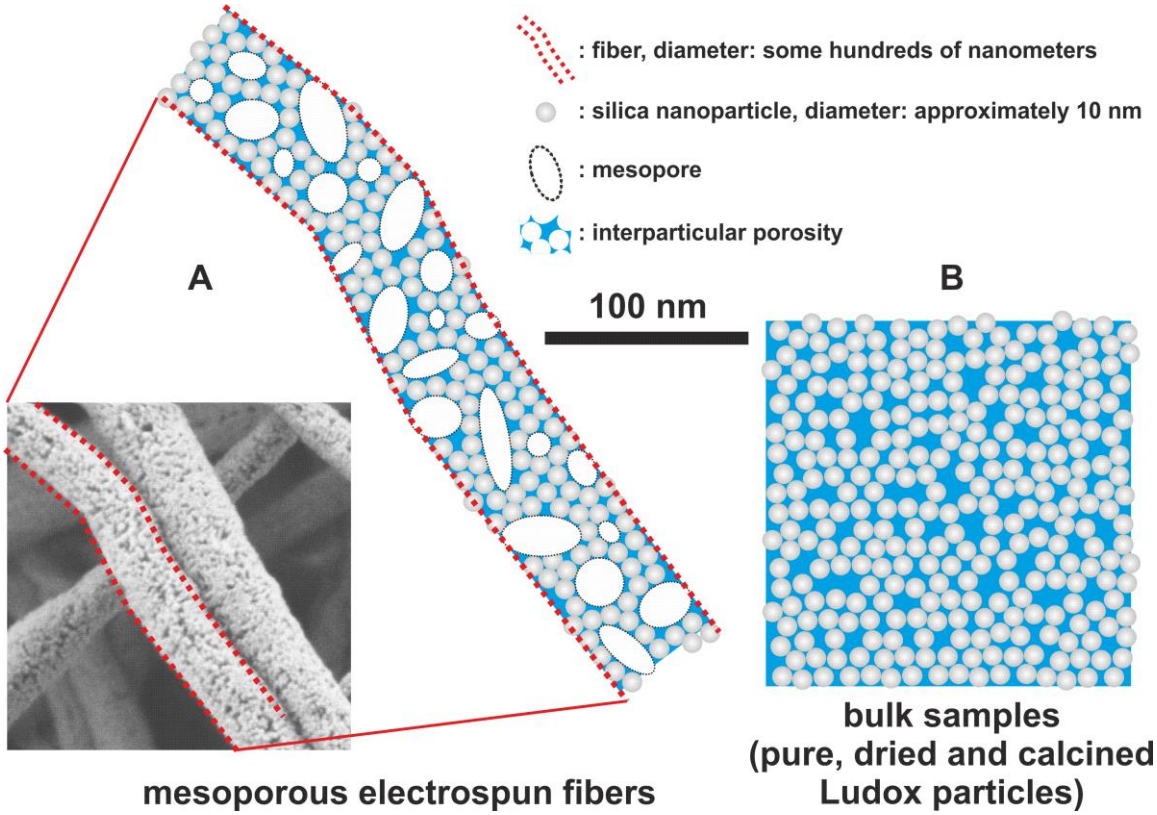

Figure 3-14: Schematic illustration of nanoparticle-packing in mesoporous electrospun fibers (A) and bulk materials prepared from pure, dried and calcined Ludox particle dispersions (B). The SEM picture in (A) is taken from figure 3-3 H illustrating the NP-fibers synthesized with 3.3 wt.-% Ludox “AS” NPs in the spinning solution (see table 3-1, sample 17).

However, if the Ludox particles are dense, non-porous materials, it is possible to calculate their theoretical specific surface area: With the density of non-porous silica (ρ_{SiO2} = 2.2 g·cm^{-3})[152] and a mean radius of 5 nm for the Ludox particles, which are assumed to be spherical, a theoretical specific surface area of 273 m^2·g^{-1} can be calculated according to equation (3-1):

$$S_m = \frac{O_r}{m} = \frac{O_r}{\rho \cdot V_r} = \frac{4 \cdot \pi \cdot r^2}{\rho \cdot \frac{4}{3} \cdot \pi \cdot r^3} = \frac{3}{\rho \cdot r} \qquad (3\text{-}1)$$

with:

S_m = specific surface area in [m^2·g^{-1}];
O_r = surface area of one particle;
m = mass of one particle;
V_r = volume of one particle;
ρ = density of the material = 2.2 g·cm^{-3} for non-porous silica.[152]

Nearly all measured specific surface areas of NP-based samples (see table 3-2, samples 3-17) are roughly in the range of 200 m²·g^{-1} which is one fourth less than the calculated theoretical value of 273 m²·g^{-1}. This discrepancy of measured and calculated specific surface area can be explained by two reasons: Either the mean diameter of the Ludox particles is slightly larger than 10 nm or the particles sinter to some extend so that the measured surface areas are smaller than the theoretically expected one. However, the interesting finding is that almost all Ludox particle based materials exhibit the same specific surface area of approximately 200 m^2·g^{-1} (see table 3-2) irrespective of the kind of Ludox particles or the preparation path, while the mesoporosities of the samples are substantially different (see figure 3-11, figure 3-13 and discussion below). Obviously, the pore structure of the prepared silica materials and hence the packing density of the Ludox particles does not influence the accessibility of the surface for the nitrogen adsorbate. Furthermore, the similarly diminished surface area compared to the theoretical one have to be a consequence of a similarly distinctive coalescence of the particles, though the corresponding pore structures are varying: The inevitable contact area and sintering of individual particles leading to the formation of a mechanically stable structure is roughly the same for almost any sample consisting of Ludox particles. Since the discrepancy between measured and calculated specific surface areas is not too large, it is reasonable that the particle structure is basically preserved throughout the calcination so that the resulting materials can be regarded as a packed structure of individual particles which do not coalesce completely. Only two bulk samples prepared from dried and calcined pure particle dispersions (see table 3-2; samples 4 and 5) exhibit noticeable lower specific surface areas which may be explained by the formation of closed, inaccessible pores and/or coalescence in these samples. In contrast, one dried and calcined spinning solution (see table 3-2; sample 11) has a significantly higher specific surface area which comes close to the theoretical expected one. This sample exhibits the by far highest mesoporosity of all samples at the same time and is an exception from the above discussed general trend which currently cannot be explained.

Concerning porosity the experiments revealed that the electrospun as well as the bulk samples obtained from the spinning solutions exhibit basically the same mesoporous structure, while the pure, dried and calcined dispersions resulted in less mesoporous silica materials. Such fundamental trend can hardly be understood in terms of SD: It was argued in chapter 2.5.4 that the two dimensions of space and time are strongly confined in electrospinning experiments which was expected to result in other pore structures compared to the bulk samples for which such confinement is not present. However, only a stronger statistical scattering of the TPVs and their accumulation with pore size was found as difference of the unspun samples compared to the spun samples without exhibiting a generally different trend in the physisorption data (see figure 3-13). There are only two arguments in the concept of SD which may explain this experimental result: Either different pore structures of the phase separated composite polymer/silica materials vanish during calcination and/or the differences are in the macropore size range, i. e. in a size range which cannot be investigated by nitrogen physisorption. The chance that the SD process is the same for the bulk and the fiber materials is implausible respecting the discussions of chapter 2.5.4. However, for the formation of a macroporous structure both preparation paths seem to proceed too fast. The example of the Nakanishi process proves that macroporous structures often require process times of several hours (see chapter 2.3.1.1) but not even the preparation of the bulk samples by drying and calcination did take so long. Concerning the calcination step the led argumentation also leaves an open question: It stays unclear why highly mesoporous materials are obtained at all in case of vanishing of differences in the pore structure during calcination. Such rearrangement of the structure would be a thermodynamically controlled process promoting the material towards its thermodynamic equilibrium structure which never is a highly mesoporous structure due to the large surface energy of mesoporous matter. Consequently, the argumentation in terms of SD stays vague and is not completely convincing concerning the above mentioned experimental results.

Considering the EICA concept the result can be interpreted differently: During the evaporation of solvent from the spinning solutions the Ludox particles agglomerate to clusters which ultimately may form a system spanning network in the polymer matrix. While this takes place within split seconds during the electrospinning experiment, this process step is slower for the bulk samples. Nevertheless, the resulting particle aggregates are clusters with a fractal structure in both cases. The slower process for the bulk samples only provides a longer time interval for rearrangement of the clusters possibly enabling the formation of clusters with larger fractal dimension d_f (see chapter 2.3.2). The subsequent calcination step removes the polymer matrix and simultaneously has to consolidate the agglomerated clusters so that a stable, self-supporting inorganic silica structure is formed when the polymer is combusted.

The final pore structure of such material decisively depends on the cluster aggregation and the fractal structure of the evolving clusters: Clusters of (Ludox) particles basically can be generated with varying fractal dimensions d_f (see figure 3-15; legend). Clusters with small d_f cannot be packed as compact as clusters with large d_f (compare figure 3-15 left and middle). As a consequence clusters with small d_f form a more open pore structure with larger pore sizes while clusters with larger d_f form a closer packed structure with smaller pores. With this picture in mind the evolution of the experimentally observed pore structures in the electrospun as well as the unspun samples can easily be understood:

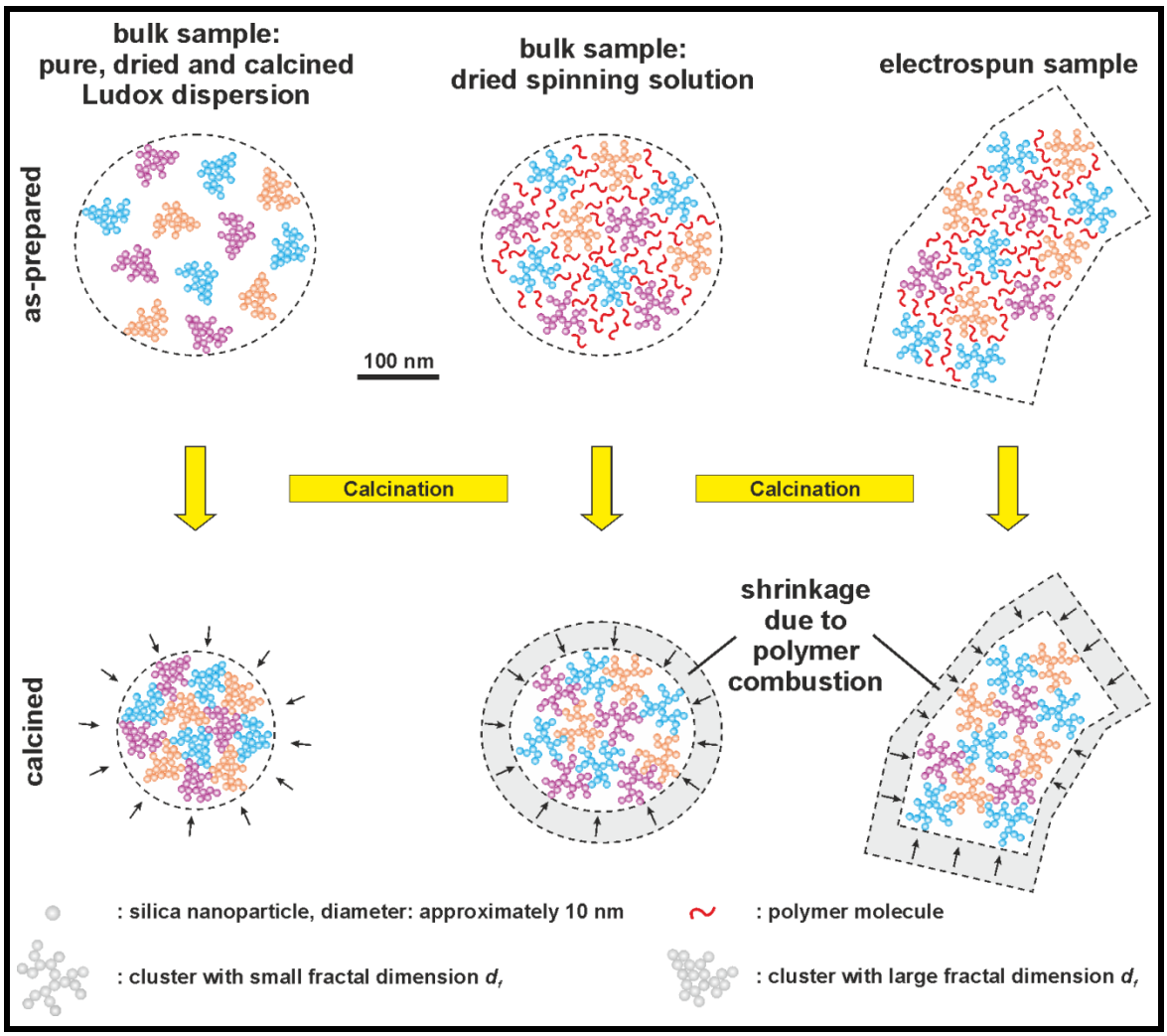

Figure 3-15: Schematic illustration of different pathways producing mesoporous silica materials using dispersed Ludox particles. Left: Preparation of silica materials by drying and calcination of pure (Ludox) particle dispersions leads to materials of relatively low mesoporosity after calcination. Middle: Drying and calcination of unspun electrospinning solutions leads to mesoporous materials with a pore structure similarly as in electrospun fibers (after combustion of the polymer). Right: Calcined electrospun oxide fibers prepared from preformed (Ludox) nanoparticles exhibit high mesoporosity because the particles first agglomerate to clusters with an open fractal structure (i. e. during electrospinning) which cannot be pack to a dense structure afterwards (i. e. during calcination). Note: Individual clusters consisting of nanoparticles are colored differently for the sake of clarity in the illustration.

If the mesoporosity of the electrospun fibers and the unspun solutions is basically the same, the clusters of Ludox particles have to be of similar fractal dimension d_f in both cases so that they result in comparably packed structures after the combustion of the polymer. Otherwise, a less mesoporous structure with smaller pore sizes is expected in the event that clusters with larger d_f are formed (see figure 3-15 left). Exactly such pore structure was observed for the samples produced from the pure, dried and calcined Ludox dispersions (see figure 3-11).

It remains to be discussed, why the different synthetic approaches generate clusters with small fractal dimension in one case and with larger fractal dimension in another case. For the electrospun fibers the time interval of solvent evaporation and particle aggregation to clusters is so short that it is reasonable to assume an instantaneous, random packing of particles which do not rearrange before the polymer/particle composite solidifies. On the basis of the physisorption data it is a matter of fact, that the particles of the dried and calcined spinning solutions also do not significantly rearrange to clusters with larger d_f though there is more time for such process. In contrast, the drying and calcination of the pure Ludox dispersions without polymer ends up with an arrangement of higher packing density though the timespan of the structure generation is the same as for the other bulk samples. Obviously, the presence or absence of the polymer is the decisive difference influencing the cluster aggregation. On the one hand the polymer increases the viscosity of the system and hence decreases the diffusion of the incorporated particles impeding a diffusion controlled rearrangement. On the other hand the polymer may be also crucial in the calcination step: During the heating interval of the calcination program the combustion of the polymer PEO does not take place until a temperature as high as approximately 340 °C is reached.[1] Meanwhile, sol-gel reactions on the particle surfaces - like the condensation of silanol-groups between adjacent particles - can take place at lower temperatures. Consequently, the polymer may act as a “void filling structure support” rather than as a typical template by supporting the loosely joined particles during the consolidation of their packing structure. The void filling polymer prevents a rearrangement of particles towards a less mesoporous packing at the beginning of the calcination procedure. In the absence of the polymer support a rearrangement of particles can take place as long as the crosslinking of the particles is not strong enough to constitute a self-supporting structure. Hence, the pore structure of the bulk samples prepared by drying and calcination of the pure Ludox dispersions is less mesoporous exhibiting a larger amount of smaller mesopores: In the absence of a polymer, the particles can directly aggregate to clusters with a larger d_f during drying of the dispersion, and/or initially formed clusters with small d_f rearrange at the beginning of the calcination procedure.

Remembering that the drying of the solutions with or without polymer was performed with the same temperature profile and hence on the same timescale, it can be expected that the dried structures exhibit clusters with similar d_f as long the polymer does not significantly interact with the Ludox particles. Interactions between ionically stabilized Ludox particles and PEO are rather attractive polar interactions than repulsive ones. The hydrophilic/hydrophobic contrast can be assumed to be low, so that possible interactions rather support the formation of an open fractal cluster structure than forcing them to segregate from the polymer matrix forming clusters with large d_f. Thus, potential polymer-Ludox particle interactions are not in contradiction to the before discussed process but may even support the formation of clusters with open fractal structure.

Examining figure 3-13 H in more detail it is found that the mesoporosity of the electrospun fibers and the dried and calcined spinning solutions is basically related though there are slight differences in the CPV plots. While the electrospun fibers obtained from different Ludox particles possess very similar TPVs (see table 3-2) and CPV plots with very similar, linear trends, the corresponding data of the bulk samples differ stronger from each other. These differences among the bulk samples are not necessarily a consequence of other interactions between the different Ludox particles in the bulk samples, though the slower solvent evaporation may facilitate that slightly different interactions are of stronger influence than in the electrospun samples. Alternatively, these differences may be understood as a stronger “statistical spread” of the TPVs and their accumulation with pore size in case of the bulk samples. While the electrospinning process is strongly confined in the both dimensions of space and time (see chapter 2.5), the less confined drying of the bulk samples may allow for an increased “statistical spread” of the resulting mesoporous structures and the physisorption results because local inhomogeneities may occur during the less confined drying process.

A further result of the physisorption experiments is that the volume (or mass) ratio of the Ludox particles to the spinning polymer does not influence the mesoporosity of the electrospun fibers (see figure 3-10) though the variation of the Ludox content in the spinning solution influences the outer, optical shape of the fibers (see chapter 3.2.2, figure 3-3). If the polymer would act as a “classical” template a simple assumption is that the polymer volume before calcination is identical to the pore volume after calcination[17] enabling to calculate a theoretical relative porosity from the polymer volume fraction in the polymer silica composite. Thus, a theoretical total pore volume was calculated from the weight ratio of SiO_2 to PEO in the spinning solutions. By using the densities ρ of SiO_2 (ρ_{SiO2} = 2.2 g·cm^{-3})[152] and PEO (ρ_{PEO} = 1.2 g·cm^{-3})[107] the weight ratios can be transformed to the corresponding volume ratios so that the calculated theoretical porosities can be opposed to the measured relative porosities obtained from the TPV data (by using equation (2-17); results see table 3-3).

The measured relative porosities are all within a narrow range between 54% and 64%. Hence, it seems justified to calculate the mean measured relative porosity and its standard deviation to 57.8 ± 2.86%.

[17] This assumption is valid as long as the composite SiO_2/PEO fibers do not exhibit additional pores before calcination and no shrinkage of any phase occurs during calcination.

Table 3-3: Theoretical and measured relative porosities of the electrospun fibers with respect to the variation of the Ludox amount in the spinning solution.

sample no.	sample category	SiO_2 source	weight ratio SiO_2/polymer	volume ratio SiO_2/polymer[1)]	theoretical relative porosity[2)] [%]	measured relative porosity[3)] [%]
6	NP-fibers	Ludox "AS" NPs	0.23	0.12	89.3	63.4
12	NP-fibers	Ludox "AS" NPs	0.50	0.27	78.7	56.8
13	NP-fibers	Ludox "AS" NPs	0.75	0.41	70.9	58.2
14	NP-fibers	Ludox "AS" NPs	1.00	0.55	64.5	60.1
15	NP-fibers	Ludox "AS" NPs	1.25	0.68	59.5	55.4
16	NP-fibers	Ludox "AS" NPs	1.25	0.68	59.5	56.7
17	NP-fibers	Ludox "AS" NPs	1.50	0.82	54.9	54.3

[1)]: calculated with the densities ρ of SiO_2 (ρ_{SiO2} = 2.2 g·cm^{-3})[152] and PEO (ρ_{PEO} = 1.2 g·cm^{-3})[107];
[2)]: calculated from the volume ratio SiO_2/polymer;
[3)]: calculated from the TPV values by using equation (2-17).

This value roughly coincidences with the theoretical relative porosity of sample 17 which is the sample with the highest SiO_2 to polymer ratio. All other samples exhibit theoretical relative porosities which are larger than the measured ones leading to the conclusion that the pore volume generated by the combustion of the polymer shrinks significantly during calcination. Neither the SD nor EICA concept generally includes such a successive shrinkage process though it may exhibit significant influence on the resulting structures. However, the discussion of the consequences of shrinkage is more or less the same with respect to both concepts. The decisive question is how far the loss of a large volume fraction of the composite alters the topography of the remaining silica phase. The very high theoretical relative porosities in table 3-3 and the above discussed cluster aggregation process via open fractal structures suggest that the silica volume alone is not able to represent a stable, self-supporting structure without any rearrangements upon polymer removal. In terms of the EICA concept shrinkage during calcination is a consequence of packing of silica clusters which are more or less homogeneously distributed in the composite material. The shrinkage has to occur to such extent that the Ludox particle network at least reaches a percolation barrier and a stable self-supporting structure is formed. Apparently, a volume fraction of approximately 42% of Ludox particles is necessary to give such a stable structure not collapsing further. Unfortunately, the volume fraction of Ludox particles in all investigated spinning solutions and fibers is lower than this 42% threshold. Consequently, shrinkage of the fibers takes place in all samples during calcination until the pore volume fraction is reduced to the apparently critical upper limit of approximately 58% (equivalent to a Ludox volume fraction of approximately 42%). This rearrangement of the as-spun structure during calcination may alternatively be interpreted as ripening step of a SD process, irrespective of the constraints of this concept concerning electrospinning discussed in chapter 2.5.4. Yet, from a colloidal chemist's point of view the rearrangement of SiO_2 particles is more reasonably discussed in terms of the EICA concept (see figure 3-15): In the electrospinning experiments the evaporation of solvent leads to the aggregation of particle clusters embedded

in the polymer matrix. During calcination the polymer is combusted leading to further aggregation of these clusters accompanied by shrinkage of the fiber volume due to the loss of the large polymer volume fraction until the aggregation of the particle clusters forms a self-supporting structure. The constant porosity being independent of the polymer to SiO_2 ratio is reasonable in terms of the EICA concept because the rearrangement does not depend on the volume of the polymer matrix but the energy available for the rearrangement of the clusters (see chapter 2.5.5). Since all samples were calcined at 550 °C the energy for the activation of rearrangements is the same in all cases, consequently leading to the same fractal structures in all above mentioned, calcined silica fibers.

As the calcination process is accompanied by a differently strong shrinkage depending on the SiO_2 to polymer ratio it also can be understood why the fibers in figure 3-3 exhibit different amounts of macroscopic cracks. The fibers from the spinning solutions with lower Ludox content (see figure 3-3 A–D) have to shrink to a larger extent than the fibers from the spinning solutions with higher Ludox content (see figure 3-3 E–J). Hence, the mechanical stress is larger, when fewer Ludox particles are present in the as-spun composite fibers provoking more cracks during calcination.

In consideration of the above discussed preparation of silica fibers from Ludox particles the preparation of electrospun silica nanofibers from sol-gel precursors is fundamentally different and cannot be discussed in the same manner, i. e. on the basis of the EICA concept. Yet, some remarks concerning the preparation of sol-gel-derived fibers should be made: The sol-gel-derived silica fibers hardly exhibit any mesoporosity (see figure 3-9) because they are not generated from preformed particles or clusters but from molecular precursors forming more dense materials. For the preparation of (meso-) porous materials from such molecular species the concept of SD is more adequate to discuss pore forming processes. As discussed in chapter 2.3.1 SD requires a thermodynamically unstable situation triggering a spatiotemporal evolution towards a phase separated system. In the case of electrospinning with sol-gel precursors two reasons may prevent spinodal phase separation. First, solutions of sol-gel precursors are often stable over a very wide range of concentrations,[18] so that a thermodynamically unstable situation cannot be achieved easily. Secondly, the very fast solvent evaporation in electrospinning experiments hardly leaves any time for a spatiotemporal evolution leading to separated “sol-gel rich” and “sol-gel poor” phases. Though it should be generally possible to prepare mesoporous inorganic fibers from sol-gel precursors this was not reached by the experiments conducted so far. In contrast to the preparation of inorganic fibers from preformed nanoparticles via the above discussed EICA pathway, the solubility of the spinning polymer is of significant impact when sol-gel precursors are used instead and SD needs to be the origin of mesoporosity (see chapter 2.5.4.2). Consequently, it is more challenging to find adequate synthesis conditions to prepare mesoporous inorganic fibers from sol-gel precursors via electrospinning. A more detailed discussion of the pivotal differences between the sol-gel and the EICA pathway for the preparation of mesoporous inorganic fibers is postponed to chapter 3.6.

[18] For example some alkoxide precursors like $Zr(OiPr)_4$ can be purchased in 80 wt.-% concentration in isopropanol proving the very high solubility of this precursor in isopropanol.

3.2.5 Conclusion on silica experiments

Some fundamental knowledge on the mechanistic processes of mesopore-generation in electrospun silica fibers was gained in the previous chapters. These results may also be relevant for electrospun fibers of other materials motivating a short summery at this point before electrospun fibers of other inorganic oxides are investigated. In the introduction of chapter 3.2 it was mentioned that experiments on silica fibers may serve as model experiments for other (oxide) materials. Consequently, this summary recapitulates the most important findings from the silica experiments briefly with special respect to fundamentals concerning structure generating processes during electrospinning of inorganic materials.

The specific surface areas of the nanoparticle-derived silica materials are mainly governed by the intrinsic properties of the building blocks: All analyzed nanoparticle-derived silica samples exhibit specific surface areas roughly around 200 $m^2 \cdot g^{-1}$ which is basically the specific surface area of the Ludox particles used as building blocks reduced by approximately one fourth as a consequence of unavoidable inter-particle contacts and sintering at these contact points. Simultaneously, the measured specific surface areas prove that the (spherical) particle shape is basically preserved throughout the calcination process and that they do not coalesce completely.

Some trends in the physisorption results on nanoparticle-derived silica materials were found to be hardly explainable by SD. On the basis of DLCA the concept of evaporation induced cluster aggregation (EICA) was introduced and the results on the silica NP-materials could be well interpreted by this model: The origin of mesoporosity was ascribed to the arrangement of individual nanoparticles to clusters with an open fractal structure which is preserved throughout the calcination. The thermal energy during calcination at 550 °C is obviously not sufficient to trigger rearrangement to a dense packing of particles. In this context it was explained that the concomitant condensation of the particles via surface sol-gel reactions is of decisive importance.

Furthermore, also the comparable mesoporosity of electrospun fibers and the corresponding unspun solutions could be understood in terms of the EICA concept: The structure formation process is basically the same in both cases with the only difference that the timescale of solvent evaporation is substantially different. Nevertheless, the aggregation of individual nanoparticles to clusters with a fractal structure is roughly the same leading to similarly porous structures after combustion of the polymer because the decisive physical interactions of the dispersed nanoparticles stay unchanged. Besides the intrinsically present macroporosity of electrospun fibers not investigated in this thesis, the only benefit of the electrospinning process concerning the resulting mesoporosity is the stronger confinement of the structure formation process in the two dimensions of space and time. It was argued that the confinement accounts for a stronger restricted structure formation leading to more homogeneous mesoporous structures for all fiber materials irrespective of the kind of Ludox particles used in the syntheses. In contrast, the corresponding bulk materials suffer from local inhomogeneities due to the absence of such confinement resulting in stronger statistical deviations in their mesoporosity and consequently in their physisorption data.

However, these results prove that the mesoporosity of the silica fibers is not significantly improved by the fibrous structure generated by electrospinning. Differences in the porosity between bulk and fibrous materials that were expected due to the intrinsically different shapes probably may be found in the size range of macropores which cannot be analyzed by nitrogen physisorption in detail. Analysis of the macroporosity should be done by mercury intrusion porosimetry, which was beyond the scope of this thesis. Nevertheless the above mentioned results strongly recommend a future project studying the macroporosity of electrospun fibers in detail.

A further result of the silica experiments is that the mesoporosity of the Ludox particle-derived fibers is independent of the weight ratio between the electrospinning polymer and the inorganic nanoparticles. Optical differences in the fibrous shape that were found by SEM investigations did not affect the mesoporosity of the fibers. These findings are a consequence of the large polymer volume fraction in the fibers before calcination and the consecutive shrinkage process during calcination. With respect to the EICA concept it was discussed that the open fractal clusters present in the as-spun composite fibers are packed in identical manner during calcination and the concomitant combustion of the polymer irrespective of the polymer volume fraction.

In contrast to the prepared NP-fibers, the obtained sol-gel-derived fibers do not show significant mesoporosity. Since the structure formation in electrospinning experiments using sol-gel precursors is different and cannot be based on and explained by the EICA concept it has to be explained by SD if the preparation of mesoporous fibers is considered. However, the timescale of structure formation during electrospinning, the solubility of sol-gel precursors and the influence of the polymer properties on SD are some important parameters which render it a difficult task to prepare mesoporous inorganic materials from sol-gel precursors via electrospinning without the addition of other porogens. Consequently, the results of the silica experiments suggest that using nanoparticles as building blocks instead of sol-gel precursors seems to be advantageous, if mesoporous structures are desired.

The above mentioned results constitute a first mechanistic understanding of the processes determining the nanostructure of nanoparticle-derived inorganic fibers. This understanding of the electrospinning process was envisaged as one major goal of this thesis and represents considerable progress in this field.

3.3 Zirconia fibers

3.3.1 Introduction and sample overview

Electrospun zirconia nanofibers were first reported by Shao et al. in 2004. They were spun with an aqueous poly(vinyl alcohol) (PVA) solution under addition of zirconium oxydichloride ($ZrOCl_2 \cdot 8H_2O$) sol-gel precursor as zirconia source.[130] Several publications dealing with zirconia-based nanofibers in the following years all used sol-gel precursors as zirconia source for electrospinning.[153–155] In 2006 Zhang et al. were the first to use commercial, aqueous suspensions of preformed zirconia nanoparticles for electrospinning instead of sol-gel precursors.[156]

Electrospun zirconia fibers are of scientific interest because zirconia is a material of technical relevance and a nanostructured shape may be beneficial for applications, such as e. g. catalytic applications (see below). Zirconia is widely used as a versatile ceramic material. The most commonly exploited properties of zirconia in technical applications are its hardness, ductility, thermostability and its ionic conductivity paired with its extraordinary chemical inertness. Furthermore, investigations on zirconia fibers may complement and/or support the results obtained for electrospun fibers of silica (see chapter 3.2) or titania[1,75] concerning the conceptual investigations on electrospun metal oxide fibers being the pivotal topic of this thesis.

3.3.1.1 Technical relevance of zirconia[128]

Zirconia is the most relevant technical ceramic material with a worldwide annual output of some megatons. Like titania, it is used as white pigment all the same. Additionally, zirconia is a relatively cheap, hard ceramic with a Mohs hardness of 7.5[152] used as prosthetic ceramic in medical applications, especially as dental material. In contrast to other ceramics zirconia fabrics are less brittle due to the crystallographic polymorphism of zirconia and the resulting manifold polycrystalline compositions of bulk materials. Zirconia can be stabilized in different crystallographic modifications by the addition of other elements which are mainly calcium, magnesium or yttrium, allowing for optimizing its mechanical properties further. These stabilized zirconia materials are also used in other important applications: Especially yttrium stabilized zirconia (YSZ) has a special relevance because it is the most relevant oxygen ion conductor applied as solid electrolyte in fuel cells or as part of lambda sensors in the automotive industry. Another very important property of zirconia is its thermostability and chemical inertness that are accompanied by a heat expansion coefficient that can be matched to steels. This makes zirconia a well-suited material for coatings and heat isolations in high temperature applications.

3.3.1.2 Zirconia as example in conceptual investigations on the synthesis of electrospun metal oxide fibers

Zirconium is the higher homologue of titanium implying that these two elements act in a chemically similar manner. Since titania fibers were investigated previously,[1,75] it is straightforward to study zirconia fibers in analogy to the former titania fibers. With such congruent proceeding it is possible to investigate, if zirconia nanofibers can be produced from nanoparticle dispersions in a similar manner as titania or silica fibers and if the results on the different materials are in accordance with each other. Physico-chemical properties of the resulting fibers are to be compared by SEM and nitrogen physisorption because these methods allow for analyzing structural properties like the fiber morphology, their surface structure and their porosity being in the focus of this thesis. Finally, combining the results from zirconia, titania and silica fibers may allow for the establishment of a fundamental concept elucidating the processes and formation mechanisms involved in the electrospinning of inorganic fibers (see chapter 3.6). There, also the investigations and results on ceria (see chapter 3.4) and tin oxide (see chapter 3.5) fibers will be considered, so that chemically different oxides will not be omitted.

In contrast to nanoparticle-based silica nanofibers, the nanoparticle-based zirconia fibers were prepared from self-synthesized dispersions. The synthesis of zirconia nanoparticles was developed in the Smarsly group by C. Suchomski (synthesis to be published). Additionally, this classical, wet chemical synthesis was modified towards a preparation in a microwave oven[157] so that two differently synthesized kinds of zirconia nanoparticles were available for the electrospinning experiments. Possessing differently prepared particles allows for investigating the influence of the synthetic approach on the electrospinning results: By comparing the experiments conducted with the microwave synthesized nanoparticles (MWS-NPs) with the experiments conducted with the classically, wet chemically synthesized nanoparticles (WCS-NPs) it can be studied if there are any differences in the resulting particles affecting the electrospinning process. Furthermore, the nanoparticle-based syntheses will be compared with sol-gel-derived zirconia fibers prepared by a synthesis adapted from literature.[153,154]

With the above mentioned experiments comparative investigations can be performed studying the influence of parameters like solvent composition, preparation method of the particles etc. Especially, the experiments concerning the solvent composition were performed with the same solvents as in the former study on titania fibers[75] resulting in a direct comparability of these experiments.

3.3.1.3 Detailed sample description

Sol-gel fibers were produced from zirconium oxydichloride octahydrate ($ZrOCl_2 \cdot 8H_2O$) precursor electrospun with PVP as spinning polymer with a mixture of ethanol and water as solvent (1/1 by weight) similarly as already published elsewhere.[153] The concentrations of the solids were 5.2 wt.-% PVP and 8.6 wt.-% $ZrOCl_2 \cdot 8H_2O$ equivalent to 3.3 wt.-% of ZrO_2, respectively.

The self-synthesized nanoparticles were electrospun with PEO in different solvents. Furthermore, reference samples for physisorption analyses were prepared by calcination of the pure nanoparticle dispersions or the readily prepared electrospinning solutions without spinning them. All solutions contained approximately 56 wt.-% methanol, while dichloromethane, water or chloroform were used as second solvent with a portion of approximately 39 wt.-% in the total solution (see table 3-4). The concentration of zirconia was fixed to approximately 2.3 wt.-% in all experiments. PEO with a molecular weight of 1,000,000 $g \cdot mol^1$ was used in a concentration of 2.8 wt.-% in the experiments with MWS-NPs or in a concentration of 2.2 wt.-% in the experiments with WCS-NPS.

3.3.2 Synthesis and WAXS and DLS characterization of zirconia nanoparticles

The zirconia nanoparticles used for the experiments are characterized by dynamic light scattering (DLS) and wide angle X-Ray diffraction (WAXS). These characterizations were conducted in order to facilitate interpretation of the physisorption results presented in chapter 3.3.4. Zirconia nanoparticles were self-synthesized by two different methods from similar reaction mixtures. The decisive difference between these two methods was the different kind of energy transfer to the reaction mixture being heating by an oil bath in the first case (resulting in the WCS-NPs) and microwave irradiation in the second case (resulting in the MWS-NPs).

Table 3-4: Overview of all synthesized zirconia samples and composition of the corresponding solutions that were used for the syntheses.

sample no.	sample category	polymer	ZrO_2 [1)]	solvent(s)	wt.-% solvents
1	sol-gel fibers	5.2 wt.-% PVP	8.6 wt.-% $ZrOCl_2 \cdot 8H_2O$ (≙ 3.3 wt.-% ZrO_2)	H_2O/EtOH	43.0/43.2
2	NP-fibers	2.2 wt.-% PEO	2.2 wt.-% ZrO_2 (WCS-NPs)	H_2O/MeOH	41.2/54.4
3	NP-fibers	2.2 wt.-% PEO	2.3 wt.-% ZrO_2 (WCS-NPs)	CH_2Cl_2/MeOH	39.0/56.5
4	NP-fibers	2.8 wt.-% PEO	2.2 wt.-% ZrO_2 (“fresh” MWS-NPs)	H_2O/MeOH	39.5/55.5
5	NP-fibers	2.8 wt.-% PEO	2.2 wt.-% ZrO_2 (“aged” MWS-NPs)	H_2O/MeOH	39.5/55.5
6	NP-fibers	2.8 wt.-% PEO	2.3 wt.-% ZrO_2 (“fresh” MWS-NPs)	CH_2Cl_2/MeOH	38.8/56.2
7	NP-fibers	2.8 wt.-% PEO	2.3 wt.-% ZrO_2 (“fresh” MWS-NPs)	$CHCl_3$/MeOH	39.1/55.9
8	dried spinning solution	2.8 wt.-% PEO	2.2 wt.-% ZrO_2 (“fresh” MWS-NPs)	H_2O/MeOH	39.5/55.5
9	dried spinning solution	2.8 wt.-% PEO	2.2 wt.-% ZrO_2 (“aged” MWS-NPs)	H_2O/MeOH	39.5/55.5
10	dried spinning solution	2.8 wt.-% PEO	2.3 wt.-% ZrO_2 (“fresh” MWS-NPs)	CH_2Cl_2/MeOH	38.8/56.2
11	dried spinning solution	2.8 wt.-% PEO	2.3 wt.-% ZrO_2 (“fresh” MWS-NPs)	$CHCl_3$/MeOH	39.1/55.9
12	pure particles	none	WCS-NPs	MeOH	91.0
13	pure particles	none	MWS-NPs	MeOH	91.0

[1)]: WCS-NPs: wet chemically synthesized nanoparticles; MWS-NPs: microwave synthesized nanoparticles.

3.3.2.1 DLS analyses

DLS analyses were performed to determine the size of the zirconia nanoparticles with methanol being the dispersion solvent. It has to be considered that the resulting hydrodynamic diameters found by DLS include the solvation shell of the particles. The corresponding histograms are shown in figure 3-16. DLS analyses on WCS-NPs and MWS-NPs were generally done shortly after the synthesis, i. e. within one or two days. Electrospinning experiments with these "fresh" particles were also performed within some days, despite special experiments with an "aged" MWS-NP dispersion that was stored for approximately eight weeks at room temperature before it was spun. Hence, DLS analysis was also performed on this dispersion shortly before the electrospinning experiments were conducted to figure out whether these "aged" MWS-NPs exhibit different properties than "fresh" MWS-NPs.

All DLS results show an apparently asymmetric distribution of particle sizes with the smallest particle sizes of each sample being the most frequently observed ones. Such asymmetric histograms of the particle size distribution are unreasonable, because generally a Gaussian distribution of sizes is expected for such particle dispersions. Thus, a more detailed investigation of the DLS analyses is necessary to identify the origin of such unreasonable results. However, these investigations are beyond the scope of this thesis, because only a qualitative comparison of mean particle sizes in the dispersions is relevant concerning the following investigations.

The WCS-NPs feature a population weighted mean diameter of D_n = 1.9 nm (see figure 3-16 A) while the "fresh" MWS-NPs exhibit a mean diameter of D_n = 4.3 nm (see figure 3-16 B) and the "aged" MWS-NPs revealed a mean value of D_n = 15.2 nm (see figure 3-16 C). Hence, the MWS-NPs are significantly larger than the WCS-NPs. From the comparison of the mean diameters of the "fresh" and "aged" MWS-NPs it can be concluded that the particles tend to agglomerate due to insufficient stabilization. This agglomeration also results in a broadening of the particle size distribution. A growth of the particles instead of agglomeration is unreasonable, because the dispersions should be free of further precursor molecules after the washing procedure. Moreover, it is implausible that the particles grow at room temperature, when the synthesis of the particles was conducted at much higher temperatures. A reaction of residual functional groups on the surface of the particles at room temperature is so slow that a further turnover of sol-gel reactions can practically be excluded. In fact the agglomeration of the particles should only proceed via attractive physical interactions like bipolar binding, i. e. mainly hydrogen bonding, or van-der-Waals interactions. Nevertheless, these large agglomerates can be considered as single particles behaving differently in dispersion than the smaller, freshly synthesized ones. It can be presumed that such agglomerates are less dispersible and tend to precipitate from dispersion at lower concentrations than smaller particles. This assumption is important, if physisorption analyses are discussed (see chapter 3.3.4, figure 3-25). The supposed agglomeration is further backed by an unreasonably high volume weighted mean diameter D_v of 98.4 nm in the DLS analysis of the "aged" MWS-NPs. The D_v value is generally strongly dominated by large particles resulting in single huge agglomerates causing unreasonable values. Hence, the D_n values are more meaningful when large agglomerates are present. The "fresh" MWS-NPs as well as the WCS-NPs have D_v values of 5.6 nm and 2.3 nm, respectively. These values are not much larger than the corresponding D_n values proving the absence of significant

amounts of larger particles or agglomerates. This is in accordance with the narrower size distributions compared to the "aged" MWS-NPs.

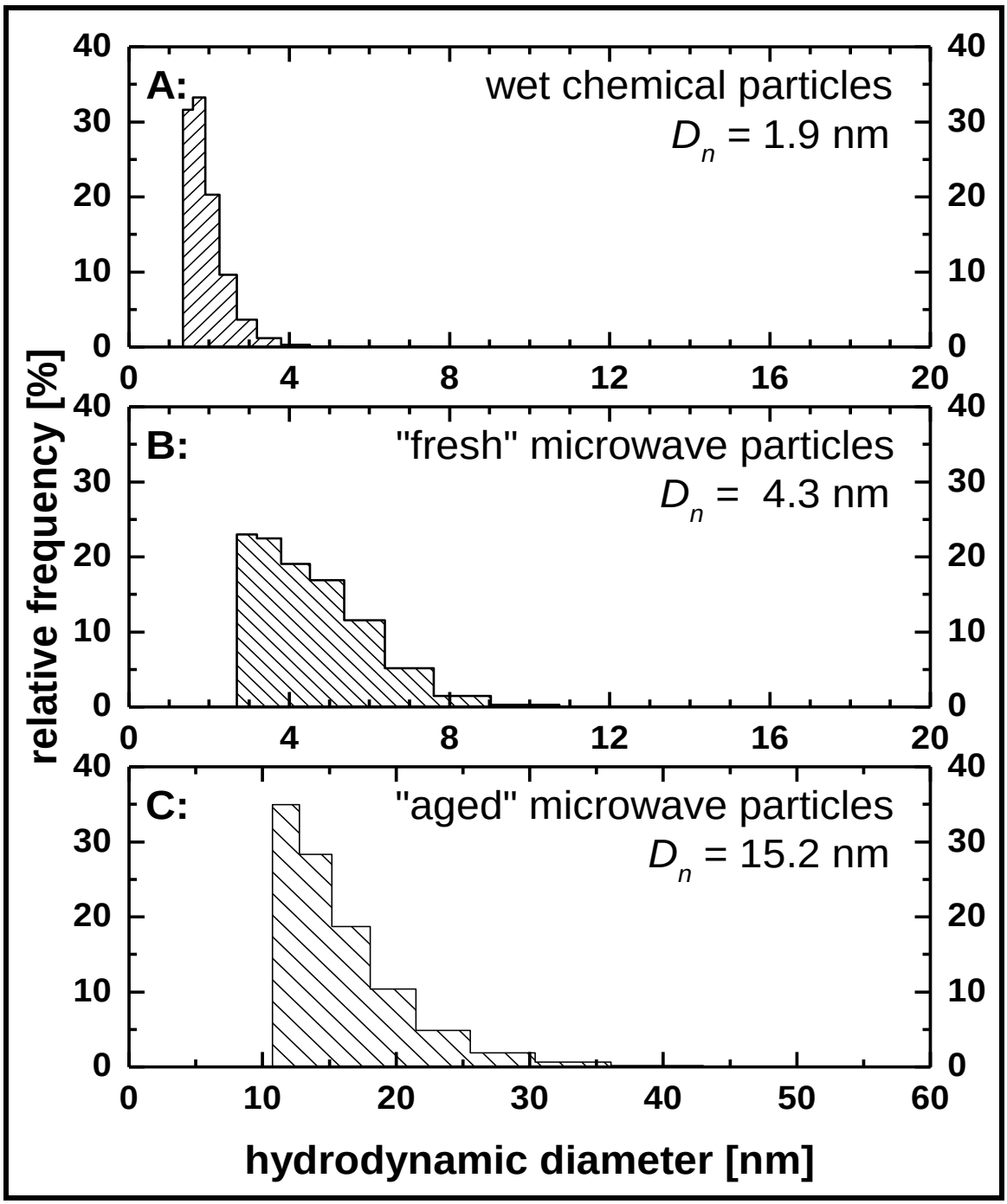

Figure 3-16: Histograms from DLS analyses of zirconia nanoparticle dispersions in methanol. A: WCS-NP dispersion; B: "fresh" MWS-NP dispersion measured one day after synthesis; C: "aged" MWS-NP dispersion measured eight weeks after synthesis. The population weighted mean diameters of the zirconia particles in the dispersions were found to be D_n = 1.9 nm (A), D_n = 4.3 nm (B) and D_n = 15.2 nm (C), respectively.

3.3.2.2 WAXS analyses

WAXS analyses were performed to characterize the crystallinity of the different zirconia samples. WAXS patterns were recorded for WCS-NPs and MWS-NPs and both kinds of particles were investigated after drying at 80 °C as well as after calcination at 550 °C. The crystallographic structure of the samples was identified to be mainly tetragonal for all samples; none of them was completely amorphous.

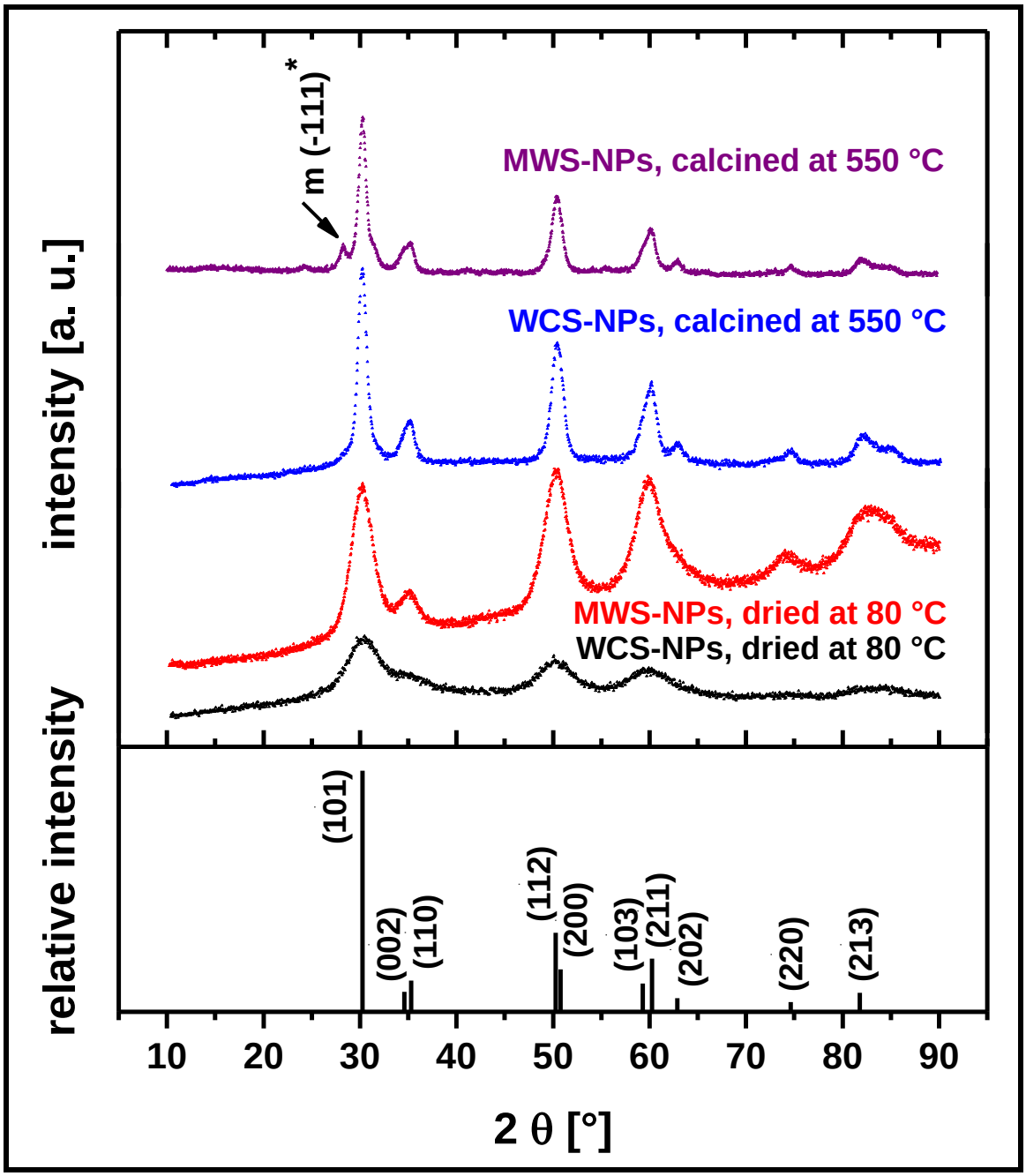

Figure 3-17: Measured XRD patterns of different zirconia NPs and indexed, relative intensities for the tetragonal phase (JCPDS card no. 01-079-1770).
***: (−111) reflection of the monoclinic zirconia phase (JCPDS card no. 00-078-0047).**
Color coding: black: WCS-NPs dried at 80 °C; red: MWS-NPs dried at 80 °C; blue: WCS-NPs calcined at 550 °C; purple: MWS-NPs calcined at 550 °C.

All significant reflections fit to the most prominent reflections of the JCPDS reference card number 01-079-1770 (see figure 3-17). Only the microwave synthesized particles calcined at 550 °C feature one less intense reflection at a scattering angle of $2\Theta = 28.2°$, which cannot be attributed to the tetragonal zirconia phase, but to the most intense reflection of the monoclinic zirconia phase (JCPDS reference card number 00-078-0047). It is known that the tetragonal phase is the preferred structure for small zirconia nanoparticles and that such small nanoparticles can transform to the monoclinic structure upon calcination at elevated temperatures and/or growth of the particles.[158,159] The transformation from the tetragonal to the monoclinic phase seems to have taken place to a small extent for the microwave synthesized particles after calcination at 550 °C being in accordance with former literature results.

Besides the identification of the crystalline phase(s) of the samples, their crystallite sizes were calculated via Rietveld refinement of the WAXS data.[19] The WAXS patterns could be well fitted by the Rietveld refinement with only slight differences between measured and fitted data for all samples (see figure 3-18). The portion of the monoclinic phase was estimated to be below 20 mass percent for the MWS-NPs after calcination at 550 °C. Due to the low intensities of the monoclinic reflections in this sample, this value can only be considered as rough estimation. For the same reason a meaningful calculation of the crystallite size for the monoclinic phase was not possible. The crystallite diameters of the tetragonal phase were found to be in the range of 1.8−8.1 nm (see table 3-5). The uncalcined WCS-NPs had the lowest mean diameter of 1.8 nm being in good agreement with the diameter estimated by DLS (see figure 3-16). This leads to the conclusion that the particles consist only of one and not an agglomeration of several crystallites. Furthermore, the low difference between the two size values estimated by DLS and XRD prove absence of a huge amorphous portion in the particles and the presence of a small hydration shell only.[20] In contrast, the MWS-NPs seem to have a much larger amorphous portion and possibly also a thicker hydration shell before calcination, because the DLS size value of 4.3 nm is much larger than the XRD value of 2.5 nm. On the other side, the difference of these values is small enough to exclude that the majority of the MWS-NPs could consist of several crystallites.

After calcination the MWS-NPs as well as the WCS-NPs possess similar mean diameters of 8.1 nm and 6.9 nm, respectively. Thus, the calcined materials, and consequently also the calcined electrospun fibers prepared from the particles, can be considered to be of similar crystallinity. The small portion of the monoclinic phase in the calcined MWS-NPs and possibly also the slightly larger size compared to the calcined WCS-NPs may be generated from the larger amorphous portion in the particles before calcination; the amorphous portion of the MWS-NPs might be transformed to the monoclinic phase directly and consequently more easily than would be possible for the WCS-NPs not possessing a significant amorphous portion before calcination.

[19] Therefore, the ICSD references for the tetragonal phase (ICSD no. 66781) and for the monoclinic phase of zirconia (ICSD no. 18190) were used.

[20] It has to be taken into account that the estimation of crystallite sizes in the range of 2 nm by Rietveld refinement goes along with a significant systematic error, because the XRD reflections of samples with such low crystallinity are very broad and consequently the refinement can never result in very precise values, inter alia for the crystallite size. Hence, the absolute size values have to be considered with caution. Nevertheless, the described general trends can be regarded as reliable.

Table 3-5: Mean crystallite diameters *d* of the different zirconia nanoparticles calculated by Rietveld refinement for the tetragonal phase.

sample	*d* [nm][1)]	standard deviation [nm][2)]
zirconia WCS-NPs, dried at 80 °C	1.8	0.32
zirconia MWS-NPs, dried at 80 °C	2.5	0.60
zirconia WCS-NPs, calcined at 550 °C	6.9	0.54
zirconia MWS-NPs, calcined at 550 °C	8.1	2.13

[1)]: The size of the particles was calculated from 21 reflections of the tetragonal phase with similar results, so that a spherical shape of the particles can be assumed. Hence, these values were averaged for each sample to give the mean crystallite diameters.
[2)]: The standard deviation indicates how strongly the calculated crystallite sizes from each reflection deviate from the mean value. A large standard deviation hints at a slight degree of anisotropy of the particle shape in the direction of different lattice planes.

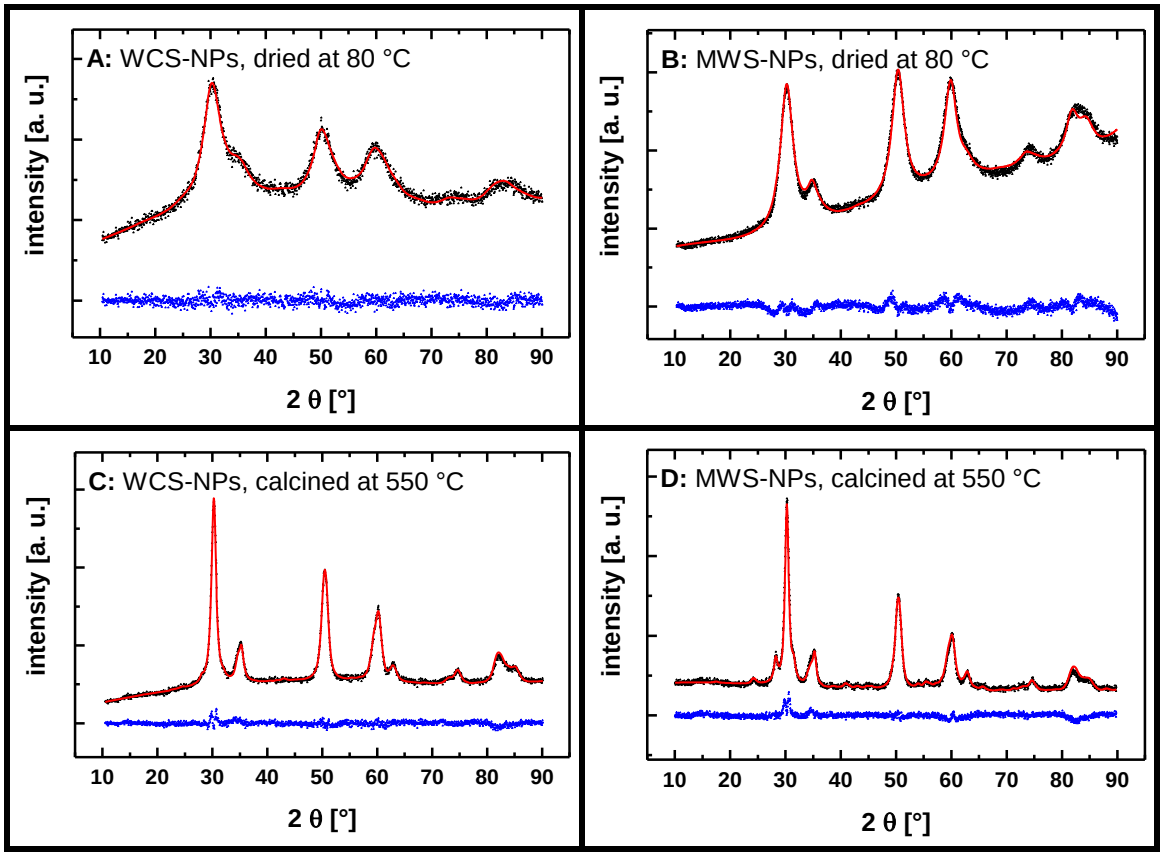

Figure 3-18: Measured XRD patterns (black dots) and Rietveld fitting data (red lines) of different zirconia NPs. Blue dots: Difference between measured and fitted data. A: WCS-NPs, dried at 80 °C; B: MWS-NPs, dried at 80 °C; C: WCS-NPs, calcined at 550 °C; D: MWS-NPs, calcined at 550 °C.

3.3.3 SEM analyses on zirconia fibers

SEM investigations were performed on all synthesized fiber samples listed in table 3-4 in order to prove the results of the electrospinning process for all fibers. However, only representative SEM analyses are presented in this section, because samples prepared from very similar solutions showed no significant differences in the SEM pictures. Concerning the optical shape of the zirconia fibers, difficulties occurred in particular samples during the calcination process. While some fibers preserved their fibrous morphology (see figure 3-21) other fibers lost their well-defined outer shape during calcination and the concomitant removal of the spinning polymer (see figure 3-20). The reason for this shape loss during calcination is not totally clear for the zirconia fibers, but in the synthesis of tin oxide fibers exactly the same difficulties occurred. For tin oxide fibers this phenomenon was investigated in more detail and it was possible to circumvent these problems yielding in preservation of the well-defined fibrous morphology after calcination (see chapter 3.5.1.3). At the moment it shall only be mentioned that the collapse of the fibrous morphology can be attributed to an insufficient sintering of the nanoparticles before the spinning polymer is removed during calcination. This finding is probably also valid for the synthesis of the zirconia fibers from nanoparticles, so that optimization of the electrospinning solution(s) should enable a synthesis of zirconia fibers allowing for preservation of the fiber shape throughout the calcination process. However, there are reasons why such optimization was not performed concerning the zirconia experiments. First, the investigations on the silica materials led to the conclusion, that the well-defined fibrous morphology is not the decisive property that determines the porosity of the samples (see chapter 3.2.5). Consequently, a well-defined outer shape of electrospun fibers after calcination is not necessary to draw meaningful conclusions concerning their porosity. Second and more importantly, the solutions in the zirconia experiments were projected to be electrospun under comparable conditions with respect to other materials in order to draw meaningful conclusions concerning the conceptual, comparative investigations on electrospun, nanoparticle-based fibers. Thus, the preparation of zirconia nanoparticles and the following electrospinning experiments were conducted under the same conditions as previously done with titania nanoparticles[75] in order to obtain results from analogous, comparable experiments. Consequently, zirconia nanoparticle dispersions were combined with the same spinning polymer, the same solvent(s) and in the same composition as the former titania nanoparticle dispersions resulting in a direct comparability of the two materials. For the scope of this thesis this comparability is much more important than an optimal optical appearance of the electrospun fibers.

Figure 3-19 depicts zirconia sol-gel fibers after calcination (see table 3-4, sample 1). The fibers possess a smooth surface typical for sol-gel fibers and quite homogeneous diameters of about 100 nm. Also cracks and beads are more or less absent in the zirconia sol-gel fibers.

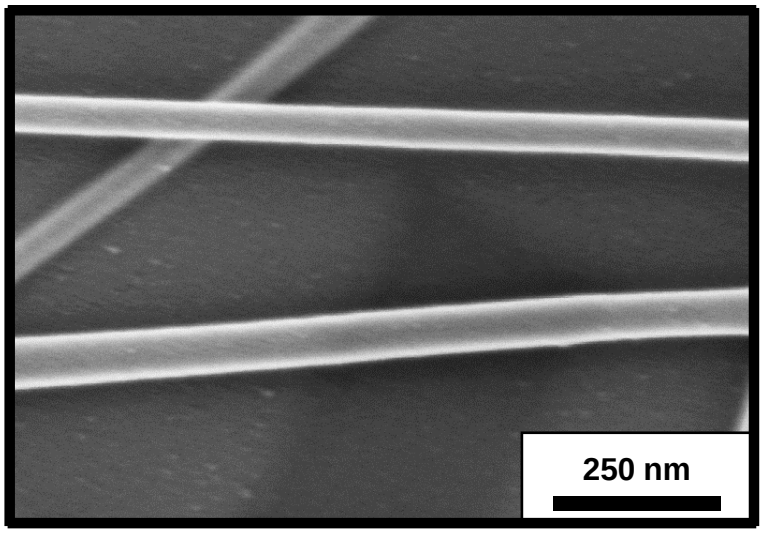

Figure 3-19: SEM picture of zirconia fibers obtained from $ZrOCl_2 \cdot 8H_2O$ as sol-gel precursor and electrospun with PVP after calcination at 550 °C (see table 3-4, sample 1).

NP-fibers prepared from zirconia MWS-NPs are illustrated in figure 3-20 and figure 3-21.

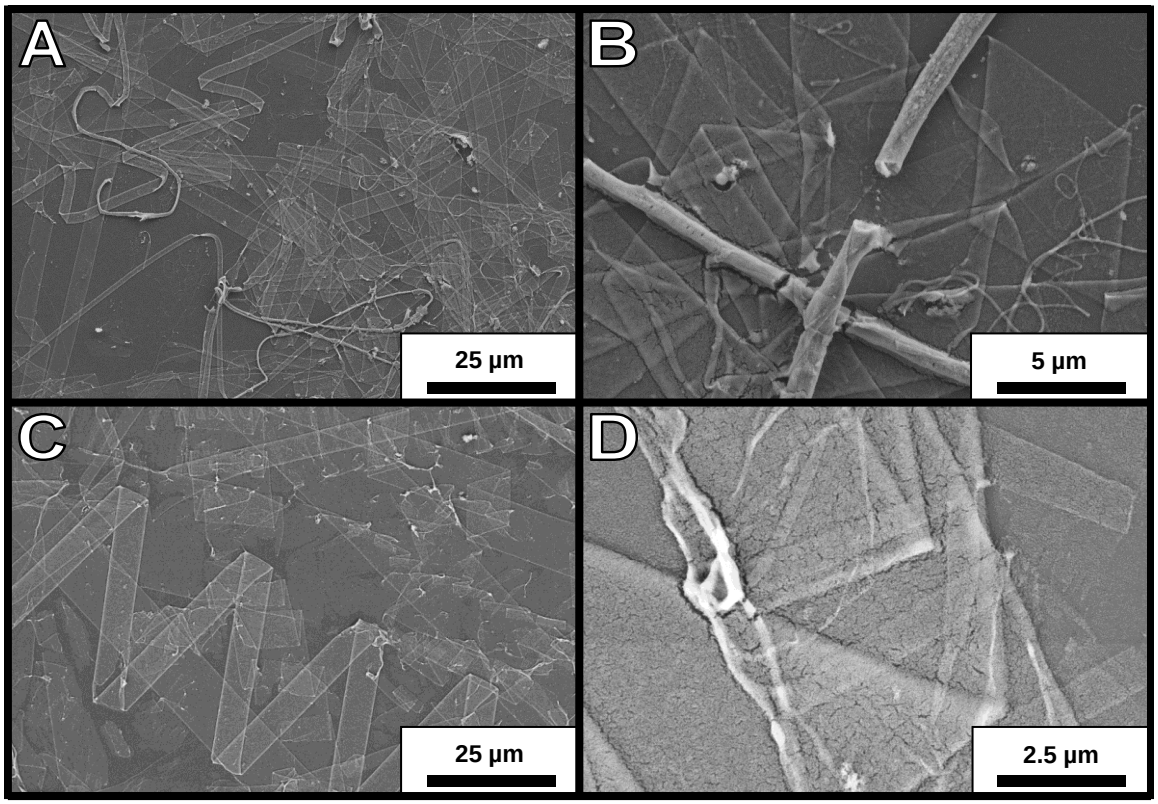

Figure 3-20: SEM pictures of zirconia fibers after calcination at 550 °C obtained from zirconia MWS-NPs and electrospun with 2.8 wt.-% PEO. Each spinning solution contained 2.3 wt.-% of zirconia MWS-NPs; A, B: Fibers prepared with $CHCl_3$ as co-solvent besides MeOH (see table 3-4, sample 7); C, D: Fibers prepared with CH_2Cl_2 as co-solvent besides MeOH (see table 3-4, sample 6).

While the fibers prepared with chloroform (see table 3-4, sample 7, figure 3-20 A, B) or dichloromethane as co-solvent (see table 3-4, sample 6, figure 3-20 C, D) lost their fibrous morphology upon calcination, the fibers prepared with water as co-solvent preserved their well-defined fibrous shape (see table 3-4, sample 4, figure 3-21) exhibiting relatively constant diameters in the range of approximately 250 nm and an optically rough surface typical for NP-fibers. Such surface roughness is intrinsically generated when individual nanoparticles sinter without coalescing completely as discussed before (see chapter 3.2.4). Beyond this surface roughness figure 3-21 C and D also indicate a significant degree of mesoporosity within the fibers that is not limited to the surface of the fibers. Mesopores all across the fiber diameter can be seen especially on the cross section of some broken fibers in figure 3-21 C. This porosity will be investigated by nitrogen physisorption in chapter 3.3.4 in detail. It also can be seen from figure 3-21 that the NP-fibers exhibit some cracks and some larger agglomerates within the sample, but they are not very numerous, so that they can be neglected in the following discussions.

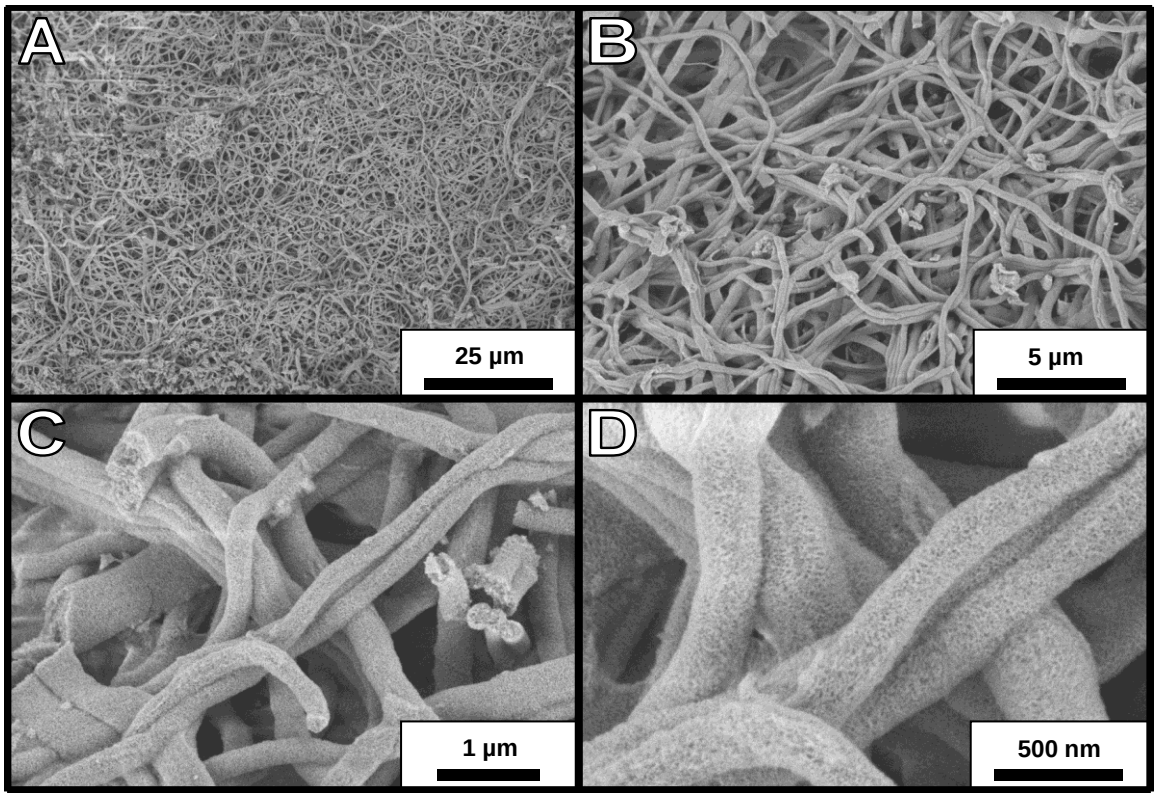

Figure 3-21: SEM pictures of zirconia fibers after calcination at 550 °C obtained from zirconia MWS-NPs and electrospun with 2.8 wt.-% PEO. Each spinning solution contained 2.2 wt.-% of zirconia MWS-NPs and H_2O as co-solvent besides MeOH (see table 3-4, sample 4); A–D: different magnifications.

The electrospinning process seems to be negatively influenced if chloroform or dichloromethane are employed as co-solvent, because fibers electrospun with the help of these solvents suffer from a less well-defined fibrous shape. Some short fiber sections can be seen (see figure 3-20 B), but mostly there are very broad "traces" with several micron thickness consisting of nanoparticles, that remain, when ribbon-like fibers are calcined.[21] These "traces" appear so thin that they cannot be regarded as inherently stable zirconia ribbons. Such bad sample quality was only accepted for the sake of a direct comparability of the following physisorption experiments to former investigations on titania fibers.[75] An optimization of the fiber morphology is expected, for instance, if a small amount of conducting salt is added to the spinning solution. The very broad ribbon-like "traces" hint at an insufficient stretching in the jet during electrospinning that may be improved by increasing the conductivity of the spinning solution. However, this addition of a conducting salt would limit the comparability of these experiments with the former experiment on titania fibers.

Electrospun fibers prepared from WCS-NPs (see table 3-4, samples 2 and 3) resulted in similar spinning results as obtained for the fibers prepared from MWS-NPs, so that the corresponding SEM images are omitted. Interestingly, the fibers from the WCS-NPs also preserved their fibrous morphology when water was used as co-solvent besides methanol, but the fibers collapsed upon calcination, when dichloromethane was used as co-solvent. It seems that the solvent dichloromethane generally has a negative influence on the formation of zirconia fibers irrespective of the method by which the particles have been synthesized. On the one hand dichloromethane evaporated faster than water facilitating the formation of thicker fibers because the jet solidifies faster. On the other hand dichloromethane has a lower dipole moment ($\mu_{CH_2Cl_2}$ = 1.60 D) compared to water (μ_{H_2O} = 1.85 D)[152] expanding the electrochemical double layer (EDL) around the dispersed zirconia nanoparticles. The thicker EDL with dichloromethane as co-solvent may suppress the aggregation of the nanoparticles in the emerging fiber facilitating a homogeneous distribution of individual particles over the relatively large cross section of "thick" fibers. Consequently, sintering of the particles to a shape-stable zirconia fiber upon calcination is hindered due to less interparticular contacts. As mentioned before the addition of a conducting salt seems to be helpful also within this argumentation, because it would help to decrease the thickness of the EDL besides facilitating stretching and thinning of the emerging fiber. A more detailed discussion concerning the sintering process of nanoparticles during the calcination of electrospun fibers will be conducted on tin oxide fibers exemplarily (see chapter 3.5.1.3).

[21] The formation of ribbon-like polymeric fibers was examined and discussed in detail in theory[95,96] and practical experiments.[197] The occurrence of a ribbon-like shape of electrospun inorganic fibers can be assumed to arise from similar formation processes.[89,97,98]

3.3.4 Physisorption: comparative analyses on zirconia fibers

In this chapter, physisorption results on electrospun fibers from sol-gel precursors or zirconia nanoparticles will be compared with results on bulk reference samples. These comparative investigations have the objective to reach a more detailed understanding of the structure generating processes during the electrospinning synthesis of zirconia fibers, similarly as already done for the silica fibers (see chapter 3.2.4). Comparisons to experiments on silica or titania materials will be performed in order to develop a structure formation model which is not limited to specific materials. Such comparisons will be deepened in chapter 3.6 considering also ceria (see chapter 3.4) and tin oxide (see chapter 3.5) materials.

First, general differences between zirconia sol-gel fibers, NP-fibers and pure, dried and calcined nanoparticles are investigated after having calcined the samples at 550 °C. Therefore, physisorption analyses on such samples are illustrated in figure 3-22 comparatively (for the composition of the spinning solutions see table 3-4).

Zirconia sol-gel fibers exhibit a surface area of 28 $m^2 \cdot g^{-1}$ and a TPV of 0.05 $cm^3 \cdot g^{-1}$ (see table 3-6, sample 1). These nanoparticle fibers (derived from MWS-NPs) possess a surface area of 78 $m^2 \cdot g^{-1}$ and a TPV of 0.23 $cm^3 \cdot g^{-1}$ (see table 3-6, sample 4). The pure, dried and calcined MWS-NPs exhibit a surface area of 41 $m^2 \cdot g^{-1}$ and a TPV of 0.01 $cm^3 \cdot g^{-1}$ (see table 3-6, sample 13) while the WCS-NPs possess a surface area of 53 $m^2 \cdot g^{-1}$ and a TPV of 0.08 $cm^3 \cdot g^{-1}$ (see table 3-6, sample 12).[22] The total pore volumes of all these samples are significantly smaller than the TPVs for similar silica materials (in terms of their expression in $cm^3 \cdot g^{-1}$, compare figure 3-9) being a direct consequence of the strongly different densities of silica and zirconia.[23] Considering the relative porosity values, it seems that the porosities of the zirconia and silica materials are within the same range hinting at similarities among the samples (for more details see chapter 3.6).

[22] It has to be mentioned that the isotherm of the pure, dried and calcined MWS-NPs does not close for small relative pressure values. This means that a small amount of adsorbate is not released during the desorption measurement. An explanation of this finding is that some adsorbate is trapped within the volume of this almost non-porous sample. Chemisorption of adsorbate can be excluded due to the chemically similar nature of this sample compared to other zirconia samples under investigation. Due to the very low porosity of this sample the incomplete desorption is insignificant concerning the comparison with other samples, so that it will be neglected in the following discussions.

[23] I. e. ρ = 2.2 g*cm^{-3} for non-porous, amorphous silica[128] and ρ = 6.1 g*cm^{-3} for non-porous zirconia in the tetragonal phase (see JCPDS card 01-079-1770).

Table 3-6: Physisorption results on electrospun zirconia nanofibers: BET[1)], CPV[2)], TPV[3)] and relative porosity[4)] values.

sample no.	sample category	weight ratio ZrO_2/polymer	ZrO_2 source	solvent(s)	BET[1)] [$m^2 \cdot g^{-1}$]	CPV[2)] [$cm^3 \cdot g^{-1}$]	TPV[3)] [$cm^3 \cdot g^{-1}$]	relative porosity[4)] [%]
1	fibers	0.64/1	sol-gel ZrO_2 from $ZrOCl_2 \cdot 8H_2O$	H_2O/EtOH	27.7	0.041	0.050	23.5
2	fibers	1.01/1	"fresh" WCS-NPs	H_2O/MeOH	38.5	0.070	0.081	33.0
3	fibers	1.06/1	"fresh" WCS-NPs	CH_2Cl_2/MeOH	71.1	0.128	0.146	47.0
4	fibers	0.76/1	"fresh" MWS-NPs	H_2O/MeOH	77.6	0.206	0.226	58.0
5	fibers	0.76/1	"aged" MWS-NPs	H_2O/MeOH	60.6	0.242	0.286	63.6
6	fibers	0.82/1	"fresh" MWS-NPs	CH_2Cl_2/MeOH	82.6	0.237	0.261	61.4
7	fibers	0.82/1	"fresh" MWS-NPs	$CHCl_3$/MeOH	91.6	0.223	0.246	60.0
8	dried solution	0.76/1	"fresh" MWS-NPs	H_2O/MeOH	60.6	0.175	0.225	57.8
9	dried solution	0.76/1	"aged" MWS-NPs	H_2O/MeOH	53.7	0.134	0.285	63.4
10	dried solution	0.82/1	"fresh" MWS-NPs	CH_2Cl_2/MeOH	39.7	0.063	0.101	38.1
11	dried solution	0.82/1	"fresh" MWS-NPs	$CHCl_3$/MeOH	46.8	0.078	0.101	38.1
12	pure particles	---	"fresh" WCS-NPs	MeOH	52.7	0.073	0.076	31.7
13	pure particles	---	"fresh" MWS-NPs	MeOH	41.4	0.011	0.012	6.8

[1)]: specific surface area calculated by the BET method;
[2)]: cumulative pore volume calculated by the DFT method; this is the pore volume of the last data point in the CPV plot;
[3)]: total pore volume calculated by using the Gurvich rule (see equation (2-11));
[4)]: calculated from the TPV values (for explanation of the data reduction see chapter 2.6.3.1).

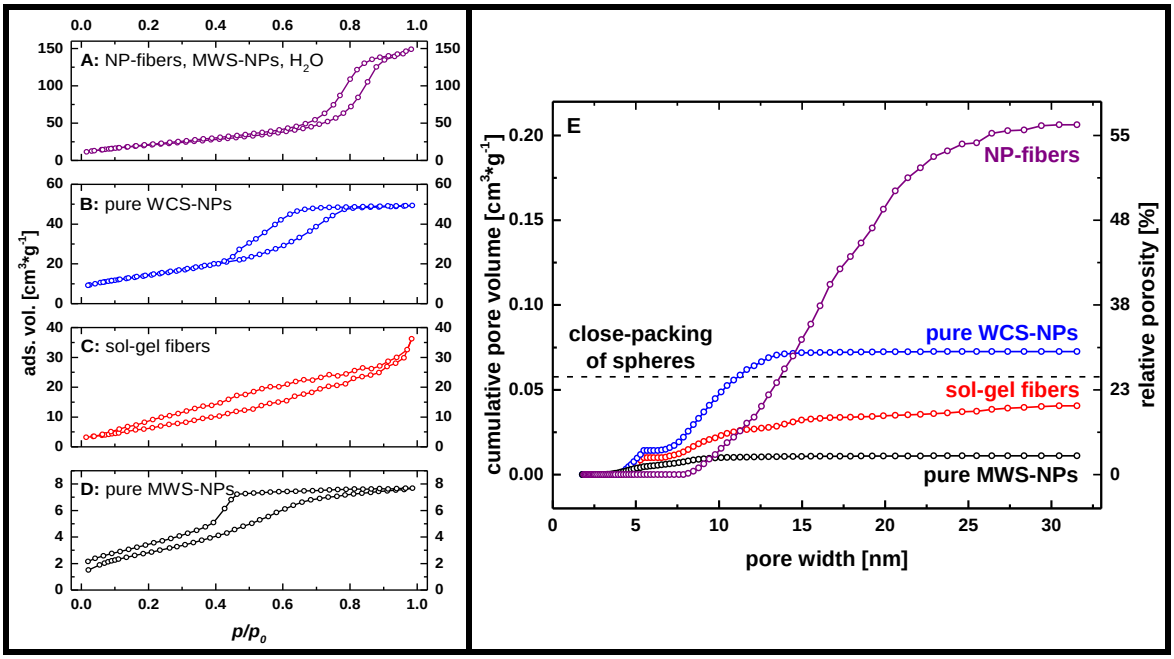

Figure 3-22: N_2-Physisorption isotherms (A–D) and CPV plots from DFT (E) of zirconia sol-gel fibers, pure zirconia nanoparticles, and zirconia fibers obtained from nanoparticles. Magnifications of the isotherms can be found in the appendices (see figure 6-26, figure 6-29, figure 6-37 and figure 6-38). Color coding: red: sol-gel fibers spun with 5.2 wt.-% PVP (see table 3-6, sample 1); blue: pure, dried and calcined WCS-NPs (see table 3-6, sample 12); black: pure, dried and calcined MWS-NPs (see table 3-6, sample 13); purple: electrospun fibers prepared from MWS-NPs in H_2O/MeOH solution with PEO as spinning polymer (see table 3-6, sample 4); dashed black line: porosity of a close-packing of spheres illustrated for comparison.

The relative discrepancies of the surface areas among the different zirconia samples are much larger than for the corresponding silica samples (compare figure 3-9). Otherwise, when the absolute discrepancies are considered, they are quite similar: All zirconia samples in figure 3-22 as well as all silica samples in figure 3-9 differ from each other within a range of about 50 $m^2 \cdot g^{-1}$. The specific surface areas of zirconia materials are on a much lower level than that of the corresponding silica samples, due to the higher density of zirconia affecting the specific surface areas which are usually referred to the mass of the samples. If, instead, the specific surface areas are referred to the molar amount of substance, the variance of the surface areas of the zirconia samples is similar to the variance of the corresponding silica samples. Such comparison of surface areas between different materials will be reconsidered chapter 3.6. Similarly as for silica fibers, a theoretical specific surface area can be calculated by equation (3-1) to 123 $m^2 \cdot g^{-1}$ by using a particle radius of 4 nm, which is reasonable from the results of the Rietveld refinement of the calcined zirconia materials (see table 3-5). The measured specific surface areas are all significantly lower (roughly around 50% compared to the theoretical value; see table 3-6) proving that sintering plays a crucial role during the calcination of the zirconia materials resulting in a much stronger decrease of the accessible surface area as in the case of the silica materials. Simultaneously, intra-particle porosity seems to be absent or at least abolished by sintering, because even the unreached theoretically calculated surface areas assumed dense, non-porous particles.

Among the zirconia samples the porosity trends are similar to those already found for silica: The electrospun NP-fibers exhibit a significantly increased porosity versus the sol-gel fibers because they possess substantial amounts of mesopores (see figure 3-22 E). In contrast, mesopores are only present to a very small extend in the sol-gel fibers and are practically absent if diameters larger than approximately 15 nm are considered. The origin of larger mesopores only present in NP-fibers probably can be ascribed to the same EICA-driven structure formation process discussed for nanoparticle-based silica fibers (see chapter 3.2.4.2). This assumption is backed by the physisorption result on the pure, dried and calcined zirconia nanoparticles: Neither the pure WCS-NPs nor the MWS-NPs exhibit a similarly high porosity as the NP-fibers proving that the porosity of the fibers does not originate from intrinsic particle properties. Rather the spatiotemporal evolution of structure formation during the experiments generates the mesoporosity in the electrospun fibers. Whether the origin of mesoporosity in the electrospun zirconia fibers is the same as in the case of the silica fibers will be discussed later (see figure 3-23) after the porosity of the pure particles is examined.

While the MWS-NPs exhibit a very low porosity with a TPV of 0.01 $cm^3 \cdot g^{-1}$ the WCS-NPs feature a larger amount of small mesopores up to a diameter of approximately 15 nm resulting in a TPV of 0.08 $cm^3 \cdot g^{-1}$. For comparison, the porosity of a close-packing of equally sized non-porous spheres is known to be 26% which equals to a TPV of 0.058 $cm^3 \cdot g^{-1}$. Taking into account that the synthesized zirconia particles possess a size distribution and assuming that they hardly reach an ideally close-packed structure, the TPV can be expected to be larger than 0.058 $cm^3 \cdot g^{-1}$. Interestingly, this is only the case for the WCS-NPs while the MWS-NPs result in a material of considerably lower porosity after calcination. As revealed by the comparative evaluation of XRD and DLS analyses on the particles (see chapter 3.3.2) the MWS-NPs exhibit an amorphous portion. The “disordered” structure of amorphous zirconia material and its rearrangement and the concomitant crystallization during calcination may facilitate sintering and coalescence of individual particles. In contrast, the WCS-NPs which are basically monocrystalline and without a considerable amorphous fraction are less prone to such strong degree of rearrangement: They can be considered as “hard spheres” similarly as discussed for the Ludox particles (see chapter 3.2.4.2) while the MWS-NPs rather represent “soft spheres”. Consequently, the sintering of the MWS-NPs includes a strong degree of coalescence of particles resulting in strongly decreased porosities compared to the packing of individual particles. In contrast, sintering of the WCS-NPs is rather comparable to the sintering process of the Ludox particles which mainly sinter at inter-particle contact areas under preservation of their individual spherical shape without coalescing completely. Nevertheless, both kinds of particles have to undergo some degree of sintering and coalescence because the Rietveld refinement of the XRD data proved a growth of the crystallites during heat treatment to sizes which are clearly larger than the particle size before calcination in both cases (see table 3-5).

In order to study the origin of mesoporosity in the NP-fibers more thoroughly the physisorption data of the fibers are compared to the physisorption analyses of dried and calcined, unspun solutions (NP-solutions) which are identical to the solutions used for electrospinning (see figure 3-23). Simultaneously, the influence of different solvents is elucidated: All investigated electrospinning solutions are based on methanol as solvent because the zirconia nanoparticles were dispersed in methanol. Otherwise, the spinning polymer PEO is not soluble in methanol, so that a second solvent was necessary to obtain a stable spinning solution. In analogy to the experiments on electrospun titania fibers three different solvents were used as co-solvent in order to dissolve PEO in the spinning solution.[75] Accordingly, three different solutions were used for the experiments, each with approximately 55 wt.-% of methanol and 39 wt.-% of the other solvent (i. e. water, chloroform or dichloromethane respectively; see table 3-4, samples 4, 6, 7 (NP-fibers) and samples 8, 10, 11 (NP-solutions)). For all these experiments the MWS-NPs were used. The results of the experiments will be compared to the former investigations on titania fibers[75] later (see chapter 3.3.5).

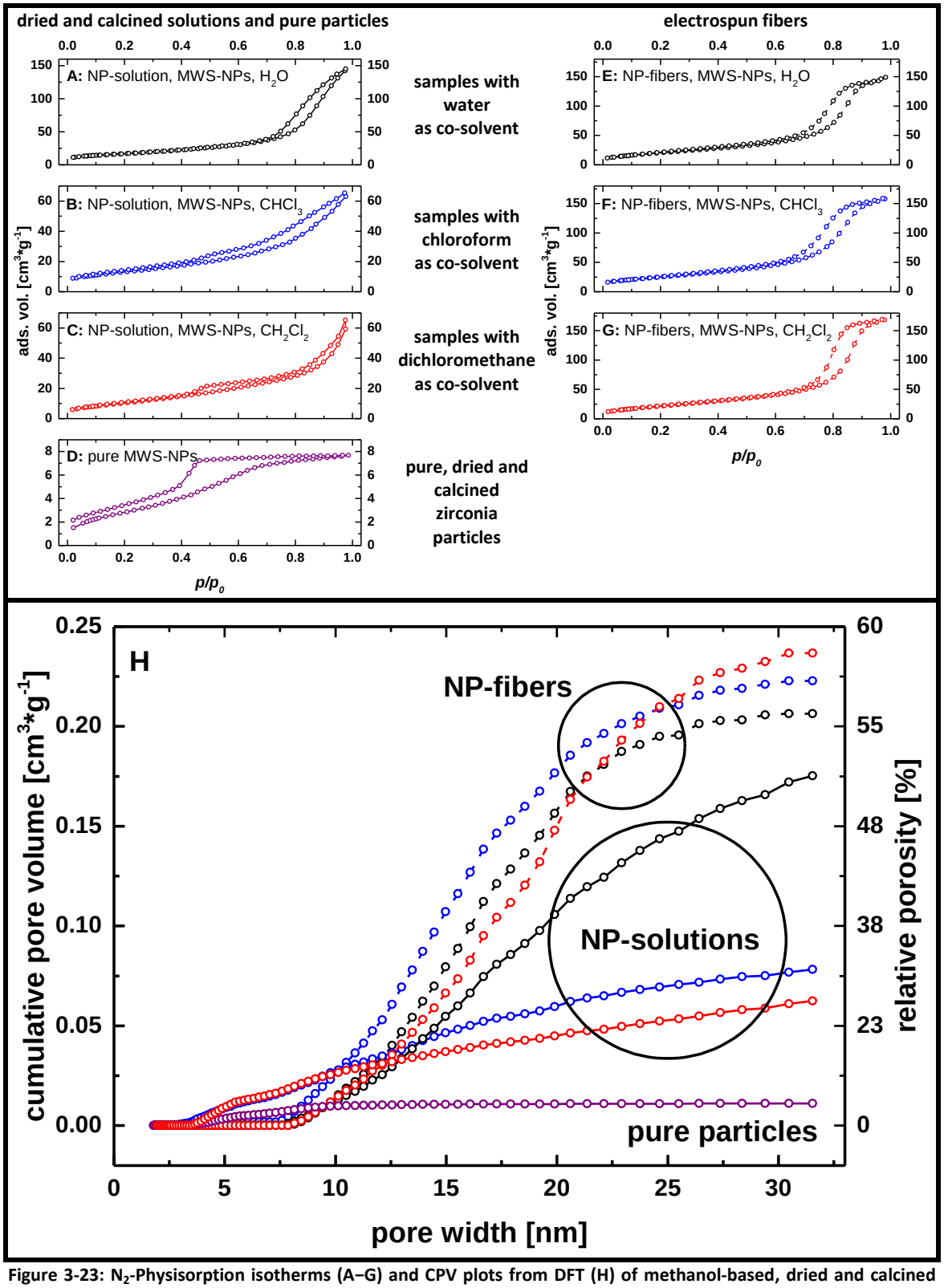

Figure 3-23: N_2-Physisorption isotherms (A–G) and CPV plots from DFT (H) of methanol-based, dried and calcined zirconia spinning solutions with MWS-NPs, of pure, dried and calcined zirconia MWS-NPs (solid lines) and electrospun fibers obtained from these solutions (dashed lines). Magnifications of the isotherms can be found in the appendices (see figure 6-29, figure 6-31–figure 6-33, figure 6-35, figure 6-36 and figure 6-38). Color coding: red: dichloromethane as co-solvent (see table 3-6, samples 6 and 10); blue: chloroform as co-solvent (see table 3-6, samples 7 and 11); black: water as co-solvent (see table 3-6, samples 4 and 8); purple: pure, dried and calcined MWS-NPs (see table 3-6, sample 13).

The specific surface areas of the different zirconia nanofibers are in the range of 77–92 $m^2 \cdot g^{-1}$ and their TVPs are between 0.23 $cm^3 \cdot g^{-1}$ and 0.26 $cm^3 \cdot g^{-1}$. In contrast, the calcined spinning solutions resulted in samples with surface areas between 40 $m^2 \cdot g^{-1}$ and 61 $m^2 \cdot g^{-1}$ and TPVs in the range of 0.10–0.23 $cm^3 \cdot g^{-1}$ (see table 3-6). Likewise electrospun silica fibers, the zirconia fibers feature surface characteristics that are within a narrow range. Similarly as the type of Ludox particle has no influence on the surface characteristics of electrospun silica fibers prepared from them, the solvent composition in the preparation of zirconia fibers from MWS-NPs also seems to be insignificant, at least concerning the three kinds of co-solvent used in the above mentioned experiments. This result seems to be contradictory to the former investigations on titania fibers: For the preparation of titania fibers from NPs, the choice of the co-solvent significantly affected the specific surface areas as well as the TPVs of the resulting fibers.[75] Further discussion of this apparent contradiction is presented below (see chapter 3.3.5).

The specific surface areas as well as the TPVs of the zirconia NP-solutions are generally lower than the corresponding values of the NP-fibers. While the values of the NP-solution containing water as co-solvent do not differ strongly from the characteristics of the NP-fibers, the other two spinning solutions containing chloroform or dichloromethane exhibit significantly lower values for both the specific surface area and the TPV. Herein, a difference of the zirconia materials compared to the previously discussed silica materials exists: In case of the different Ludox particles in the spinning solutions, all dried and calcined Ludox NP-solutions had similar characteristics as the corresponding electrospun fibers (see figure 3-13). Otherwise, the findings on zirconia materials can be comparable to the investigations on the electrospun titania fibers: Similarly as for the calcined zirconia NP-solutions, the electrospun titania NP-fibers also had different specific surface areas and TPVs dependent on the co-solvent used besides methanol.[75] These comparisons will be discussed more thoroughly in chapter 3.3.5.

Next, the influence of different particle properties on the resulting structure of electrospun NP-fibers will be investigated. As mentioned before, zirconia nanoparticle dispersions were prepared via two different methods, i. e. via a wet chemical approach with “classical” heating and via a microwave assisted route. In figure 3-22 it was shown that bulk materials obtained by drying and calcination of the pure dispersions of these two kinds of particles possess significantly different pore structures. In figure 3-24 the physisorption characteristics of bulk samples obtained from the pure particle dispersions are compared to the data of electrospun fibers consisting of these particles. The WCS-NPs and the MWS-NPs were electrospun with the same solvent composition consisting of methanol and water or dichloromethane, respectively. The concentration of the spinning polymer PEO was 2.2 wt.-% in the experiments with the WCS-NPs and thus slightly lower as in case of the MWS-NPs that were spun with the help of 2.8 wt.-% PEO. This adaption of the polymer concentration was necessary to ensure a stable spinning process for both kinds of fibers, but its influence is believed to be negligible concerning the following discussion. This assumption can be drawn from respecting the experiments on silica fibers in which the weight ratio between polymer and particles was varied (see figure 3-10). If even a multiple increase in the silica particle concentration does not alter the resulting porous structure, a slight increase in the polymer concentration can be expected not to do so either.

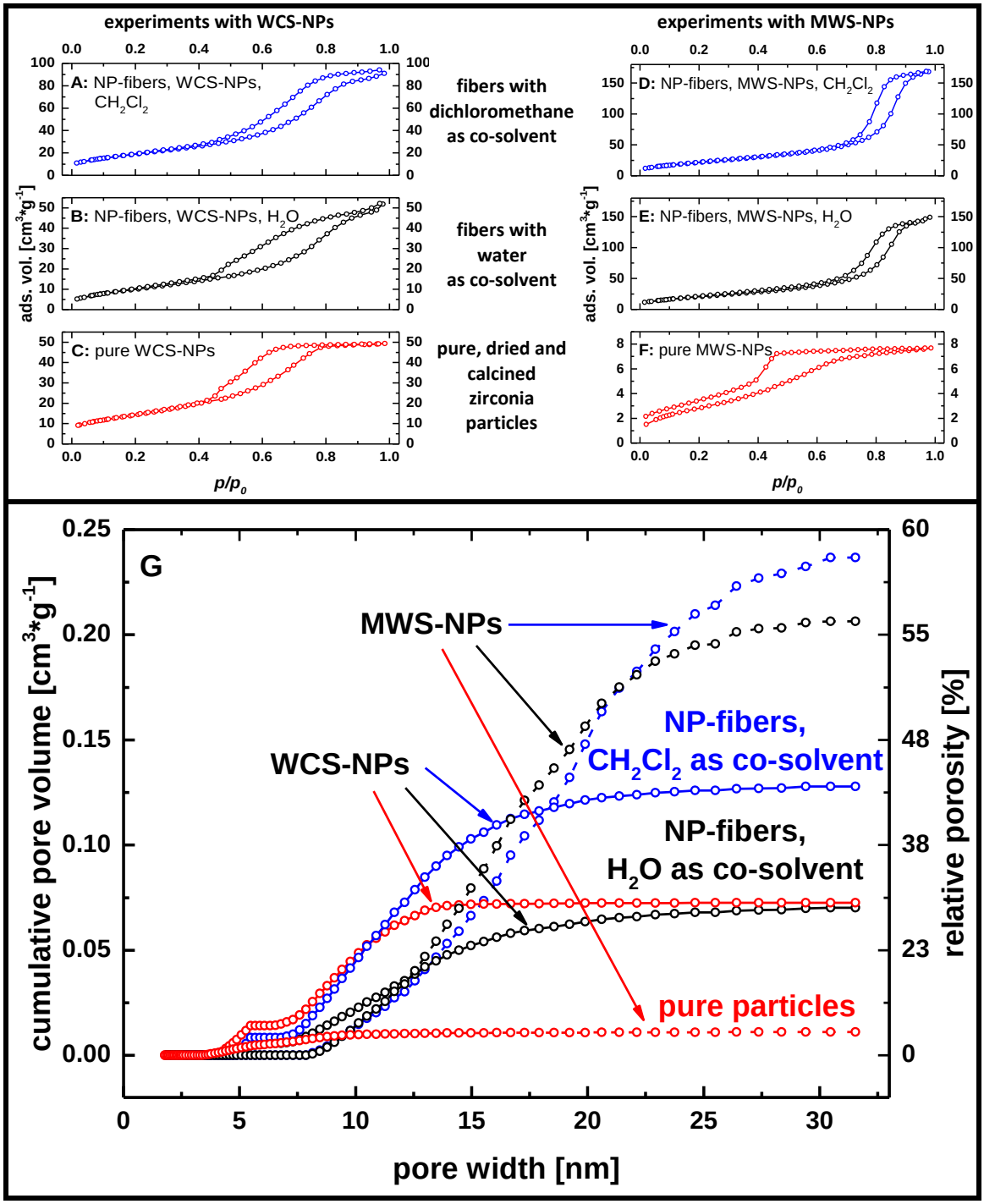

Figure 3-24: N_2-Physisorption isotherms (A–F) and CPV plots from DFT (G) of zirconia fibers obtained from differently synthesized nanoparticles and of these two kinds of zirconia nanoparticles. Solid lines: results from experiments with WCS-NPs; dashed lines: results from experiments with MWS-NPs. Magnifications of the isotherms can be found in the appendices (see figure 6-27–figure 6-29, figure 6-31, figure 6-37 and figure 6-38). Color coding: red: pure, dried and calcined NPs (see table 3-6, samples 12 and 13); blue: zirconia fibers prepared with dichloromethane as co-solvent (see table 3-6, samples 3 and 6); black: zirconia fibers prepared with water as co-solvent (see table 3-6, samples 2 and 4).

As mentioned before, the surface areas of the pure, dried and calcined particles are similar for both preparation methods, i. e. 41 $m^2 \cdot g^{-1}$ or 53 $m^2 \cdot g^{-1}$ respectively (see table 3-6, samples 12 and 13). The surface areas of the electrospun fibers prepared with the help of dichloromethane are also comparable for both preparation methods of the particles, but the values of 71 $m^2 \cdot g^{-1}$ or 83 $m^2 \cdot g^{-1}$ (see table 3-6, samples 3 and 6) are slightly higher. Only the surface areas of the fibers electrospun with the help of water differ significantly from each other when the two differently prepared kinds of particles are compared: The WCS-NPs resulted in electrospun fibers with a surface area of 39 $m^2 \cdot g^{-1}$ and the MWS-NPs resulted in fibers with a specific surface area of 78 $m^2 \cdot g^{-1}$ (see table 3-6, samples 2 and 4). As discussed before, the various specific surface areas are hint to a different degree of sintering during the calcination of the samples.

The comparison of the porosities of the samples illustrated in figure 3-24 discloses further interesting results: Since the bulk samples obtained from the two different pure NP dispersions revealed an eminently higher porosity for the sample obtained from the WCS-NPs (see figure 3-22) this was also expected for the corresponding electrospun fibers. Yet, in case of the fibers, the MWS-NPs produce the more mesoporous fibers compared to the WCS-NPs (see figure 3-24 G). Obviously, the electrospinning experiment influences the behavior of the particles to a totally different trend which has to be explained by the presence of the spinning polymer. Recapitulating the discussion of the silica experiments, it was concluded that the spinning polymer acts as a “void filling structure support” rather than as a template. Concerning the zirconia fibers this model can also explain the high porosity of the fibers obtained from the MWS-NPs: If the MWS-NPs are embedded in a polymer matrix, the amorphous portion of the particles is able to crystallize or at least “consolidate” before the polymer is combusted resulting in “hard spheres” which sinter in a similar manner as the WCS-NPs or the Ludox particles. In other words, the polymer matrix prevents the strong degree of coalescence which was observed and discussed for the bulk samples prepared without the addition of polymer. This hypothesis is backed by the results of the dried and calcined spinning solutions (see figure 3-23): The spinning solutions containing the MWS-NPs resulted in bulk materials with increased mesoporosity which is at least as high as the porosity of close-packed spheres (i. e. 26%) suggesting that the calcination process with polymer changes the sintering from a “soft sphere” towards a “hard sphere” behavior of the particles. In accordance with this argumentation it is also comprehensible that the MWS-NPs produce the more mesoporous fibers than the WCS-NPs: Since the DLS analyses proved the MWS-NPs to be generally larger than the WCS-NPs (see figure 3-16) the obtained porosities also have to be larger if both kinds of particles basically behave like “hard spheres” packing to a porous material: Sintering of particle surfaces decreases the porosity of a material slightly and to a smaller extent the larger the particles are.

The bulk sample obtained from the pure, dried and calcined WCS-NP dispersion and the fibers prepared from these particles with water as co-solvent in the spinning solution exhibit nearly identical TPVs but a slightly different trend in the CPV plots (see figure 3-24; table 3-6, samples 2 and 12). While the bulk sample only exhibits mesopores with diameters up to approximately 12 nm, the fiber sample features less small mesopores in this size range but also possesses larger mesopores. However, the porosities of both samples accumulate to the same TPV. This result is in accordance with the nanoparticle packing process illustrated for the silica materials before (see figure 3-15): In the fiber sample the nanoparticle aggregation leads to clusters with smaller fractal dimension and consequently to larger mesopores. Interestingly, the overall packing is identical for this two samples resulting in the same TPVs for both and implying a better packing of the open fractal clusters in the fibers, so that less small mesopores are obtained. The reason for such behavior is not clear but may be correlated to sintering of particles especially diminishing the amount of small pores.

The last evaluation to be conducted concerning figure 3-24 is the influence of the co-solvent on the porosity of the resulting fibers. However, this discussion is postponed to chapter 3.3.5 and will be discussed there in conjunction with other results demonstrating the influence of solvent properties.

Finally, a series of experiments with methanol-based spinning solutions and water as co-solvent was performed. In this series five samples can be compared whose physisorption data are illustrated comparatively in figure 3-25. The five samples are:

1. The NP-fibers prepared from “fresh” MWS-NPs,
2. the bulk sample derived from the dried and calcined NP-solution containing “fresh” MWS-NPs,
3. the NP-fibers prepared from “aged” MWS-NPs,
4. the bulk sample derived from the dried and calcined NP-solution containing “aged” MWS-NPs,
5. the NP-fibers prepared from WCS-NPs.

Apart from the different particles used, the composition of the five spinning solutions is comparable in all other respects (see table 3-4, samples 2, 4, 5, 8 and 9).

Figure 3-25 reveals that the different particles result in significantly different porosities of the fibers or bulk sample, respectively. Such significant differences were not found for silica fibers, neither concerning the different Ludox dispersions (see figure 3-11), nor concerning the different amount of the Ludox particles in the spinning solutions (see figure 3-10). However, the silica experiments all used dispersions with Ludox particles of similar size, while the sizes of the zirconia nanoparticles in the dispersions were proven to be significantly different (see DLS results; figure 3-16). The previously introduced model of the EICA concept implies that the particle size decisively affects the resulting structure which seems to be backed by the results depicted in figure 3-25. Nevertheless, on first sight no general correlation between the particles size and the resulting porosities can be identified from figure 3-25. If only the fiber samples are considered, the resulting total porosity of the electrospun fibers increases the larger the particle size in the dispersion gets (compare figure 3-16). In contrast, such trend cannot be observed for bulk samples derived from the dried and calcined NP-solutions. For these samples, the larger, “aged” MWS-NPs lead to a less mesoporous sample than the smaller, “fresh” MWS-NPs as far as it can be seen from the CPV plots. Yet, only interpreting the CPV plots is misleading. Also taking the TPVs of these samples into account (see table 3-6, samples 8 and 9), it is shown that actually the sample obtained from the NP-solution containing the “aged” MWS-NPs possesses the higher porosity. The large TVP only accumulates with pore sizes larger than approximately 32 nm, which cannot be evaluated by the DFT method. The CPV plots in figure 3-25 do not run into “saturation” for the samples with the “aged” MWS-NPs indicating the presence of pores with diameters larger than 32 nm in contrast to the other samples in figure 3-25. Accordingly, the samples with the “aged” MWS-NPs exhibit the highest TPVs of 0.29 $cm^3 \cdot g^{-1}$ for both samples (see table 3-6, sample 5 and 9).

At the same time, the slopes in the CPV plots of the fibers prepared from the “fresh” and “aged” MWS-NPs are more or less the same though shifted by approximately 7 nm concerning the pore width (see figure 3-25 F) indicating a shift in the sizes of the porous structure: Coincidental, the mean particle size of the “aged” MWS-NPs (15.2 nm) is approximately 11 nm larger than the mean particle size of the “fresh” MWS-NPs (4.3 nm, see figure 3-16) leading to the conclusion that the larger, “aged” particles seem to increase the pore sizes within the fibers by the same order of magnitude as the size of the particles (i. e. the building blocks of the fibers) increases. This influence of the particle size on the pore size of the resulting fibers causes the “saturation” of the CPV plot of the “aged” MWS-NPs fibers to be in a pore size range beyond the maximum analyzable value for DFT analysis (i. e. beyond approximately 32 nm). Since the TPV of these fibers is only slightly higher than its CPV (0.24 $cm^3 \cdot g^{-1}$, see table 3-6, sample 5) it is suggested that “saturation” has to occur at a pore size only slightly larger than 32 nm.

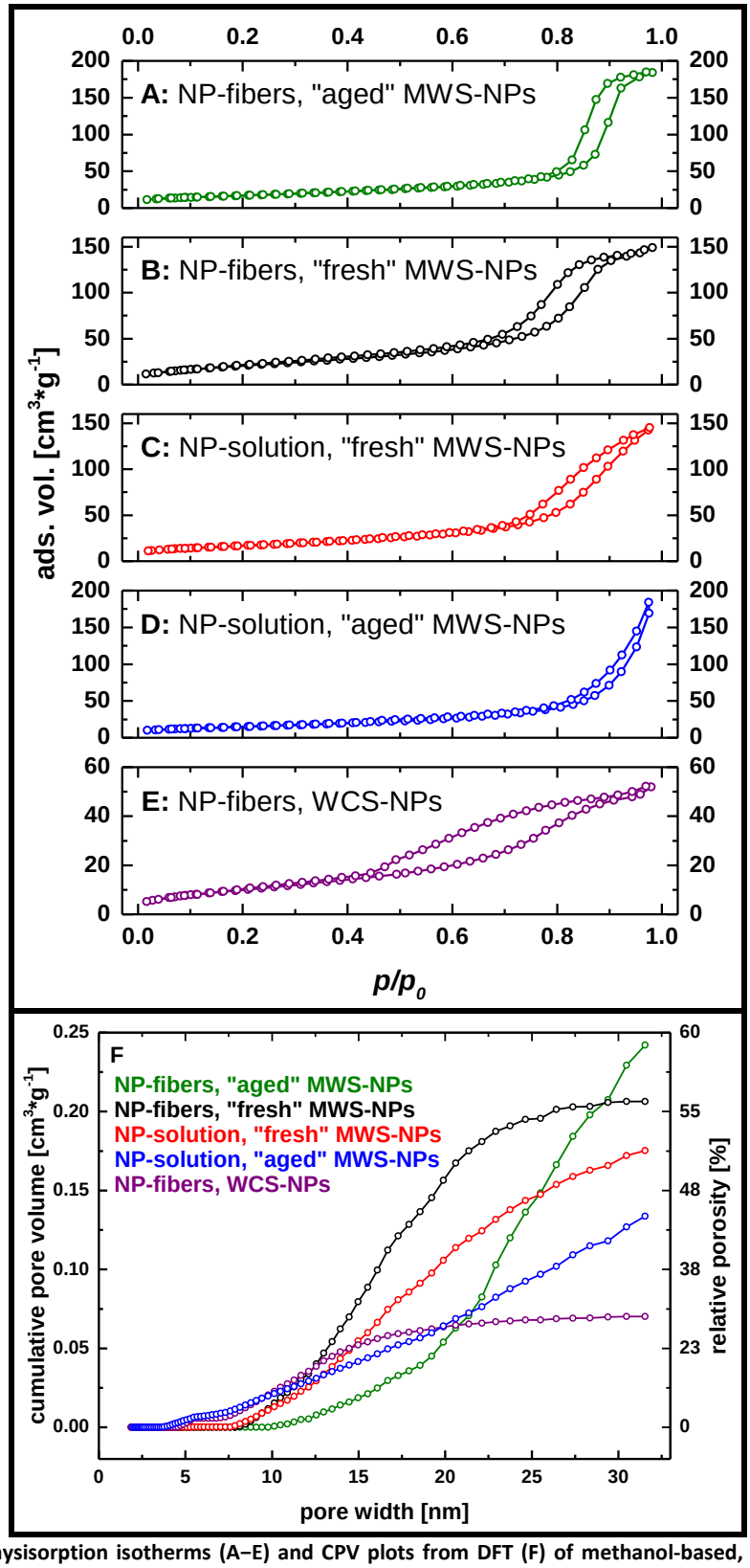

Figure 3-25: N_2-Physisorption isotherms (A–E) and CPV plots from DFT (F) of methanol-based, dried and calcined spinning solutions and electrospun fibers prepared therefrom with differently synthesized zirconia nanoparticles. Magnifications of the isotherms can be found in the appendices (see figure 6-27, figure 6-29, figure 6-30, figure 6-33 and figure 6-34). Color coding: green: fibers prepared from "aged" MWS-NPs (see table 3-6, sample 5); black: fibers prepared from "fresh" MWS-NPs (see table 3-6, sample 4); red: dried and calcined spinning solution with "fresh" MWS-NPs (see table 3-6, sample 8); blue: dried and calcined spinning solution with "aged" MWS-NPs (see table 3-6, sample 9); purple: fibers prepared from WCS-NPs (see table 3-6, sample 2).

3.3.5 Comparison of physisorption results on zirconia and titania materials: Influence of solvent and nanoparticle properties

When the result on the zirconia materials are compared to former result on titania fibers[75] (see also chapter 2.5.2), some differences between the two materials are apparent. Although the experiments on these two materials were analogously and started with comparable spinning solutions, there are some disparities in the zirconia and titania solutions that have to include the origin of the differences found among the resulting materials:

- The weight ratio between methanol and the other respective solvent was similar but not identical; in the zirconia experiments the weight ratio was approximately 1/0.7 (MeOH/second solvent) and in the titania experiments it was approximately 1/1.
- The molecular weight of the spinning polymer PEO was 1,000,000 $g \cdot mol^{-1}$ for the zirconia samples and 300,000 $g \cdot mol^{-1}$ for the titania samples.
- The syntheses of zirconia and titania nanoparticles were conducted under dissimilar conditions, so that their characteristics like dispersibility, surface structure etc. which are assigned during the syntheses might be different. However, even if all experimental conditions in the particle syntheses were kept identical, the substitution of a titania precursor like $Ti(OiPr)_4$ by the analogous zirconia precursor $Zr(OiPr)_4$ may have significant influence. Although zirconium is the higher homologue of titanium and although these elements should therefore exhibit similar chemical behavior, the different element identity may alter the nanoparticle synthesis ultimately leading to unequal particle properties affecting following structure formation processes (compare discussion in chapter 2.5.4.2).

The differences in the starting solutions seem to be nonessential resulting in a general comparability of the zirconia and titania spinning solutions. Otherwise, these slight differences may be significant enough to result in noticeably different results in the physisorption analyses.[24] The comparison of the above mentioned titania and zirconia experiments is particularly suited to elucidates the influence of the solvent composition and the properties of the employed nanoparticles on the resulting mesoporous structures. In this context, the following results need consideration:

- The titania fibers possess a lower mesoporosity if they are electrospun with water as co-solvent instead of chloroform or dichloromethane as co-solvent. If water is used as co-solvent the resulting mesoporosity is roughly the same as for the titania sample obtained from the pure, dried and calcined nanoparticle dispersion.
- If zirconia fibers are prepared under comparable conditions, the resulting fibers are all mesoporous irrespective of the choice of co-solvent in the spinning solution though the degree of mesoporosity depends on the solvent composition as well as on the kind of nanoparticles (WCS-NPs vs. MWS-NPs).

[24] The fact, that the former titania study was solely interpreted in terms of SD while the zirconia experiments in the previous chapter are mainly considered in terms of the EICA concept does not derogate this basic comparability: The results on the titania materials can also be interpreted in terms of the EICA model with basically the same arguments as it was demonstrated before for the silica or zirconia materials. Hence, it is dispensable to repeat such argumentation for the titania samples here.

- In case of the WCS-NPs, the basic trend in the porosities of the zirconia fibers is the same as for the titania fibers: With water as co-solvent, the fibers are similarly mesoporous as the pure, dried and calcined particles while the mesoporosity is increased with dichloromethane as co-solvent.
- With the zirconia MWS-NPs more mesoporous fibers are obtained than with the WCS-NPs irrespective of the co-solvent. Water as well as dichloromethane as co-solvent in combination with the MWS-NPs results in basically the same mesoporosity in the electrospun zirconia fiber.
- In contrast, the zirconia bulk samples obtained from the unspun zirconia solutions containing MWS-NPs featured a noticeably higher mesoporosity with water as co-solvent compared to the case of dichloromethane or chloroform being co-solvent. While the sample synthesized with water as co-solvent exhibits a porosity which is relatively close to the porosity of the corresponding zirconia fibers prepared with MWS-NPs, the other two bulk samples are significantly less mesoporous.
- The influence of chloroform or dichloromethane as co-solvent on the structure formation in the unspun zirconia NP-solutions and the titania NP-fibers is vice versa: Chloroform or dichloromethane as co-solvent result in highly mesoporous titania fibers while the bulk zirconia samples suffer from a decreased mesoporosity if these co-solvents were used.

Surveying all these results does not allow for drawing clear conclusions in the sense of fundamental trends correlating to either particle or solvent properties. The interdependence of influences from solvent and particle properties prevents a decided interpretation. Furthermore, it is unclear which solvent property is decisive for the generation of highly mesoporous materials from preformed, dispersed nanoparticles. In the previous discussions mainly two properties of solvents were used as arguments to explain their influence on structure formation processes: their volatility and their polarity. However, the above mentioned results prove that both properties seem to be similarly relevant for structure formation. In some cases (e. g. the electrospun titania NP-fibers) the use of the more volatile solvents dichloromethane or chloroform instead of water as co-solvent results in more mesoporous materials because the faster solvent evaporation shortens the time interval of particle arrangement. Similarly as discussed before, this may facilitate the formation of clusters with a small fractal dimension and consequently the formation of highly mesoporous materials. In other cases (e. g. the bulk zirconia materials obtained from the unspun NP-solutions containing MWS-NPs) the less volatile solvent water results in more mesoporous materials. In such case, the polarity of the solvent may exert the decisive influence: The higher polarity of water compared to chloroform or dichloromethane decreases the thickness of the EDL around the nanoparticles promoting their agglomeration. In consequence, this effect may also facilitate the formation of clusters with a small fractal dimension and thus the formation of highly mesoporous materials.

Additionally, the influence of the solvent polarity directly correlates to the influence of particle properties. Depending on the surface structure of nanoparticles and its population with functional groups their surfaces can be of different polarity affecting interactions with solvents and thus the stabilization (or destabilization) of particle dispersions. Though most nanoparticles exhibit polar surfaces, this is not always the case. For example, ceria nanoparticles investigated in chapter 3.4 were dispersible in non-polar solvents like n-hexane suggesting them to possess surfaces of low polarity. Consequently, the influence of solvent polarity may be inverted if experiments with nanoparticles of unequal surface polarity are compared. An example in this context is the high mesoporosity of zirconia materials prepared from MWS-NPs, especially the bulk sample from the unspun NP-solution with water as co-solvent (see figure 3-23) which was not expected if the results are compared to the experiments with zirconia WCS-NPs or titania nanoparticles. Possibly, the particle synthesis using microwave irradiation results in particles with a different surface polarity. Hence, more detailed analyses on the nanoparticle synthesis, the surface structure of the resulting particle and their stabilization in dispersion are strongly recommended for future projects. Such investigations were beyond the scope of this thesis though they probably will help to understand the above mentioned results in even more detail.

3.3.6 Conclusion on zirconia experiments

The experiments and results on the zirconia materials are relevant to the overall topic of this thesis in different aspects:

First, the findings are in fundamental accordance with the results on silica materials: Like for silica fibers, the fiber porosity of zirconia materials can be increased by electrospinning nanoparticles instead of sol-gel precursors. For both materials this increased porosity is not a consequence of an intrinsic porosity of the nanoparticles representing the building blocks of the fibers, but of their arrangement during the electrospinning experiments. The arrangement of nanoparticles in the different zirconia materials were interpreted and understood in terms of basic concepts of colloidal chemistry resulting in a structure formation model called EICA (evaporation-induced cluster aggregation).

However, the experiments on the zirconia materials do not only give further evidence concerning conclusions drawn from the silica experiments before, but also expand this mechanistic understanding by further results. Similarly as found for electrospinning experiments using titania nanoparticles[75] the use of different solvent mixtures for electrospinning of solutions containing self-synthesized zirconia nanoparticles resulted in differently mesoporous zirconia fibers. Although zirconium and titanium are chemically similar elements from the same group, the behavior of the particles during electrospinning in analogous solvent mixtures is quite different. The comparison of the experiments on titania and zirconia revealed how complex and sensitive the aggregation of nanoparticles during electrospinning is concerning different solvent and/or particle properties.

In this context, differently synthesized zirconia nanoparticles were used for electrospinning experiments to elucidate the influence of different particle properties on the EICA process during spinning. Unfortunately it was not possible so far to correlate the observed mesoporosity of the synthesized materials to a particular feature of the particles, though it was seen that the particle size plays a crucial role. For a more sophisticated understanding it would be necessary to characterize the particle properties in much more detail. Besides the characterization of the particle size via DLS (see figure 3-16) and their crystallinity via WAXS (see figure 3-17 and figure 3-18) it would be necessary to study the surface properties of the particles by analyzing which functional groups act as ligands on the surface of the nanoparticles and in which population density they occur. This task is accompanied by the question how exactly the different particles are stabilized, because different surface groups contribute differently to the surface potential of the particles. While the surface potential can be investigated by *Zeta*–potential measurements, functional groups and their population density can be investigated complementarily by other methods such as elemental analysis, ^{1}H-NMR, ^{13}C-NMR, IR- or Raman spectroscopy. Only if all these methods are utilized a further in-depth understanding of the aggregation process of nanoparticles in multi-component spinning solutions is achievable.

3.4 Ceria fibers

3.4.1 Introduction and sample overview

Electrospun ceria nanofibers were first reported by Yang et al. They were prepared from aqueous poly(vinyl alcohol) (PVA) solution under addition of cerium nitrate ($Ce(NO_3)_3 \cdot 6H_2O$) sol-gel precursor as ceria source in 2005.[131] Several publications dealing with ceria-based nanofibers in the following years all used sol-gel precursors as ceria source for electrospinning.[160–163] To the best of my knowledge there are no publications on electrospun ceria fibers prepared from preformed ceria nanoparticles up to now.

The preparation and investigation of electrospun ceria fibers is motivated by several reasons: Ceria is a material of technical relevance, especially in the field of heterogeneous catalysis, and a nanostructured shape may be beneficial to such applications. Technically relevant applications of ceria materials will be introduced shortly below. Furthermore, there is a general interest in the context of this thesis concerning the conceptual investigations on electrospun metal oxide fibers. Investigations on ceria fibers may further complement and/or support the results already found for electrospun fibers of silica (see chapter 3.2), titania,[1,75] or zirconia (see chapter 3.3).

Moreover, the preparation of ceria fibers were the first experiments of catalytic studies on mixed ceria/zirconia fibers in our institute.[84,85] Catalysis is often performed as heterogeneous process using a solid catalyst in a liquid or gaseous environment. Consequently, the catalytic performance strongly depends on the surface properties of the material. It is expected that porous materials with increased specific surface area and good accessibility improve the catalytic performance. Hence, the preparation of nanostructured ceria-based catalysts via electrospinning can be beneficial to their performance if the surface area and/or its accessibility are optimized by the preparation via electrospinning.

3.4.1.1 Technical relevance of ceria

Ceria is a material of significant relevance in catalytic applications.[164] Catalysts containing ceria are especially interesting for the heterogeneously catalyzed HCl oxidation (the so-called Deacon process)[85,165–167] or the hydrogen production for fuel cells from different reactants.[168] Furthermore, ceria is used in catalytic converters for the emission control of automobiles.[169] For the most catalytic applications ceria is not used as pure material, but in combination with other metal oxides. Particularly mixed oxides of ceria and zirconia have attracted considerable interest in scientific research, because the combination of these two oxides results in synergetic benefits from both materials. Ceria and zirconia are able to form solid solutions with the general formula $Ce_xZr_{1-x}O_2$ ($0 \leq x \leq 1$). In such material the catalytic activity is mainly based on the ceria portion while the zirconia portion primarily acts as stabilizing support.[85] The catalytic activity of ceria originates from its redox properties that also result in the capability of ceria to store oxygen. Cerium oxides can be reversibly oxidized and reduced between the tetravalent Ce^{4+} and the trivalent Ce^{3+} state. This redox activity of cerium is the key feature for the catalytic activity of oxides containing cerium.[164]

The Deacon process, invented in 1868,[170] is of special technical relevance because it is a process to convert chloride from HCl to Cl_2. HCl is a waste by-product in the chemical industry that accumulates worldwide to some 10 Mio. tons annually.[171] Recycling of HCl via the Deacon process is an economically and ecologically advantageous alternative to the conventional disposal of HCl via electrolysis or neutralization to salts.[172,173] Concerning the Deacon process, ceria is a promising candidate to substitute the rare and hence very expensive ruthenium oxide catalyst,[167,174] although pure ceria is not stable under the harsh reaction conditions in the Deacon process. However, it was found that ceria can be stabilized under these conditions when zirconia is used as stabilizing support and $Ce_xZr_{1-x}O_2$ solid solutions are used as catalytic material in the Deacon process.[85] Moreover, the zirconia portion in the solid solution does not only act as stabilizing support. The solid solution $Ce_xZr_{1-x}O_2$ can also be considered as a ceria material that is more or less strongly "doped" by zirconium substituting cerium atoms in the lattice of the material. Consequently, also the redox properties of ceria can be modified by such zirconium "doping".[25] In other words, a systematic variation of the cerium/zirconium content in the $Ce_xZr_{1-x}O_2$ catalyst influences both the activity and the stability of the material. Recent results revealed that the optimum composition of $Ce_xZr_{1-x}O_2$ catalysts for the Deacon process lies within the range of $0.3 \leq x \leq 0.8$.[85] In that study 20 atomic percent (20 at.-%) of zirconium were found to be sufficient to stabilize the material against corrosion and 30 at.-% of cerium are found to be sufficient to ensure a catalytic activity that is on the same level as the activity of pure ceria.

3.4.1.2 Ceria as example for conceptual investigations on the synthesis of electrospun metal oxide fibers

Cerium is one of the lanthanides and therefore chemically quite different from elements like titanium or zirconium. Against this background the investigations on electrospun ceria fibers may prove whether the general conceptual results deduced from the investigations on electrospun silica, titania or zirconia fibers are also valid for materials like lanthanide oxides. While the similar results on electrospun fibers prepared from self-synthesized titania or zirconia nanoparticles may be a consequence of the chemical similarity of these two materials, the preparation of electrospun fibers from self-synthesized ceria nanoparticles may yield in other results due to the different chemistry of ceria and its precursors. Otherwise, if the following experiments on ceria fibers also produce similar results to the experiments on titania or zirconia fibers, this will be important proof of the general validity of the former conceptual conclusions.

3.4.1.3 Detailed sample description

Ceria sol-gel fibers were produced from cerium trichloride heptahydrate ($CeCl_3 \cdot 7H_2O$) precursor electrospun with PVP as spinning polymer similarly as already published elsewhere.[153] As solvent a mixture of ethanol, methanol, dimethylformamide (DMF) and water was used (see table 3-7). The concentrations of the solids were 3.4 wt.-% PVP and 5.6 wt.-% $CeCl_3 \cdot 7H_2O$ equivalent to 2.6 wt.-% of CeO_2.

[25] It has to be mentioned that the term „doping" in this context is not limited to its classical definition as a process which only substitutes small amounts of the host structure atoms. In the above mentioned context significant portions in the range of tens of percent of the host structure atoms are substituted.

Dispersed ceria nanoparticles were kindly provided by my colleague Mrs. Maren Möller and electrospun with PEO and different solvents, namely pure $CHCl_3$ or a mixture of $CHCl_3$ and n-hexane. The concentration of the ceria NPs was set to 2.2 wt.-% in all experiments. PEO with a molecular weight of 300,000 $g \cdot mol^{1}$ was used in a concentration of approximately 2.8 wt.-% or 5.6 wt.-% (see table 3-7). The influence of the polymer concentration and the solvent composition are to be analyzed and discussed in the following. Moreover, a reference samples for physisorption analyses was prepared by drying and calcining the pure nanoparticle dispersion with n-hexane as dispersion solvent.

Table 3-7: Overview of all synthesized ceria samples and composition of the corresponding solutions that were used for the syntheses.

sample no.	sample category	polymer	CeO_2 [1)]	solvent(s)	wt.-% solvent(s)
1	sol-gel fibers	3.4 wt.-% PVP	5.6 wt.-% $CeCl_3 \cdot 7H_2O$ (≙ 2.6 wt.-% CeO_2)	EtOH/MeOH/DMF/H_2O	69.5/13.8/5.0/2.7
2	NP-fibers	2.9 wt.-% PEO	2.2 wt.-% CeO_2 (MWS-NPs)	$CHCl_3$	94.9
3	NP-fibers	2.8 wt.-% PEO	2.2 wt.-% CeO_2 (MWS-NPs)	$CHCl_3$/n-hexane	38.8/56.2
4	NP-fibers	5.6 wt.-% PEO	2.2 wt.-% CeO_2 (MWS-NPs)	$CHCl_3$/n-hexane	36.5/55.7
5	pure particles	none	MWS-NPs	n-hexane	91.8

[1)]: MWS-NPs: microwave synthesized nanoparticles.

3.4.2 Properties of the ceria nanoparticles: Brief presentation of DLS and WAXS results

Ceria nanoparticles kindly provided by my colleague Mrs. Maren Möller were dispersed in concentrations of up to 8.5 wt.-% in n-hexane or chloroform respectively. DLS analyses of a dispersion with n-hexane as solvent revealed a population weighted mean value of D_n = 10.8 nm for the hydrodynamic diameter of the ceria particles.

WAXS patterns were recorded from ceria particles dried at 80 °C as well as from particles calcined at 550 °C. The crystallographic structure of both samples was identified to be mainly cubic CeO_2 though some amorphous background in the XRD patterns cannot be excluded. All reflections of both patterns fit to the most prominent reflections of the JCPDS reference card number 00-034-0394.

Besides the identification of the crystalline phase of the samples, the crystallite sizes were calculated via Rietveld refinement.[26] The refinement revealed mean crystallite diameters of 5.8 ± 1.2 nm for the dried, uncalcined ceria NPs and 5.6 ± 0.5 nm[27] for the calcined ones confirming that the ceria crystallites did not grow during the calcination at 550 °C. The slight differences are within experimental error.

The comparison of the average crystallite size of uncalcined ceria NPs of 5.8 nm with the population weighted mean diameter of D_n = 10.8 nm from DLS analysis suggests that most of the particles consist of only one crystallite possibly possessing an amorphous shell besides its solvation shell. Only for particles with sizes beyond the mean hydrodynamic diameter it cannot be excluded that the particles consist of an agglomerate of several ceria crystallites. A more detailed characterization of the ceria dispersions and their synthesis is in progress and will be published elsewhere soon.

3.4.3 SEM analyses on ceria fibers

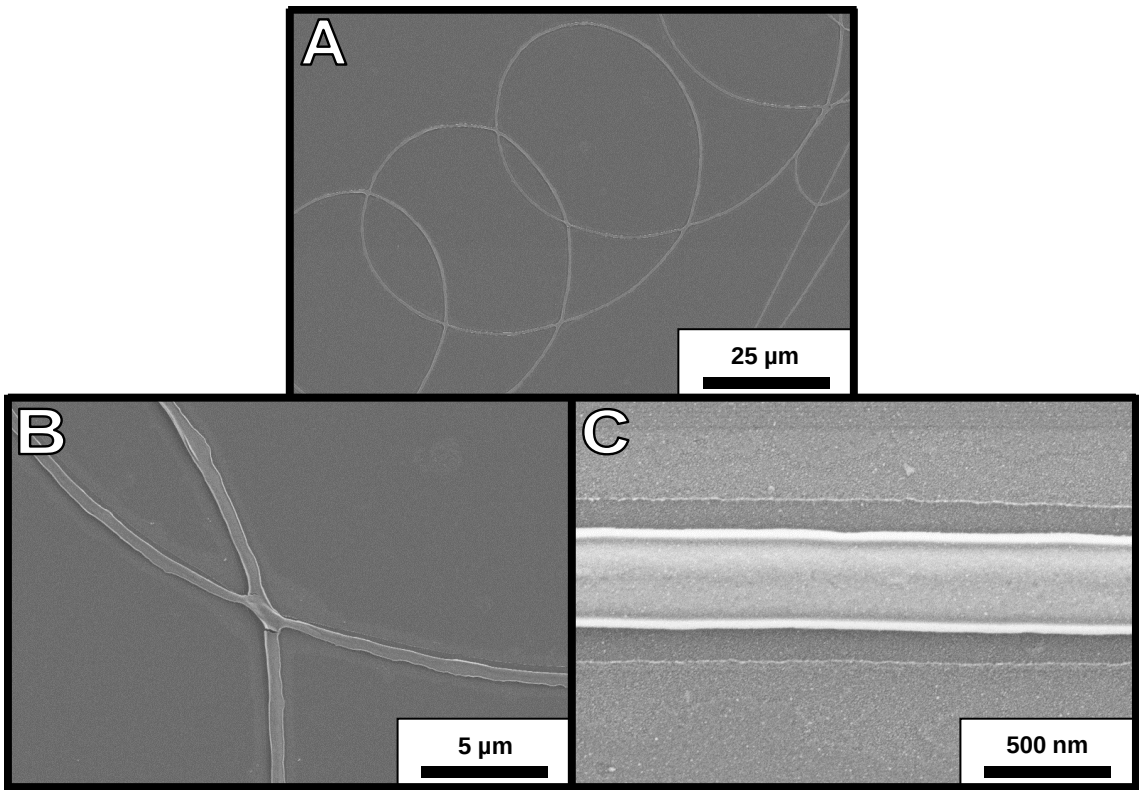

Figure 3-26: SEM pictures of ceria fibers obtained from $CeCl_3 \cdot 7H_2O$ as sol-gel precursor and electrospun with PVP after calcination at 550 °C (see table 3-7, sample 1); A–C: different magnifications.

[26] Therefore, the ICSD reference for the cubic phase of ceria (ICSD no. 621705) was used.

[27] The size of the particles was calculated from 9 reflections of the cubic phase with similar results, so that a spherical shape of the particles can be assumed. Hence, these values were averaged for each sample to give the mean crystallite diameters. The standard deviation indicates how strongly the calculated crystallite sizes from each reflection deviate from the mean value. A large standard deviation hints at a slight degree of anisotropy of the particle shape in the direction of the different lattice planes.

Figure 3-26 depicts ceria sol-gel fibers after calcination (see table 3-7, sample 1). The fibers possess a smooth surface typical for sol-gel fibers and quite homogeneous diameters of about 400 nm. Also cracks and beads are more or less absent in the ceria sol-gel fiber; they do not possess any conspicuous feature that needs special comment.

Nanoparticle-based fibers prepared from ceria nanoparticles are illustrated in figure 3-27 and figure 3-28. Homogeneous fibers spun from pure chloroform as solvent were obtained after spinning with the help of 2.9 wt.-% PEO and calcination at 550 °C (see table 3-7, sample 2, figure 3-27). The resulting fibers exhibit relative constant diameters in the range of approximately 400 nm and an optically rough surface typical for nanoparticle-based fibers. The fiber mat possesses some macroscopic cracks in the fibers and crossings between individual fibers sintered during calcination resulting in connections providing a relatively stable, three-dimensional fiber network.

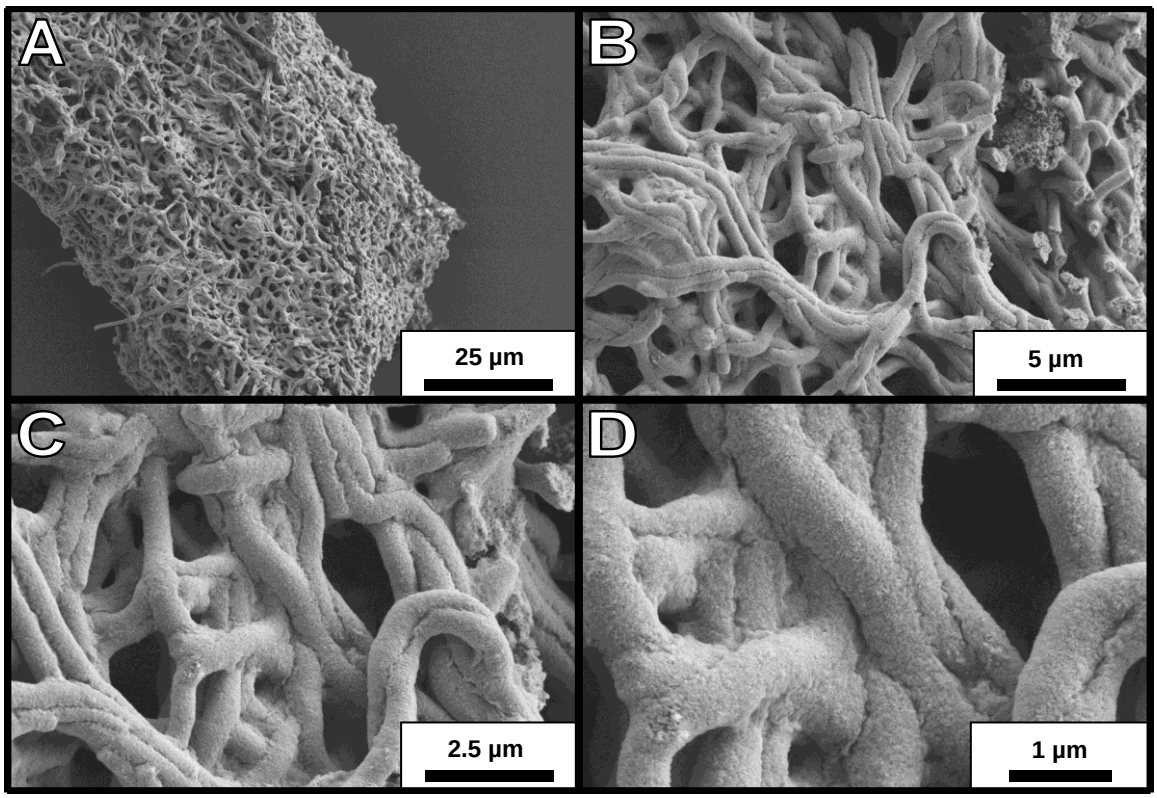

Figure 3-27: SEM pictures of ceria fibers after calcination at 550 °C obtained from ceria NPs and electrospun with PEO. The spinning solution contained 2.2 wt.-% of ceria MWS-NPs, 2.9 wt.-% PEO and $CHCl_3$ as solvent (see table 3-7, sample 2); A–D: different magnifications.

Electrospinning of a solution with the same amount of ceria NPs from a solvent mixture of chloroform and n-hexane (also with the help of 2.8 wt.-% PEO) did not result in such homogeneous fibers (see table 3-7, sample 3, figure 3-28 A, B). Only short fiber fragments with diameters in the range of 1 µm were found after calcination. Composite PEO/ceria fibers with varying diameters were formed before calcination, but the fibers lost their morphology probably due to shrinkage and the concomitant mechanical stress during calcination. If the polymer concentration is raised to 5.6 wt.-% PEO in a spinning solution with identical composition in all other respects a homogeneous fiber mat is obtained after calcination (see table 3-7, sample 4, figure 3-28 C, D) featuring a similar appearance to the fibers spun from pure $CHCl_3$ as solvent (see figure 3-27). With the help of 5.6 wt.-% PEO ceria fibers of relatively constant diameters of approximately 400 nm are formed possessing sporadic macroscopic cracks and exhibiting few larger agglomerates (see figure 3-28 C). However, the agglomerates are not very numerous, so that they can be neglected in the following discussions. The fibers do not only exhibit the typical surface roughness of NP-fibers, but figure 3-28 D also reveals some degree of mesoporosity within the fibers which is not limited to the surface of the fibers. Especially on the cross section of individual broken fibers mesopores all across the fiber diameter can be faintly seen. This mesoporosity will be investigated in detail in chapter 3.4.4 by nitrogen physisorption.

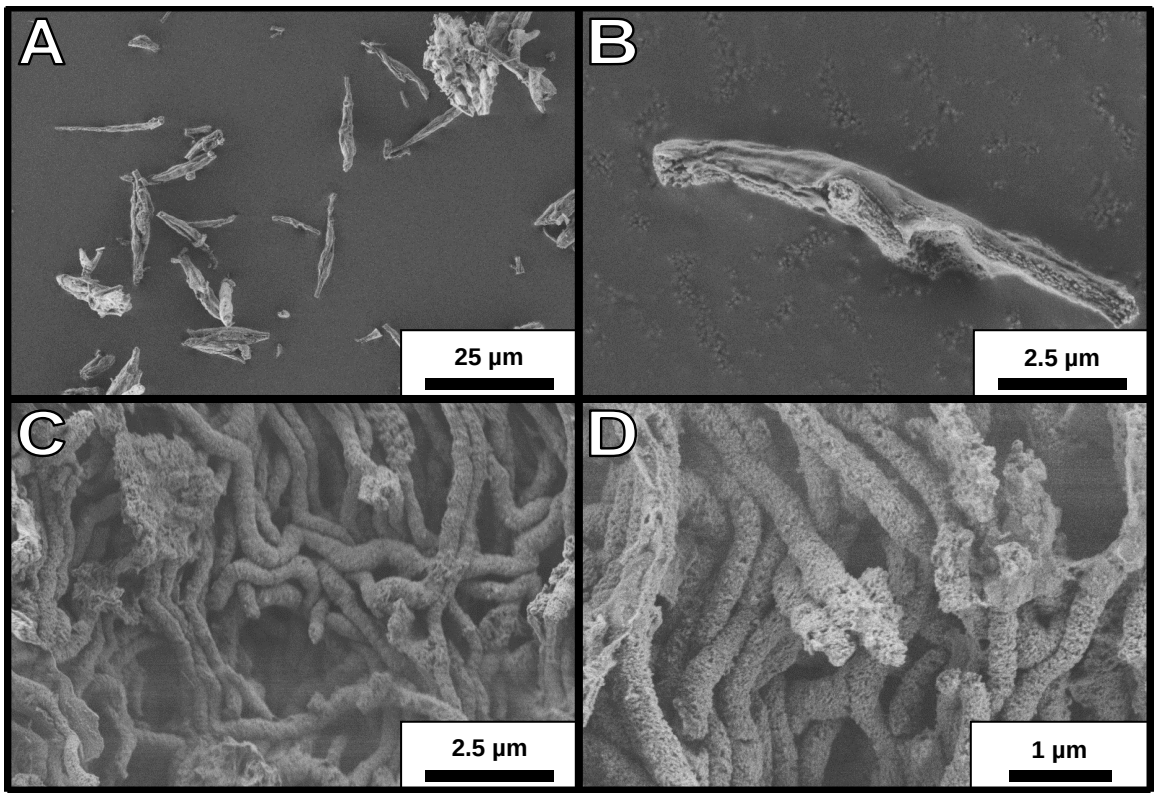

Figure 3-28: SEM pictures of ceria fibers after calcination at 550 °C obtained from ceria NPs and electrospun with PEO. Each spinning solution contained 2.2 wt.-% of ceria MWS-NPs and n-hexane and $CHCl_3$ as solvents (see table 3-7); A, B: fibers spun with 2.8 wt.-% PEO (see table 3-7, sample 3); C, D: fibers spun with 5.6 wt.-% PEO (see table 3-7, sample 4).

Interestingly, electrospinning of the ceria nanoparticle dispersion required twice the concentration of PEO, when the solvent is changed from pure $CHCl_3$ to the mixed $CHCl_3$/n-hexane solution. Obviously, the nonpolar solvent n-hexane changes the properties of the electrospinning solution drastically, so that the polymer concentration has to be increased substantially to achieve similar spinning results. This finding demonstrates the strong impact of solvent properties (e. g. electric conductivity, dipole moment, dielectric constant, etc.) on the electrospinning process.

3.4.4 Physisorption: comparative analyses on ceria fibers

In this chapter, physisorption results on all ceria samples introduced before (see table 3-7) will be discussed. The results will be directly correlated to the former results on silica (see chapter 3.2.4), zirconia (see chapter 3.3.4) or titania fibers[75] and discussed with respect to the principle concept concerning the electrospinning of inorganic fibers deduced from the experiments on these materials so far. The experiments on ceria fibers were not numerous enough to deduce distinctive conclusions only from these experiments. Hence, the focus in the following discussion will lie on the question, whether the results on the ceria samples are in accordance with the results on the other materials and the fundamental evaporation-induced cluster aggregation (EICA) process generating mesoporosity during electrospinning syntheses.

Ceria sol-gel fibers spun with 3.4 wt.-% PVP feature a surface area of 35 $m^2 \cdot g^{-1}$ and a TPV of 0.18 $cm^3 \cdot g^{-1}$ (see table 3-8, sample 1). The pure, dried and calcined ceria nanoparticles exhibit a similar surface area of 32 $m^2 \cdot g^{-1}$ but a much lower TPV of 0.02 $cm^3 \cdot g^{-1}$ (see table 3-8, sample 5). Compared to the zirconia sol-gel fibers and the pure, dried and calcined zirconia MWS-NPs the results on the corresponding ceria materials are analogous: The pure, dried and calcined particles synthesized in a microwave reactor for both materials possess similar specific surface areas to the sol-gel fibers of the same material, but a significantly lower overall porosity. The syntheses in a microwave reactor seems to produce particles which result in dense materials exhibiting nearly no mesoporosity after their calcination and the concomitant sintering at 550 °C. Estimating an expected value for the specific surface area of ceria materials consisting of dense, non-porous spherical particles by applying equation (3-1) results in a value of 139 $m^2 \cdot g^{-1}$ if a particles radius of 3 nm and a density of ρ_{CeO_2} = 7.2 $g \cdot cm^{-3}$ are used. A radius of 3 nm is reasonable due to the results of the Rietveld refinement on the XRD data of the calcined materials (see chapter 3.4.2). Since the measured specific surface areas are considerably lower than this theoretical value, it can be concluded that sintering plays a crucial role during the calcination of the ceria particles resulting in a decrease of the accessible surface area.

Table 3-8: Physisorption results on electrospun ceria nanofibers: BET[1)], CPV[2)], TPV[3)] and relative porosity[4)] values.

sample no.	sample category	weight ratio CeO_2/polymer	CeO_2 source	solvent(s)	BET[1)] [$m^2 \cdot g^{-1}$]	CPV[2)] [$cm^3 \cdot g^{-1}$]	TPV[3)] [$cm^3 \cdot g^{-1}$]	relative porosity[4)] [%]
1	fibers	0.75/1	sol-gel CeO_2 from $CeCl_3 \cdot 7H_2O$	EtOH/MeOH/DMF/H_2O	35.3	0.073	0.184	56.9
2	fibers	0.78/1	MWS-NPs	$CHCl_3$	120.1	0.243	0.289	67.5
3	fibers	0.82/1	MWS-NPs	$CHCl_3$/n-hexane	125.7	0.148	0.345	71.3
4	fibers	0.40/1	MWS-NPs	$CHCl_3$/n-hexane	148.7	0.140	0.207	59.9
5	pure particles	---	MWS-NPs	n-hexane	32.4	0.022	0.024	14.9

[1)]: specific surface area calculated by the BET method;
[2)]: cumulative pore volume calculated by the DFT method; this is the pore volume of the last data point in the CPV plot;
[3)]: total pore volume calculated by using the Gurvich rule (see equation (2-11));
[4)]: calculated from the TPV values (for explanation of the data reduction see chapter 2.6.3.1).

If these ceria MWS-NPs are electrospun to fibers, totally different surface characteristics are obtained: First, the ceria NP-fibers possess much larger specific surface areas in the range of 120−149 $m^2 \cdot g^{-1}$ (see table 3-8, samples 2-4). Such increase of the specific surface areas of the fibers compared to the pure particles is much larger than it was observed for other materials like silica (see table 3-2) or zirconia (see table 3-6). The DFT plots uncover that the ceria NP-fibers possess a significant amount of pores with a width below approximately 5 nm (see figure 3-29 F). Neither silica NP-fibers (see figure 3-9 E) nor zirconia NP-fibers (see figure 3-22 E) possess similar porosity in this pore size range. The resulting specific surface areas coincides quite well with the expected value of a ceria material consisting of non-porous, packed nanoparticles (r = 3 nm, see above). This result suggests that sintering and coalescence of nanoparticles takes place only to a minor extent during the calcination of the electrospun ceria fibers which is in accordance with the EICA concept: As discussed before for silica materials the polymer matrix in the composite as-spun fibers acts as void filling structure support preventing the coalescence of the nanoparticles which occurs if no polymer is present (see above and chapter 3.2.4.2). Since the ceria particles do not grow under the thermal treatment at 550 °C (see chapter 3.4.2), the condensation of ceria particles during calcination obviously only takes place punctually at contact points between adjacent particles resulting in highly mesoporous materials including also very small inter-particle voids.

Moreover, the spinning polymer PEO may interact differently with the ceria particles than with the silica or zirconia particles. It is known that ionic liquids like 1-Hexadecyl-3-methylimidazolium chloride (C_{16}MImCl) can act as template for small pores in the size range of micro- and small mesopores.[26] Similarly, polymer chains can also act as a template for such small pores.[147–149] Thus, the PEO chains from the spinning polymer may support the formation of small pores in between the ceria particles. Especially the ceria NP-fibers spun with 5.6 wt.-% PEO exhibit a slight degree of microporosity, which cannot be observed for other NP-fibers (see figure 3-29 C and F). In contrast to the EICA process, this “micropore-templating” seems to depend on the ratio between polymer and particles, so that a larger polymer amount generates an increased microporosity (compare sample 3 and 4 in table 3-7 and table 3-8; see figure 3-29 B, C and F). The assumption that the ceria particles may interact differently with PEO than nanoparticles of other materials is reasonable, because the ceria nanoparticles can only be dispersed in solvents of low polarity while nanoparticles of the most other material are only dispersible in more polar solvents. In order to gain more knowledge on the surface structure of the particles and their interactions with other substances, more detailed analyses of the ceria NP dispersions are projected. These ongoing investigations are planned to include e. g. *Zeta*–potential measurements, elemental analysis, ^{1}H-NMR, ^{13}C-NMR, IR- or Raman spectroscopy but were not finished within the course of this thesis.

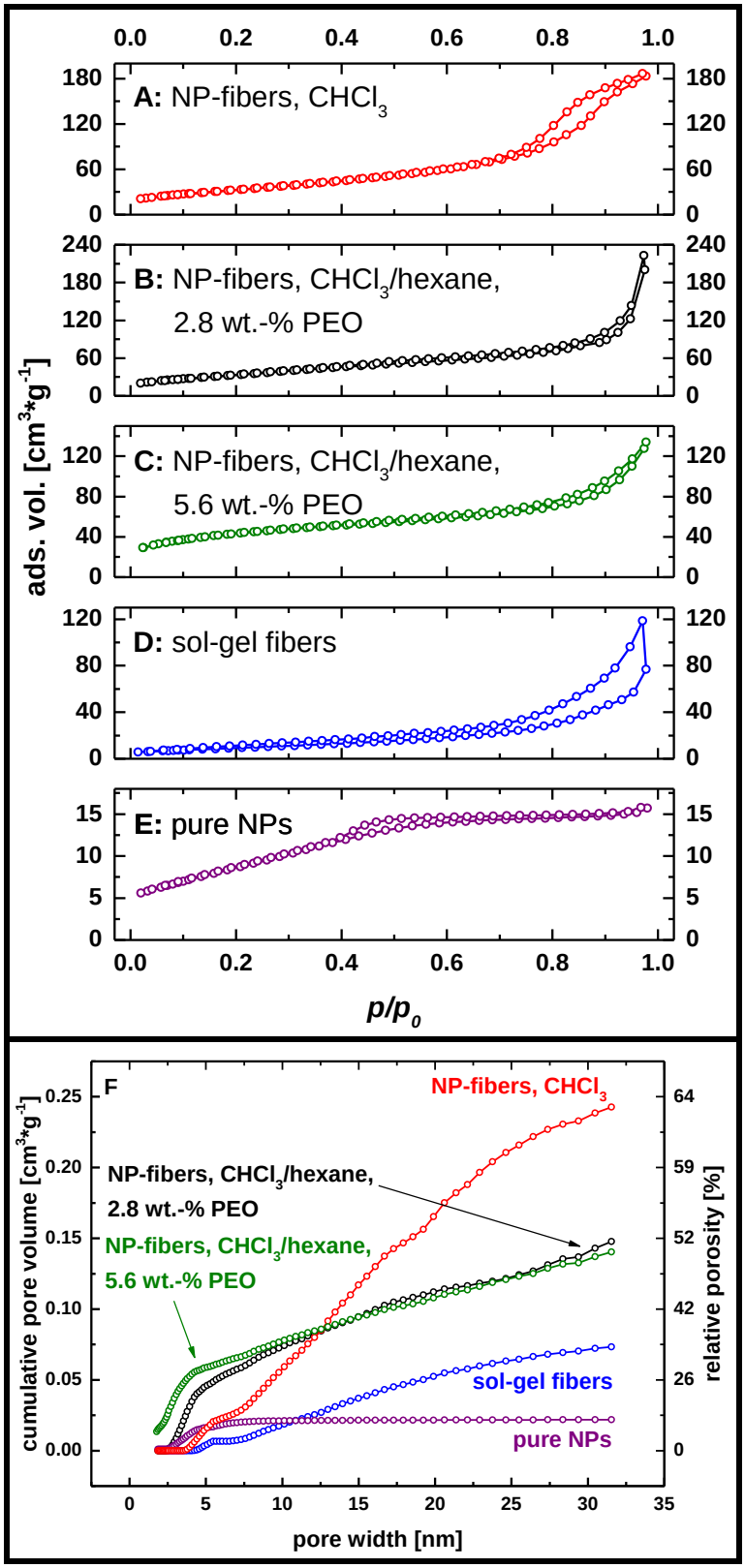

Figure 3-29: N_2-Physisorption isotherms (A–E) and CPV plots from DFT (F) of different ceria fibers and of pure ceria NPs. Magnifications of the isotherms can be found in the appendices (see figure 6-39–figure 6-43). Color coding: red: fibers prepared from ceria NPs spun from pure $CHCl_3$ as solvent with 2.9 wt.-% PEO (see table 3-8, sample 2); black: fibers prepared from ceria NPs spun from mixed $CHCl_3$/n-hexane as solvent with 2.8 wt.-% PEO (see table 3-8, sample 3); green: fibers prepared from ceria NPs spun from mixed $CHCl_3$/n-hexane as solvent with 5.6 wt.-% PEO (see table 3-8, sample 4); blue: sol-gel fibers spun with 3.4 wt.-% PVP (see table 3-8, sample 1); purple: pure, dried and calcined ceria NPs (see table 3-8, sample 5).

However, concerning larger mesopores with diameters beyond approximately 10 nm the ceria fibers exhibit similar properties to other materials: All three ceria NP-fiber samples exhibit large TPVs in the range of 0.20−0.31 $cm^3 \cdot g^{-1}$. These values are significantly increased compared to the TPVs of the pure, dried and calcined particles or the ceria sol-gel fibers. Examining the relative porosity, it is obvious that also the ceria NP-fibers feature porosities in the same range as NP-fibers of other materials proving the porosities to originate from an analogous EICA process (for a more detailed discussion see chapter 3.6). The CPV plots in figure 3-29 F reveal that the EICA process produces the most mesoporous ceria material, if the particles are spun with pure $CHCl_3$ as solvent generating noticeable numerous pores with diameters beyond 15 nm. If the solvent of the spinning solution is substituted by a mixture of $CHCl_3$ and n-hexane with the same amount of polymer, the porosity in this range is reduced probably due to altered solvent-particle interactions during electrospinning (see figure 3-29 B and F). Doubling the polymer concentration to 5.6 wt.-% PEO in the spinning solution with $CHCl_3$ and n-hexane as solvents (see figure 3-29 C and F) the mesoporosity is essentially the same as for the corresponding sample with only 2.8 wt.-% PEO. The only difference is the already above discussed, slightly changed microporosity. Similarly as demonstrated in case of the silica fibers also the ceria experiments prove that the polymer to particle ratio in the spinning solution does not significantly affect the mesoporosity of the resulting fibers (see figure 3-10 and figure 3-15).

Reconsidering the SEM investigations from chapter 3.4.3, it is found, that the physisorption analyses yielded results which were not all expected from the SEM pictures. The physisorption analyses evidenced the highest porosity for the fibers spun from pure $CHCl_3$ as solvent (see table 3-8, sample 2), but the SEM pictures of this sample (see figure 3-27) seem to illustrate fibers with a lower porosity than the fibers in figure 3-28 D (samples spun with 5.6 wt.-% PEO from $CHCl_3$ and n-hexane as solvents). However, the fibers shown in figure 3-28 D indeed exhibit a lower porosity as proven by the physisorption analyses (see table 3-8, sample 4). Thus, it is misleading to evaluate SEM pictures concerning mesoporosity. Though the visibly observable pores surely contribute to the overall porosity, they do not necessarily dominate the mesoporosity. Probably the pores observed by SEM are already too large to be analyzed by nitrogen physisorption and thus cannot be seen in the CPV plot. This assumption is corroborated by the TPV values of the ceria NP-fibers that are significantly larger than the CPV values (see table 3-8) so that pores beyond diameters of 32 nm have to be present in these samples.

3.4.5 Conclusion on ceria experiments

The results on the ceria materials evidence that ceria dispersions can be used to prepare electrospun NP-fibers exhibiting similar porosity characteristics like the previously analyzed silica, zirconia or titania NP-fibers. Hence, also the electrospinning experiments conducted with ceria nanoparticles can be incorporated into the principal concept concerning the formation of mesoporosity in electrospun inorganic fibers from preformed nanoparticles. The conclusions drawn from the experiments on silica (see chapter 3.2.5) or zirconia (see chapter 3.3.6) materials are basically also valid for the ceria fibers, although ceria and its precursors feature a totally different chemistry compared to e. g. zirconia and its precursors. This is important proof of the general validity of the fundamental conceptual conclusions of this thesis.

3.5 Tin oxide fibers

3.5.1 Introduction and sample overview

Stable tin compounds are known for the oxidation states Sn(+II) and Sn(+IV) leading to the existence of different tin oxides. Besides SnO and SnO_2 also tin oxides with both oxidation states like Sn_3O_4 are known. From all these oxides SnO_2 is the thermodynamically most stable and also technically most important one.[128] Thus, the following introduction focusses on this oxide.

Electrospun tin oxide nanofibers were first reported by Wang et al. in 2004.[132] They were prepared from Sn(+IV) sol-gel precursor as tin oxide source dissolved in chloroform and spun with poly(ethylene oxide) (PEO). Already shortly before electrospun antimony doped tin oxide fibers were prepared by combining Sn(+IV) and Sb(+III) sol-gel precursors in a solution of isopropanol with PVP as spinning polymer.[175]

Several publications dealing with tin oxide-based nanofibers mainly used sol-gel precursors as tin oxide source for electrospinning in the following years. One major scope of these publications was the characterization of tin oxide fibers with respect to their application for gas sensing devices.[176–181] For such applications, also other materials were incorporated into tin oxide based materials, for example palladium,[176] carbon nanotubes,[177] copper[179] or potassium chloride.[181] Besides the application in sensing tin oxide is one component of almost any transparent conducting oxide (TCO): Tin oxide is the major component in antimony doped tin oxide (ATO; typically up to 7 at.-% antimony as dopant) or fluorine doped tin oxide (FTO; typically below 5 at.-% fluorine as dopant) and the minor component in indium tin oxide (ITO; typically up to 10 at.-% tin oxide as dopant).[89,182,183] Accordingly, electrospun fibers of such TCO materials are also of considerable scientific interest.[178,184–186] In this context, ITO or ATO fibers are often prepared from nanoparticles instead of the corresponding sol-gel precursors, because ITO and ATO particle dispersions with well controlled and analyzed stoichiometry are commercially available, so that they easily can be used for electrospinning experiments. In contrast, there are no publications on electrospun fibers of pure tin oxide prepared from preformed tin oxide nanoparticles up to now.

Motivation for preparing and investigating electrospun tin oxide fibers emerge directly from this state of the literature: First, tin oxide is a semiconducting material of technical relevance, especially in the field of sensor technology or TCO materials. A nanostructured shape in form of electrospun fibers is probably beneficial to certain applications which will be introduced below. Secondly, there is a general interest in the context of this thesis concerning the conceptual investigations on electrospun metal oxide fibers. Investigations on tin oxide fibers may further complement and/or support the results already found for electrospun fibers of other materials (see chapter 3.2−3.4). In this context the investigations on tin oxide are of special importance, because the experiments on tin oxide elucidate some aspects not investigated so far (see chapter 3.5.1.2).

3.5.1.1 Technical relevance of tin oxide

Tin oxide is a material of considerable relevance concerning several applications. A basic and traditional application is the use of tin(+IV) oxide for glazings or vitreous enamels.[128] Nowadays, scientifically more relevant applications of tin oxide are found in the fields of TCOs or sensor technology, especially for gas sensing.[78]

The economic relevance of TCO materials received a tremendous growth since touch panels, flat screens and smartphones are widely used and seem to have become indispensable for our everyday life. ITO exhibits such outstanding properties concerning transparency and conductivity among TCO materials that this material is omnipresent in the above mentioned devices. Due to the rareness of indium and its exploding prices as a consequence of the huge demand for the above mentioned devices,[187] there is a need to substitute ITO by other TCOs, for example FTO or ATO, in which tin oxide is the major component.

In the field of gas sensing tin oxide is a thoroughly investigated material applied for sensing of various gases.[78] Generally, gas sensing devices exploit the influence of adsorbed gas species on the surface of tin oxide onto the semiconducting properties of the material: The conductivity of tin oxide changes with kind and amount of adsorbed gas molecules. Consequently, nanostructured tin oxides with easily accessible, large specific surface areas are of considerable interest due to this basic working principle: With increasing specific surface area of the active material an increased sensitivity of the sensor is expected. Thus, the general analysis of the surface structure of electrospun tin oxide within this thesis can be considered as a first step to future projects investigating tin oxide fibers with respect to gas sensing applications.

3.5.1.2 Tin oxide as example for conceptual investigations on the synthesis of electrospun metal oxide fibers

The investigations on electrospun tin oxide fibers are relevant in the overall context of this thesis because tin oxide is a representative for main group oxides proving whether the general conceptual conclusions deduced from the investigations on other materials (see chapters 3.2−3.4) are also valid for main group oxides. Although silica is also a main group oxide, the investigations on tin oxide are important, because tin oxide is a typical metal oxide in contrast to silica. Additionally, two other aspects are of even greater importance for this thesis:

The first aspect is the preparation of inorganic electrospun fibers by the “brick and mortar” (B+M) concept originally introduced for the preparation of thin-films via dip-coating.[2] It will be shown that the B+M-concept can be transferred to the preparation of inorganic electrospun fibers with tin oxide representing an exemplary material. Consequently, the following analyses will compare sol-gel and NP-fibers with B+M-fibers of tin oxide in order to elucidate differences and similarities of these different preparative concepts.

Furthermore, the experiments on electrospun tin oxide fibers were the only ones for which it was possible to prepare sol-gel as well as NP-fibers with the help of the same spinning polymer. While for all other materials the sol-gel-based fibers were spun with PVP and the NP-fibers with PEO, tin oxide fibers were electrospun from either sol-gel precursors or nanoparticles with the help of poly(methyl methacrylate) (PMMA). Additionally, tin oxide sol-gel fibers have also been prepared with PVP as spinning polymer in order to investigate the influence of PVP as spinning

polymer. Hence, the experiments on tin oxide provide results that enable a direct comparability of sol-gel-derived fibers and NP-fibers from a very fundamental point of view. If the two spinning polymers applied for the preparation of tin oxide sol-gel fibers (i.e. PVP and PMMA) do not considerably influence their mesoporosity and the NP-fibers spun from PMMA exhibit a significantly different mesoporosity, this would be a very fundamental prove of the fundamental concepts concerning the formation of mesoporosity in electrospun fibers established within this thesis so far.

3.5.1.3 Preliminary investigations: the "calcination dilemma"

Numerous unsuccessful electrospinning experiments were conducted before tin oxide NP-fibers were obtained. The first experiments on tin oxide NP-fibers employed PEO as spinning polymer similarly as in the investigations on other oxides.[188] Unfortunately, all tin oxide NP-fibers spun with PEO lost their fibrous shape upon calcination, although well-defined electrospun fibers with homogeneous diameters were obtained for the composite PEO/nanoparticle fibers. Obviously, the fibers disintegrated during calcination due to insufficient sintering, so that the preformed tin oxide nanoparticles are not interconnected to each other after calcination. Thus, "gluing" of the nanoparticles was expected to solve this problem suggesting the B+M-concept to be an adequate way to overcome this dilemma. In the B+M-concept, sol-gel precursors are added as "molecular glue" to a dispersion of nanoparticles which are considered as "bricks".[2] However, even after addition of different amounts of $SnCl_2 \cdot 2H_2O$ to the nanoparticle containing spinning solution the problem persisted: The composite PEO/tin oxide fibers lost their well-defined fibrous shape upon calcination. Also the sol-gel precursor was not able to prevent the disintegration during heat treatment indicating an insufficient reactivity of both the sol-gel precursor and the tin oxide nanoparticles to preserve a fibrous shape after calcination.

This phenomenon indicates an important requirement for the synthesis of electrospun inorganic fibers from preformed nanoparticles: The nanoparticles need to be interconnected to each other before the spinning polymer is removed by heat treatment; otherwise the fibrous shape apparently cannot be preserved. In other words, condensation of the nanoparticles has to take place before the spinning polymer is decomposed during calcination. Accordingly, not the maximum temperature of the heat treatment is decisive for the condensation of the particles in the as-spun composite fibers but the properties of the spinning polymer. Before polymers are decomposed to gaseous compounds they melt with rising temperature. Consequently, condensation of nanoparticles has to start before the melting temperature T_m of the spinning polymer is reached. Likewise, also the glass transition temperature T_g has to be taken into account because polymers soften beyond T_g facilitating the loss of the fibrous shape to start below the melting point already.[28] Using PEO which exhibits quite low T_g and T_m values (see table 3-9) for the synthesis of tin oxide fibers obviously suffers from insufficient condensation of tin oxide nanoparticles before softening and/or melting of the polymer occurs. Such a "calcination dilemma" probably also occurred in case of zirconia fiber syntheses for which loss of the fibrous shape was also observed in individual cases after calcination (see chapter 3.3.3).

[28] Note, that the glass transition temperature T_g of polymers is always lower than their melting temperature T_m.

Table 3-9: Comparison of some properties of PMMA and PEO: T_g and T_m values.

polymer	M_w [g·mol^{-1}]	T_g [°C]	T_m [°C]
PEO	300,000	−67	65
PMMA	350,000	105	>150

Data from several sources[107,189–191]

To circumvent this problem the spinning polymer was changed to another one with higher T_g and T_m. PMMA with a melting point higher than 150 °C (see table 3-9) is a promising candidate to overcome the above discussed challenge also exhibiting a good solubility in common solvents. Consequently, all following spinning experiments with tin oxide nanoparticles were conducted using this polymer finally producing fibers of well-preserved fibrous shape even after calcination (see chapter 3.5.3). Further details are presented below.

3.5.1.4 Detailed sample description

Two samples of tin oxide sol-gel fibers were produced from tin dichloride dihydrate ($SnCl_2 \cdot 2H_2O$) precursor electrospun with different spinning polymers. The first sample was electrospun with PVP as spinning polymer similarly as already published elsewhere.[176] As solvent a mixture of ethanol and dimethylformamide (DMF) was used (see table 3-10). The concentrations of the dissolved solids were 4.8 wt.-% PVP and 3.6 wt.-% $SnCl_2 \cdot 2H_2O$ equivalent to 2.4 wt.-% of SnO_2. The second sol-gel-derived tin oxide fibers were electrospun using 5.4 wt.-% PMMA in a solvent mixture of DMF and tetrahydrofuran (THF). The concentration of the precursor was 4.4 wt.-% $SnCl_2 \cdot 2H_2O$ being equivalent to 2.9 wt.-% of SnO_2 in this case, so that in both sol-gel spinning solutions approximately the same ratio of polymer to SnO_2 was present (approximately 2/1).

Table 3-10: Overview of all synthesized tin oxide samples and composition of the corresponding solutions that were used for the syntheses.

sample no.	sample category	polymer	SnO_2 [1)]	solvent(s)	wt.-% solvent(s)
1	sol-gel fibers	4.8 wt.-% PVP	3.6 wt.-% $SnCl_2 \cdot 2H_2O$ (≙ 2.4 wt.-% SnO_2)	EtOH/DMF	59.4/32.1
2	sol-gel fibers	5.4 wt.-% PMMA (350K)	4.4 wt.-% $SnCl_2 \cdot 2H_2O$) (≙ 2.9 wt.-% SnO_2)	DMF/THF	47.1/43.1
3	NP-fibers	7.0 wt.-% PMMA (350K)	3.7 wt.-% SnO_2 (WCS-NPs)	THF	89.3
4	NP-fibers	9.8 wt.-% PMMA (996K)	3.5 wt.-% SnO_2 (WCS-NPs)	THF	86.7
5	B+M-fibers	6.4 wt.-% PMMA (350K)	2.4 wt.-% $SnCl_2 \cdot 2H_2O$ (≙ 1.6 wt.-% SnO_2) + 1.6 wt.-% SnO_2 (WCS-NPs)	THF/DMF/EtOH	58.6/18.2/12.8
6	pure particles	none	WCS-NPs	THF	94.3

1): WCS-NPs: wet chemically synthesized nanoparticles.

Self-synthesized nanoparticles were electrospun with PMMA as spinning polymer and THF as solvent. With concentrations of 7.0 wt.-% PMMA and 3.7 wt.-% SnO_2 NPs the ratio of polymer to SnO_2 was also set to approximately 2/1 in order to achieve a direct comparability to the SnO_2 sol-gel fibers. Additionally, SnO_2 NP-fibers were obtained from a THF solution containing 3.5 wt.-% SnO_2 nanoparticles and 9.8 wt.-% PMMA with a higher molecular weight of 996.000 $g \cdot mol^{-1}$ in order to investigate the influence of the polymer concentration in the spinning solution. In all other cases PMMA with a molecular weight of 350.000 $g \cdot mol^{-1}$ was used.

SnO_2 B+M-fibers were prepared from the following solution: 6.4 wt.-% PMMA were used as spinning polymer in a solvent mixture of THF, DMF and ethanol. The solvent mixture resulted from the combination of a sol-gel solution of $SnCl_2 \cdot 2H_2O$ in ethanol with a nanoparticle containing spinning solution in a solvent mixture of DMF and THF. 2.4 wt.-% $SnCl_2 \cdot 2H_2O$ (equivalent to 1.6 wt.-% SnO_2) as sol-gel precursor and 1.6 wt.-% SnO_2 NPs were combined in this solution, so that the equivalent portions of sol-gel- and NP-based SnO_2 are employed in the B+M-approach. In combination this results an overall amount of 3.2 wt.-% SnO_2 in the solution and a ratio of polymer to SnO_2 of 2/1.

Finally, a reference sample for physisorption analysis was prepared by drying and calcining the pure tin oxide nanoparticle dispersion with THF as dispersion solvent.

3.5.2 Synthesis and WAXS and DLS characterization of tin oxide nanoparticles

A general approach synthesizing dispersible metal oxide nanoparticles is the so-called “benzyl alcohol route”.[71] With this synthetic concept dispersible oxide nanoparticles of diverse simple and binary oxides can be prepared.[192–196] With a modified procedure originally conducted in an autoclave[194] the synthesis of SnO_2 nanoparticles dispersible in concentrations of up to 5.7 wt.-% in THF was achieved. Oil bath temperatures not higher than 180 °C were sufficient to prepare these dispersible tin oxide nanoparticles in a wet chemical synthesis. Detailed information concerning the exact reaction conditions are presented in the experimental section (see chapter 6.2.2.1.5).

The obtained tin oxide nanoparticles were characterized by dynamic light scattering (DLS) and wide angle X-Ray diffraction (WAXS) as presented below. These characterizations were intended to help understanding the physisorption results presented in chapter 3.5.4.

3.5.2.1 DLS analysis

DLS analysis was performed to determine the size of the tin oxide nanoparticles in dispersion with THF as solvent. The resulting hydrodynamic diameters include the solvation shell of the particles and will be related to the crystallite sizes estimated by WAXS analyses (see chapter 3.5.2.2).

The histogram obtained from the DLS analysis of the tin oxide dispersion shows an asymmetric distribution of particle sizes (see figure 3-30). Such asymmetric histogram of the particle size distribution is unreasonable, because generally a Gaussian distribution of sizes is expected for that kind of particle dispersion. Thus, more detailed investigations of the DLS analysis are necessary to identify the origin of such an unreasonable result. However, these investigations are beyond the scope of this thesis, because only a qualitative estimation of the mean particle size of the tin oxide particles in dispersion is relevant concerning the following study on fiber formation processes.

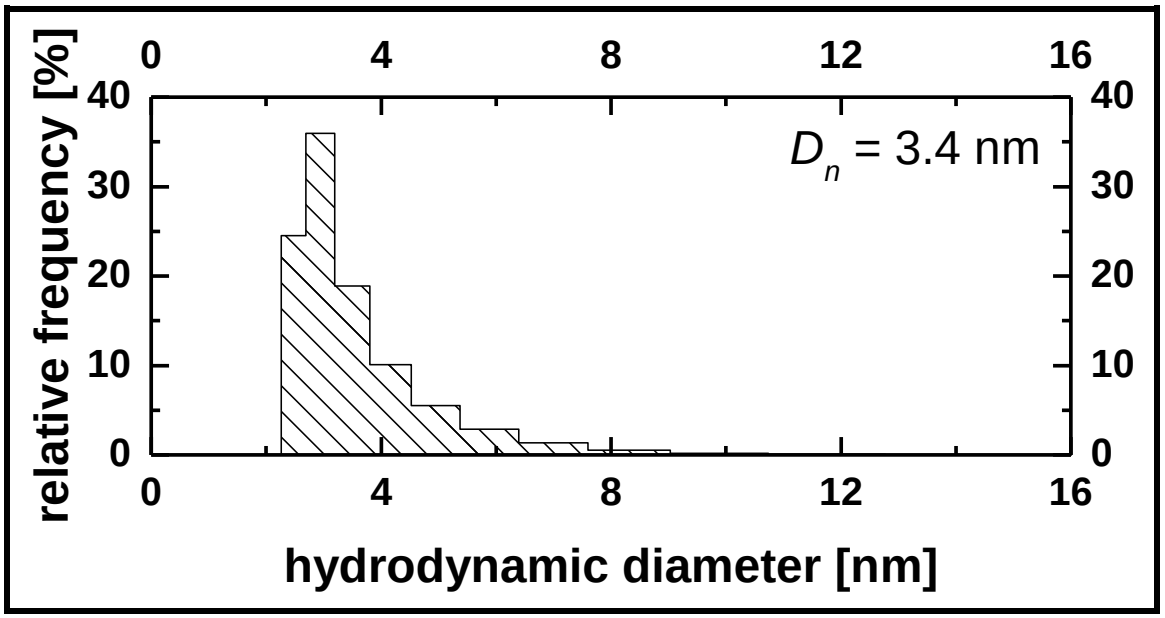

Figure 3-30: Histogram from the DLS analysis of a tin oxide nanoparticle dispersion in THF. The NPs were synthesized via a classical wet chemical approach. The population weighted mean diameter of the tin oxide particles in the dispersion was found to be D_n = 3.4 nm.

The tin oxide nanoparticles exhibit a population weighted mean diameter of D_n = 3.4 nm and 95% of all particles feature diameters smaller 5.4 nm (see figure 3-30). The size distribution is relatively broad; all particle diameters found in the sample are within the range of 2.3 - 15.2 nm. Consequently, the volume weighted mean diameter of the tin oxide NPs of D_v = 4.9 nm is significantly larger than the D_n value, because some larger particles dominate this value. All results from the DLS analysis are similar to the former investigations on zirconia dispersions (see figure 3-16). The tin oxide NPs are also relatively small, similarly as the zirconia WCS-NPs.

3.5.2.2 WAXS analyses

WAXS patterns were recorded for tin oxide particles dried at 80 °C as well as for particles calcined at 550 °C in order to characterize their crystallinity. Additionally, WAXS analyses on sol-gel- as well as on B+M-derived tin oxide fibers, each calcined at 550 °C, were performed to investigate whether the tin oxide source (i. e. sol-gel precursors or nanoparticles) influences the crystallinity of the resulting material.

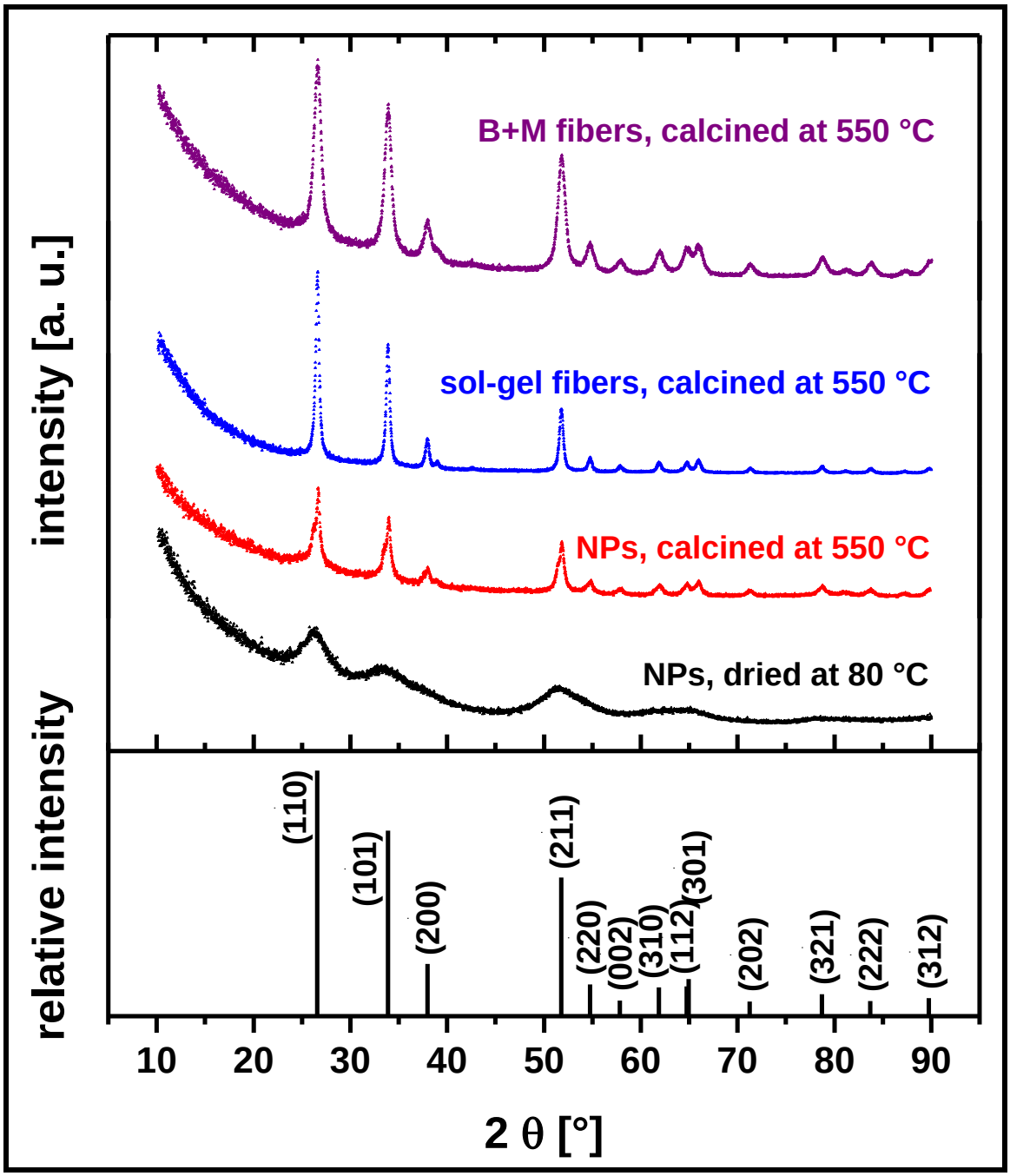

Figure 3-31: Measured XRD patterns of different tin oxide samples and indexed, relative intensities for the tetragonal phase (JCPDS card no. 01-071-0652). Color coding: black: WCS-NPs dried at 80 °C; red: WCS-NPs calcined at 550 °C; blue: sol-gel fibers calcined at 550 °C; purple: B+M-fibers calcined at 550 °C.

The crystallographic structure of all samples was identified to be mainly tetragonal SnO_2 although an amorphous background could not be ruled out for any of the patterns. All reflections of each WAXS pattern fit to the most prominent reflections of the JCPDS reference card number 01-071-0652 (see figure 3-31). While the uncalcined tin oxide NPs exhibit very broad reflections with a strong background suggesting very small crystallite sizes and a significant amorphous portion in the material, the three calcined samples feature much narrower and more intense reflections. In contrast to the ceria NPs the calcination procedure increases the crystallite sizes in the tin oxide materials.

Besides the identification of the crystalline phase(s) of the samples by the WAXS analyses, the crystallite sizes were calculated via Rietveld refinement resulting in a more detailed analysis of the crystallinity of the samples.[29] All measured WAXS patterns can be fitted well by the Rietveld refinement with only slight differences between measured and fitted data (see figure 3-32).

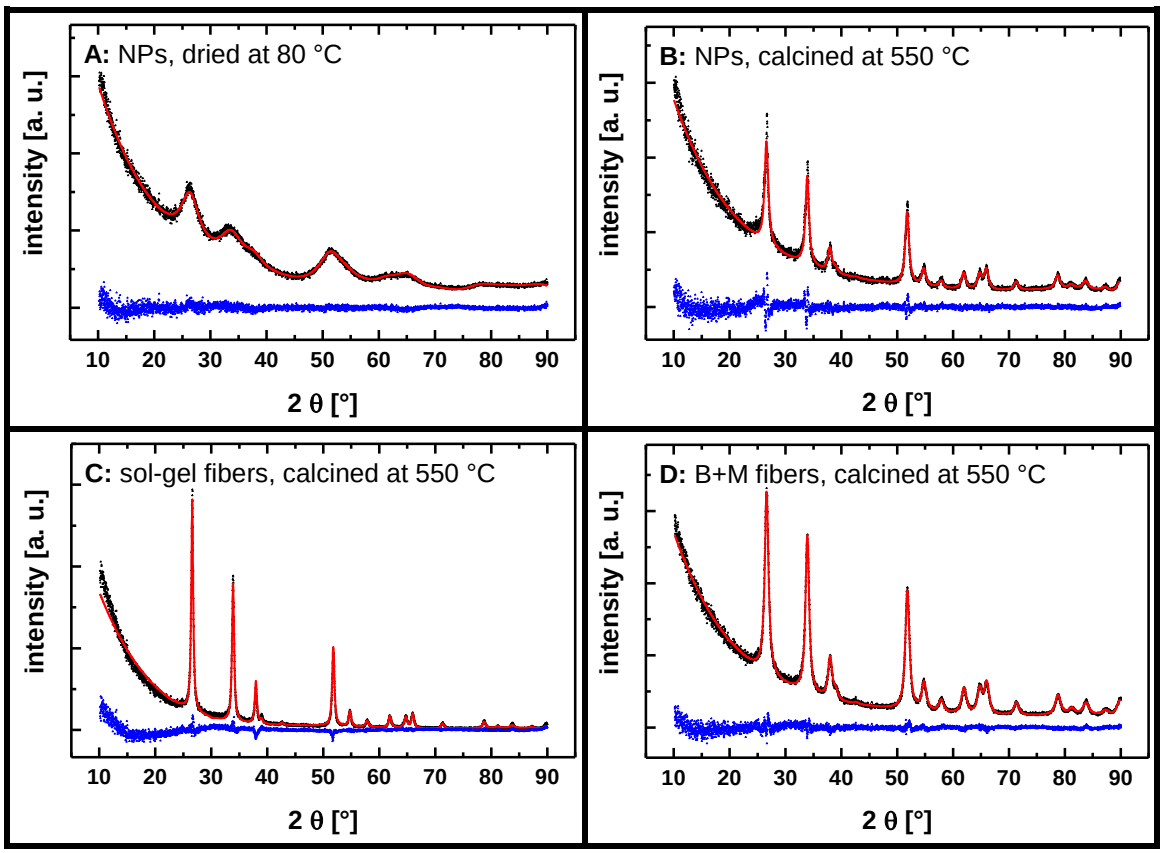

Figure 3-32: Measured XRD patterns (black dots) and Rietveld fitting data (red lines) of different tin oxide samples. Blue dots: Difference between measured and fitted data. A: WCS-NPs, dried at 80 °C; B: WCS-NPs, calcined at 550 °C; C: sol-gel fibers, calcined at 550 °C; D: B+M-fibers, calcined at 550 °C.

[29] Therefore, the ICSD reference for the tetragonal phase of tin oxide (ICSD no. 56001) was used.

The refinement revealed mean crystallite diameters of 1.4 ± 0.1 nm for the dried, uncalcined tin oxide NPs and 7.6 ± 0.4 nm for the calcined ones, confirming that the tin oxide crystallites did grow during the calcination at 550 °C (see table 3-11).[30] Comparing the crystallite size of the uncalcined tin oxide nanoparticles with the mean hydrodynamic diameter found by DLS (3.4 nm), a significant difference between the two values is found. Such large difference can be interpreted in two different manners. One possibility is that each dispersed particle consists of several crystallites. The other possibility is that the dispersed tin oxide particles consist of only one crystallite and a large portion of amorphous SnO_2. The strong background in the XRD pattern suggests that the second interpretation is more reasonable although the first one cannot be ruled out doubtlessly from the available data. Moreover, larger particles with sizes beyond the mean size value might consist of agglomerates of several tin oxide crystallites each with an amorphous shell. However, the internal particle structure can be assumed to be irrelevant concerning their interactions in the electrospinning experiments, which is the important property concerning the discussion of the following physisorption analyses (see chapter 3.5.4). Hence, a more detailed characterization of the particles by transmission electron microscopy (TEM) was not conducted, although this method generally would be adequate to clearly distinguish amorphous and crystalline portions of the particles, which might be interesting for other projects.

Table 3-11: Mean crystallite diameters *d* of the different tin oxide samples calculated by Rietveld refinement for the tetragonal phase.

sample	*d* [nm][1)]	standard deviation [nm][2)]
tin oxide NPs, dried at 80 °C	1.4	0.12
tin oxide NPs, calcined at 550 °C	7.6	0.36
tin oxide sol-gel fibers, calcined at 550 °C	15.0	0.87
tin oxide B+M-fibers, calcined at 550 °C	7.7	0.34

1): The size of the particles was calculated from 22 reflections of the tetragonal phase with similar results, so that a spherical shape of the particles can be assumed. Hence, these values were averaged for each sample to give the mean crystallite diameters.

2): The standard deviation indicates how strongly the calculated crystallite sizes from each reflection deviate from the mean value. A large standard deviation hints at a slight degree of anisotropy of the particle shape in the direction of different lattice planes.

[30] It has to be taken into account that the estimation of crystallite sizes below 2 nm by Rietveld refinement is attended by a significant systematic error, because the XRD reflections of samples with such low crystallinity are very broad and consequently the refinement can never result in very precise values, inter alia for the crystallite size. Hence, the absolute size values have to be considered with caution. Nevertheless the described general trends can be regarded as reliable.

Rietveld refinement of WAXS data of the fiber samples revealed mean crystallite diameters of 15.0 ± 0.9 nm for the sol-gel fibers and 7.7 ± 0.3 nm for the B+M-fibers (see table 3-11). These values indicate that the B+M-fibers exhibit the same mean crystallite size as the pure, calcined tin oxide particles, while the crystallites in the sol-gel fibers are twice as large. When the pure sol-gel fibers are calcined, the growth of the crystallites can be considered as "unhindered" producing crystallite sizes as large as 15 nm. Contrariwise, the crystallite growth in the B+M-fibers seems to be "hindered" compared to the pure sol-gel fibers: As a matter of fact the addition of sol-gel precursor "mortar" to the tin oxide nanoparticle "bricks" did not increase the crystallite size compared to the pure nanoparticles. Obviously, the "mortar" is so well distributed in between the "bricks" that the mortar cannot agglomerate to domains larger than approximately 8 nm. Otherwise, larger crystallites from the sol-gel precursor could be expected as is the case in the pure sol-gel fibers. Furthermore, the "mortar" surrounding the "bricks" also did not result in a growth of the "brick" size. Accordingly, the sol-gel precursor did not act as "feed" for the bricks to grow beyond the size they reach without the addition of the sol-gel precursor. This finding suggests that the sol-gel "mortar" generates new, individual crystallites in between the "bricks". Consequently, the crystallinity of the B+M-fibers resembles more the pure nanoparticles than the sol-gel fibers. This represents a fundamental, interesting finding concerning the B+M-fibers being relevant for the following discussions again (see chapter 3.5.5).

3.5.3 SEM analyses on tin oxide fibers

Figure 3-19 depicts tin oxide sol-gel fibers electrospun with PMMA (see table 3-10, samples 2, figure 3-19 A–D) or PVP (see table 3-10, samples 1, figure 3-19 E, F) after calcination. The surface of the tin oxide sol-gel fibers is not as smooth as the surface of other sol-gel fibers investigated within this thesis (see figure 3-1, figure 3-19 and figure 3-26). A slight surface roughness, similarly as observed for NP-fibers, can be seen (see figure 3-19 D, F) which needs to be respected concerning the interpretation of the nitrogen physisorption data on the sol-gel fibers (see chapter 3.5.4). The diameters of both tin oxide sol-gel fibers are quite homogeneous. The fibers obtained with PMMA as spinning polymer possess diameters of about 200 nm while the fibers spun with PVP are much thinner with diameters of about 50 nm. Cracks and beads are more or less absent in both kinds of tin oxide sol-gel fibers.

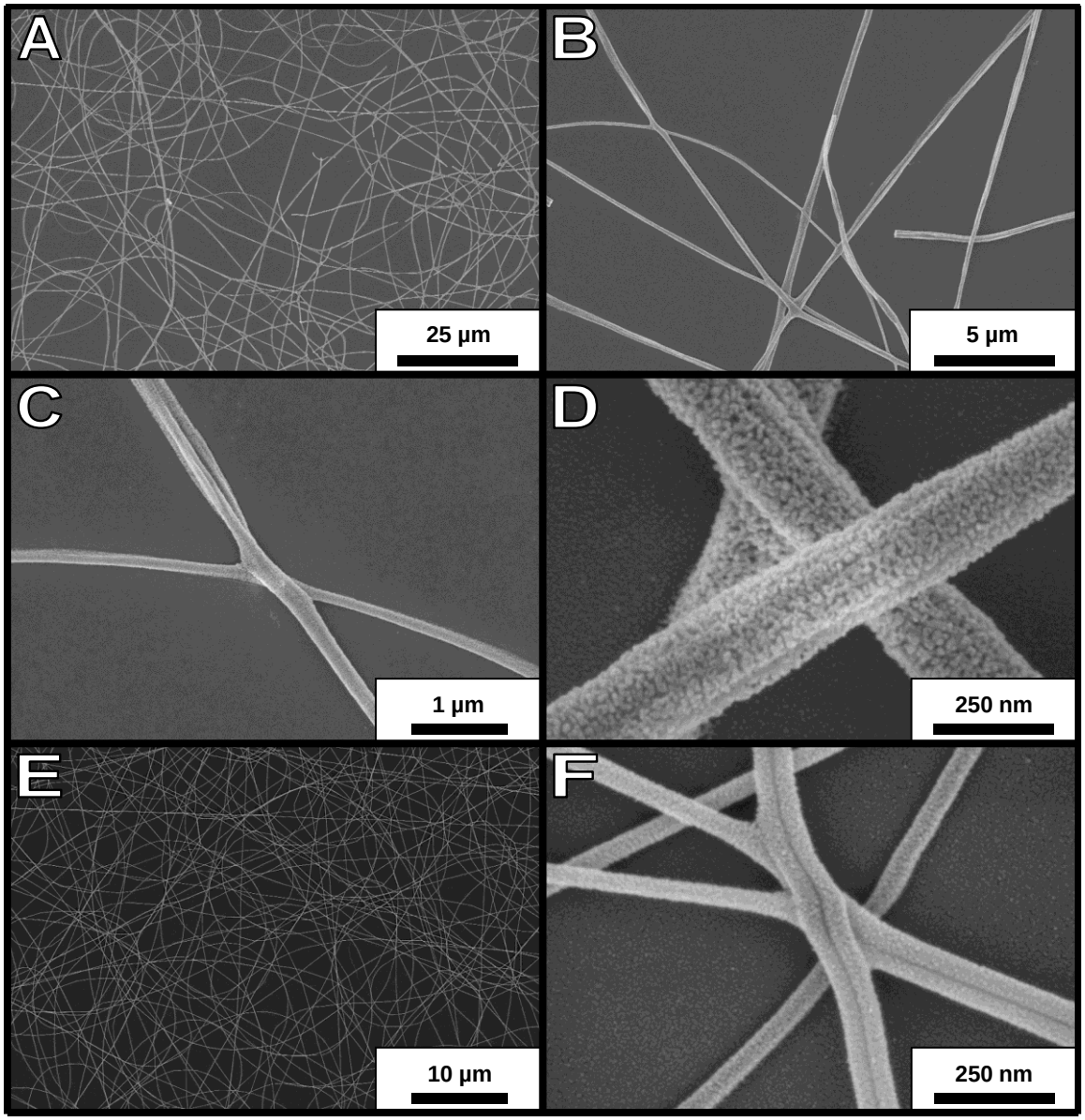

Figure 3-33: SEM pictures of tin oxide fibers obtained from $SnCl_2 \cdot 2H_2O$ as sol-gel precursor after calcination at 550 °C. A–D: electrospun with 5.4 wt.-% PMMA (see table 3-10, sample 2); E, F: electrospun with 4.8 wt.-% PVP (see table 3-10, sample 1).

Tin oxide NP-fibers are illustrated in figure 3-34. Homogeneous fibers spun with pure THF as solvent were obtained after spinning with 7.0 wt.-% (see table 3-10, samples 3, figure 3-34 A–C) or 9.8 wt.-% (see table 3-10, samples 4, figure 3-34 D–F) PMMA and calcination at 550 °C. The fibers spun with 7.0 wt.-% PMMA exhibit sporadic large beads of wrinkled shape (see figure 3-34 A). This wrinkled shape suggests a porous structure of the beads: Such wrinkled beads occur when cavities within a bead collapse. This phenomenon is already known for polymer fibers, in which cavities are generated by excess solvent being temporarily trapped in the bead or fiber if a solid skin on the jet surface is formed during electrospinning.[197] Similarly, such collapsed, wrinkled beads can also occur when the polymer is removed from composite polymer/inorganic fibers during calcination. Possibly these wrinkled beads are an indication of an overall porous structure not only of the beads but also of the whole fiber sample.

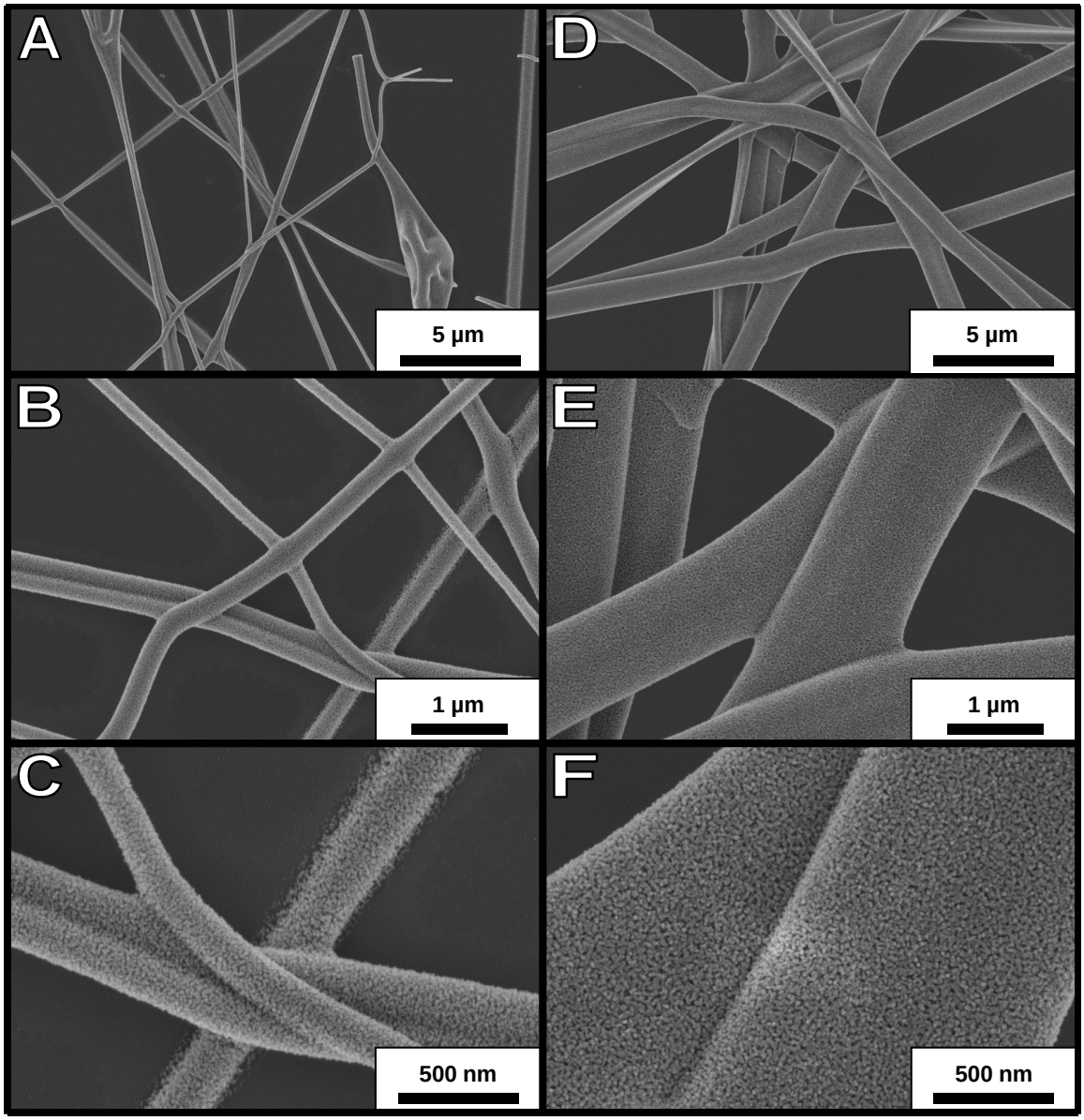

Figure 3-34: SEM pictures of tin oxide fibers obtained from NPs and electrospun with PMMA after calcination at 550 °C. A–C: electrospun with 7.0 wt.-% PMMA (M_w = 350,000 g·mol^{-1}) in the spinning solution (see table 3-10, sample 3); D–F: electrospun with 9.8 wt.-% PMMA (M_w = 996,000 g·mol^{-1}) in the spinning solution (see table 3-10, sample 4).

The fibers spun with 7.0 wt.-% PMMA exhibit significantly varying diameters in a range of approximately 200−400 nm. The fibers spun with 9.8 wt.-% PMMA exhibit much thicker diameters of about 1 µm and are without beads. The increased diameters of the fibers are a consequence of the much higher viscosity of the spinning solution. In addition to the higher polymer concentration also the molecular weight of the PMMA was 996,000 g·mol^{-1} for this sample, instead of 350,000 g·mol^{-1} for all other samples spun with PMMA. In all other respects the two NP-fiber samples are similar. Both samples exhibit only few cracks and an optically rough surface typical for NP-fibers.

SEM pictures of tin oxide B+M-fibers reveal no distinctive features differing from the NP-fibers (see figure 3-35). They exhibit an analogously rough surface, almost no cracks and no beads. The diameters of the B+M-fibers are relatively constant and in the range of approximately 250 nm. There are no conspicuous features on the B+M-fibers which require special comment. Similarly as the B+M-fibers were indistinguishable from the NP-fibers concerning their crystallinity (see WAXS analyses, chapter 3.5.2), also the SEM pictures reveal no significant differences.

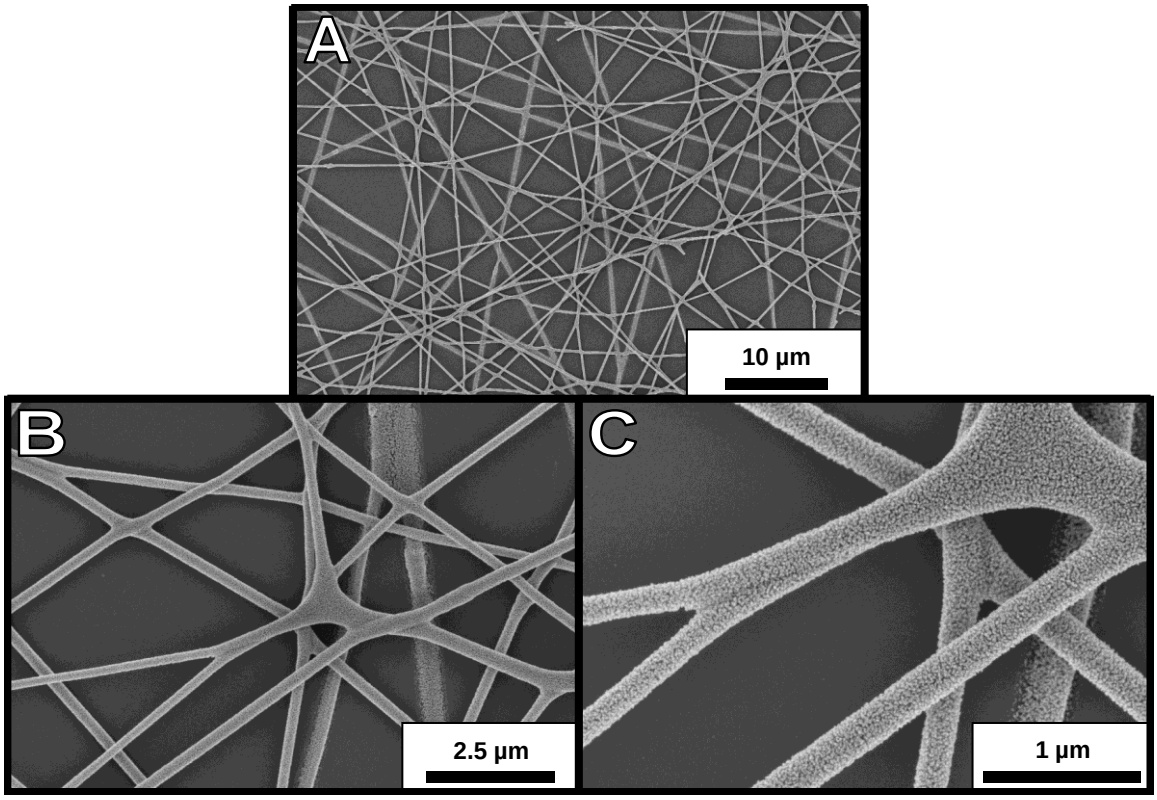

Figure 3-35: SEM pictures of tin oxide B+M-fibers obtained from $SnCl_2 \cdot 2H_2O$ as sol-gel precursor and tin oxide NPs electrospun with PMMA after calcination at 550 °C (see table 3-10, sample 5); A–C: different magnifications.

3.5.4 Physisorption: comparative analyses on tin oxide fibers

In this chapter, physisorption results on tin oxide samples (see table 3-10) will be discussed in direct correlation to former results on other materials (see chapters 3.2−3.4). Interpretation of the results will be performed with respect to the principle concept concerning electrospinning of inorganic fibers established so far. The tin oxide experiments were not numerous enough to repeat the deductions obtained from the experiments on the other materials. Hence, the following discussion focuses on the question whether the results on the tin oxide samples are in accordance with the results of the former chapters and the principle concept obtained so far.

Moreover, the physisorption results on tin oxide fibers provide evidence of two important aspects concerning the principle concept for electrospinning of inorganic fibers not investigated on the former materials: The comparability of sol-gel-derived fibers and NP-fibers as well as the preparation of inorganic fibers via a B+M approach are these important aspects (see chapter 3.5.1.2) not only proving the general concept established so far but possibly also extending it substantially.

Tin oxide fibers from $SnCl_2 \cdot 2H_2O$ as sol-gel precursor spun with 4.8 wt.-% PVP possess a specific surface area of 37 $m^2 \cdot g^{-1}$ and a TPV of 0.13 $cm^3 \cdot g^{-1}$ (see table 3-12, sample 1). When the same precursor is spun with 5.4 wt.-% PMMA a specific surface area of 29 $m^2 \cdot g^{-1}$ and an identical TPV of 0.13 $cm^3 \cdot g^{-1}$ are obtained (see table 3-12, sample 2). The difference between the specific surface areas can be ascribed to the considerably different thicknesses of the fibers (see figure 3-33). Comparing the DFT-derived CPV plots no substantial differences between the two sol-gel fiber samples are revealed (see figure 3-36 G). While the fibers spun with PVP feature slightly more pores with diameters below approximately 16 nm, the fibers spun with PMMA exhibit some more pores beyond this pore size. Up to pore sizes of approximately 32 nm both sol-gel fiber samples accumulate nearly identical CPVs of 0.070 $cm^3 \cdot g^{-1}$ and 0.075 $cm^3 \cdot g^{-1}$, respectively. Thus, the differences between the two samples are more or less negligible and obviously the different spinning polymers do not affect the mesoporous structure of the calcined tin oxide fibers essentially. Only the viscosity of the spinning solution influences the results in so far, that substantially increased fiber diameters are obtained in one case resulting in a slightly larger specific surface area.

Table 3-12: Physisorption results on electrospun tin oxide nanofibers: BET[1)], CPV[2)], TPV[3)] and relative porosity[4)] values.

sample no.	sample category	weight ratio SnO_2/polymer	SnO_2 source	solvent(s)	BET[1)] [$m^2 \cdot g^{-1}$]	CPV[2)] [$cm^3 \cdot g^{-1}$]	TPV[3)] [$cm^3 \cdot g^{-1}$]	relative porosity[4)] [%]
1	fibers	0.50	sol-gel SnO_2 from $SnCl_2 \cdot 2H_2O$	EtOH/DMF	36.9	0.070	0.134	48.4
2	fibers	0.54	sol-gel SnO_2 from $SnCl_2 \cdot 2H_2O$	DMF/THF	28.6	0.075	0.130	47.7
3	fibers	0.53	WCS-NPs	THF	41.7	0.143	0.157	52.3
4	fibers	0.35	WCS-NPs	THF	47.3	0.151	0.165	53.6
5	fibers	0.50	$SnCl_2 \cdot 2H_2O$ and WCS-NPs	THF/DMF/EtOH	55.2	0.182	0.201	58.4
6	pure particles	---	WCS-NPs	THF	149.7	0.155	0.173	54.7

[1)]: specific surface area calculated by the BET method;
[2)]: cumulative pore volume calculated by the DFT method; this is the pore volume of the last data point in the CPV plot;
[3)]: total pore volume calculated by using the Gurvich rule (see equation (2-11));
[4)]: calculated from the TPV values (for explanation of the data reduction see chapter 2.6.3.1).

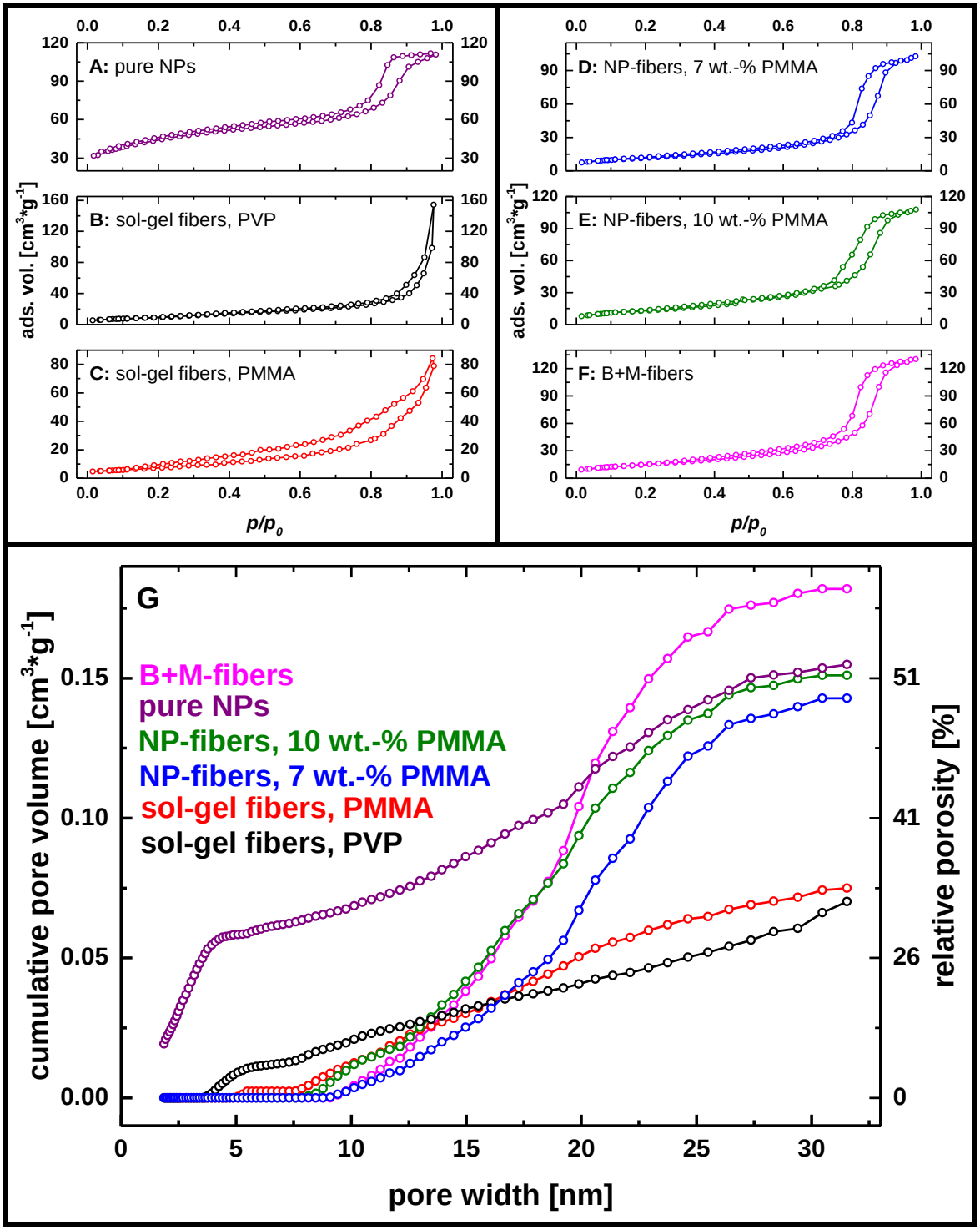

Figure 3-36: N_2-Physisorption isotherms (A–F) and CPV plots from DFT (G) of different tin oxide fibers and of pure tin oxide NPs. Magnifications of the isotherms can be found in the appendices (see figure 6-44–figure 6-49). Color coding: purple: pure, dried and calcined tin oxide NPs (see table 3-12, sample 6); black: sol-gel fibers spun with 4.8 wt.-% PVP (see table 3-12, sample 1); red: sol-gel fibers spun with 5.4 wt.-% PMMA (see table 3-12, sample 2); blue: fibers prepared from tin oxide NPs spun with 7.0 wt.-% PMMA (see table 3-12, sample 3); green: fibers prepared from tin oxide NPs spun with 9.8 wt.-% PMMA (see table 3-12, sample 4); pink: B+M-fibers obtained from $SnCl_2 \cdot 2H_2O$ as sol-gel precursor and tin oxide NPs electrospun with 6.4 wt.-% PMMA (see table 3-12, sample 5).

The pure, dried and calcined tin oxide nanoparticles exhibit a very large specific surface area of 150 $m^2 \cdot g^{-1}$ and a TPV of 0.17 $cm^3 \cdot g^{-1}$ (see table 3-12, sample 6) being in the same order of magnitude as the TPVs of the electrospun tin oxide fibers. From the DFT-derived CPV plot the origin of the large specific surface area can be explained by a considerable amount of micropores and small mesopores in this material (see figure 3-36 G) resulting in a cumulative pore volume as large as 0.06 $cm^3 \cdot g^{-1}$ for pores with diameters below 4 nm. No other nanoparticle sample investigated within this thesis exhibits such a large portion of small pores which cannot be understood so far. In order to explain the outstanding microporosity of the tin oxide particles a more detailed study of the nanoparticle synthesis is necessary. However, this was beyond the scope of this thesis, so that such investigations were omitted and are a task for a future project. The trend of the CPV plot of the pure particles for pore diameters beyond 4 nm size is comparable to the plots of the tin oxide sol-gel fibers explaining the comparable TPVs of these samples only differing by 0.04 $cm^3 \cdot g^{-1}$. This pore volume of 0.04 $cm^3 \cdot g^{-1}$ originates from the microporosity of the particles.

Interestingly, tin oxide NP-fibers prepared from the above discussed tin oxide nanoparticles did not possess such small pores. The NP-fibers only feature pores with diameters larger than approximately 8 nm. Consequently, their specific surface areas of 42 $m^2 \cdot g^{-1}$ and 47 $m^2 \cdot g^{-1}$ are also much smaller (see table 3-12, samples 3 and 4). Why the small pores vanish upon electrospinning of the tin oxide nanoparticles cannot be explained so far, but it may become obvious, when the origin of the microporosity of the pure, dried and calcined tin oxide particles is investigated in detail. Probably, simple arguments like packing effects and/or confinement in electrospinning experiments are not sufficient to explain such finding.

The specific surface areas of the tin oxide NP-fibers are slightly higher, but in the same order of magnitude compared to the sol-gel fibers. So far the results on tin oxide fibers are in accordance with the results on the other materials investigated before: With TPV values of 0.16 $cm^3 \cdot g^{-1}$ and 0.17 $cm^3 \cdot g^{-1}$ which are not very much larger than the corresponding DFT-derived CPV values (see table 3-12, samples 3 and 4) the mesoporosity of the tin oxide NP-fibers is increased compared to the sol-gel fibers (see figure 3-36 G) in the same manner as found before for other materials. Hence, also for tin oxide a structure formation process in the sense of the EICA concept seems to take place during the electrospinning of nanoparticle containing spinning solutions producing such increased mesoporosity.

The two different tin oxide NP-fiber samples confirm again, that neither the dimensions of the electrospun fibers nor the mass ratio of nanoparticles to spinning polymer (0.53 versus 0.35) influences the mesoporosity of the resulting fibers (see table 3-12, samples 3 and 4). Also the different molecular weights of the spinning polymers (350,000 $g \cdot mol^{-1}$ versus 996,000 $g \cdot mol^{-1}$) in this two experiments did not affect the mesoporosity of the resulting tin oxide fibers significantly, although it was demonstrated, that this changes the fiber diameters substantially (see figure 3-34). Both samples possess nearly identical specific surface areas and CPV plots irrespective of the differences found by SEM analysis. This finding is in accordance with the results and the fundamental EICA concept concerning electrospinning of inorganic materials which was deduced in the former chapters.

It has to be recalled that SEM investigations of the tin oxide sol-gel fibers revealed some surface roughness (see figure 3-33) which seems to be similar to the surface roughness of typical NP-fibers (see figure 3-34). Yet, significant discrepancies of the physisorption results between these different kinds of fibers are found similarly as for the previously investigated other materials proving that the optical evaluation of SEM pictures is inadequate to appraise the porosity of electrospun fibers. However, tin oxide sol-gel fibers possess some small mesopores with diameters below approximately 8 nm not found in NP-fibers (see figure 3-36 G). Presumably, the surface roughness found by SEM correlates to these small mesopores, but this roughness does not dominate the overall porous structure of the sol-gel fibers.

Finally, the results on electrospun B+M-fibers have to be discussed: The B+M-fibers possess a slightly larger specific surface area (55 $m^2 \cdot g^{-1}$) and TPV (0.20 $cm^3 \cdot g^{-1}$) than the tin oxide NP-fibers (see table 3-12, samples 3 and 5). In both samples the ratio of tin oxide to spinning polymer is the same. In the B+M-fiber synthesis the tin oxide is derived to equal parts from a sol-gel precursor and nanoparticles. Also the polymer concentrations in the spinning solutions are nearly identical. Thus, the two samples are well comparable and the porosity of the B+M-fibers is interestingly not only similar but even slightly higher than the porosity of the NP-fibers. Respecting the results on other material which clearly demonstrated that sol-gel-derived inorganic fibers always feature lower porosities than NP-fibers of the same material, it was expected, that the porosity of B+M-fibers lies somewhere in between the values of sol-gel- and nanoparticle-derived fibers. This expectation would be in accordance with the basic B+M-concept: If sol-gel precursors act as “mortar” or “molecular glue” for the nanoparticle “bricks”, it seems to be reasonable that the sol-gel precursors fill up some pores/voids in the material reducing the porosity compared to the corresponding fibers prepared without sol-gel precursors. Yet, such pore-filling cannot be observed (see figure 3-36 G) which may be owed to the pore size distribution in the fiber samples: Neither the NP-fibers nor the B+M-fibers possess pores with diameters below 8 nm. Especially such small pores can get filled by sol-gel precursors, while larger pores are possibly only coated by sol-gel precursors but hardly can get filled completely. Consequently, no significant pore-filling is observed, as long as small mesopores are generally absent in the NP-fibers. Moreover, the B+M-fibers even feature a slightly larger CPV for all pores beyond this 8 nm size (figure 3-36 G, samples 3 and 5). In conclusion also the B+M-fiber synthesis seems to be dominated by the EICA process generating the porous structure during electrospinning irrespective of the added sol-gel precursor. Consequently, the B+M-fibers exhibit nearly the same properties as the NP-fibers which is a general conclusion also with respect to the WAXS and SEM analyses (see chapters 3.5.2 and 3.5.3) offering great potential for further projects (see chapter 3.5.5).

3.5.5 Conclusion on tin oxide experiments

The experiments on the tin oxide materials resulted in several important findings: First, this is the first report on pure, electrospun tin oxide fibers prepared via the nanoparticle approach as well as via the B+M-approach. Secondly, it was demonstrated from preliminary qualitative investigations that the choice of the spinning polymer is important, if NP-fibers are to be prepared. The melting point of the polymer has to lie above the temperature at which the nanoparticles get interconnected to each other by condensation. Consequently, tin oxide NP-fibers could only be obtained with PMMA but not with PEO as spinning polymer due to their different melting temperatures.

Regarding the EICA concept with respect to electrospinning the results on tin oxide fibers gave prove of two important aspects not investigated on other materials so far: The one aspect is the comparability of sol-gel fibers and NP-fibers: Tin oxide is the only material on which it was demonstrated doubtlessly that the generally different porosities of sol-gel fibers and NP-fibers are not a consequence of a templating effect of the spinning polymer, because tin oxide is the only material for which sol-gel fibers and NP-fibers could be prepared from spinning solutions containing the same polymer PMMA. For all other materials there were only indications why such assumption is reasonable. Thus, this result is essential evidence in the context of the general electrospinning concept irrespective of the considered material and exhibits a substantive demonstration of its fundamental validity. The second aspect is the preparation of inorganic fibers according to the B+M-concept: Tin oxide fibers were prepared and characterized from a B+M spinning solution with equivalent amounts of sol-gel and nanoparticle-derived tin oxide. None of the characterization methods used, namely SEM, WAXS and nitrogen physisorption (see chapters 3.5.2–3.5.4), revealed any significant difference of these B+M-fibers compared to NP-fibers leading to the conclusion that the nanoparticle “bricks” dominate all analyzed properties of the resulting B+M-fibers. This is a very promising result concerning further investigations that should be projected for the future:

It was reported previously that sol-gel and nanoparticle-derived materials exhibit different properties relevant in applications: A comparative photoelectrochemical study of sol-gel- and nanoparticle-based titania thin-films revealed a drastically higher efficiency of the sol-gel-derived films concerning catalysis in the water spilling reaction,[79] although the nanoparticle-based films had significantly larger specific surface areas and thus more reactive sites. It was concluded that the nanoparticle-based films suffer from worse electronic connectivity due to grain boundaries interrupting electronic conduction paths within the material. It is conceivable that such grain boundary problems can be overcome, if the interconnection of the nanoparticle grains is improved by the addition of a sol-gel precursor suggesting the B+M-concept to be able to combine the benefits of both approaches: the large specific surface areas and porosities of nanoparticle-based structures with the better electronic conductivity of sol-gel-derived materials. Indications for similar synergetic effects in B+M-materials were already shown within the first presentation of this concept, but are by far not understood in detail up to now,[2] resulting in great potential for future studies: If it is possible to address and/or predict such synergetic effects occurring in B+M-materials, substantially improved properties for applications may be achievable. This may for example lead to gas sensors with improved performance, if tin oxide materials are considered.

3.6 Comparison of various materials: Consequences of principle synthetic concepts

In the former chapters 3.2−3.5 the preparation of oxide fibers of several elements from different building blocks was studied. These investigations revealed that fibers with characteristically different mesoporosities are obtained depending on the building blocks employed for the fiber synthesis. The origin of such different mesoporosities was proven to be a consequence of the structure formation processes taking place during the fiber synthesis. For the preparation of oxide nanofibers from preformed, dispersed nanoparticles fundamentals of colloidal chemistry were used to explain the formation of mesoporosity within electrospun fibers. Since the driving force of this process is the evaporation of solvent resulting in the aggregation of nanoparticles to clusters, it was termed evaporation induced cluster aggregation (EICA). In contrast, the preparation of oxide nanofibers from sol-gel precursors of the same materials did not produce mesoporous fibers in a similar manner since the EICA process cannot take place in sol-gel systems due to the absence of preformed nanoparticles. The preparation of mesoporous sol-gel fibers requires (spinodal) phase separation and/or templating as discussed in chapters 2.2.1 and 2.3.1. However, the preconditions for such processes in sol-gel electrospinning systems were not investigated in detail in this thesis. Finding adequate conditions for the formation of mesoporous sol-gel fibers by electrospinning is a very complex task legitimating a further thesis as discussed earlier.

However, it was not discussed so far whether there are fundamental quantitative trends concerning the mesoporosity of the structures studied in this thesis independent of the material under investigation. If the mesoporosity of electrospun fibers could be predicted on the basis of the preparation path and irrespective of the material under consideration, this would be a tremendous gain for the directed synthesis of mesoporous materials via electrospinning, additional progress concerning the understanding of formation mechanisms during electrospinning, and thus an outstanding result for this thesis.

Hence, the results of the former chapters 3.2−3.5 will be compared in this section in order to investigate the predictability of structure formation processes in electrospinning experiments, especially concerning the EICA process and the resulting mesoporous structures. Consequently, the results on the different materials investigated so far need to be converted to comparable values respecting the differing densities of the materials (see chapter 2.6.3).

The following comparisons will be split concerning the analysis of mesoporosity conducted by DFT analyses of the physisorption data (see chapter 3.6.1), and concerning the specific surface areas determined by the BET method from the same data (see chapter 3.6.2). A pivotal summary of the EICA process explaining the mesoporous structures formed in NP-based materials is presented in chapter 4.

3.6.1 Comparison of mesoporosities of different oxide materials

Relative porosities were calculated according to equation (2-17) enabling a comparison of the mesoporous structures of different materials concerning their CPVs in only one diagram (see figure 3-37 and table 3-13). Besides the materials prepared and investigated within this thesis, results on several titania samples investigated earlier[1] and already published elsewhere[75] are also incorporated into the following discussions.[31]

For each material sol-gel fiber samples (see figure 3-37 A), pure, dried and calcined nanoparticles (see figure 3-37 B) and fibers derived from preformed nanoparticles (NP-fibers, see figure 3-37 C) are compared in the following. Additionally, tin oxide B+M-fibers are included into the NP-fiber sample group, because it was found that they exhibit no significant differences concerning their pore structure compared to the NP-fibers (see chapter 3.5.4). Bulk materials obtained from unspun nanoparticle containing spinning solutions are omitted in this chapter, since it was found that these materials exhibit similar mesoporosity as the corresponding electrospun fibers proving the fundamentals of the EICA concept. Nevertheless, it has to be pointed out that the expected differences in the macroporosity of these spun and unspun materials are not investigated in detail in this thesis and thus are not considered further here. Furthermore, the discussion of each individual sample from the former chapters 3.2−3.5 is dispensable in the overall context.

Sol-gel-derived fibers of different materials are presented in figure 3-37 A. Apart from the silica sample all sol-gel fibers exhibit noticeably mesoporous structures. Ceria and tin oxide sol-gel fibers possess CPV plots with a nearly identical trend accumulating to a relative porosity slightly below 35%. Likewise, also zirconia and titania sol-gel fibers feature CPV plots with trends that are very close to each other and both accumulate to a relative porosity around 22% (see table 3-13 and figure 3-37 A). While The CPV plots of all metal oxide sol-gel fibers reveal the presence of mesopores of any size up to approximately 30 nm and simultaneously the absence of any microporosity, the silica sol-gel fibers exhibit mainly microporosity summing up to a relative porosity of approximately 17% (for pore diameters smaller than 2 nm). In addition the silica sol-gel fibers exhibit only slight mesoporosity resulting in a relative porosity of 23% if all pores with diameters up to 32 nm are considered. The different characteristics of the silica sol-gel fibers might be attributable to the fact that silica exhibits a different sol-gel chemistry producing mainly microporous sol-gel fibers under the electrospinning conditions in contrast to metal oxide sol-gel fibers which are mainly mesoporous. However, irrespective of this special difference, the CPV plots of all sol-gel fibers are within a limited range differing significantly from the corresponding range of the other sample groups (see figure 3-37 D).

[31] A short summarization of the result on the titania materials including detailed physisorption data is presented in chapter 2.5.2.

Table 3-13: Comparison of relative porosities calculated from the DFT-derived CPV values of selected, representative samples from all materials investigated within this thesis including former results on titania.[75] The samples are selected and grouped with respect to the preparation method to illustrate general trends that are connected to the preparation method. For more precise sample information see table 3-1, table 3-4, table 3-7 and table 3-10, respectively.

sample category	material	sample acronym	see	CPV[1] [$cm^3 \cdot g^{-1}$]	relative porosity[2] [%]
sol-gel fibers (SG-F)	SiO_2	SiO_2-SG-F	table 3-1, sample 2	0.133	22.7
	ZrO_2	ZrO_2-SG-F	table 3-4, sample 1	0.041	19.8
	CeO_2	CeO_2-SG-F	table 3-7, sample 1	0.073	34.6
	SnO_2	SnO_2-SG-F	table 3-10, sample 2	0.075	34.4
	TiO_2	TiO_2-SG-F	table 2-2, sample 1	0.082	24.2
pure, dried and calcined particles (PP)	SiO_2	SiO_2-PP	table 3-1, sample 3	0.244	34.9
	ZrO_2	ZrO_2-PP (MWS)	table 3-4, sample 13	0.011	6.3
	ZrO_2	ZrO_2-PP (WCS)	table 3-4, sample 12	0.073	30.7
	CeO_2	CeO_2-PP	table 3-7, sample 5	0.022	13.6
	SnO_2	SnO_2-PP	table 3-10, sample 6	0.155	52.0
	TiO_2	TiO_2-PP	table 2-2, sample 2	0.120	31.9
nanoparticle-based fibers (NP-F)	SiO_2	SiO_2-NP-F	table 3-1, sample 6	0.574	55.8
	ZrO_2	ZrO_2-NP-F	table 3-4, sample 6	0.237	59.1
	CeO_2	CeO_2-NP-F	table 3-7, sample 2	0.243	63.6
	SnO_2	SnO_2-NP-F	table 3-10, sample 4	0.151	51.4
	SnO_2	SnO_2-B+M-F	table 3-10, sample 5	0.182	56.0
	TiO_2	TiO_2-NP-F	table 2-2, sample 4	0.285	56.6

[1]: cumulative pore volume obtained by the DFT method; this is the pore volume calculated from the last data point in the CPV plot;
[2]: calculated from the CPVs (for explanation of the data reduction see chapter 2.6.3.1).

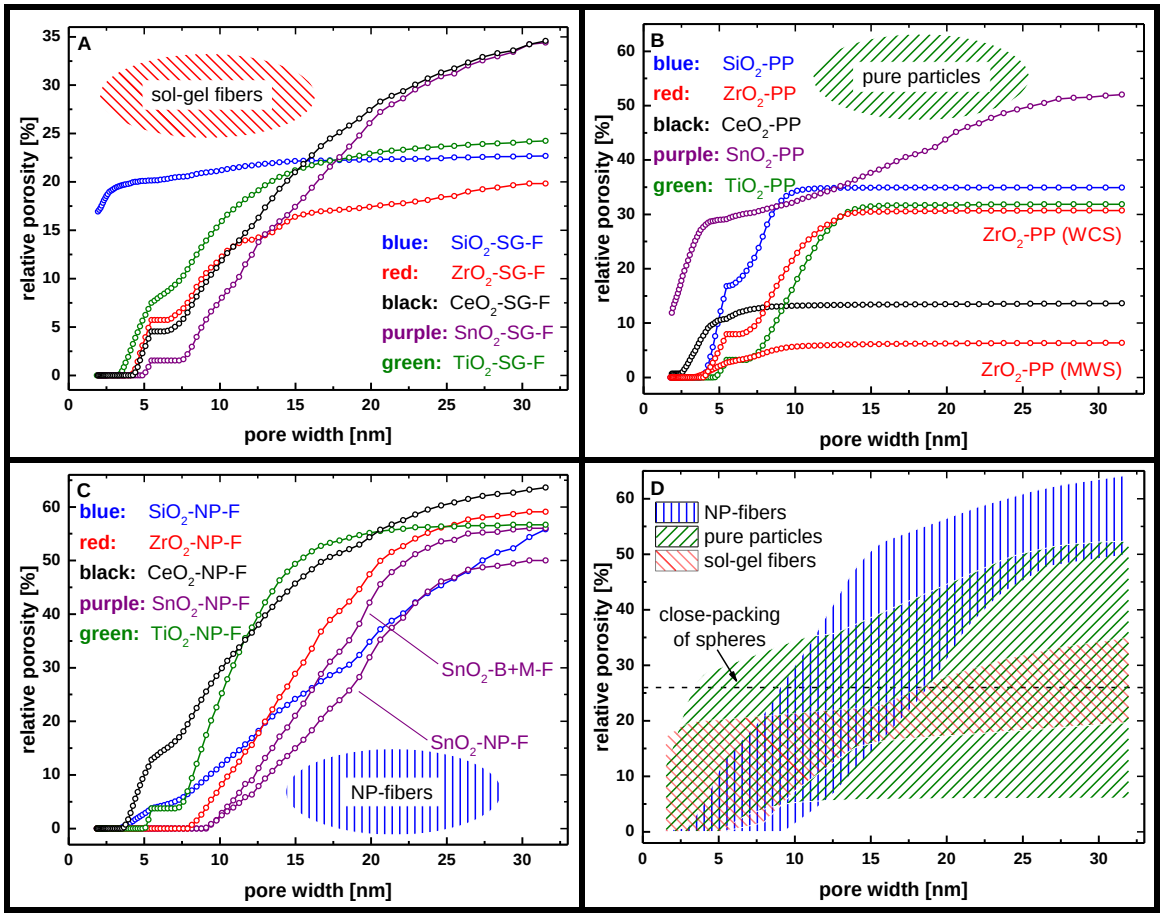

Figure 3-37: CPV plots obtained from DFT calculations (A–C) of selected, representative samples of all materials investigated within this thesis including former results on titania.[75] The samples are selected and grouped regarding the preparative approach to illustrate general trends that are connected to the preparation method. The groups are: sol-gel-based fibers (A); pure particle samples (B) and NP-fibers (under addition of the SnO_2 B+M-fibers) (C). D: Comparative illustration of the different reagions in which the CPV plots of the different samples groups (A–C) lie. Sample acronyms can be understood by refering to table 3-13 and the references therein.

The CPV plots of the pure, dried and calcined particles (see figure 3-37 B) differ much stronger from each other depending on the material consequently resulting in a wider range of 6−52% for the cumulated relative porosities. While the tin oxide particles are the only ones with distinct microporosity and, besides the ceria particles, the only ones with significant amounts of small mesopores with sizes below approximately 4 nm, all other materials, i. e. titania, zirconia and silica, exhibit pore sizes solely in the range of 4−15 nm. Moreover, the tin oxide particle sample is the only one exhibiting pore sizes larger than 15 nm. Due to all these differences the resulting CPVs span a very wide range much wider than the corresponding range of the sol-gel fibers (see figure 3-37 D). Reasons for the varying behavior of the pure particle samples were already mentioned in the former chapters and will be recapitulated in the discussion at the end of this chapter, after a brief overview over the CPV data of the corresponding NP-fibers.

The corresponding NP-fibers and the tin oxide B+M-fibers features fundamentally different mesoporous structures compared to the sol-gel fibers and the pure particles as evidenced by characteristically different trends in the CPV plots (see figure 3-37 C and D). The differences are striking and a consequence of the EICA process. The cumulative relative porosities of the NP-fibers illustrated in figure 3-37 C all lie within in a narrow range of 51−64% and the trends of the corresponding CPV plots are very similar to each other. None of the NP-fibers exhibit any microporosity and all CPV plots possess similar slopes only with a shifted onset. While the tin oxide NP-fibers exhibit no pores with diameters below approximately 9 nm, the ceria NP-fibers feature a lower limit of pore sizes around 3 nm. The other materials have their "porosity onset" somewhere between these two extrema. From this onset on, all CPV plots show similar slopes and consequently they are more or less parallel to each other, especially if the plots of the tin oxide, zirconia and ceria NP-fibers are considered. In other words, all NP-fibers possess basically the same mesoporosity irrespective of the material if pore sizes beyond approximately 9 nm are considered. Only the DFT plots of the titania and the silica NP-fibers exhibit slightly different trends: The silica fibers are the only NP-fibers with a significant amount of pores larger than 25 nm in diameter and the titania NP-fibers are the only ones in which no significant amount of pores with sizes beyond approximately 20 nm can be found. For all other materials the largest pore sizes present to a significant degree are around a size of 25 nm. Nevertheless, also the CPV plot trends of the silica and titania NP-fibers lie within the narrow range which is spanned by the NP-fibers of the other materials.

In summary, the comparison of all data illustrated in figure 3-37 reveals fundamentally different trends concerning mesoporosity of the differently synthesized materials: While the mesoporous structure of electrospun sol-gel fibers features different trends, fibers obtained from preformed dispersed nanoparticles exhibit a well-defined mesoporous structure which is practically identical for several oxide materials. The different trends in the CPV-plots of the sol-gel fibers are based on altering conditions influencing the structure formation during their synthesis: As introduced and discussed before (see e. g. chapters 2.5) details of the sol-gel process which differ with the material to be synthesized, possible templating effects of the spinning polymer and/or (spinodal) phase separation, which may occur in sol-gel systems, allow for varying mesoporous structures of electrospun sol-gel-based oxide fibers. For example, the slightly increased mesoporosity of the ceria and the tin oxide sol-gel fibers presumably can be attributed to such effects. Thus, the mesoporosity of sol-gel fibers remains unpredictable as long as these effects cannot be addressed straightforwardly for such complex electrospinning systems.

In contrast, the well-defied mesoporous structure of the NP-fibers is a consequence of the EICA process generating the same mesoporosity for different materials. As long as preformed, dispersible oxide nanoparticles can be incorporated into a spinning solution, a mesoporous fiber can be obtained via the EICA process no matter which oxide is considered. The mesoporosity of the NP-fibers seems to be predictable since the CPV-plots calculated by the DFT method end up in the narrow range of 51−64% for the relative porosity for all materials.[32] Though not illustrated in figure 3-37 it has to be restated that materials resulting from unspun, dried and calcined spinning solutions are also mesoporous. Their structure resembles the mesoporous structure of the corresponding NP-fibers though it is not that well-defined and predictable. The bulk materials suffer from the missing confinement of the electrospinning experiments which restricts the structure formation process to a very limited timescale and space.

Turning to the preparation of bulk materials from the same nanoparticles by drying and calcination of the pure particle dispersions does not result in comparable mesoporous materials because sintering and coalescence of the particles often prevents a similar mesoporous structure. Consequently, the mesoporosities of the pure particle samples span a very wide range of 6−52% for the cumulated relative porosities.

In Conclusion, the quintessence of the comparison of the CPV-plots of all materials is that the EICA process not only explains the occurrence of mesoporosity in electrospun fibers prepared from oxide nanoparticles but also allows predicting the mesoporous structure. The strikingly similar CPV-plots for all nanoparticle-based oxide fibers are a consequence of the EICA process which is summarized in chapter 4.

[32] It has to be noted, that NP-fibers of each material with increased porosity were selected for Figure 3-37 in order to demonstrate which porosities can be achieved by the NP-approach. Cases in which lower porosities occurred under slightly different experimental conditions (see e. g. chapter 3.3.5) demonstrate the limitations and preconditions for the EICA process which are recapitulated in chapter 4.

3.6.2 Comparison of specific surface areas of different oxide materials

In order to compare the specific surface areas of different materials the S_m values from table 3-2, table 3-6, table 3-8 and table 3-12 were converted to S_v and S_n values (see table 3-14) as suggested in chapter 2.6.3. The same samples as for the comparison of the porosities (see table 3-13) were selected in order to investigate whether there are any analogies between the specific surface area characteristics and the relative porosities of these samples. The results are also listed with respect to the preparation method in order to identify if there are any common features of the samples that depend on the synthetic approach.

Table 3-14: Comparison of the specific surface areas of selected, representative samples of all materials investigated within this thesis including former results on titania.[75] The samples are selected and grouped with respect to the preparation method to illustrate general trends that are connected to the preparation method. The specific surface areas are calculated in three different dimensions ($m^2 \cdot g^{-1}$, $m^2 \cdot cm^{-3}$ and $m^2 \cdot mol^{-1}$) to figure out which one is most adequate to compare different materials. For more precise sample information see table 3-1, table 3-4, table 3-7 and table 3-10. Blue highlighted numbers are the minima and red highlighted numbers are the maxima within a sample category illustrated for each dimension of *S*, respectively.

sample category	material	sample acronym	see	S_m [1] $[m^2 \cdot g^{-1}]$	S_v [2] $[m^2 \cdot cm^{-3}]$	S_n [2] $[m^2 \cdot mol^{-1}]$
sol-gel fibers (SG-F)	SiO_2	SiO_2-SG-F	table 3-1, sample 2	**234.6**	**516**	**$14.1 \cdot 10^3$**
	ZrO_2	ZrO_2-SG-F	table 3-4, sample 1	**27.7**	**169**	**$3.4 \cdot 10^3$**
	CeO_2	CeO_2-SG-F	table 3-7, sample 1	35.3	254	$6.1 \cdot 10^3$
	SnO_2	SnO_2-SG-F	table 3-10, sample 2	28.6	200	$4.3 \cdot 10^3$
	TiO_2	TiO_2-SG-F	table 2-2, sample 1	67.8	264	$5.4 \cdot 10^3$
pure, dried and calcined particles (PP)	SiO_2	SiO_2-PP	table 3-1, sample 3	**215.3**	474	$12.9 \cdot 10^3$
	ZrO_2	ZrO_2-PP (MWS)	table 3-4, sample 13	41.4	253	**$5.1 \cdot 10^3$**
	ZrO_2	ZrO_2-PP (WCS)	table 3-4, sample 12	52.7	321	$6.5 \cdot 10^3$
	CeO_2	CeO_2-PP	table 3-7, sample 5	**32.4**	**233**	$5.6 \cdot 10^3$
	SnO_2	SnO_2-PP	table 3-10, sample 6	149.7	**1048**	**$22.6 \cdot 10^3$**
	TiO_2	TiO_2-PP	table 2-2, sample 2	73.0	285	$5.8 \cdot 10^3$
nanoparticle-based fibers (NP-F)	SiO_2	SiO_2-NP-F	table 3-1, sample 6	**213.9**	471	$12.9 \cdot 10^3$
	ZrO_2	ZrO_2-NP-F	table 3-4, sample 6	82.6	504	$10.2 \cdot 10^3$
	CeO_2	CeO_2-NP-F	table 3-7, sample 2	120.1	**865**	**$20.7 \cdot 10^3$**
	SnO_2	SnO_2-NP-F	table 3-10, sample 4	**47.3**	**331**	**$7.1 \cdot 10^3$**
	SnO_2	SnO_2-B+M-F	table 3-10, sample 5	55.2	386	$8.3 \cdot 10^3$
	TiO_2	TiO_2-NP-F	table 2-2, sample 4	163.7	638	$13.1 \cdot 10^3$

[1]: specific surface area calculated by the BET method;
[2]: converted from S_m $[m^2 \cdot g^{-1}]$.

When the different specific surface area data from table 3-14 are compared, there are several findings:

- The S_m values span a wide range of 28−235 $m^2 \cdot g^{-1}$.
- Consequently, also the S_v and S_n values span wide ranges of 169−1048 $m^2 \cdot cm^{-3}$ and $3.4 \cdot 10^3$−$22.6 \cdot 10^3$ $m^2 \cdot mol^{-1}$ respectively.
- If the different sample groups are considered, there are no clear trends. Neither the pure particles nor the NP-fibers exhibit significantly different data ranges in any dimension of the specific surface areas compared to the sol-gel fibers.
- Also within the specific sample groups, there is in principle no clear, deducible trend concerning the data of the different materials in any dimension of the data.[33]
- The maxima and minima highlighted in table 3-14 change with the sample group and the dimension of *S* without any interpretable basic trend. Only seemingly random extrema were found (see below).
- The zirconia sol-gel fibers exhibit the lowest specific surface area of all sol-gel fibers, irrespective of the dimension of *S*.
- Likewise, the tin oxide NP-fibers exhibit the lowest specific surface area of all NP-fibers irrespective of the dimension of *S*. Simultaneously, the pure tin oxide nanoparticles exhibit the highest specific surface areas in the dimensions S_v and S_n. This is a direct consequence of the microporosity of the pure tin oxide particles which vanishes in the corresponding NP-fibers.
- Ceria as the material with the highest density possesses extraordinary high S_v and S_n values for the NP-fibers and very low values for the pure particles in the dimensions S_m and S_v. These data of the ceria material demonstrate clearly the "dimension dilemma" that is connected to the comparison of specific surface areas. It remains unclear in which dimension the specific surface areas should preferably be compared to other materials.

Most of the above mentioned findings cannot be ascribed to a specific reason and hence can only be summarized to some vague conclusions, which are less substantial than the very clear, fundamental results concerning the mesoporosity of the samples. There is neither any analogy to the relative porosities of the different materials nor any common feature arising from the synthetic preparation method applied. These findings are in principle independent of the dimension of the specific surface area.

[33] The fact that the silica materials exhibit by far the highest S_m values is a trivial consequence of the by far lowest density of all materials and thus not a relevant result.

Generally, the specific surface areas of the different samples are not an intrinsic property originating from a special feature of sol-gel precursors or the nanoparticles used as building blocks of the samples. In the previous chapters it was already discussed that the specific surface areas of nanoparticle-based materials is usually found to be lower than a theoretical value calculated by equation (3-1) as a consequence of condensation and sintering during calcination. Since the degree of condensation and sintering varies strongly with the chemical nature of the material it is not surprising that the specific surface areas of the different nanoparticle-based metal oxides strongly depend on the material under consideration. Furthermore, microporosity is of decisive influence on the specific surface areas so that very high specific surface areas are found for materials featuring microporosity like the samples of pure tin oxide particles and silica sol-gel fibers.

In conclusion, it is not possible to assemble the above mentioned findings to some basic trends in the sense of a fundamental concept in a similar manner as it was possible for the relative porosities. Hence, further investigations of the specific surface areas of different oxides including analyses of their microporosity are a challenging task for future studies.

4 The EICA concept: Applicability and limits allowing for the directed preparation of oxide nanofibers with highly mesoporous structure

The comparative analyses of the physisorption results in chapters 3.6.1 revealed fundamental trends which are independent of the material under consideration constituting the basis of a general concept concerning the directed synthesis of highly mesoporous oxide materials via electrospinning. This section briefly summarizes this concept as the main result of this thesis.

Electrospun sol-gel fibers were shown to exhibit generally lower mesoporosity than inorganic fibers derived from solutions containing nanoparticles. The increased mesoporosity of nanoparticle-based fibers can be explained on the basis of fundamental principles of colloidal chemistry concerning the aggregation of dispersed nanoparticles. Starting from a homogeneous dispersion experiencing solvent evaporation a new model of evaporation-induced cluster aggregation (EICA) based on the DLVO theory was developed (see figure 4-1). The EICA model is similar to the model of diffusion limited cluster aggregation (DLCA) but EICA is predominantly governed by evaporation while DLCA is controlled by the diffusion of particles. However, the increased mesoporosity of nanoparticle-based fibers originates from their packing behavior. Based on the simple idea that dispersed nanoparticles basically behave like “hard” spheres stabilized by their surface potential and the surrounding electrochemical double layer (EDL) their packing in electrospinning solutions is driven by the decreasing thickness of the EDL due to the proceeding solvent evaporation. Since solvent evaporation during electrospinning is extraordinary fast, dispersed nanoparticles aggregate instantaneously as soon as the EDL is thin enough that they experience net attractive forces. Furthermore, the very fast evaporation facilitates a random aggregation resulting in clusters or a network of low fractal dimension. With this simple EICA model the basic trends in all physisorption experiments on nanoparticle-based oxide materials can be understood irrespective of the chemical nature of the oxide under investigation.

When the nanoparticles are aggregated in a random manner in the composite as-spun fibers a mesoporous structure is inherently present if the spinning polymer can be removed under preservation of the open fractal arrangement of the particles. Calcination of the fibers leads to the combustion of the polymer while adjacent particles condense and sinter on their surfaces.

It was discussed that the structures of samples prepared under usage of a polymer – i. e. bulk as well as fiber samples – are all highly mesoporous because the polymer acts as “void filling structure support” rather than as a “classical” - i. e. micelle forming - template. In contrast, materials obtained from the pure nanoparticle dispersions after drying and calcination are generally less mesoporous and featured only small mesopores which are typically smaller than the particle diameter while also larger pores are obtained if a polymer was used for the preparation of the samples. The polymer supports the open fractal structure in the “as-prepared” samples of the oxide nanoparticles during calcination. Since the open fractal arrangement is basically preserved throughout the calcination process if a polymer was present, it was deduced that the particles condense and sinter to a self-supporting network before the

polymer melts and combusts. Less mesoporous materials are obtained if the polymer is absent, because the missing structure support allows rearrangement of the particles during calcination before condensation and sintering consolidates the “as-prepared” structure.

When the mesoporous structure of nanoparticle-based fibers was compared to corresponding bulk samples prepared by drying and calcination of electrospinning solutions without spinning them a “confinement effect” during electrospinning was discovered. This “confinement effect” in the electrospinning experiments was found to be the main benefit of the preparation of mesoporous materials via electrospinning and concerns the two dimensions of time and space: The very fast solvent evaporation during electrospinning, representing a confinement in time, and the small volume of the electrospinning jet, representing the confinement in space, result in a well-controlled preparative process. This well-controlled process results in excellently reproducible mesoporous structures of the inorganic fibers prepared via electrospinning, which exhibit remarkably high and similar mesoporosity for all materials irrespective of the nanoparticles used in the synthesis. If the same electrospinning solutions are used to prepare bulk samples, other structures also exhibiting mesoporosity are obtained. However, in this case the missing confinement leads to much stronger variations in the mesoporous structures of these materials.

The ratio of the spinning polymer to the inorganic nanoparticles in the spinning solution was found to have no significant influence on the mesoporous structure of the resulting fibers. This phenomenon is a consequence of the EICA process: The extent of volume lost due to polymer combustion only influences the degree of shrinkage during calcination but does not affect the internal open fractal structure of the prearranged clusters in the composite as-prepared materials.

In the case of zirconia or titania materials several further experiments were conducted in order to investigate the influence of parameters like molecular weight of the spinning polymer, solvent composition or nanoparticle properties (e. g. size and surface structure). Moreover, also atmospheric conditions (i. e. temperature and humidity in the spinning chamber) were found to affect the structure formation process during spinning.

All these parameters constitute an at least eight-dimensional phase diagram of the spinning solution which hardly can be established and understood in all details (see chapter 2.5.4.2). Consequently, also the individual influence of the above mentioned parameters cannot be comprehended from the limited amount of experiments conducted so far, neither in the sense of the EICA concept nor in the sense of SD. Especially the interdependence of influences from solvent and particle properties prevents a decided interpretation. Furthermore, it is unclear which solvent property is decisive for the generation of highly mesoporous materials from preformed, dispersed nanoparticles (see chapter 3.3.5).

However, irrespective of some differences which are based on the influences of the above mentioned parameters, all nanoparticle-based fibers still exhibit significantly increased mesoporosity compared to sol-gel-derived fibers because the EICA process is fundamentally different from structure formation in sol-gel-based materials.

As a matter of fact, the EICA concept cannot be considered for structure formation processes in sol-gel-based materials because no preformed nanoparticles are present. Hence, structure formation in sol-gel-based electrospun fibers has to be explained by the concept of SD. Since sol-gel precursors are highly soluble in typically applied solvents[34] a thermodynamically unstable solution composition as a precondition for a SD cannot be achieved easily for sol-gel-based electrospun fibers. For a directed synthesis of highly mesoporous electrospun fibers from sol-gel precursors it is necessary to find adequate precursors and spinning solutions which are prone to undergo phase separation because the initial situation in the spinning solution is already close to a phase boundary of the system. Since this requirement is predominantly controlled by chemical properties which vary with the precursors, and thus the elements considered, it is a challenging task to find a fundamental, conceptual strategy to prepare mesoporous fibers from sol-gel precursors. In contrast, the EICA process predominantly governed by physical interactions, which usually do not change dramatically with nanoparticles of different elements, allows for a directed synthesis of highly mesoporous fibers irrespective of the desired oxide material.

Nevertheless, the physisorption results obtained from nanoparticle-based electrospun fibers of different materials revealed at least some chemical influence: When a theoretical specific surface area is calculated using measured particle sizes and equation (3-1), it was demonstrated that the measured specific surface areas are generally lower than the theoretically expected ones though depending on the particles to a varying degree. This phenomenon was basically attributed to the altering tendency of the oxide materials to sinter which directly correlates to their chemical nature. The sintering tendency of different oxides depends on their thermodynamical stability.

It was exemplarily demonstrated for tin oxide materials that the preparation of electrospun fibers via the brick and mortar method results in fibers which cannot be distinguished from NP-fibers by any analytical method used within the presented investigations (i. e. WAXS, SEM and physisorption). This synthetic approach is very promising concerning applications of nanofibers because it could be demonstrated that the brick and mortar concept is beneficial concerning physical properties like electronic conduction within the prepared material.[2]

[34] For example some alkoxide precursors like $Zr(OiPr)_4$ can be purchased in 80 wt.-% concentration in isopropanol proving the very high solubility of this precursor in isopropanol.

It was not possible to gain similar conceptual results concerning the specific surface areas of electrospun fibers and/or nanoparticles as for the porosity of such materials. First, there is the principle “dimension dilemma” for the comparison of specific surface areas if different materials are to be compared. While a dimensionless relative porosity as physical index quantity enables unequivocal comparability of different materials concerning porosity, such index quantity cannot be generated concerning specific surface areas. The specific surface areas of different materials can basically be comparable in three different dimensions, namely as S_m [$m^2 \cdot g^{-1}$], S_n [$m^2 \cdot mol^{-1}$] or S_v [$m^2 \cdot cm^{-3}$] values (see chapter 2.6.3). All three dimensions are generally reasonable, but it is a matter of consideration, in which dimension specific surface areas should preferably be compared. Moreover, microporosity strongly affects specific surface areas of porous materials principally. Nitrogen physisorption analyses conducted within this thesis revealed that pure nanoparticles exhibit significant microporosity in some cases without being able to characterize this microporosity in detail. Interestingly, it was found that this microporosity vanishes in electrospun fibers prepared from these particles, which cannot be explained so far. Hence, it is necessary to analyze the microporosity of such nanoparticles in detail to gain insights into parameters which determine the occurrence of microporosity. Such a study may likely also lead to a better understanding of the specific surface areas determined within this thesis.

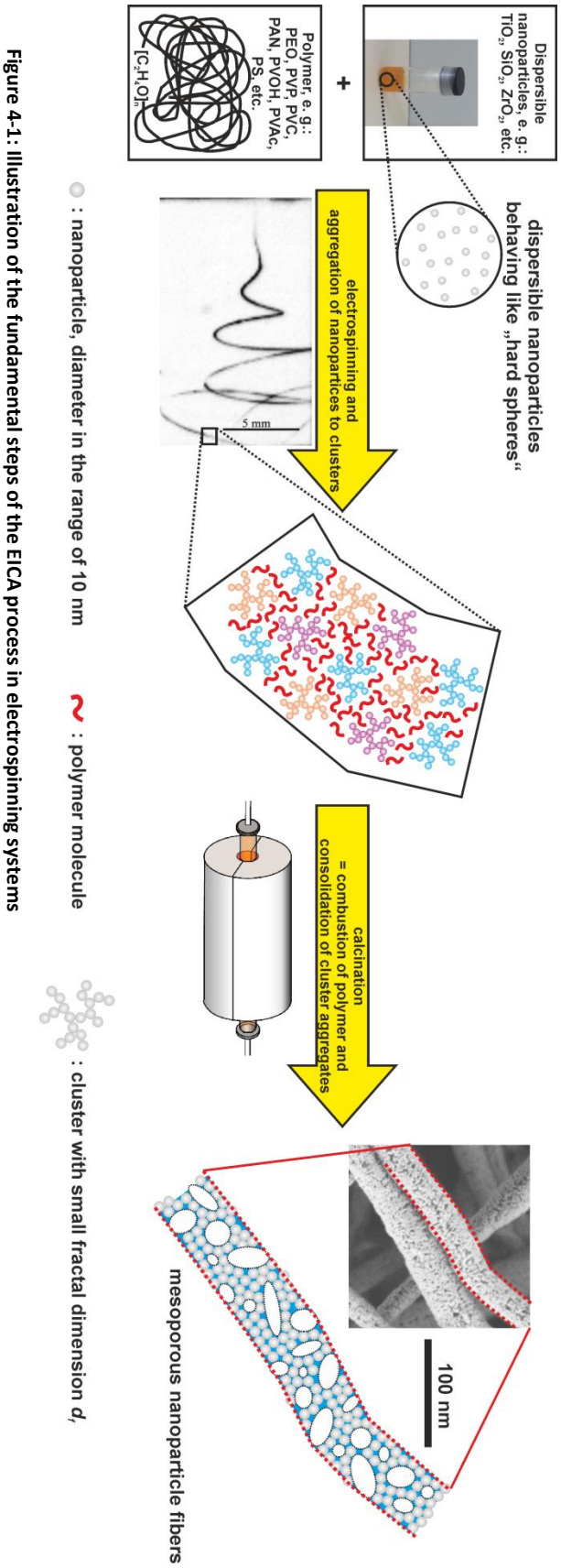

Figure 4-1: Illustration of the fundamental steps of the EICA process in electrospinning systems

5 Summary and outlook

5.1 Summary

This thesis demonstrates alternative synthetic approaches to prepare metal oxide nanofibers using sol-gel precursors, preformed nanoparticles or a combination of both (so-called “brick and mortar” approach). Electrospun fiber mats, which intrinsically exhibit large inter-fiber void spaces representing macropores, are an adequate candidate to prepare hierarchically porous materials by implementing additional meso- and/or microporosity into the fibers. This thesis identifies a new sophisticated concept to prepare porous fibers straightforwardly by comparing alternative synthetic approaches yielding electrospun oxide fibers. Moreover, these studies exhibit the first comprehensive study of electrospun metal oxide fibers concerning the generation of mesoporosity during the electrospinning experiment resulting in a fundamental conceptual understanding of structure-generating processes taking place in such systems.

In the initial part of this thesis the physisorption analyses conducted on electrospun silica fibers investigated the general applicability of DFT analysis on electrospun fibers resulting in the selection of one specific DFT kernel assuming spherical pore geometry for pore sizes beyond 5 nm diameters for the analysis of electrospun fibers. It was discussed that the analysis of electrospun fibers with this DFT kernel is adequate to characterize the mesoporosity of electrospun fiber materials comparatively in terms of the trend of cumulative pore volume (CPV) plots and the accumulation of pore volume with increasing pore size. Otherwise, it was demonstrated that the exact determination of pore sizes cannot be accomplished by this method because it cannot be guaranteed that the assumed pore geometries in the DFT model are in accordance with the pore geometries in the fibers. Consequently, the calculated pore sizes have to be considered as a rough estimation only.

After these basic methodic analyses a systematic study on well-selected silica materials was conducted in order to gain insight into the origin of mesoporosity which is frequently observed in electrospun fibers prepared from preformed, dispersed nanoparticles. In contrast, similar mesoporosity was never observed if metal oxide fibers were synthesized by using sol-gel precursors as a starting material. Such comprehensive study resulted in the establishment of a fundamental concept explaining the occurrence of mesoporosity in nanoparticle-derived electrospun fibers. This concept of evaporation-induced cluster aggregation (EICA) is summarized an explained in detail in chapter 4.

Subsequent to the silica experiments, further metal oxide nanofibers of zirconia, ceria, and tin oxide were electrospun, each using sol-gel precursors and, alternatively, nanoparticles as building blocks for the fibers. Tin oxide fibers were also prepared by combining both sources of the oxide in a “brick and mortar” (B+M) approach. All these experiments provided evidence for the fundamental electrospinning concept initially established from the silica experiments and several further conclusions from these experiments were implemented into the basic EICA concept, which in summary is generally valid for all kinds of inorganic oxide fibers.

As stated in chapter 2.2.1 (see figure 2-2) approaches to prepare porous materials are mostly based on the opposing basic concepts of decomposition or templating. However, it was found that the EICA process is neither based on typical decomposition nor on templating. EICA is rather a process of (random) aggregation of nanoparticles in a polymer matrix which is only acting as a "void filling structure support" and not as a classical template. Moreover, the EICA process resulted in very similar mesoporous structures for all investigated oxide materials facilitating to predict the mesoporous structure of other oxide materials that can be prepared by this approach. This predictability is a consequence of the nature of the EICA process predominantly governed by physical parameters like evaporation speed of the solvent or (physical) stabilization of the dispersed nanoparticles, which are comparable for all investigated systems of different oxide materials. In contrast, the preparation of sol-gel-based electrospun fibers is strongly influenced by chemical parameters like the reactivity of the sol-gel precursors leading to strongly different structure formation processes depending on the considered metal oxide. These altering conditions prevent postulating a fundamental preparation concept for sol-gel-based (mesoporous) electrospun fibers comparable to the EICA concept.[35]

Further parameters of influence are e. g. the solvent composition of the spinning solution, surface properties of the nanoparticles determining their dispersibility or temperature and humidity in the spinning chamber. These parameters also influence the EICA process as demonstrated exemplarily for zirconia or titania materials (see chapter 3.3.5). Unfortunately, these parameters are interdependent preventing to deduce a clear cause-and-effect chain for these details so far: The employed multi-component spinning solutions are so complex that in practice they never can be understood in all aspects leaving some questions of detail unanswered (see chapter 5.2).

Nevertheless, the developed electrospinning concept is a powerful tool to address mesoporosity in the synthesis of inorganic nanofibers and to explain resulting structures of sol-gel-derived, nanoparticle-derived and B+M-derived fibers with hierarchically porous structure. While mesoporosity can be generated as intra–fiber porosity by the approaches investigated within the scope of this thesis, electrospun fiber mats intrinsically exhibit large inter-fiber void spaces representing macroporosity. Such hierarchical meso-/macroporous nanoarchitectures are of considerable interest for application in electrochemical devices, heterogeneous catalysis or sensing as introduced earlier (see e. g. chapters 3.3.1.1, 3.4.1.1 or 3.5.1.1). The established fundamental electrospinning concept represents significant scientific progress in the field of nanostructured materials, as it contributes to the understanding of mesopore-generating processes during electrospinning of oxide fibers and consequently enables a directed synthesis of mesoporous inorganic fibers. The EICA model, developed within this thesis, along with the well-elaborated set of guidelines provides materials scientists with new tools for accurately creating customized mesoporous fiber materials.

[35] As a matter of fact the EICA process cannot take place in sol-gel-based electrospinning systems because no preformed nanoparticles are present.

5.2 Outlook

The results of this thesis directly lay the foundations for further projects which can benefit from the knowledge gained and/or which can probably expand the pivotal results acquired so far.

First, the beneficial hierarchical pore structure of mesoporous electrospun oxide fibers has to be confirmed in applications. Therefore, especially gas sensing experiments with tin oxide fibers and catalytic experiments with ceria and $Ce_xZr_{1-x}O_2$ fibers are already projected. Ceria and $Ce_xZr_{1-x}O_2$ fibers are under investigation as catalysts in the heterogeneous oxidation of hydrochloric acid (Deacon process) in the institute exhibiting promising results (see chapter 3.4.1.1). Recent results on electrospun fibers comparing nanoparticle-based and sol-gel-based ceria fibers concerning the Deacon process are already submitted[198] or published.[199] However, these investigations are limited to pure ceria materials suffering from insufficient stability in the Deacon process. Otherwise, investigations on ceria-zirconia solid solutions, known to be chemically more stable in the Deacon process, are limited to sol-gel-derived fibers so far, which exhibit lower mesoporosity than nanoparticle-derived fibers. Consequently, using nanoparticles consisting of ceria-zirconia solid solutions for the synthesis of electrospun fibers and investigating these fibers concerning the Deacon process should be performed as a next step.

Apart from such applications, there are also fundamental questions remaining which are worthwhile being studied. The macroporosity of electrospun fiber mats is generally believed to be intrinsically present, although detailed analyses of fiber mat macroporosity are missing so far. Hence, future work should include mercury porosimetry to analyze electrospun fiber mats, though it is challenging and elaborate to produce enough fibers to conduct such measurements. However, mercury porosimetry and its correlation to nitrogen physisorption results can also deliver a more precise characterization of mesoporosity beyond a pore size of approximately 30 nm, which is the upper limit of reliability for nitrogen physisorption analysis, if no other complemental method is applied in addition.

Furthermore, detailed analysis of microporosity in electrospun fibers and the nanoparticles employed in the fiber syntheses should be performed to gain an improved understanding of the origin of specific surface areas which are obtained for the synthesized materials. So far, it is not completely understood, in which cases microporosity occurs that causes substantially increased specific surface areas.

The porosity of nanoparticles is strongly influenced by the conditions during their synthesis. As shown e. g. in chapter 3.3, syntheses in microwave reactors seem to result in more dense materials compared to syntheses conducted in a “classical” wet chemical approach. Accordingly, more detailed analyses on the dispersible nanoparticles are recommended for future projects. Such investigations should also address the surface properties of the particles determining their dispersibility and thus their behavior in electrospinning solutions. For a more detailed understanding of the impact of particle properties on the mesoporosity of electrospun fibers, it is essential to comprehend, how the particles are stabilized in dispersion. Hence, analysis of density and nature of functional groups on the surface of the particles by methods like elemental analysis, ^{1}H-NMR, ^{13}C-NMR, IR- or Raman spectroscopy should be performed in order to gain a further in-depth understanding of the behavior of such particles.

6 Appendices

6.1 Abbreviations

350 K	abbreviation for molecular weight M_w [kg·mol^{-1}], i. e. 350 K corresponds to a molecular weight of M_w = 350,000 g·mol^{-1}
ads. vol.	adsorbed volume
AFM	atomic force microscopy
at.-%	atomic percent
ATO	antimony doped tin oxide (typically 10 at.-% antimony and 90 at.-% tin oxide)
B+M	brick and mortar; a concept used for the preparation of inorganic materials by combining a sol-gel precursors and preformed nanoparticles
B+M-fibers	electrospun fibers prepared according to the brick and mortar concept
BET	acronym for the Brunauer-Emmett-Teller method for the calculation of specific surface areas (S_m)
CPV	cumulative pore volume: obtained by DFT calculations
DFT	density functional theory
DLCA	diffusion-limited cluster aggregation
DLS	dynamic light scattering
DLVO (theory)	Derjagin-Landau-Verwey-Overbeek (theory): describes interactions of colloidal particles
DMF	dimethylformamide
D_n	population weighted mean hydrodynamic diameter of particles measured by DLS
D_v	weight weighted mean hydrodynamic diameter of particles measured by DLS
EICA	Evaporation-induced cluster aggregation
EISA	evaporation-induced self-assembly
EDL	electrochemical double-layer
EtOH	ethanol
FTO	fluorine doped tin oxide (typically 5 at.-% fluorine and 95 at.-% tin oxide)
GISAS	grazing-incidence small-angel scattering
h	hour(s)
HCl	hydrochloric acid
ICSD	Inorganic Crystal Structure Database
ITO	indium tin oxide (typically 90 at.-% indium and 10 at.-% tin oxide)
JCPDS	Joint Committee on Powder Diffraction Standards
LCST	lower critical solution temperature
MeOH	methanol
min.	minute(s)
M_w	weight weighted mean molecular weight of polymers in [g·mol^{-1}]
MWS-NPs	microwave synthesized nanoparticles
NLDFT	non-linear density functional theory

NP	nanoparticle
NP-fibers	electrospun fibers derived from preformed nanoparticles
OiPr	isopropyl
PEO	poly(ethylene oxide)
PLD	pulsed laser deposition
PMMA	poly(methyl methacrylate)
PVA	poly(vinyl alcohol)
PVP	poly(vinylpyrrolidone)
QSDFT	quenched-solid density functional theory
rpm	rotations per minute
SANS	small-angle neutron scattering
SAXS	small-angle X-ray scattering
SD	spinodal decomposition
SEM	scanning electron microscopy
S_m	specific surface area in $[m^2 \cdot g^{-1}]$
S_n	specific surface area in $[m^2 \cdot mol^{-1}]$
sol-gel fibers	electrospun fibers derived from sol-gel precursors
S_v	specific surface area in $[m^2 \cdot cm^{-3}]$
TCO	transparent conducting oxide
TEM	transmission electron microscopy
TEOS	tetraethyl orthosilicate
TIPS	thermally induced phase separation
T_b	boiling temperature
T_g	glass transition temperature
THF	tetrahydrofuran
T_m	melting temperature
TMOS	tetramethyl orthosilicate
TPV	total pore volume: calculated by the Gurvich rule (see equation (2-11))
UCST	upper critical solution temperature
VIPS	vapor induced phase separation
WAXS	wide-angle X-ray scattering
WCS-NPs	wet chemically synthesized nanoparticles
wt.-%	weight percent

6.2 Experimental details

6.2.1 Chemicals

Water has passed an ion exchanger before it was used in the syntheses.

All other chemicals were used as received and without further purification.

Table 6-1: Inorganic precursors

name	formula	CAS number	purity	supplier
tetramethyl orthosilicate (TMOS)	$Si(OCH_3)_4$	681-84-5	98%	Sigma Aldrich
zirconyl chloride octahydrate	$ZrOCl_2 \cdot 8H_2O$	13520-92-8	99.5%	Sigma Aldrich
cerium(III) chloride heptahydrate	$CeCl_3 \cdot 7H_2O$	18618-55-8	99.9%	Sigma Aldrich
Tin(II)chloride dehydrate	$SnCl_2 \cdot 2H_2O$	10025-69-1	---	ABCR

Table 6-2: Solvents

name	formula	CAS number	purity	supplier
benzyl alcohol	C_7H_8O	100-51-6	99%	Grüssing
chloroform	$CHCl_3$	67-66-3	99.9%	Carl Roth
dichloromethane	CH_2Cl_2	75-09-2	---	---[36]
diethyl ether	$C_4H_{10}O$	112-30-1	---	---[36]
dimethylformamide	C_3H_7NO	68-12-2	99%	Sigma Aldrich
n-hexane	C_6H_{14}	110-54-3	---	---[36]
methanol	CH_4O	67-56-1	99.9%	Carl Roth
ethanol	C_2H_6O	64-17-5	99.9%	VWR
water	H_2O	7732-18-5	---	---[36]
1,3-propanediol	$C_2H_8O_2$	504-63-2	98%	Sigma Aldrich
tetrahydrofuran	C_4H_8O	109-99-9	99.9%	Carl Roth

Table 6-3: Polymers

name	abbreviation	formula	CAS number	M_w [g·mol^{-1}][1)]	purity	supplier
poly(ethylene oxide)	PEO	$[C_2H_4O]_n$	25322-68-3	1,000,000	---	Alfa Aesar
poly(ethylene oxide)	PEO	$[C_2H_4O]_n$	25322-68-3	300,000	---	Alfa Aesar
poly(vinylpyrrolidone)	PVP	$[C_6H_9NO]_n$	9003-39-8	1,300,000	---	Alfa Aesar
poly(methyl methacrylate)	PMMA	$[C_5H_8O_2]_n$	9011-14-7	350,000	---	Sigma Aldrich
poly(methyl methacrylate)	PMMA	$[C_5H_8O_2]_n$	9011-14-7	996,000	---	Sigma Aldrich

[1)]: M_w is typically abbreviated as K-value: e. g. 350K refers to a polymer with an M_w = 350,000 g·mol^{-1}.

Table 6-4: Other reagents

name	formula	CAS number	purity	supplier
hydrochloric acid	HCl	7647-01-0	37 wt.-% in H_2O	---[36]
Ludox "AS-30" dispersion	SiO_2 in H_2O	7631-86-9 50-00-0 55965-84-9	30 wt.-% SiO_2 in H_2O	Sigma Aldrich
Ludox "HS-30" dispersion	SiO_2 in H_2O	7631-86-9 50-00-0 55965-84-9	30 wt.-% SiO_2 in H_2O	Sigma Aldrich
Ludox "SM-30" dispersion	SiO_2 in H_2O	7631-86-9 7732-18-5 1313-59-3	30 wt.-% SiO_2 in H_2O	Sigma Aldrich

[36] This chemical was obtained from the internal chemical supply of our faculty.

6.2.2 Synthetic methods

All concentrations given in weight percent are referred to the total mass of the solution.

6.2.2.1 Preparation of / supply with nanoparticle dispersions

6.2.2.1.1 Titania nanoparticle dispersions

The preparation of titania nanoparticle dispersions is described elsewhere.[75]

6.2.2.1.2 Silica nanoparticle dispersions

Silica nanoparticle dispersions were purchased from Sigma Aldrich in a batch size of one liter. Three different silica dispersions, know under the registered trademark name "Ludox" were used for the experiments. The three different Ludox dispersions all exhibit a solid content of 30 wt.-% SiO_2, but differ in their specification concerning their stabilization and slight differences in their size. For the detailed specifications the reader is referred to the literature.[143] The following dispersions were employed in this thesis

- Ludox "HS30" dispersion: sodium stabilized dispersion; typical diameter of the particles is specified to be 12 nm;
- Ludox "AS 30" dispersion: ammonium stabilized dispersion;
- Ludox "SM30" dispersion: sodium stabilized dispersion advertised to contain "high-surface area" particles; typical diameter of the particles is specified to be 7 nm.

6.2.2.1.3 Zirconia nanoparticle dispersions

Zirconia nanoparticle dispersions were gratefully provided by my project collaborator Mrs. Maren Möller. The zirconia nanoparticles were prepared via two methods, one using microwave irradiation as heating source, the second using classical oil-bath heating. The wet chemically synthesized nanoparticles (WCS-NPs) were dispersed in methanol in a concentration up to 10 wt.-%. The nanoparticles prepared in a microwave reactor (MWS-NPs) were also dispersed in methanol in a concentration up to 10 wt.-%.

6.2.2.1.4 Ceria nanoparticle dispersions

Ceria nanoparticle dispersions were gratefully provided by my project collaborator Mrs. Maren Möller. The ceria nanoparticles were prepared in a microwave reactor. The nanoparticles were dispersed in n-hexane in a concentration up to 8.2 wt.-% or chloroform in a concentration up to 5.8 wt.-%.

6.2.2.1.5 Tin oxide nanoparticle dispersions

Tin oxide nanoparticle dispersions were prepared in a wet chemical approach by using $SnCl_2 \cdot 2H_2O$ as precursor. First, 2.06 *g* precursor were dissolved in 5 *mL* ethanol. In another vessel 240 *mg* 1,3-propandiol were added to 20 *mL* benzyl alcohol. After having combined both solutions the reaction mixture was heated to 180 °C for 1 h using an oil bath. After cooling to room temperature the mixture was poured into 300 *mL* diethyl ether giving a slightly yellow precipitate that was separated by centrifugation (6 min. at 6000 rpm) and washed with diethyl ether. The precipitate was dispersed in THF in concentrations up to 5.7 wt.-%. For an increased particle concentration in the dispersion, a droplet of concentrated hydrochloric acid (37%) was added to THF.

6.2.2.2 Determination of dispersion concentrations

The concentration of nanoparticle dispersion was determined as follows: First, the solvent of a small portion of a nanoparticle dispersion under investigation (typically around 1 g dispersion) was removed in a drying oven at 80 °C. Afterward the solid residue was heated in a furnace up to 550 °C (standard calcination protocol, see chapter 6.2.2.8) and the mass concentration of the dispersion (in wt.-%) was calculated by dividing the mass of the calcined residue by the mass of the initially dried dispersion. The balance used for the determination of the masses had an accuracy of ± 0.1 mg.

6.2.2.3 Electrospinning: setup and general conditions

The electrospinning setup was self-constructed with the help of the institute`s mechanical and electrical workshops at the initial stage of this thesis project. It was assembled from the following purchased components:

- Two one-channel high voltage power supplies of the type "TSI-HV-series" (Scientific Instruments, 73529 Schwäbisch Gmünd, Germany) with a maximum potential of ±30 kV and a maximum current of 0.3 mA were used. One high voltage power supply was connected to the capillary tip of the syringe containing the spinning solution and the second one having opposite polarity was connected to the collector, which was a self-constructed round plate of brass exhibiting a diameter of 10 cm.
- For a constant feed rate of the spinning solution a syringe pump of the type "11Plus-MA1 70-2208" (Harvard Apparatus, 01746 Holliston, Massachusetts, USA) was employed.
- For spinning experiments under controlled atmospheric conditions a climate control device of the type VC^3 4018 (Vötsch Industrial Technology GmbH, 72336 Balingen, Germany) could be connected to the spinning chamber in order to set the temperature in the spinning chamber to value in narrow range of approximately ± 1 °C and the humidity within an interval of approximately ± 5%.

The whole setup was placed in a chamber constructed from acrylic glass.

The spinning experiments were conducted as follows: The spinning solution was drawn into a plastic syringe of typically 1 mL volume (B. Braun Ag, 34209 Melsungen, Germany) equipped with a capillary tip of typically 0.6 mm inner diameter, which was clipped perpendicular to its axis and deburred prior to use to provide a homogeneous electric field. The feed rate of the syringe pump was initially set to a typical value of about 500 $mL \cdot h^{-1}$ and the voltage of the power supply connected to the capillary tip was slowly increased until the electric charge on the solution overcomes the surface tension. Afterwards the feed rate of the syringe pump was optimized to a value at which constant spinning was guaranteed by applying a feed rate which promotes the same solution volume as can be withdrawn by the electric field. On the collector a potential of 2 kV with opposite polarity to the potential on the capillary tip was applied throughout the experiment. After the feed rate of the syringe pump was set to the appropriate value a sheet of aluminum foil was placed on the collector to collect the fibers. For SEM investigation a small piece of silicon wafer (approximately 5x5 mm^2) was placed onto the collector for some seconds. If PEO was used as spinning polymer the humidity in the spinning

chamber was set to a value which was in a range of approximately 20−30%, because electrospinning of PEO generally suffers from bead formation at higher humidity.[200]

6.2.2.4 Preparation of sol-gel nanofibers

6.2.2.4.1 Silica sol-gel fibers

Silica sol-gel fibers were prepared by mixing 2.0 g tetramethyl orthosilicate (TMOS), 6.36 g methanol and 4.0 g of a 1M aqueous solution of hydrochloric acid under stirring. Afterwards 0.651 g poly(vinylpyrrolidone) (PVP, M_w = 1.300.000 g·mol^{-1}) were added under stirring to dissolve the polymer until a homogeneous solution was obtained. This spinning solution contained 5 wt.-% PVP and 15 wt.-% TMOS (equaling 6 wt.-% SiO_2).
A second solution was prepared in a similar manner by adding 1.075 g PVP (instead of 0.651 g) to an otherwise identical solution resulting in a spinning solution containing 8 wt.-% PVP and 15 wt.-% TMOS (equaling 6 wt.-% SiO_2) was obtained.

6.2.2.4.2 Zirconia sol-gel fibers

Zirconia sol-gel fibers were prepared by mixing 0.505 g zirconyl chloride octahydrate ($ZrOCl_2 \cdot 8H_2O$), 0.815 g ethanol, 2.51 g water and 2.00 g of a previously prepared 15 wt.-% solution of poly(vinylpyrrolidone) (PVP, M_w = 1.300.000 g·mol^{-1}) in ethanol. This solution was stirred until a homogeneous solution was obtained. The obtained solution contained 5.2 wt.-% PVP and 8.6 wt.-% $ZrOCl_2 \cdot 8H_2O$ (equaling 3.3 wt.-% ZrO_2).

6.2.2.4.3 Ceria sol-gel fibers

Ceria sol-gel fibers were prepared by mixing 246 mg cerium(III) chloride heptahydrate ($CeCl_3 \cdot 7H_2O$), 609 mg methanol, 604 mg ethanol and 221 mg dimethylformamide (DMF). This solution was heated for ten minutes in on open vessel at 125 °C in order to produce a complex from the sol-gel precursor and DMF.[89] Afterwards this solution was filled up to a total mass of 1,600 mg by adding ethanol. Furthermore 121 mg water and 1,013 g of a previously prepared 15 wt.-% solution of poly(vinylpyrrolidone) (PVP, M_w = 1.300.000 g·mol^{-1}) in ethanol were added. This solution was stirred until a homogeneous solution was obtained. The obtained spinning solution contained 3.4 wt.-% PVP and 5.6 wt.-% $CeCl_3 \cdot 7H_2O$ (equaling 2.6 wt.-% CeO_2).

6.2.2.4.4 Tin oxide sol-gel fibers

Tin oxide sol-gel fibers were prepared by mixing 90 mg tin(II) chloride dihydrate ($SnCl_2 \cdot 2H_2O$), 800 mg ethanol and 800 mg dimethylformamide (DMF). This solution was heated for ten minutes in on open vessel at 125 °C in order to produce a complex from the sol-gel precursor and DMF.[89] Afterwards 800 mg of a previously prepared 15 wt.-% solution of poly(vinylpyrrolidone) (PVP, M_w = 1.300.000 g·mol^{-1}) in ethanol were added. This solution was stirred until a homogeneous solution was obtained. The obtained solution contained 4.8 wt.-% PVP and 3.6 wt.-% $SnCl_2 \cdot 2H_2O$ (equaling 2.4 wt.-% SnO_2).

6.2.2.5 Preparation of nanoparticle-based nanofibers

Preliminary, polymer stock solutions of polymers used for electrospinning were prepared in the following concentrations:

- 15 wt.-% PVP (Mw = 1,300,000 g·mol^{-1}) in ethanol or methanol respectively;
- 5 wt.-% PEO (Mw = 300,000 g·mol^{-1}) in water, chloroform or dichloromethane respectively;
- 15 wt.-% PMMA (Mw = 350,000 g·mol^{-1}) in tetrahydrofuran.

Electrospinning solutions were obtained by combining the above mentioned polymer stock solutions with a nanoparticle dispersions (see chapter 6.2.2.1) and, if necessary, additional solvent in adequate portions in order to result in the compositions listed in table 3-1, table 3-4, table 3-7 and table 3-10 respectively. Solutions containing PMMA with a molecular weight of 996,000 g·mol^{-1} or PEO with a molecular weight of 1,000,000 g·mol^{-1} were obtained by dissolving the solid polymer in the nanoparticle dispersions directly.
Spinning solutions containing silica or zirconia nanoparticles were prepared by using PEO with a molecular weight of 1,000,000 g·mol^{-1}, while ceria nanoparticle containing solutions were obtained by using PEO with a molecular weight of 300,000 g·mol^{-1}.

6.2.2.6 Preparation of "brick and mortar" nanofibers

First, 1.055 g poly(methyl methacrylate) (PMMA, M_w = 350.000 g·mol^{-1}) were dissolved in 2.972 g tetrahydrofuran (THF) and 3.018 g dimethylformamide (DMF) resulting in a concentration of 15 wt.-% PMMA in the mixed solvent (composition THF/DFM = 1/1). Furthermore, a second solution of 28.5 mg tin(II) chloride dihydrate ($SnCl_2 \cdot 2H_2O$) in 154 mg ethanol was prepared.

Afterwards 76.7 mg of the 15 wt.-% PMMA solution were combined with 508 mg of a tin oxide nanoparticle dispersion in THF (with a solid content of 3.7 wt.-% SnO_2 = 19.0 mg SnO_2) and the solution of $SnCl_2 \cdot 2H_2O$ in ethanol (182 mg). This solution was shortly stirred until a homogeneous solution was obtained so that tin oxide "brick and mortar" fibers (B+M-fibers) could be spun from this solution. The obtained solution contained 6.4 wt.-% PMMA, 2.4 wt.-% $SnCl_2 \cdot 2H_2O$ (equaling 1.6 wt.-% SnO_2), 1.6 wt.-% SNO_2-NPs. The solvent composition was: 58.6 wt.-% THF, 18.2 wt.-% DMF and 12.8 wt.-% ethanol.

6.2.2.7 Preparation of bulk samples

Bulk samples consisting of pure, dried and calcined nanoparticles were obtained by removing the solvent of the pure nanoparticle dispersion (see chapter 6.2.2.1) in a drying oven at 80 °C. Afterward the solid residue was heated in a furnace up to 550 °C (standard calcination protocol, see chapter 6.2.2.8).
Bulk samples of electrospinning solutions containing nanoparticles and a spinning polymer were obtained by the same protocol starting from the readily prepared spinning solutions (see chapter 6.2.2.5).

6.2.2.8 Standard calcination protocol

The standard heat treatment protocol used for all calcination processes of this thesis was as follows: The sample was heated from room temperature to 550 °C within 110 min. afterward the oven was kept at 550 °C for further 2 h before the sample was cooled to room temperature naturally.

6.2.3 Characterization techniques

6.2.3.1 Dynamic light scattering (DLS)

Dynamic light scattering (DLS) analyses were conducted on a device of the type "StabiSizer" (ParticleMetrix, 40668 Meerbusch, Germany). For data and measurement processing the implemented software "Microtech FLEX 10.5.4" was employed. For referencing purposes the pure dispersion solvent was measured prior to the analysis of the dispersion.

6.2.3.2 Wide-angle X-Ray scattering (WAXS)

Wide-angle X-Ray scattering (WAXS) experiments were performed in a θ−2θ geometry using an X'Pert PRO diffractometer (Panalytical, Almelo, Netherlands) with Cu K_α radiation of λ = 0.154 nm. WAXS patterns were recorded in the range of 10°−90° concerning 2θ. The sample holder was a silicon single crystal cut into the direction of the (911) lattice plane. The cathode voltage was 40 kV at a current of 40 mA. The detector was a X'Celerator counter.

For the identification of the crystalline phases the "Highscore Plus" program was applied and for the Rietveld refinement the "Fullprof-Suite (version 2.05)" program was employed. As fitting function the Thompson-Cox-Hastings pseudo-Voigt approach was applied[201,202] resulting in a refinement with $\chi^2 < 25$.

6.2.3.3 Scanning electron microscopy (SEM)

For morphological studies a high resolution scanning electron microscope (SEM) of the type "Merlin" (Carl Zeiss AG, 73447 Oberkochen, Germany) was applied. The pictures were recorded at working distances in the range of 2−5 mm, an acceleration voltage of 1−5 kV and a sample current of 70−100 pA. Images were acquired detecting by the secondary electrons emitted from the sample. At high magnification the imaging mode was switched to the also implemented inlens detector.

All samples were coated with a thin layer of platinum to increase their conductivity prior to analyses on a sputter coater of the type "Scancoat 6" (BOC Edwards GmbH, 85551 Kirchheim, Germany). The sputtering time was kept as low as 20 s in order to guarantee that the surface structure of the samples is not changed by the surface layer of platinum.

6.2.3.4 Nitrogen physisorption

Physisorption experiments were conducted on a device of the type "Autosorb-6" (Quantachrome Instruments, Boynton Beach, Florida, USA) with nitrogen as adsorbate at 77 K. For data processing the implemented software "AS1win" was employed which supports the standard reduction algorithms including the Brunauer-Emmett-Teller (BET) method used to quantify surface areas. It extends the Langmuir theory for adsorbate monolayer to multilayer formation on the sample. This is a suitable physisorption model for non-microporous materials and calculates the surface area from the cross section of the adsorbate on the surface. For the analysis of pore size distributions the non-linear density functional theory (NLDFT) was applied and the adequate kernel for electrospun fibers was found as discussed in chapter 3.2.3.1. For the determination of total pore volumes the Gurvich rule was used according to equation (2-11) analyzing the second point of the desorption branch of the isotherm which typically lies in the range of $p/p_0 = 0.97$.

The plots of all measured isotherms are presented in large magnification in chapters 6.3.2-6.3.6. Since the DFT-plots were more important in the discussions of chapter 3, the illustration of the isotherms in a magnification facilitating to depict all details adequately was omitted there.

6.3 Additional figures

6.3.1 Comparisons of measured and DFT-calculated isotherms of several silica materials

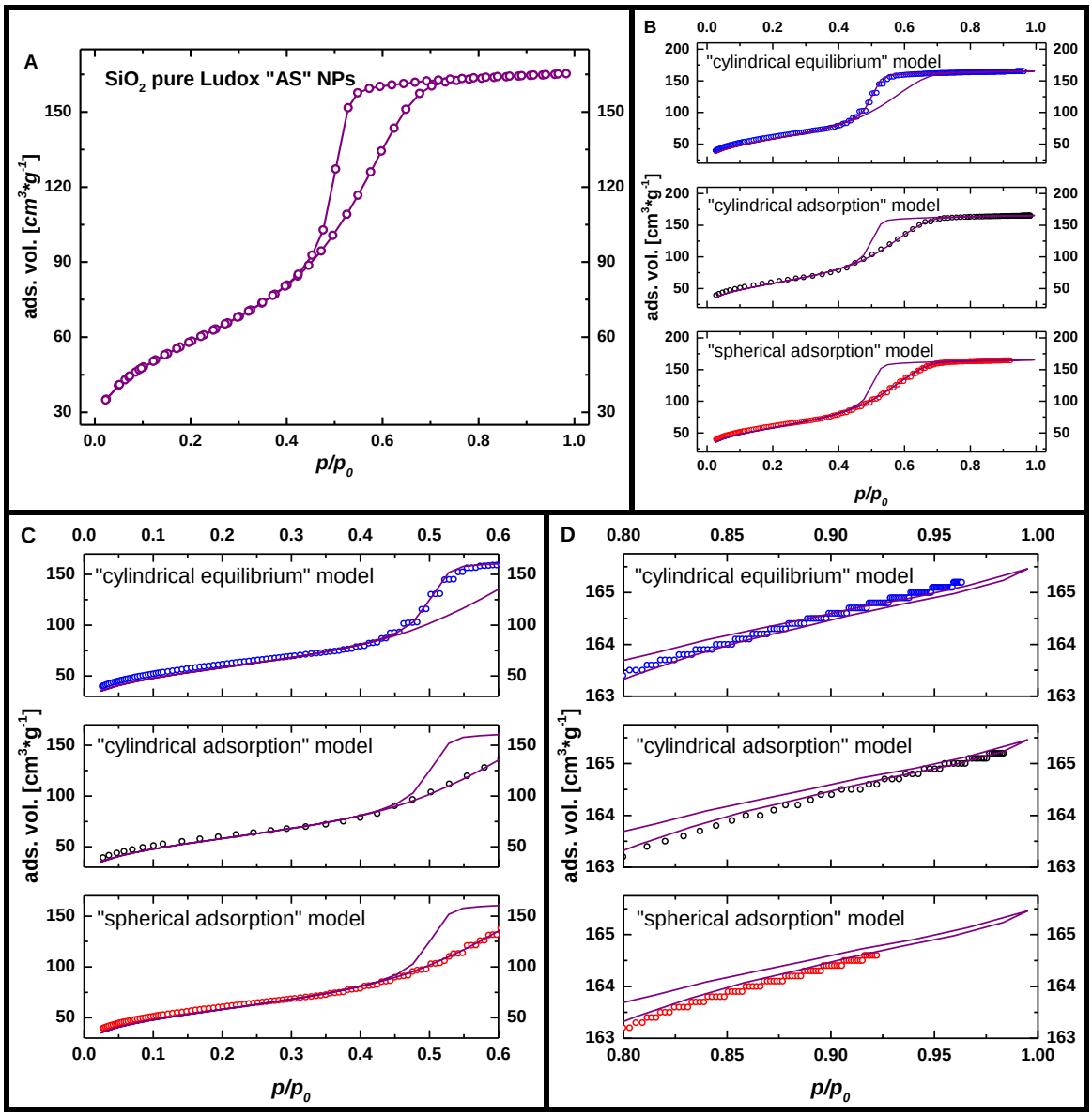

Figure 6-1: A: Measured isotherm of pure Ludox "AS" silica NPs (see table 3-1, sample 3); B–D: Comparison of the measured isotherm illustrated in A with isotherms calculated by DFT; B: overview of the complete p/p_0 range ($0 \le p/p_0 \le 1$); C: magnification of the low relative pressure range ($0 \le p/p_0 \le 0.6$); D: magnification of the high relative pressure range ($0.8 \le p/p_0 \le 1.0$). Color coding: purple: measured isotherm; black: data calculated by the "cylindrical adsorption" model; blue: data calculated by the "cylindrical equilibrium" model; red: data calculated by the "spherical adsorption" model.

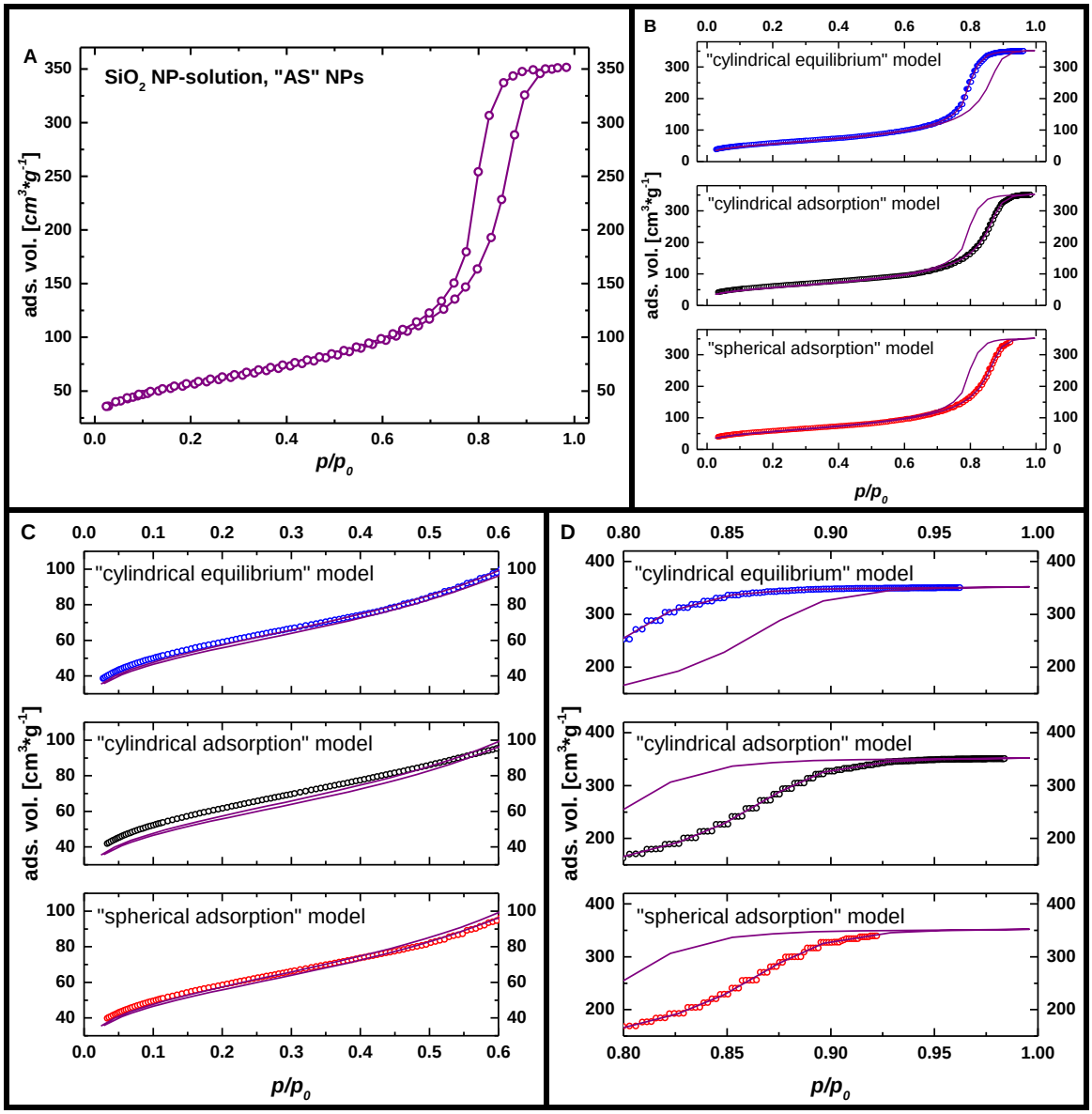

Figure 6-2: A: Measured isotherm of dried and calcined silica NP-solution obtained from Ludox "AS" NPs (see table 3-1, sample 9); B–D: Comparison of the measured isotherm illustrated in A with isotherms calculated by DFT; B: overview of the complete p/p_0 range ($0 \le p/p_0 \le 1$); C: magnification of the low relative pressure range ($0 \le p/p_0 \le 0.6$); D: magnification of the high relative pressure range ($0.8 \le p/p_0 \le 1.0$). Color coding: purple: measured isotherm; black: data calculated by the "cylindrical adsorption" model; blue: data calculated by the "cylindrical equilibrium" model; red: data calculated by the "spherical adsorption" model.

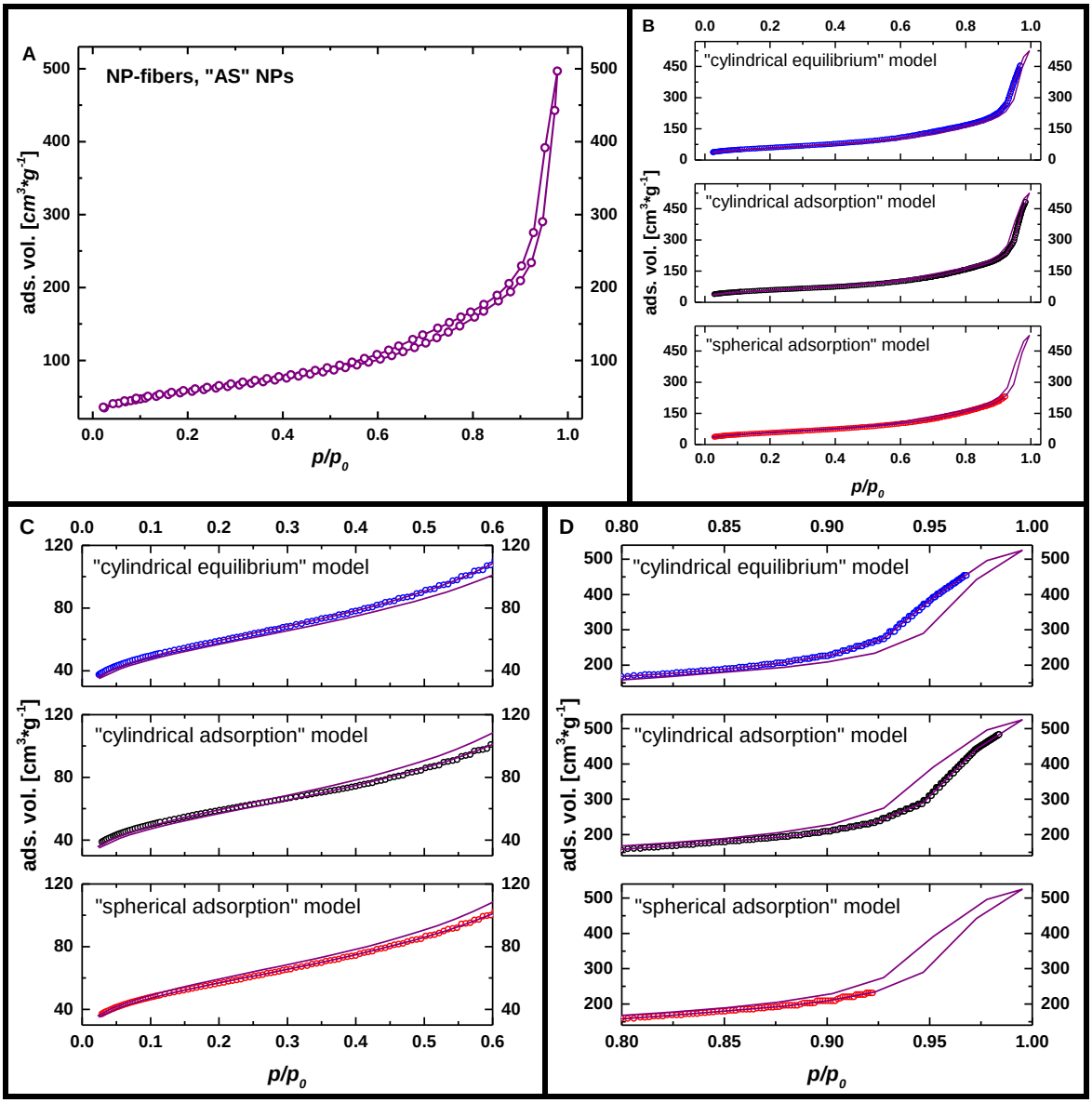

Figure 6-3: A: Measured isotherm of silica NP-fibers obtained from Ludox "AS" NPs (weight ratio SiO_2/PEO = 1.0/1; see table 3-1, sample 14); B–D: Comparison of the measured isotherm illustrated in A with isotherms calculated by DFT; B: overview of the complete p/p_0 range ($0 \le p/p_0 \le 1$); C: magnification of the low relative pressure range ($0 \le p/p_0 \le 0.6$); D: magnification of the high relative pressure range ($0.8 \le p/p_0 \le 1.0$). Color coding: purple: measured isotherm; black: data calculated by the "cylindrical adsorption" model; blue: data calculated by the "cylindrical equilibrium" model; red: data calculated by the "spherical adsorption" model.

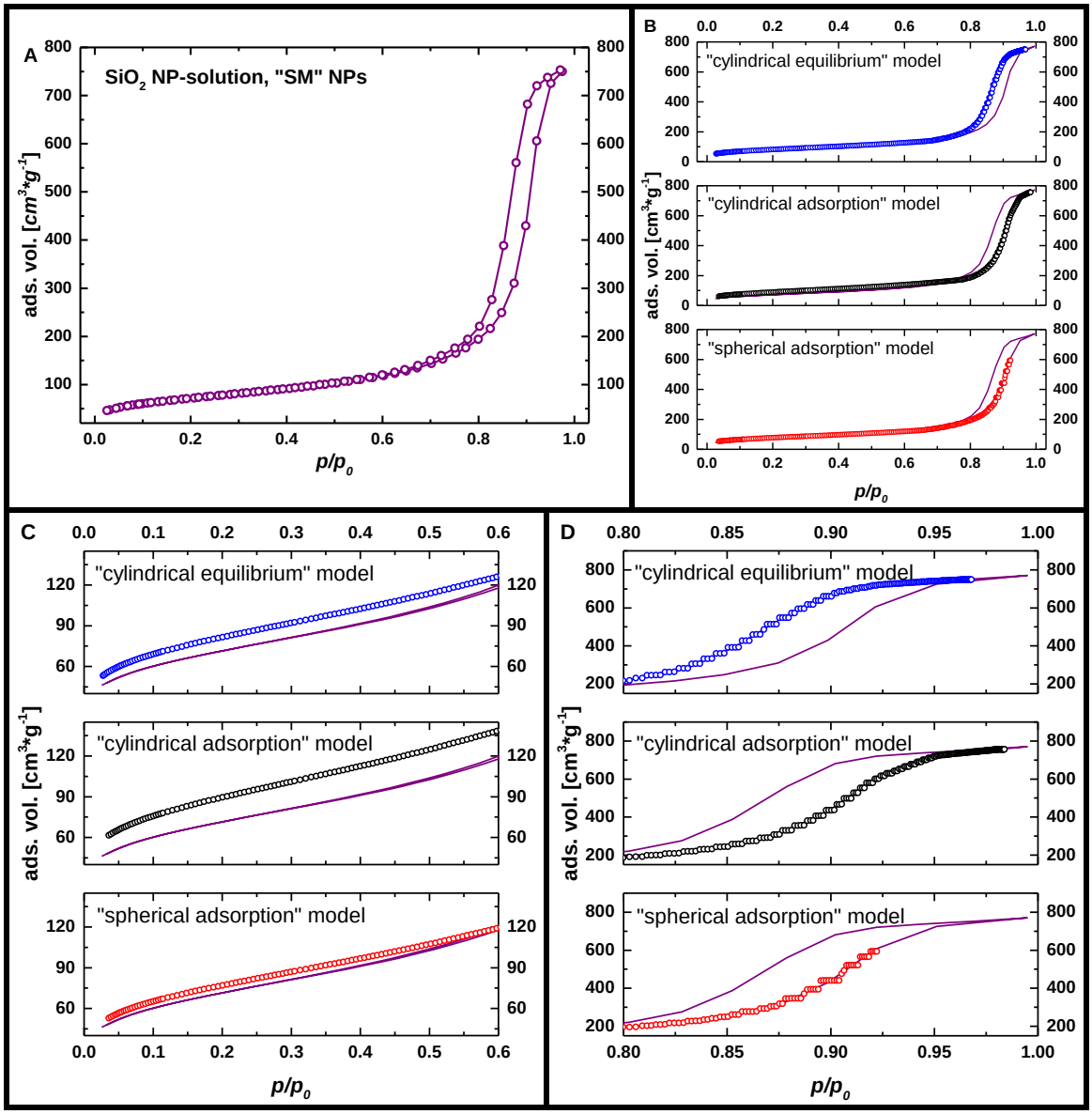

Figure 6-4: A: Measured isotherm of dried and calcined silica NP-solution obtained from Ludox "SM" NPs (see table 3-1, sample 11); B–D: Comparison of the measured isotherm illustrated in A with isotherms calculated by DFT; B: overview of the complete p/p_0 range ($0 \le p/p_0 \le 1$); C: magnification of the low relative pressure range ($0 \le p/p_0 \le 0.6$); D: magnification of the high relative pressure range ($0.8 \le p/p_0 \le 1.0$). Color coding: purple: measured isotherm; black: data calculated by the "cylindrical adsorption" model; blue: data calculated by the "cylindrical equilibrium" model; red: data calculated by the "spherical adsorption" model.

6.3.2 Nitrogen physisorption isotherms of titania materials

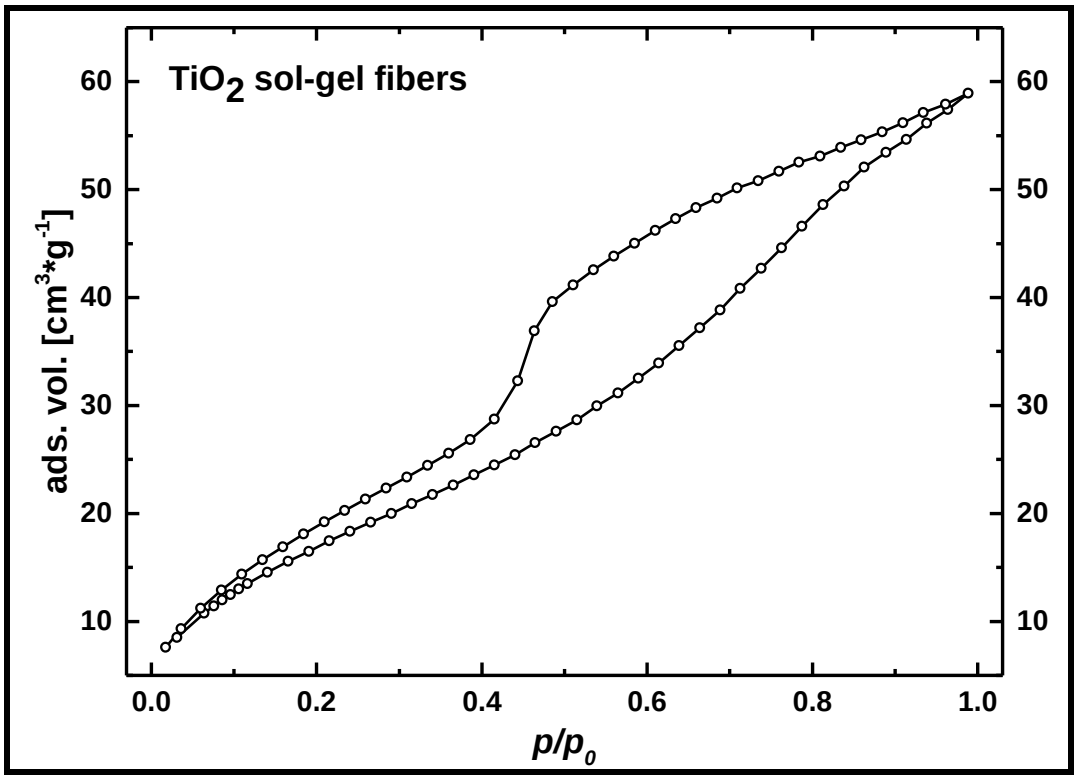

Figure 6-5: N_2-Physisorption isotherm of TiO_2 sol-gel fibers (see table 2-2, sample 1).

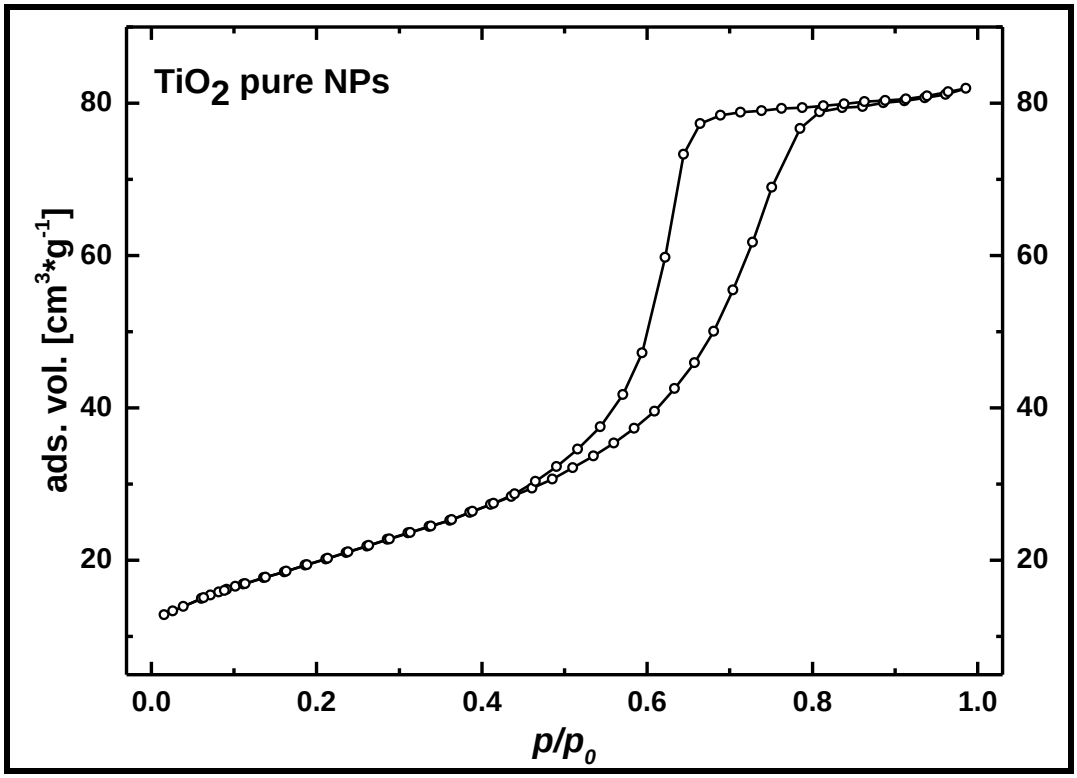

Figure 6-6: N_2-Physisorption isotherm of pure TiO_2 nanoparticles (see table 2-2, sample 2).

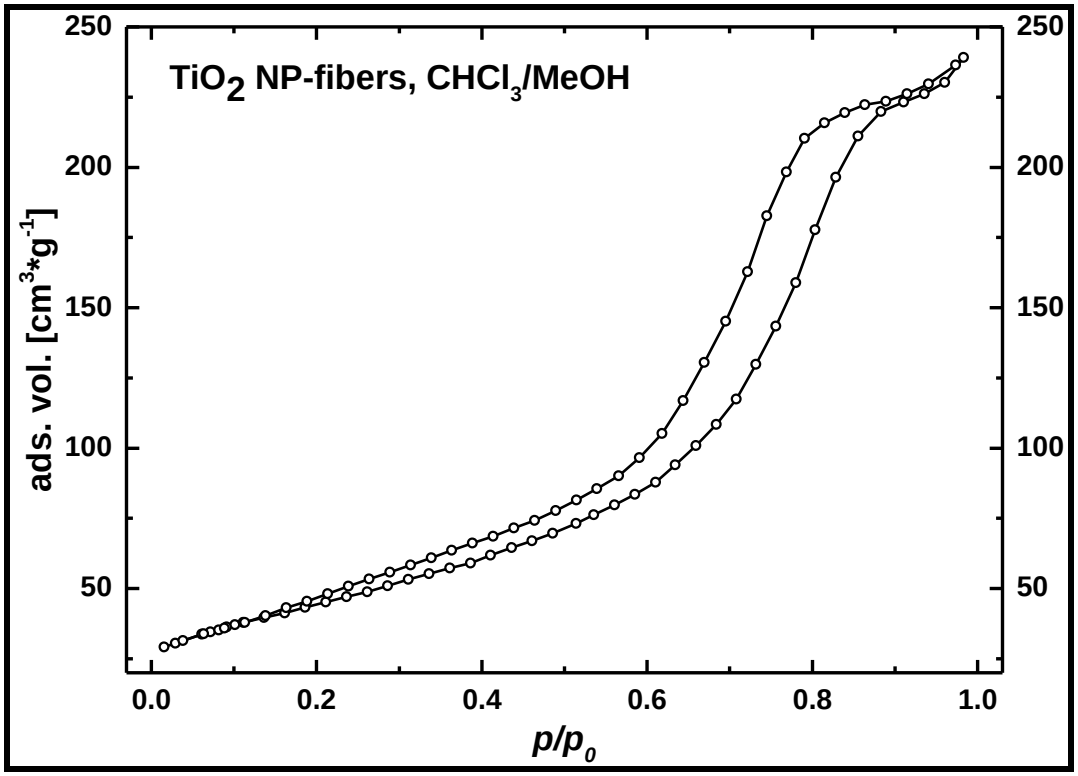

Figure 6-7: N_2-Physisorption isotherm of TiO_2 NP-fibers spun from $CHCl_3$/MeOH solvent mixture (see table 2-2, sample 3).

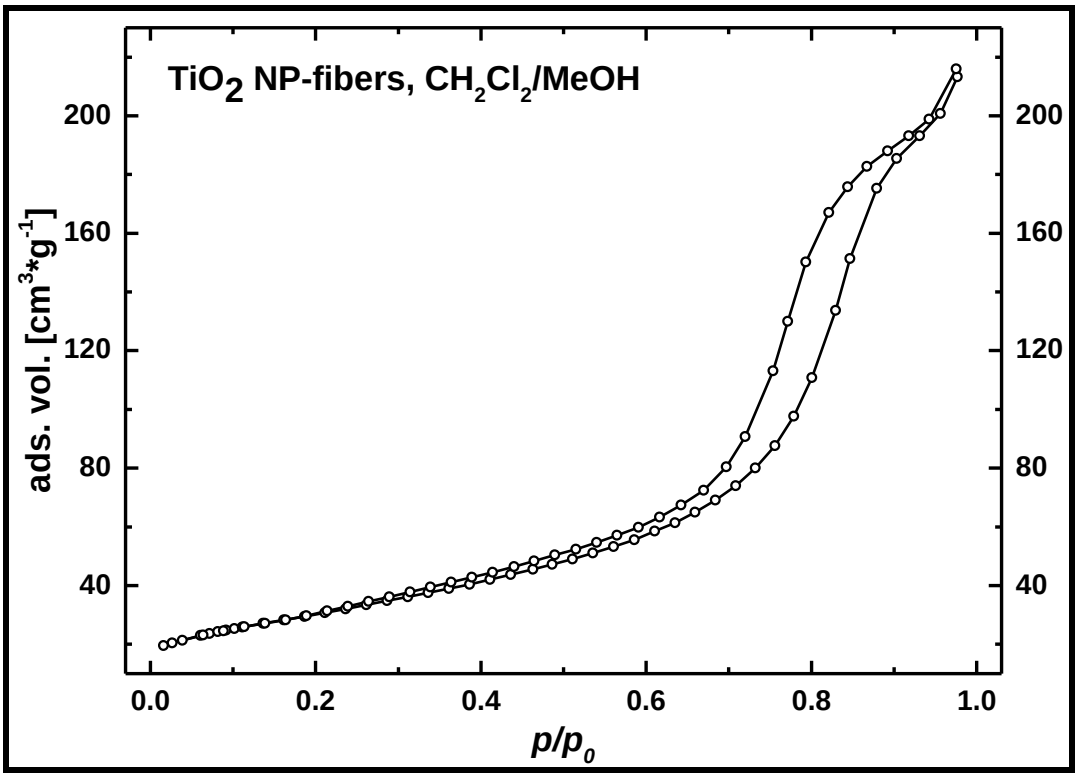

Figure 6-8: N_2-Physisorption isotherm of TiO_2 NP-fibers spun from CH_2Cl_2/MeOH solvent mixture (see table 2-2, sample 4).

6.3.3 Nitrogen physisorption isotherms of silica materials

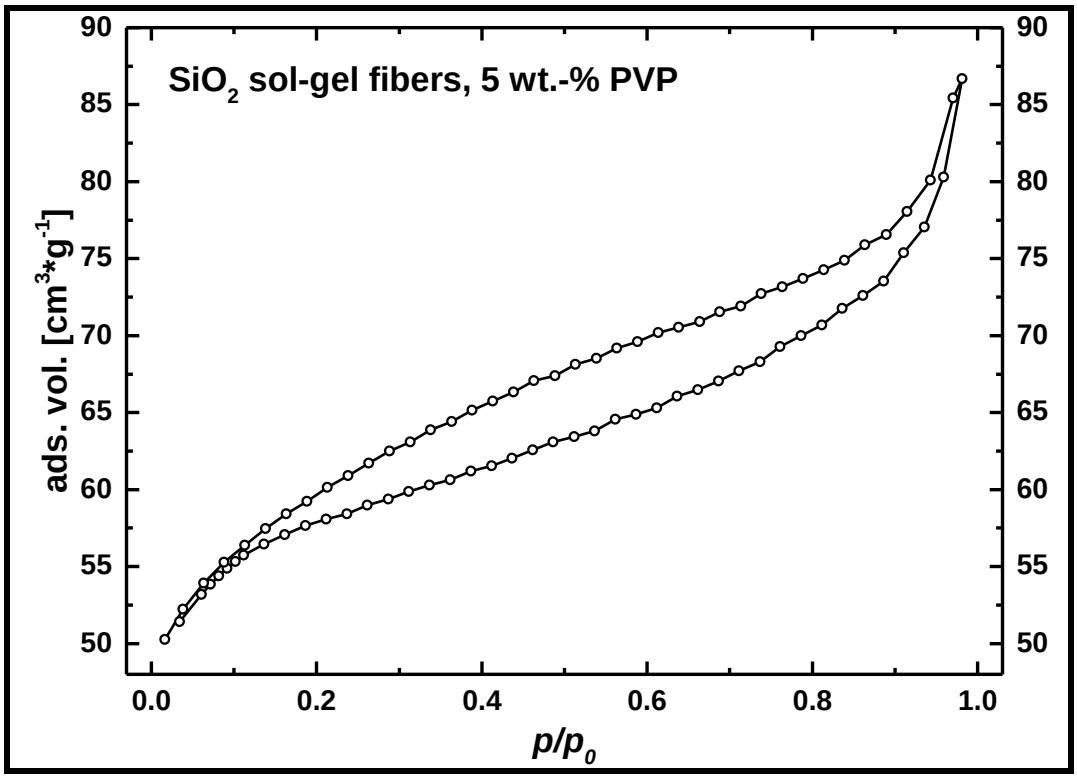

Figure 6-9: N_2-Physisorption isotherm of SiO_2 sol-gel fibers spun with 5 wt.-% PVP (see table 3-1, sample 1).

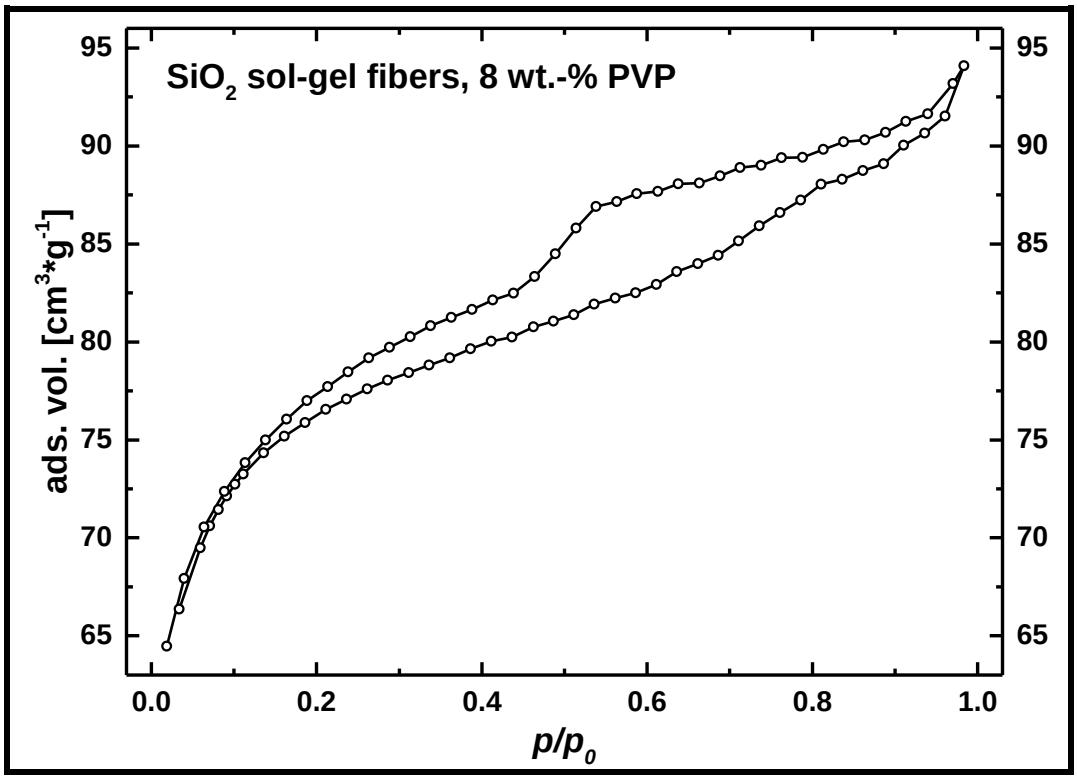

Figure 6-10: N_2-Physisorption isotherm of SiO_2 sol-gel fibers spun with 8 wt.-% PVP (see table 3-1, sample 2).

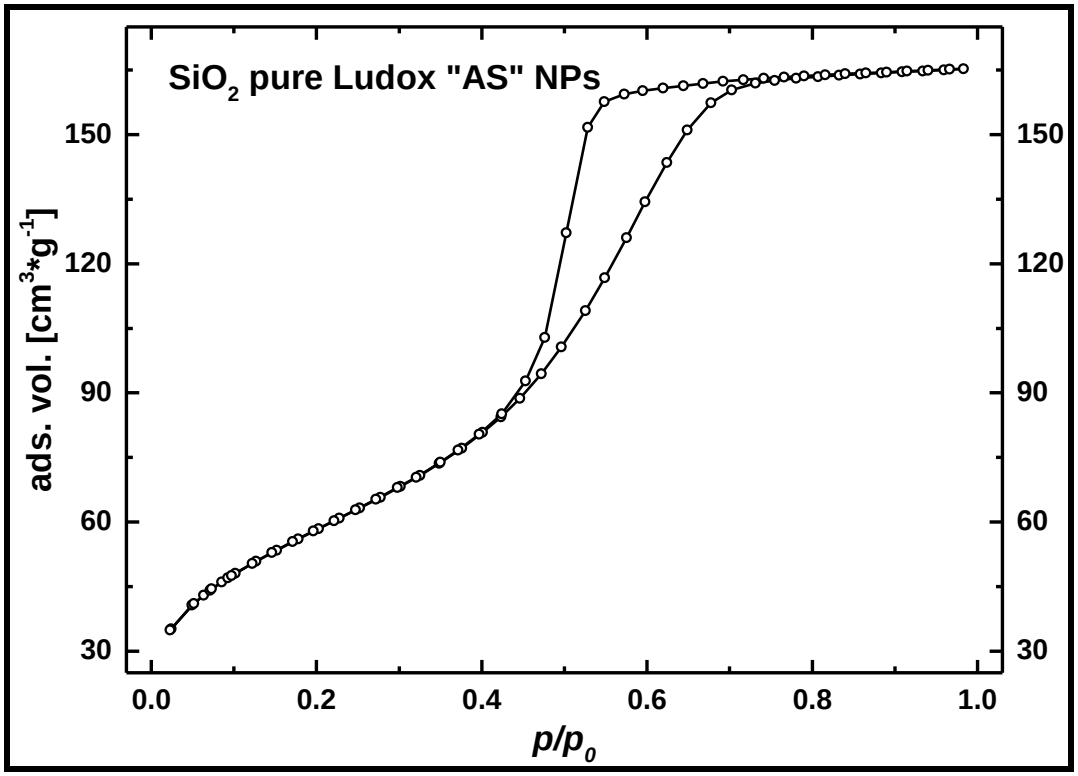

Figure 6-11: N_2-Physisorption isotherm of pure SiO_2 Ludox "AS" NPs (see table 3-1, sample 3).

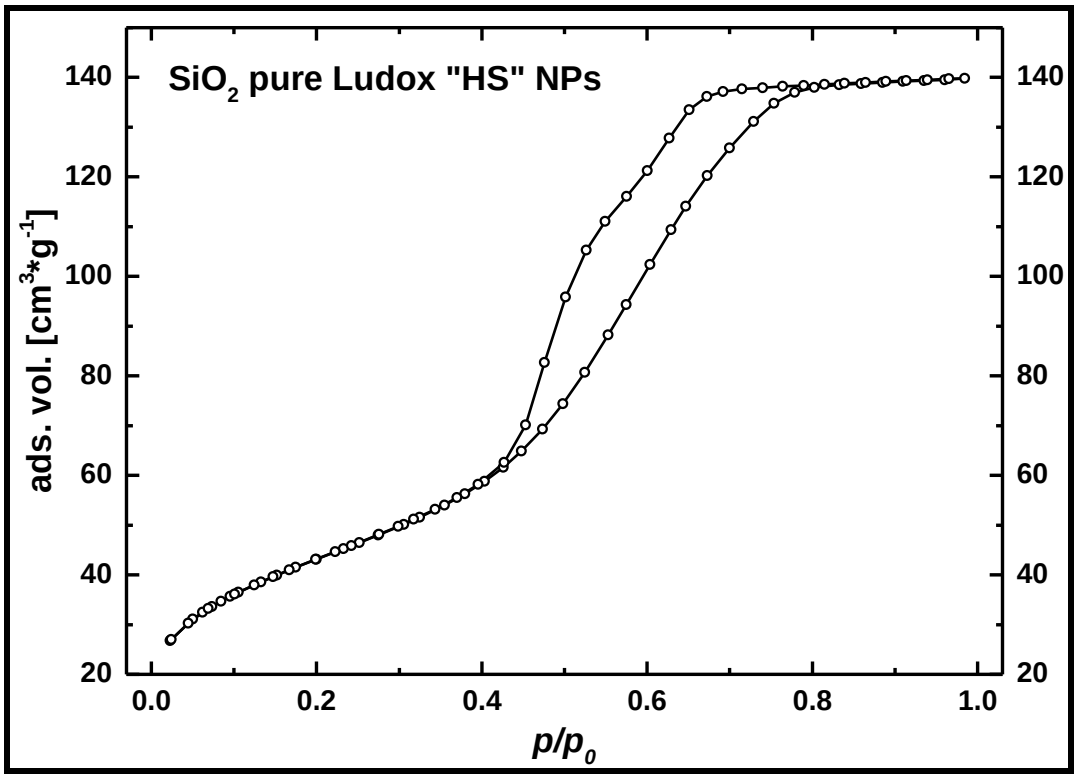

Figure 6-12: N_2-Physisorption isotherm of pure SiO_2 Ludox "HS" NPs (see table 3-1, sample 4).

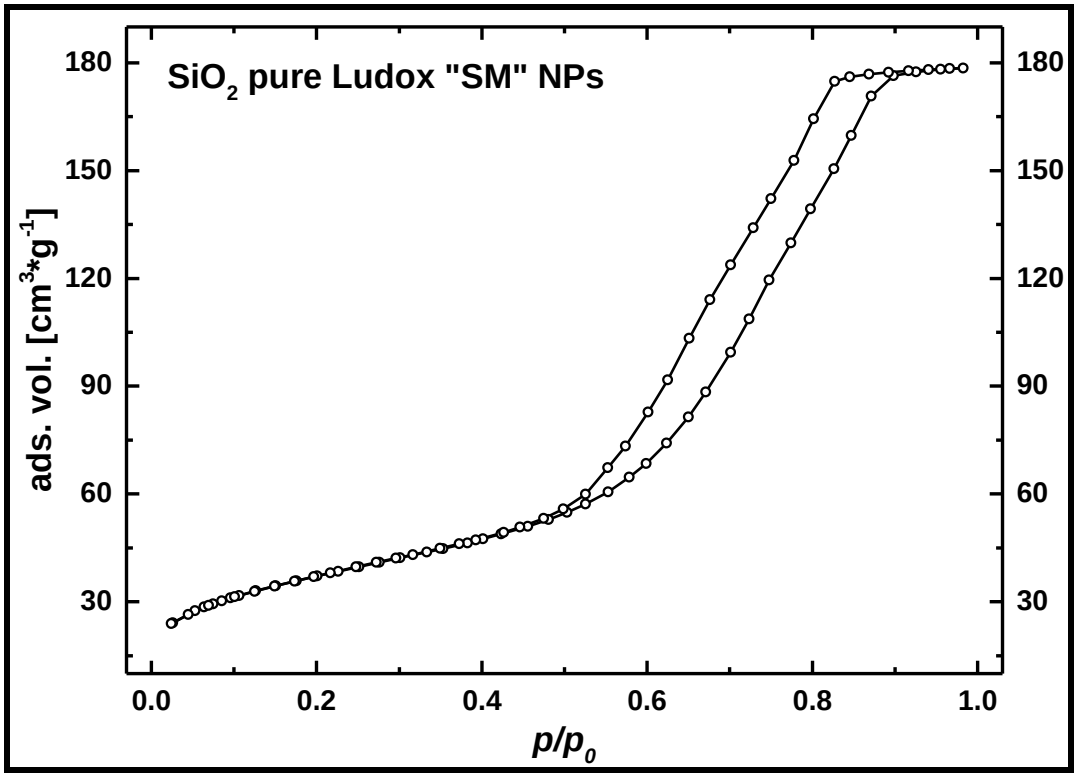

Figure 6-13: N_2-Physisorption isotherm of pure SiO_2 Ludox "SM" NPs (see table 3-1, sample 5).

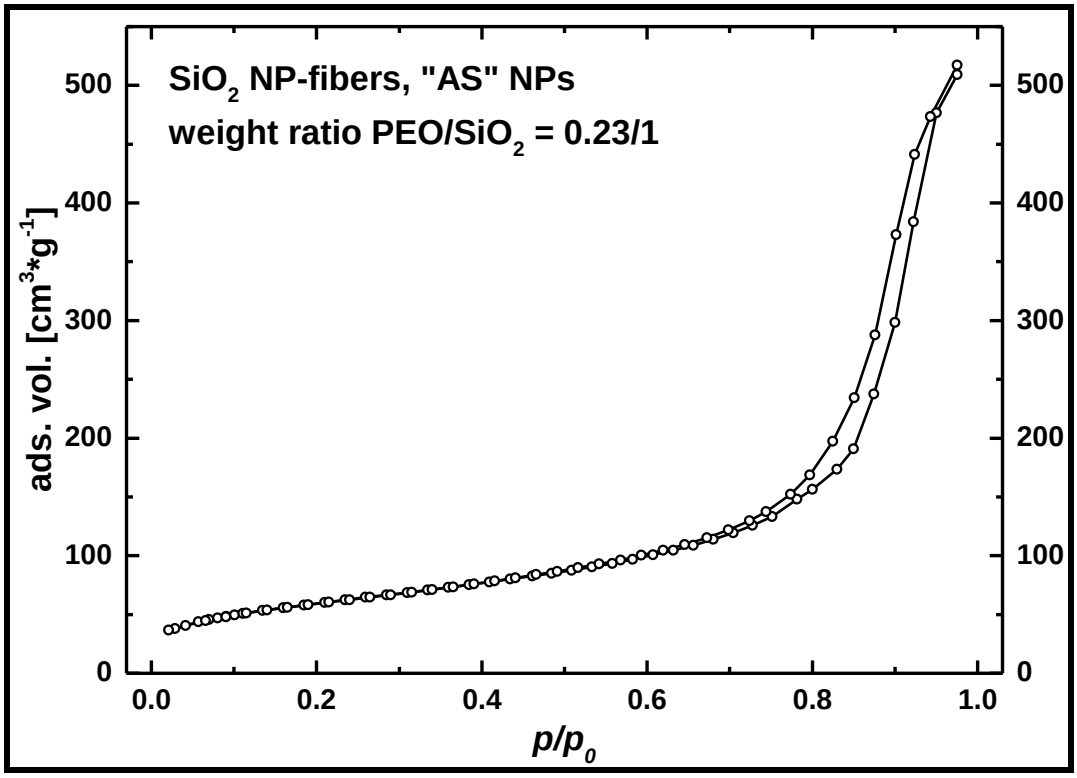

Figure 6-14: N_2-Physisorption isotherm of SiO_2 NP-fibers obtained from Ludox "AS" NPs; weight ratio PEO/SiO_2 = 0.23/1 (see table 3-1, sample 6).

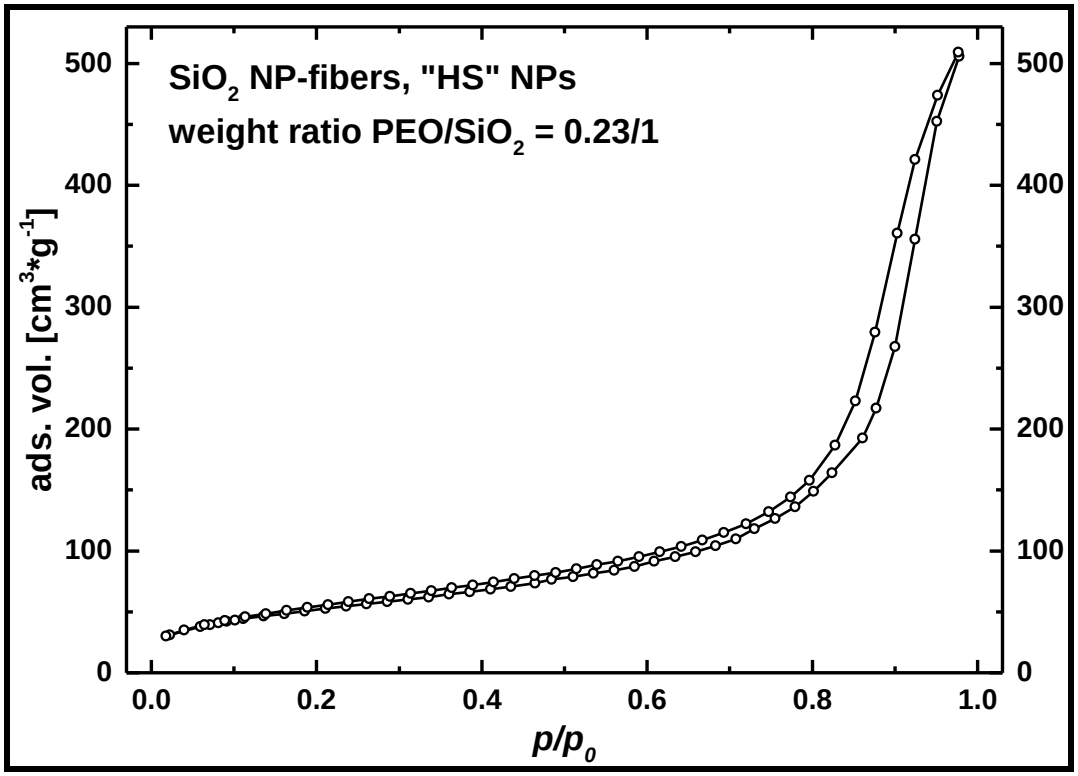

Figure 6-15: N_2-Physisorption isotherm of SiO_2 NP-fibers obtained from Ludox "HS" NPs; weight ratio PEO/SiO_2 = 0.23/1 (see table 3-1, sample 7).

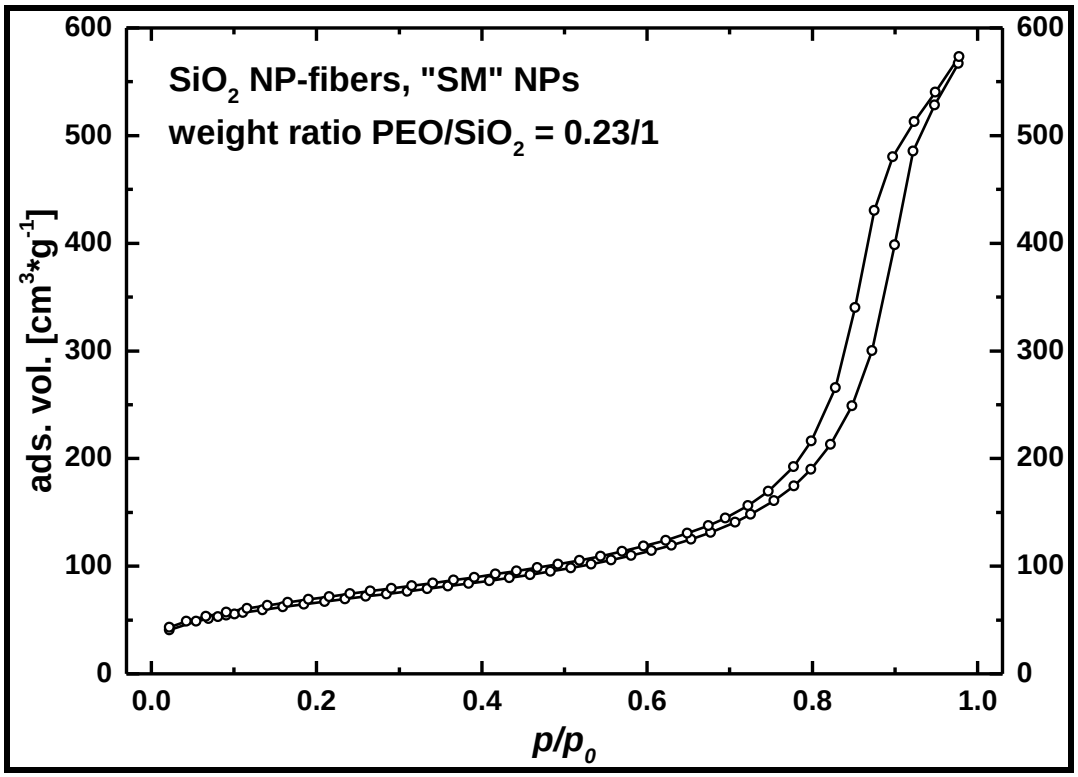

Figure 6-16: N_2-Physisorption isotherm of SiO_2 NP-fibers obtained from Ludox "SM" NPs; weight ratio PEO/SiO_2 = 0.23/1 (see table 3-1, sample 8).

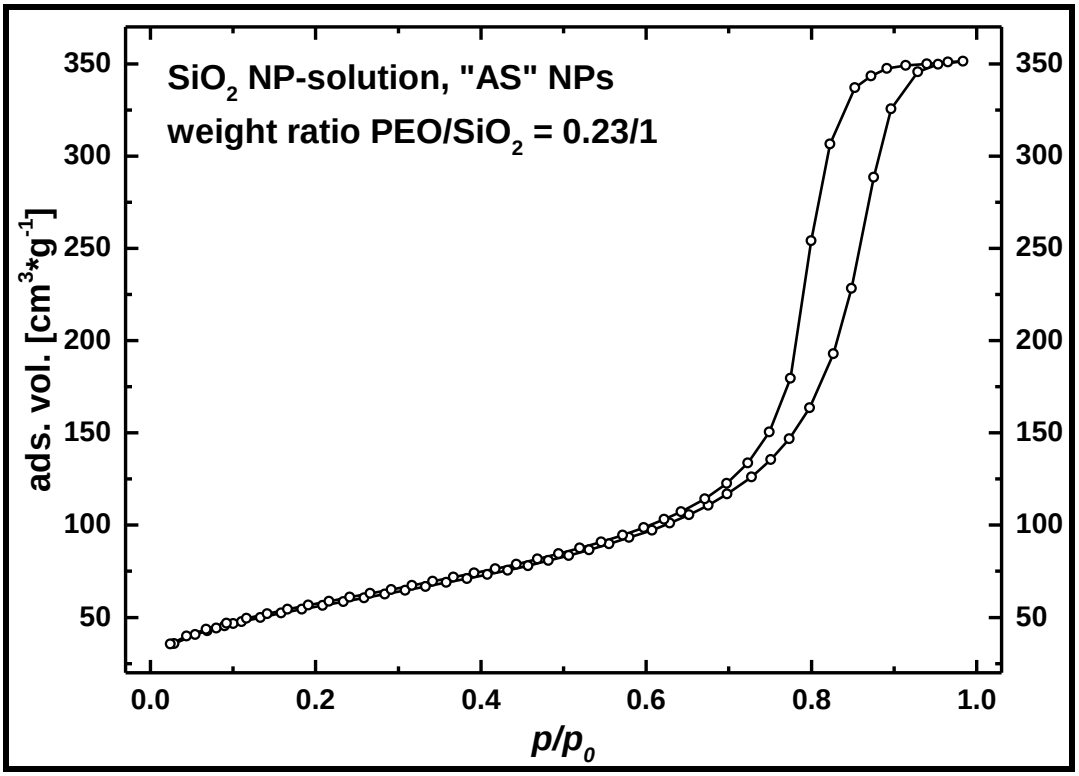

Figure 6-17: N_2-Physisorption isotherm of bulk sample obtained from dried and calcined SiO_2 NP-solution containing Ludox "AS" NPs, PEO and H_2O; weight ratio PEO/SiO_2 = 0.23/1 (see table 3-1, sample 9).

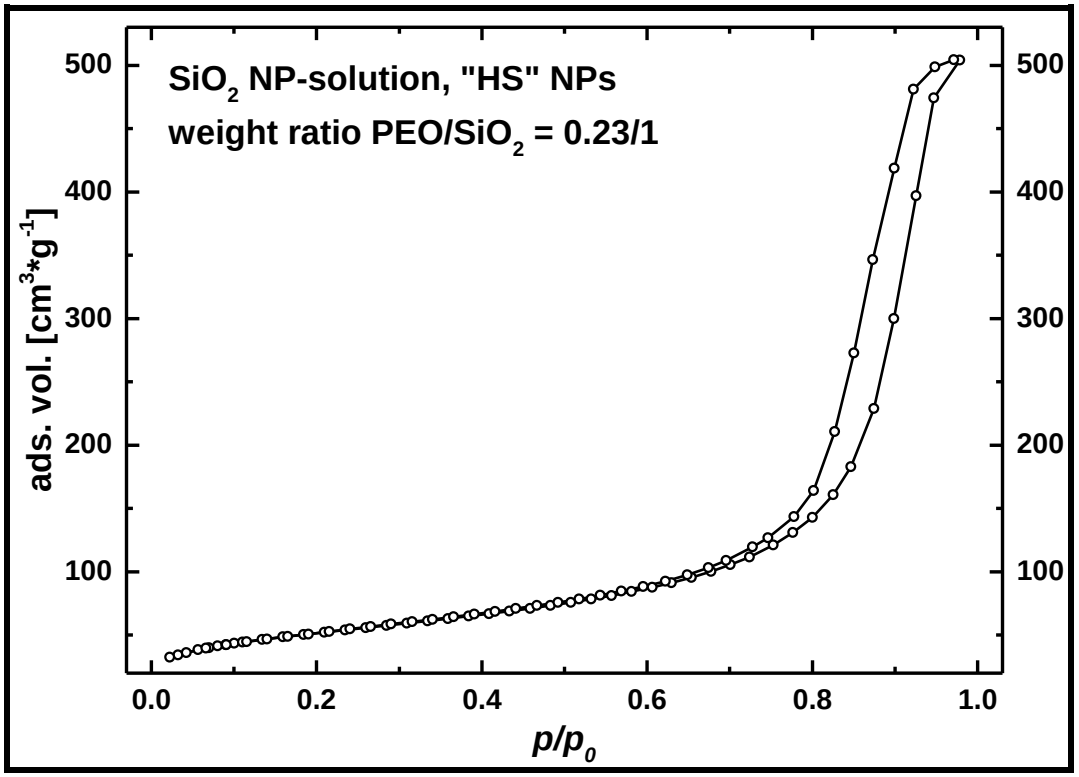

Figure 6-18: N_2-Physisorption isotherm of bulk sample obtained from dried and calcined SiO_2 NP-solution containing Ludox "HS" NPs, PEO and H_2O; weight ratio PEO/SiO_2 = 0.23/1 (see table 3-1, sample 10).

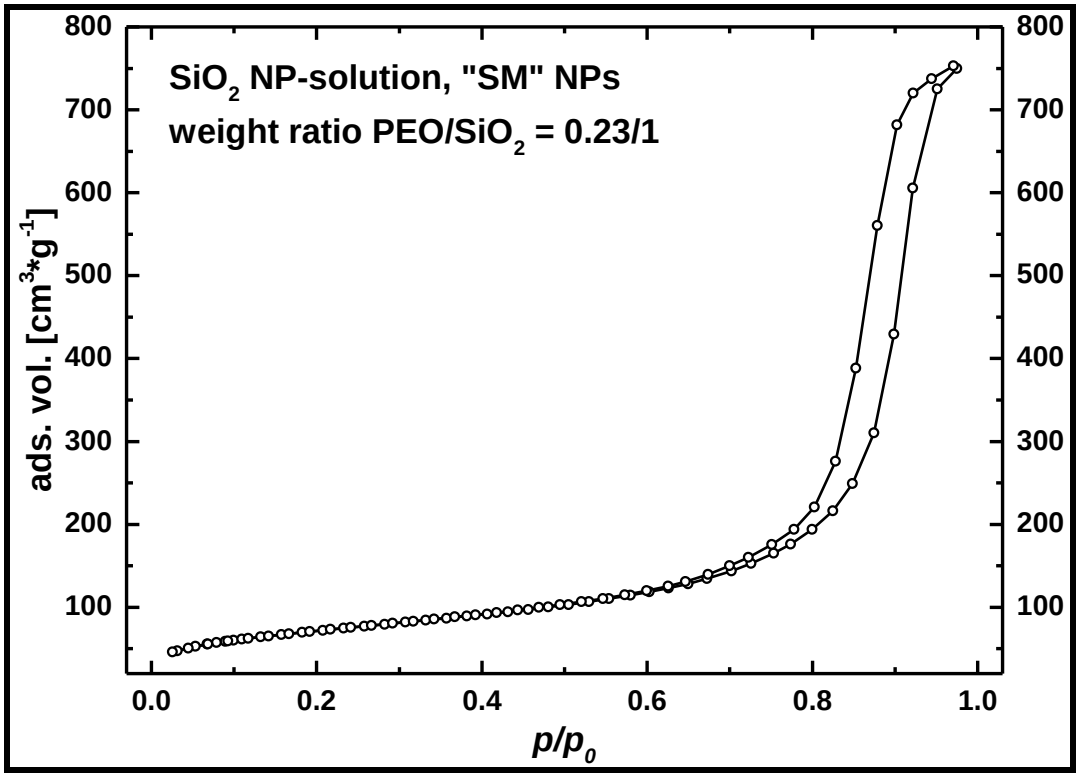

Figure 6-19: N_2-Physisorption isotherm of bulk sample obtained from dried and calcined SiO_2 NP-solution containing Ludox "SM" NPs, PEO and H_2O; weight ratio PEO/SiO_2 = 0.23/1 (see table 3-1, sample 11).

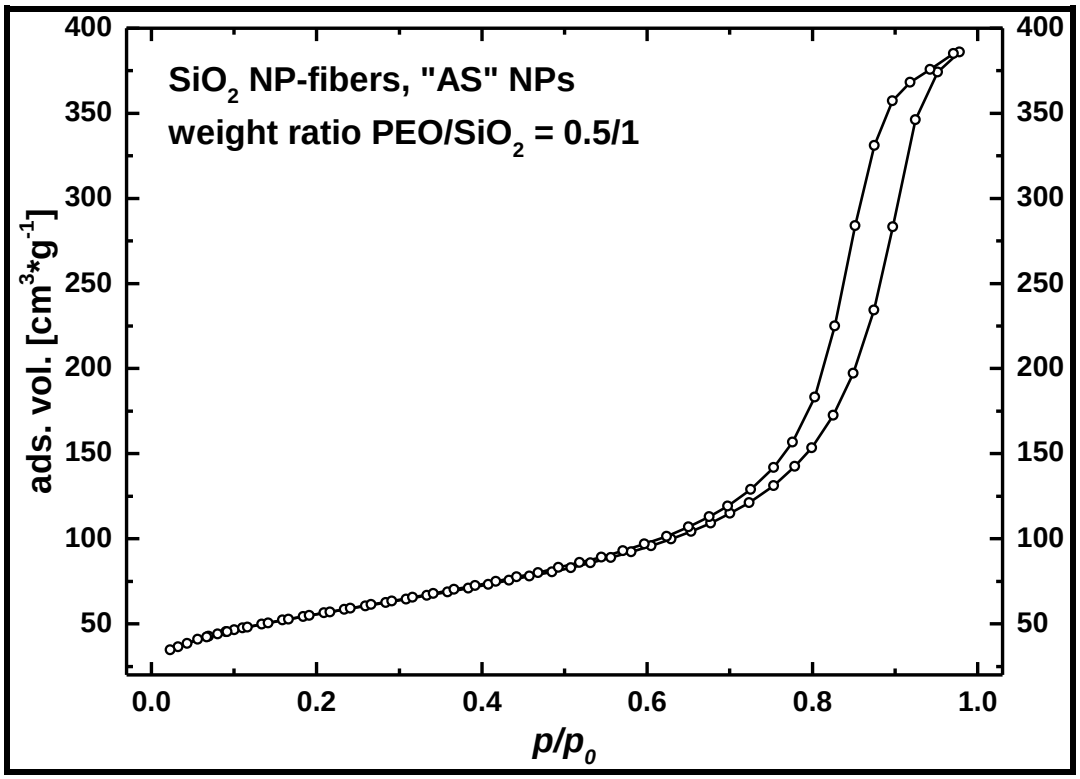

Figure 6-20: N_2-Physisorption isotherm of SiO_2 NP-fibers obtained from Ludox "AS" NPs; weight ratio PEO/SiO_2 = 0.5/1 (see table 3-1, sample 12).

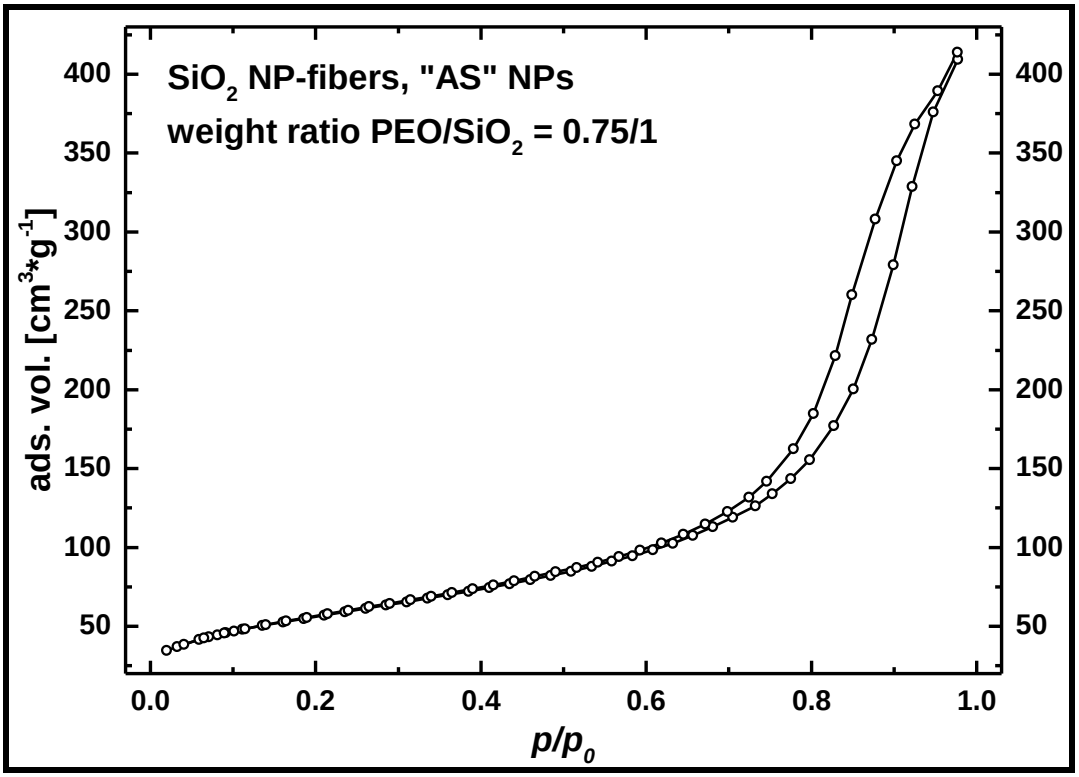

Figure 6-21: N_2-Physisorption isotherm of SiO_2 NP-fibers obtained from Ludox "AS" NPs; weight ratio PEO/SiO_2 = 0.75/1 (see table 3-1, sample 13).

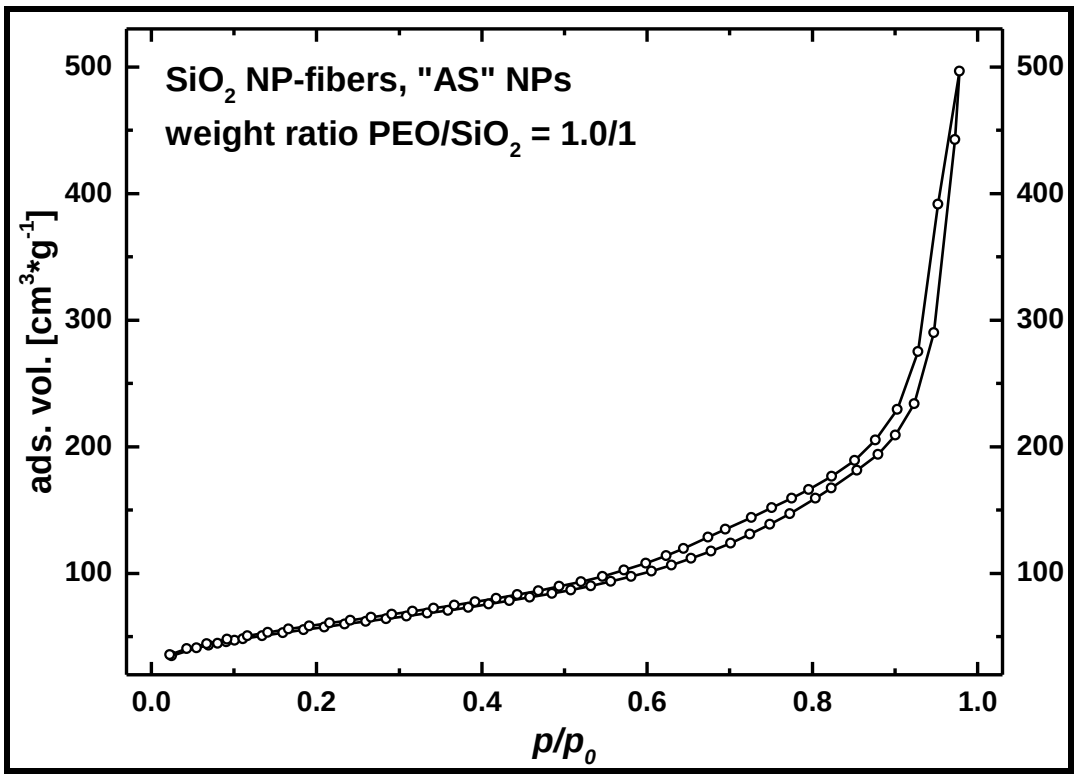

Figure 6-22: N_2-Physisorption isotherm of SiO_2 NP-fibers obtained from Ludox "AS" NPs; weight ratio PEO/SiO_2 = 1.0/1 (see table 3-1, sample 14).

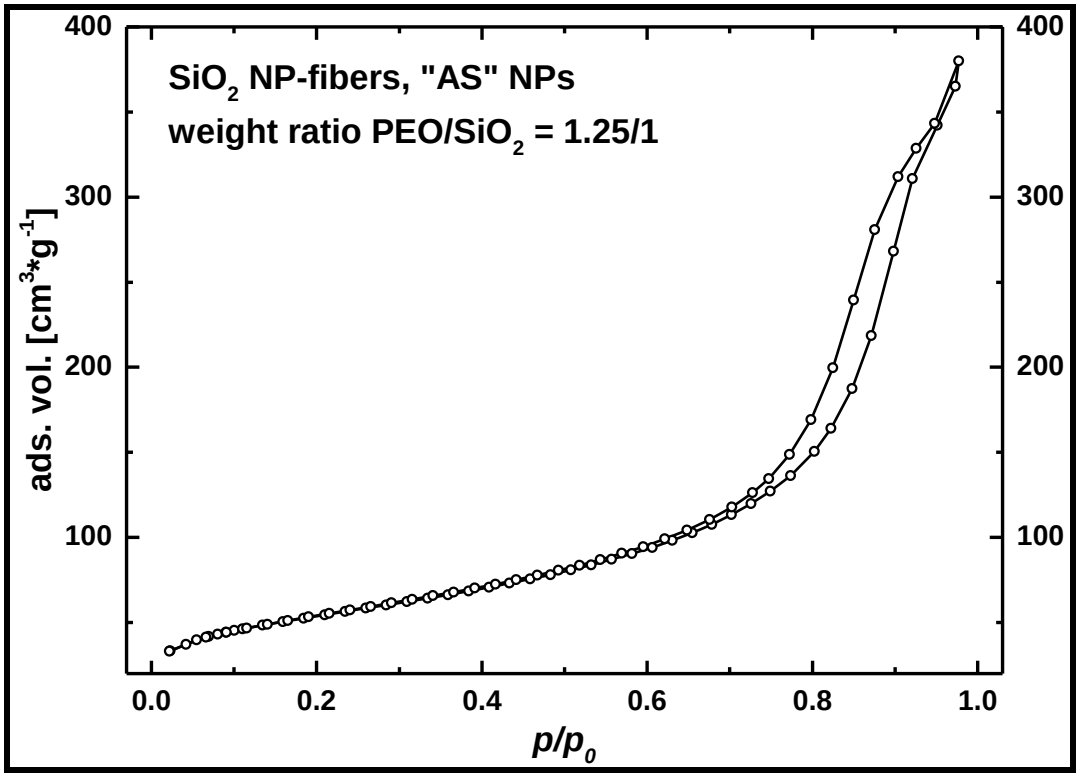

Figure 6-23: N_2-Physisorption isotherm of SiO_2 NP-fibers obtained from Ludox "AS" NPs; weight ratio PEO/SiO_2 = 1.25/1 (see table 3-1, sample 15).

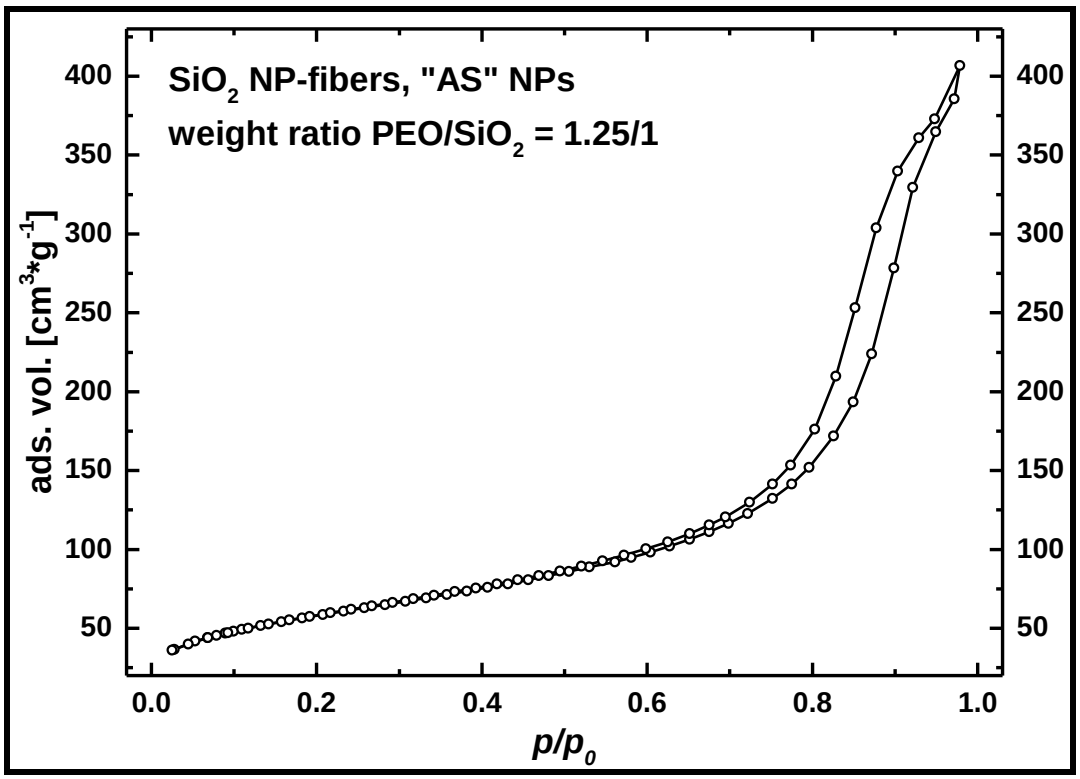

Figure 6-24: N_2-Physisorption isotherm of SiO_2 NP-fibers obtained from Ludox "AS" NPs; weight ratio PEO/SiO_2 = 1.25/1 (see table 3-1, sample 16).

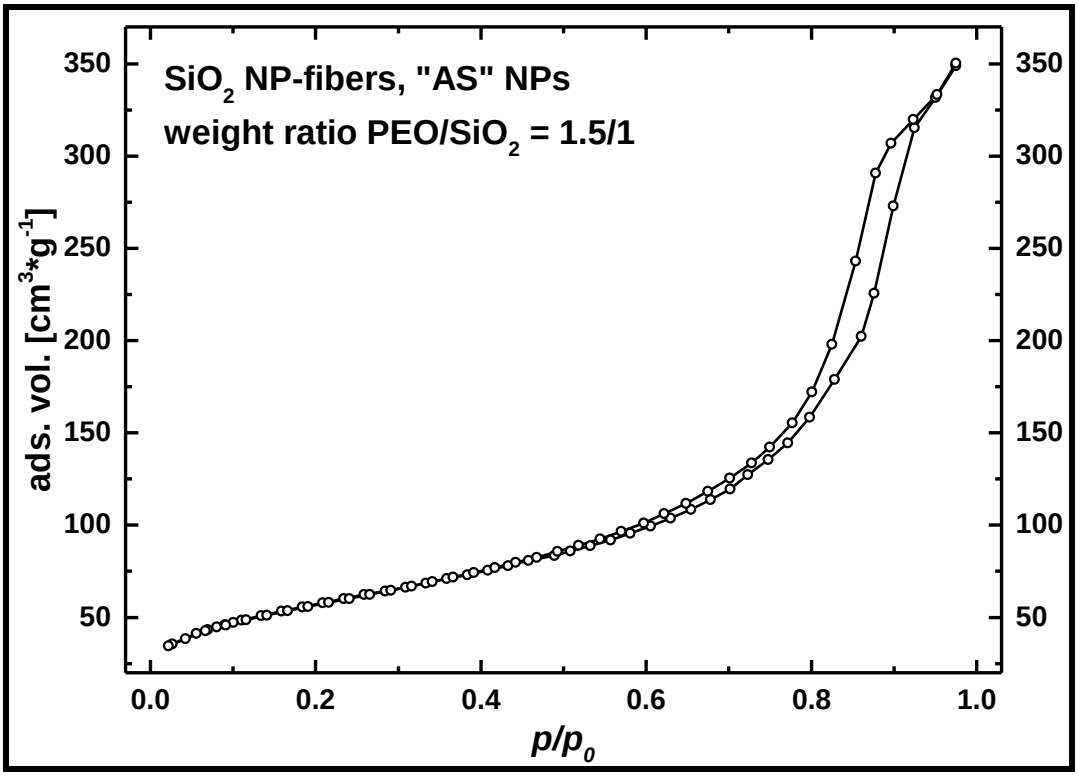

Figure 6-25: N_2-Physisorption isotherm of SiO_2 NP-fibers obtained from Ludox "AS" NPs; weight ratio PEO/SiO_2 = 1.5/1 (see table 3-1, sample 17).

6.3.4 Nitrogen physisorption isotherms of zirconia materials

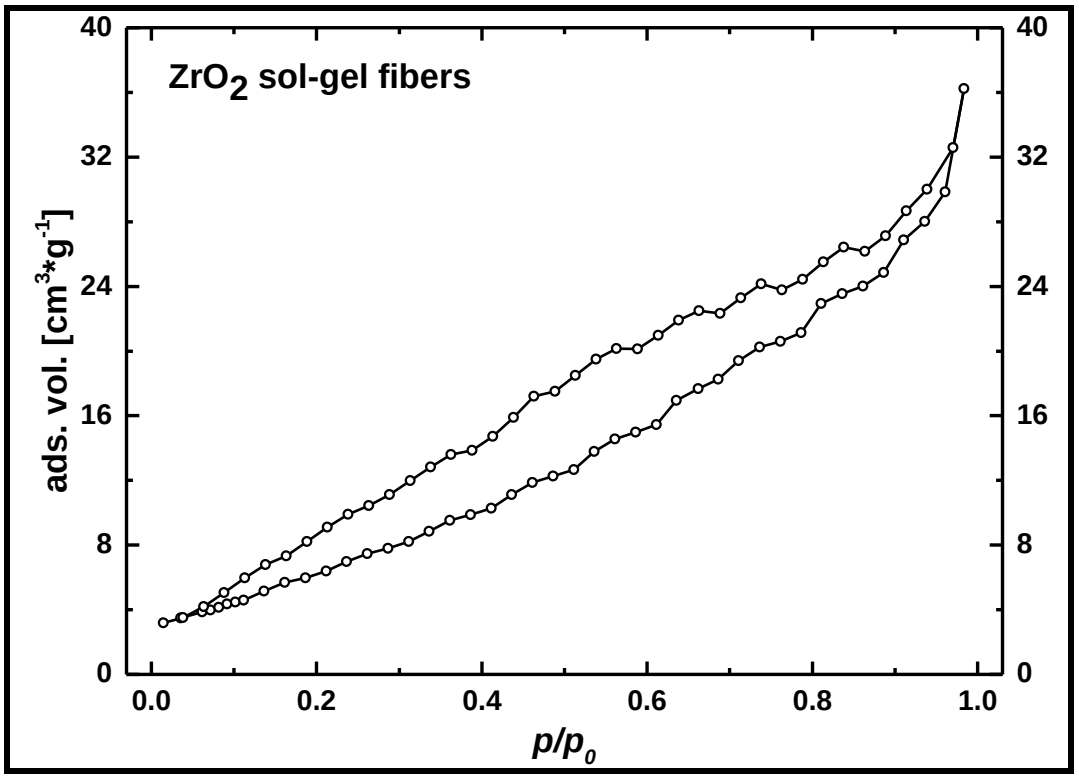

Figure 6-26: N_2-Physisorption isotherm of ZrO_2 sol-gel fibers (see table 3-4, sample 1).

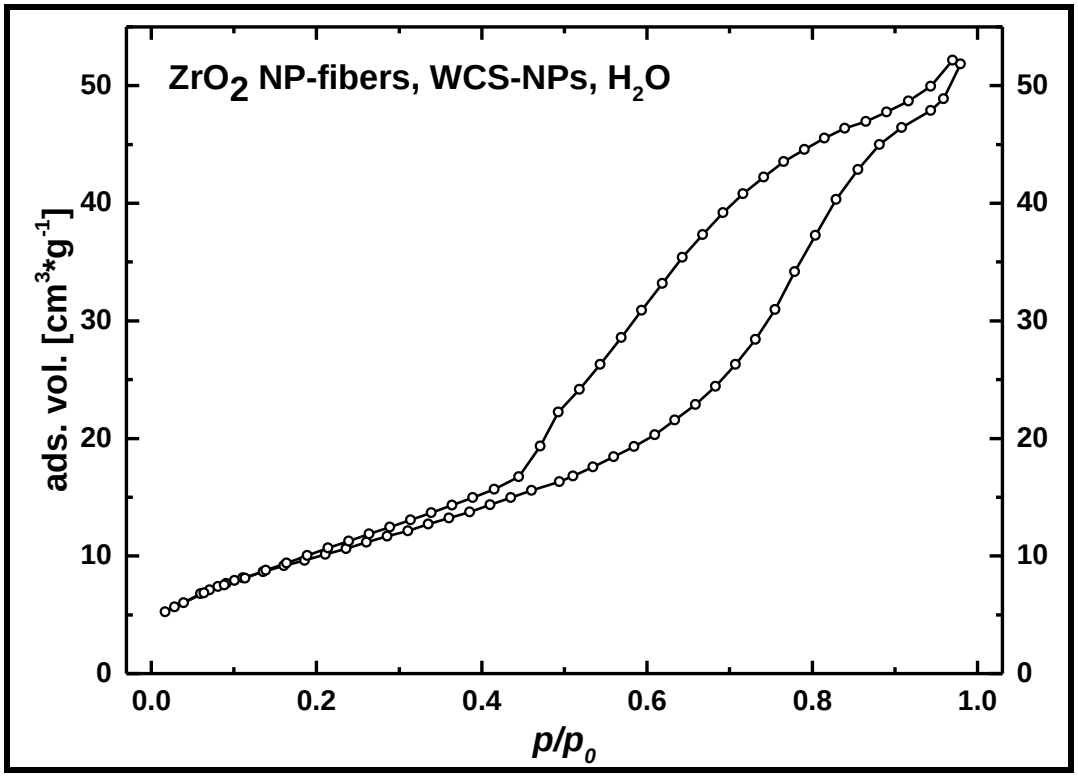

Figure 6-27: N_2-Physisorption isotherm of ZrO_2 NP-fibers obtained from WCS-NPs and spun from H_2O/MeOH solvent mixture (see table 3-4, sample 2).

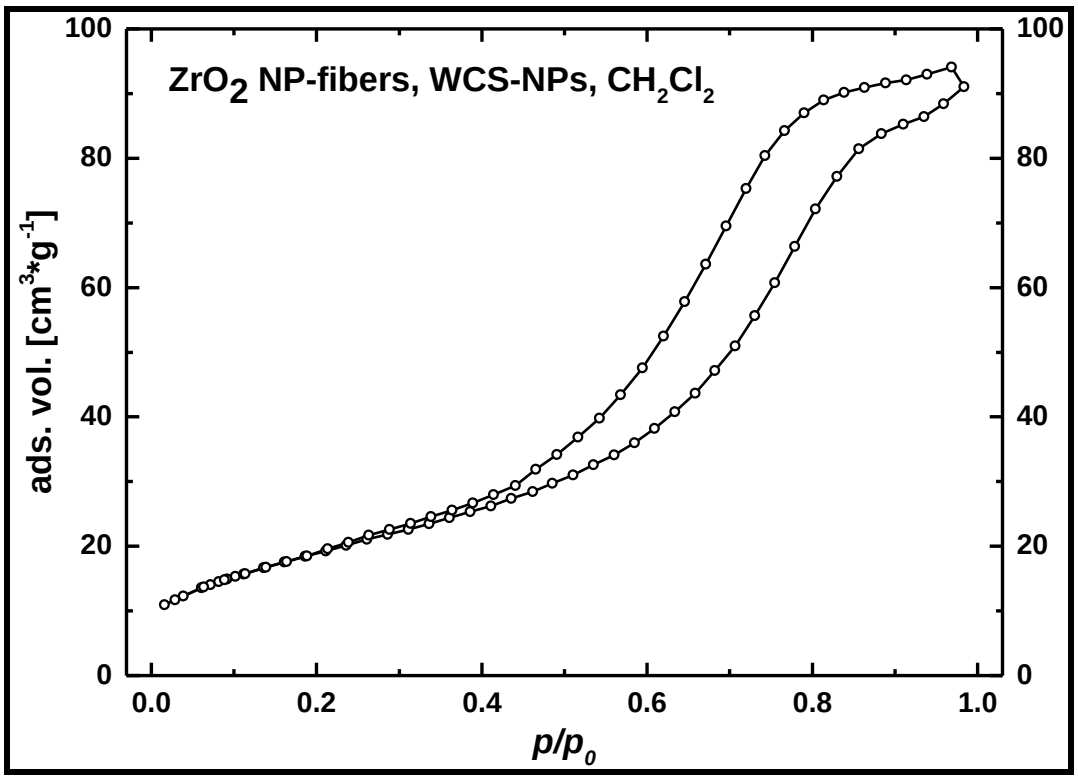

Figure 6-28: N_2-Physisorption isotherm of ZrO_2 NP-fibers obtained from WCS-NPs and spun from CH_2Cl_2/MeOH solvent mixture (see table 3-4, sample 3).

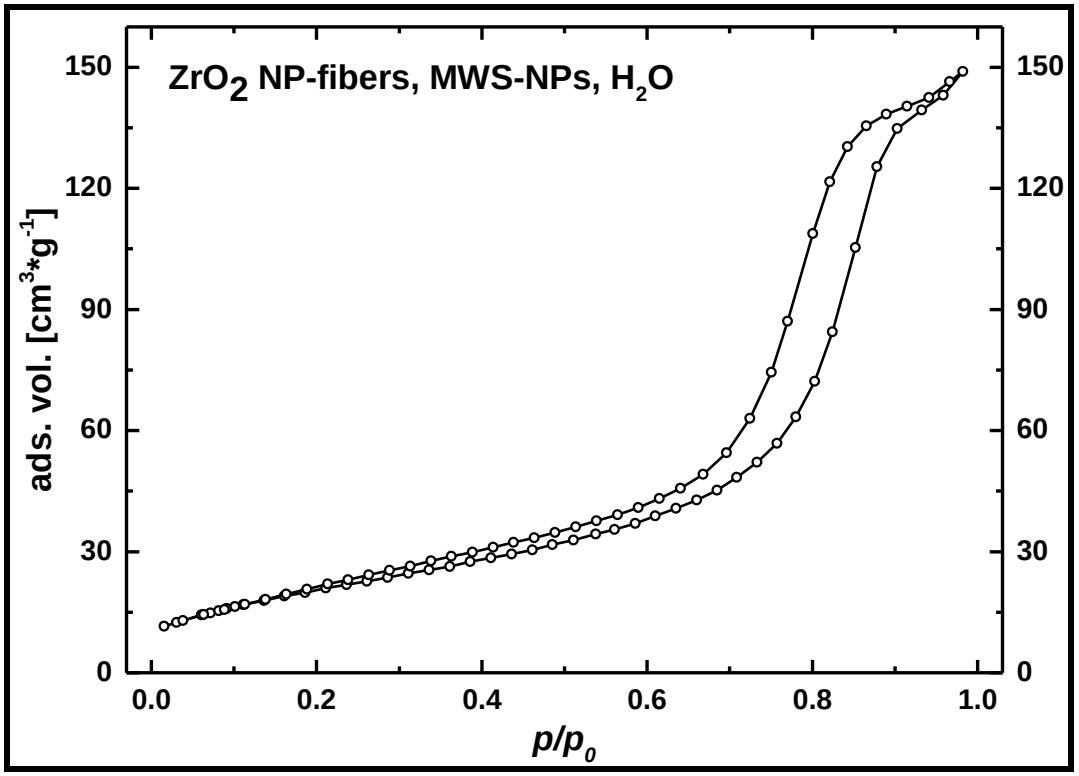

Figure 6-29: N_2-Physisorption isotherm of ZrO_2 NP-fibers obtained from MWS-NPs and spun from H_2O/MeOH solvent mixture (see table 3-4, sample 4).

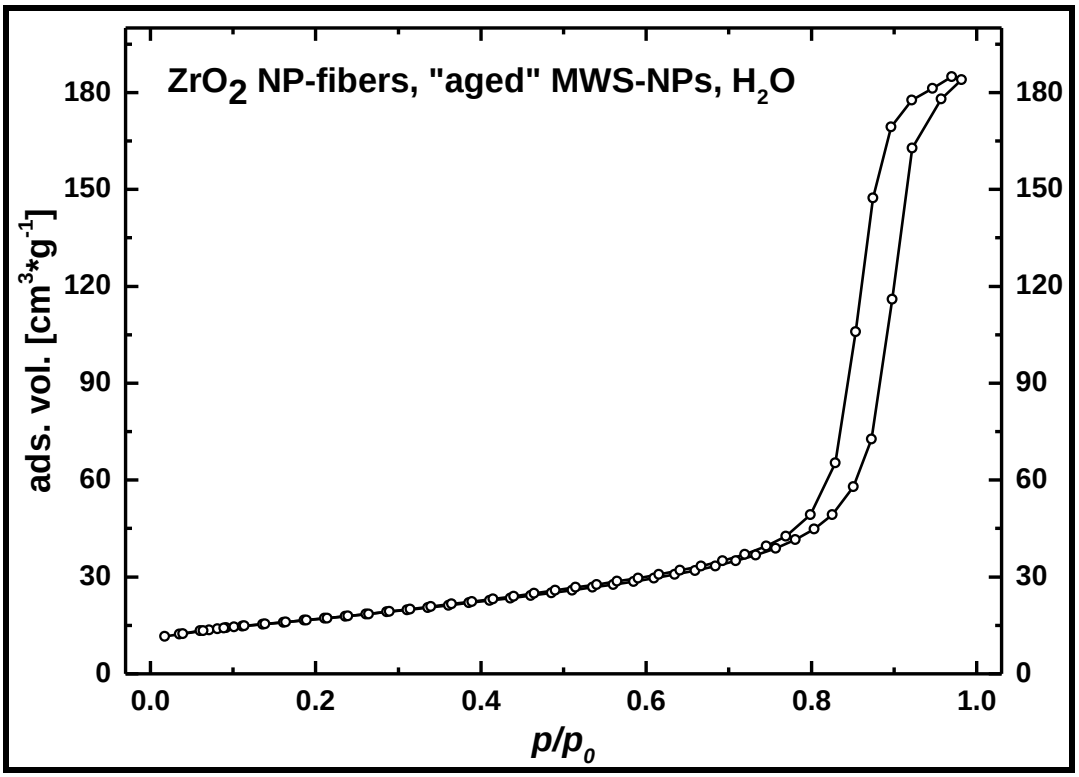

Figure 6-30: N_2-Physisorption isotherm of ZrO_2 NP-fibers obtained from "aged" MWS-NPs and spun from H_2O/MeOH solvent mixture (see table 3-4, sample 5).

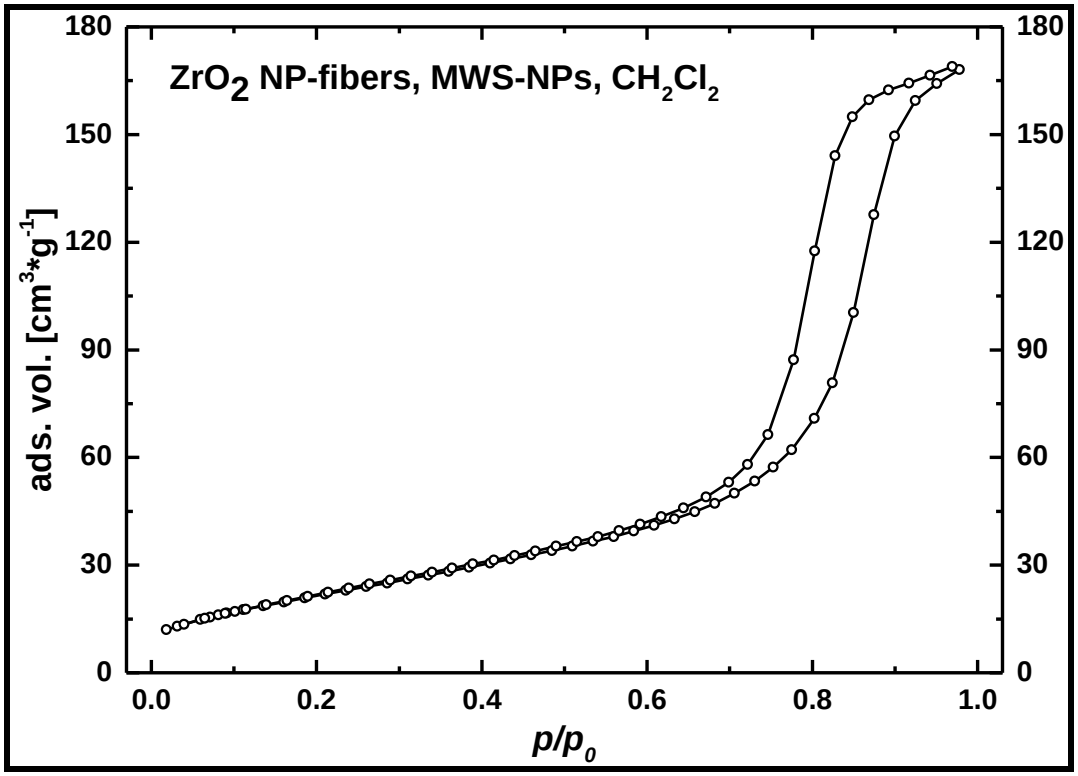

Figure 6-31: N_2-Physisorption isotherm of ZrO_2 NP-fibers obtained from MWS-NPs and spun from CH_2Cl_2/MeOH solvent mixture (see table 3-4, sample 6).

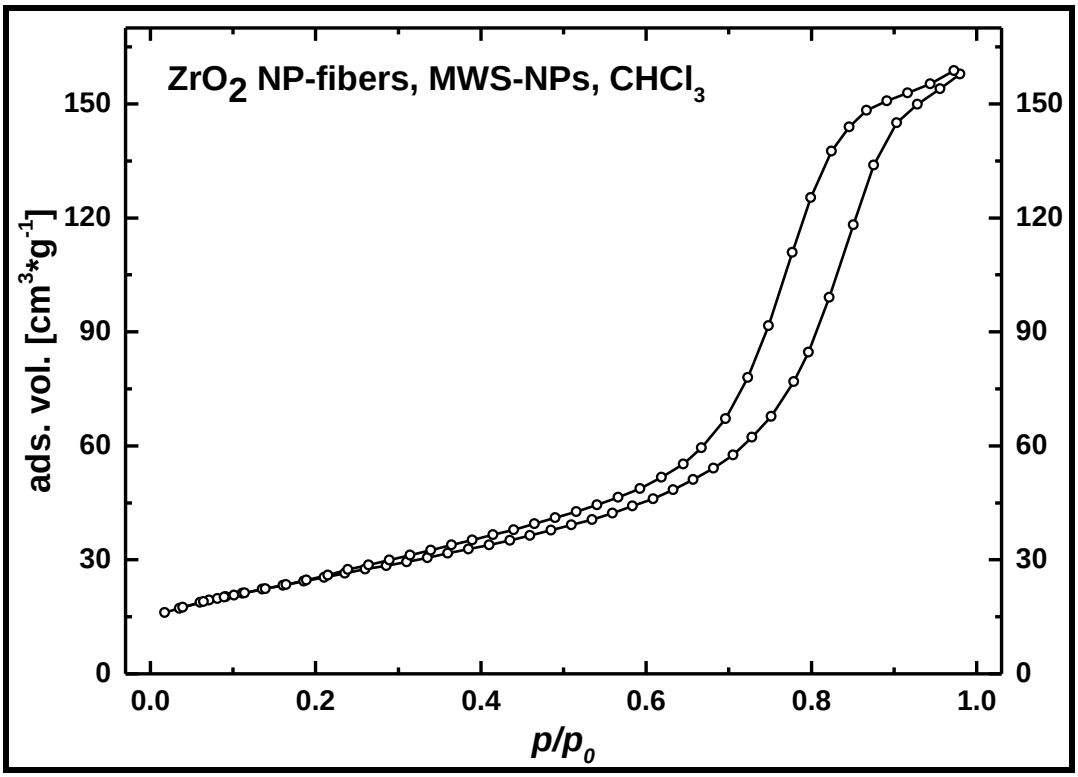

Figure 6-32: N_2-Physisorption isotherm of ZrO_2 NP-fibers obtained from MWS-NPs and spun from $CHCl_3$/MeOH solvent mixture (see table 3-4, sample 7).

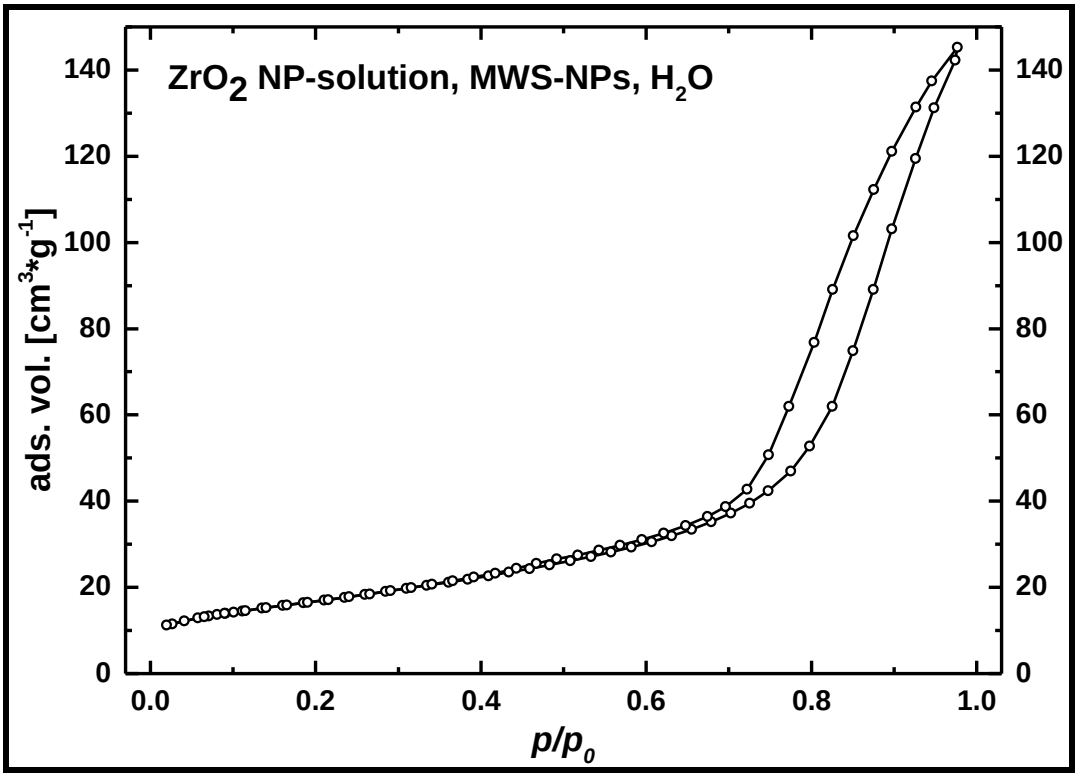

Figure 6-33: N_2-Physisorption isotherm of bulk sample obtained from dried and calcined ZrO_2 NP-solution containing MWS-NPs, PEO, H_2O and MeOH (see table 3-4, sample 8).

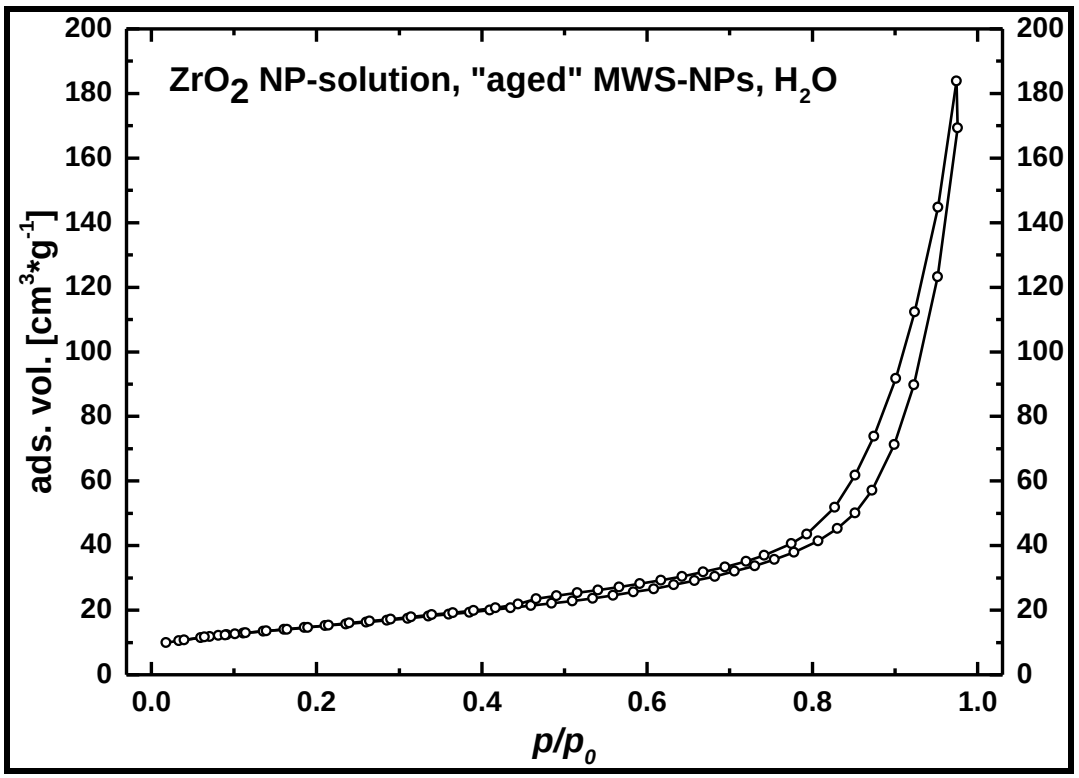

Figure 6-34: N_2-Physisorption isotherm of bulk sample obtained from dried and calcined ZrO_2 NP-solution containing "aged" MWS-NPs, PEO, H_2O and MeOH (see table 3-4, sample 9).

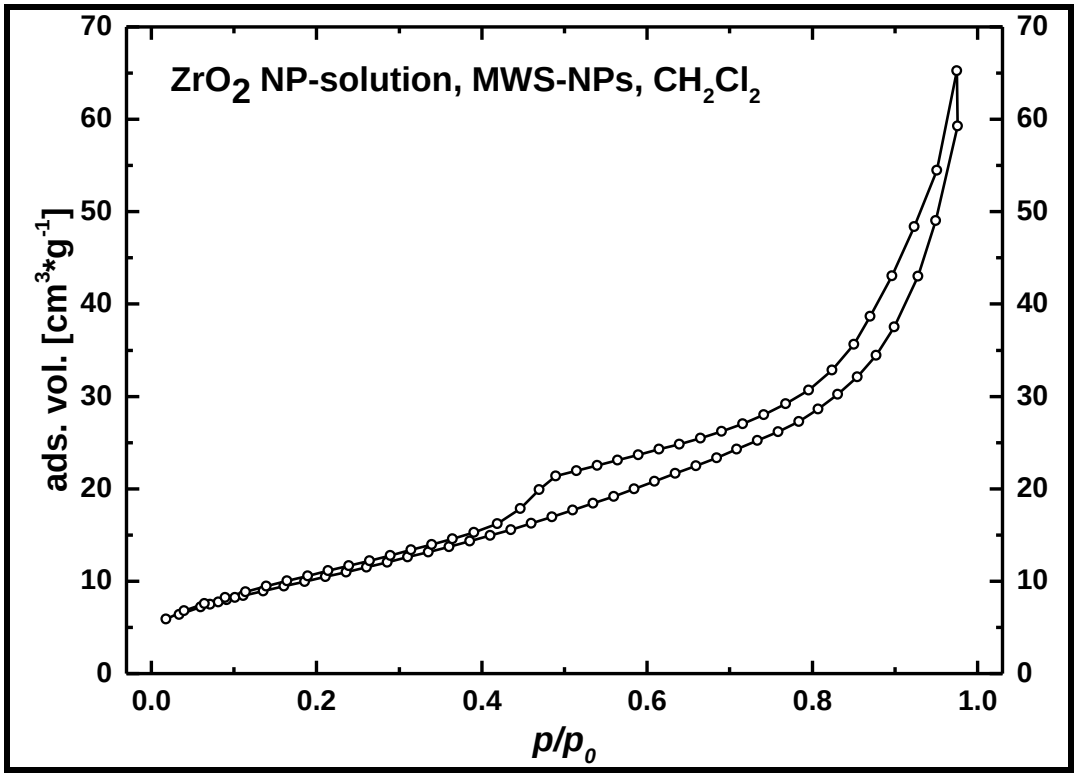

Figure 6-35: N_2-Physisorption isotherm of bulk sample obtained from dried and calcined ZrO_2 NP-solution containing MWS-NPs, PEO, CH_2Cl_2 and MeOH (see table 3-4, sample 10).

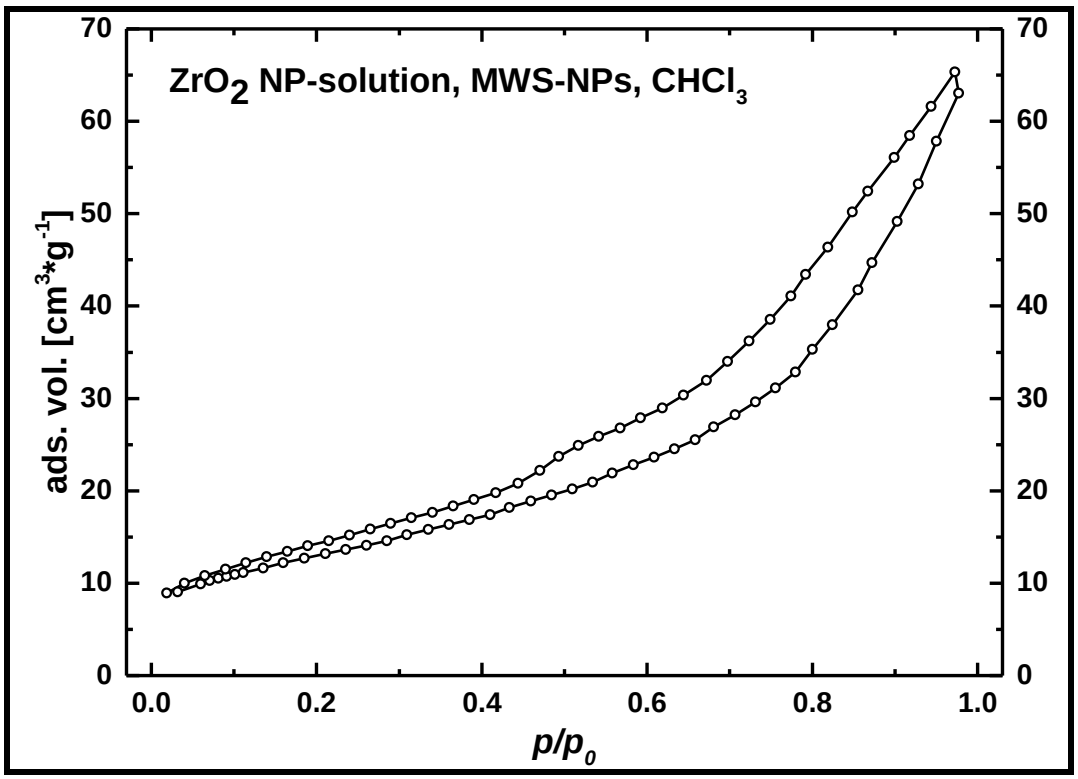

Figure 6-36: N_2-Physisorption isotherm of bulk sample obtained from dried and calcined ZrO_2 NP-solution containing MWS-NPs, PEO, $CHCl_3$ and MeOH (see table 3-4, sample 11).

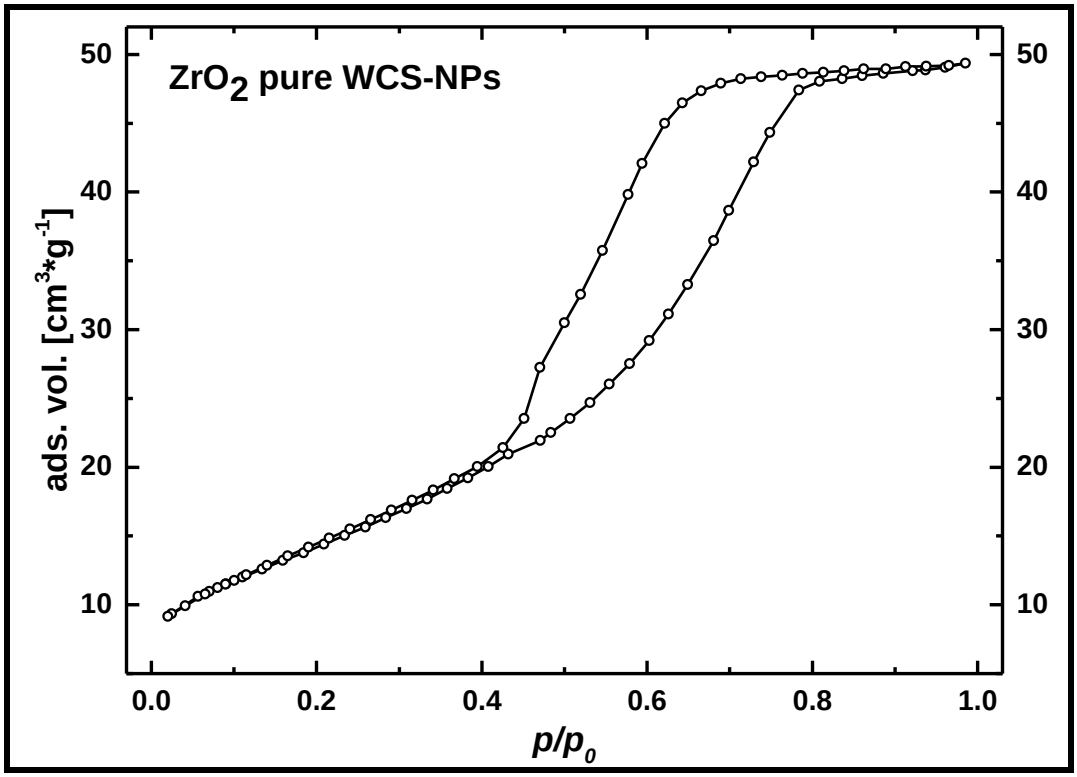

Figure 6-37: N_2-Physisorption isotherm of pure ZrO_2 WCS-NPs nanoparticles (see table 3-4, sample 12).

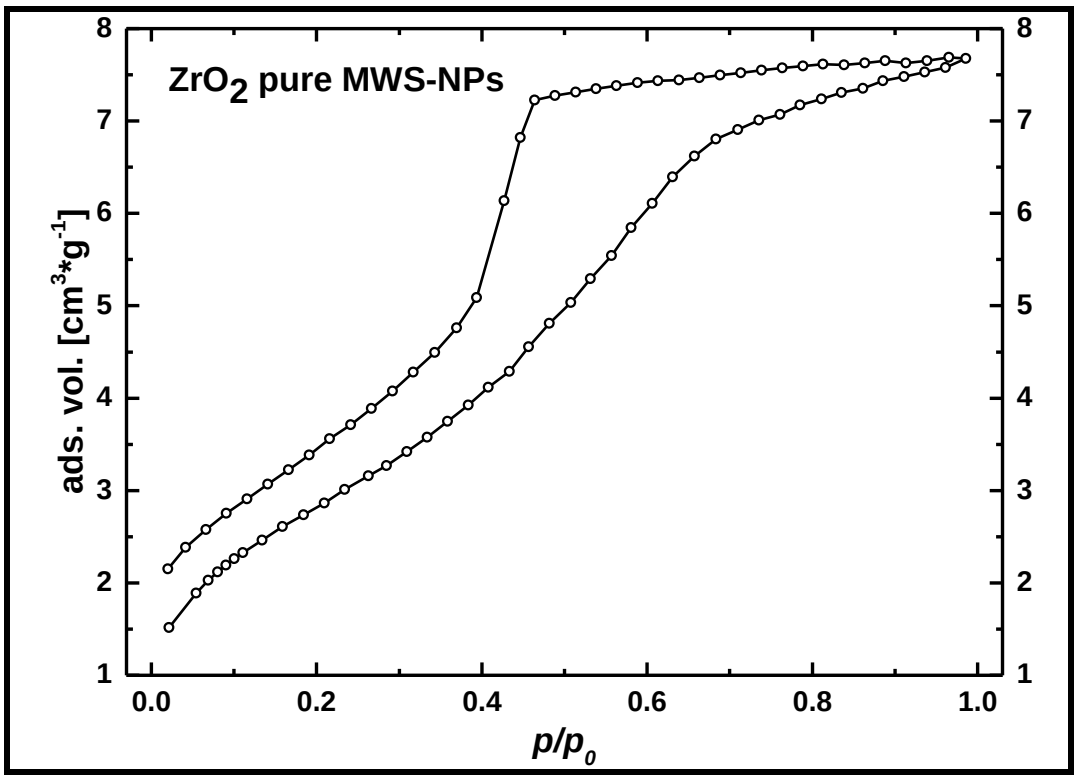

Figure 6-38: N_2-Physisorption isotherm of pure ZrO_2 MWS-NPs (see table 3-4, sample 13).

6.3.5 Nitrogen physisorption isotherms of ceria materials

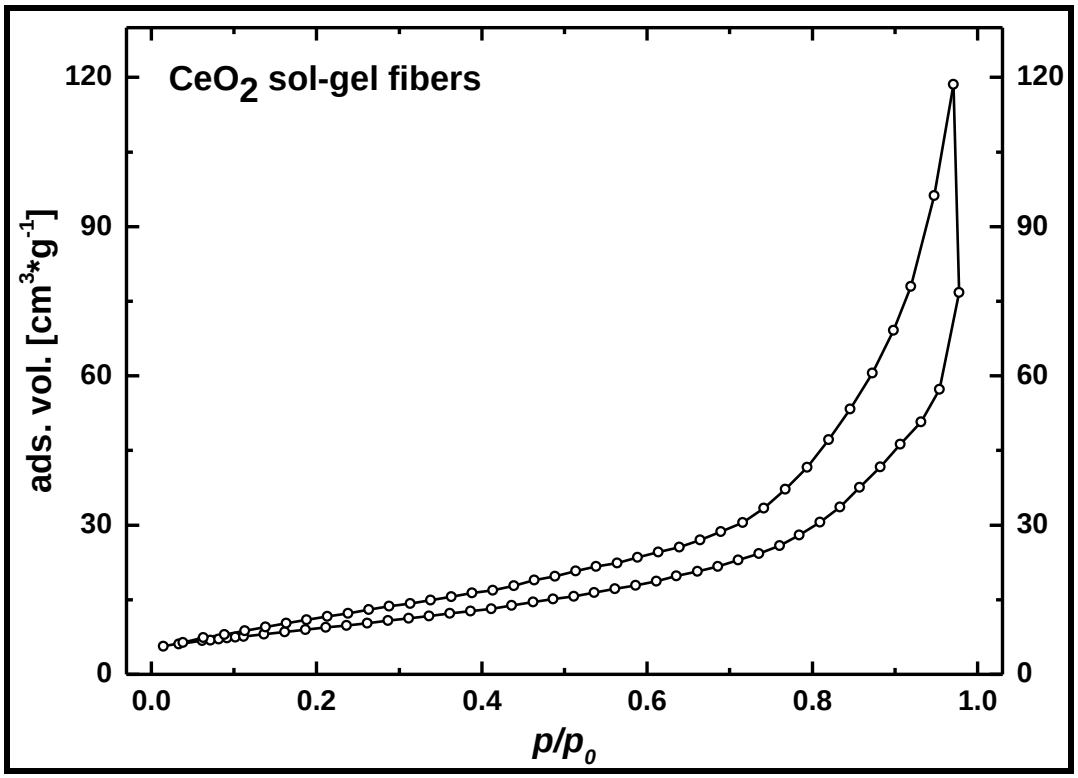

Figure 6-39: N_2-Physisorption isotherm of CeO_2 sol-gel fibers (see table 3-7, sample 1).

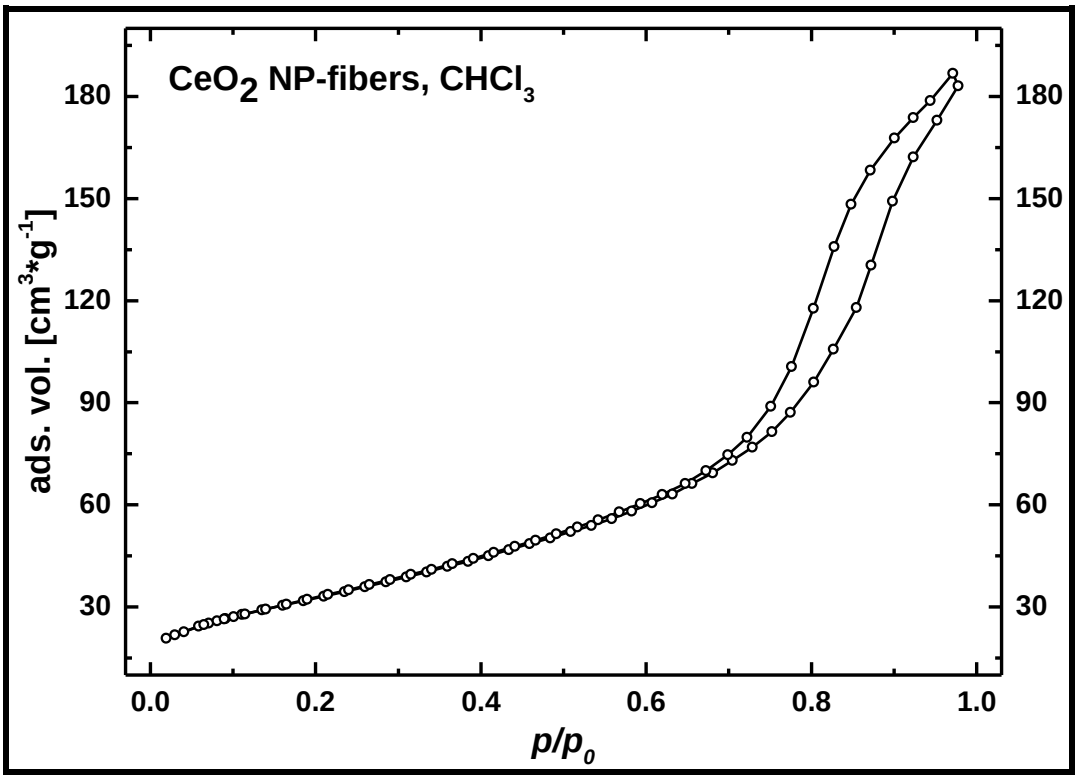

Figure 6-40: N_2-Physisorption isotherm of CeO_2 NP-fibers spun from $CHCl_3$ (see table 3-7, sample 2).

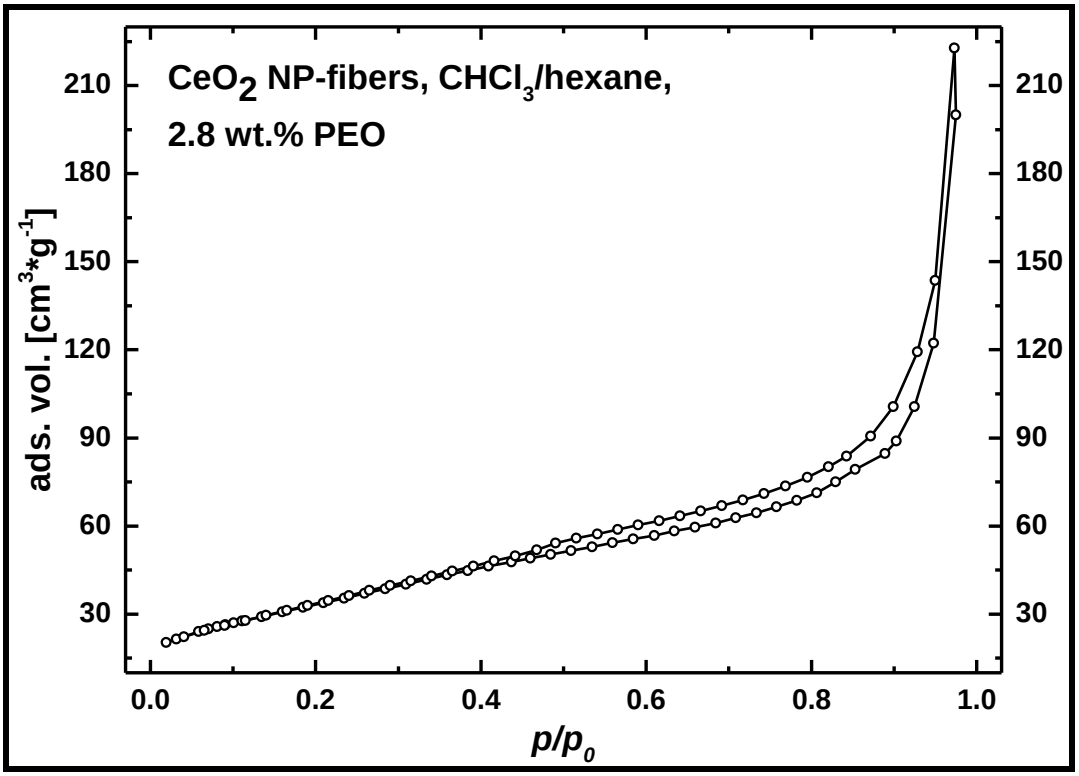

Figure 6-41: N_2-Physisorption isotherm of CeO_2 NP-fibers spun with 2.8 wt.-% PEO from $CHCl_3$/n-hexane solvent mixture (see table 3-7, sample 3).

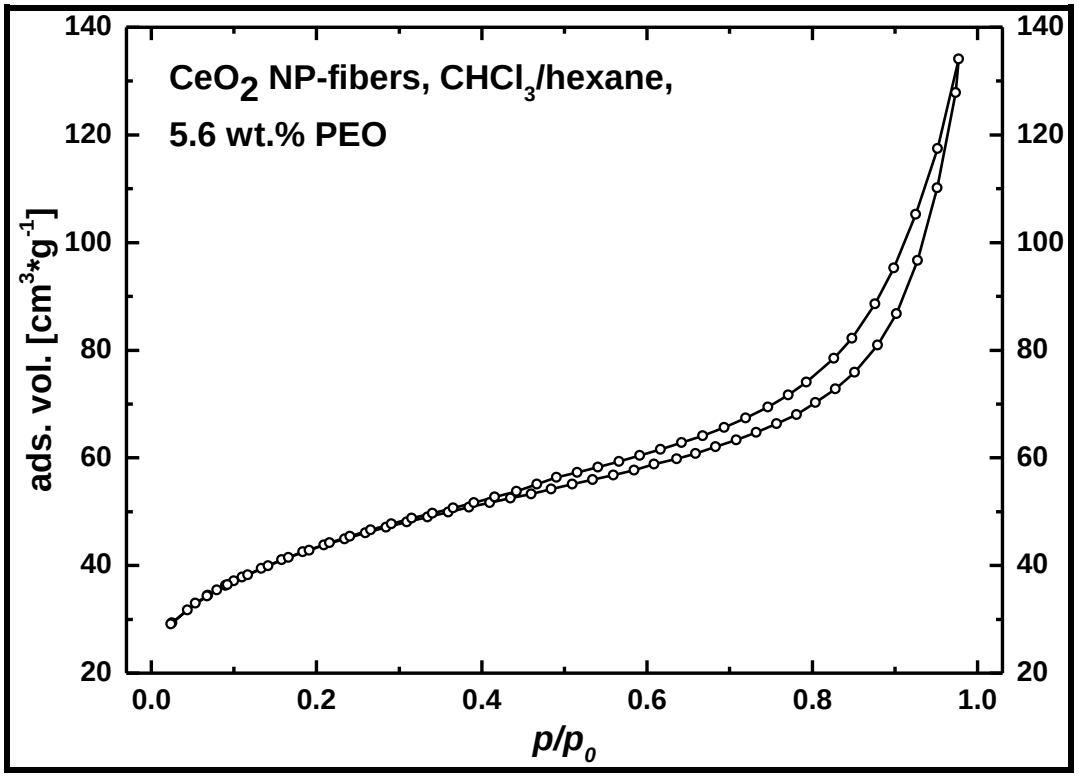

Figure 6-42: N_2-Physisorption isotherm of CeO_2 NP-fibers spun with 5.6 wt.-% PEO from $CHCl_3$/n-hexane solvent mixture (see table 3-7, sample 4).

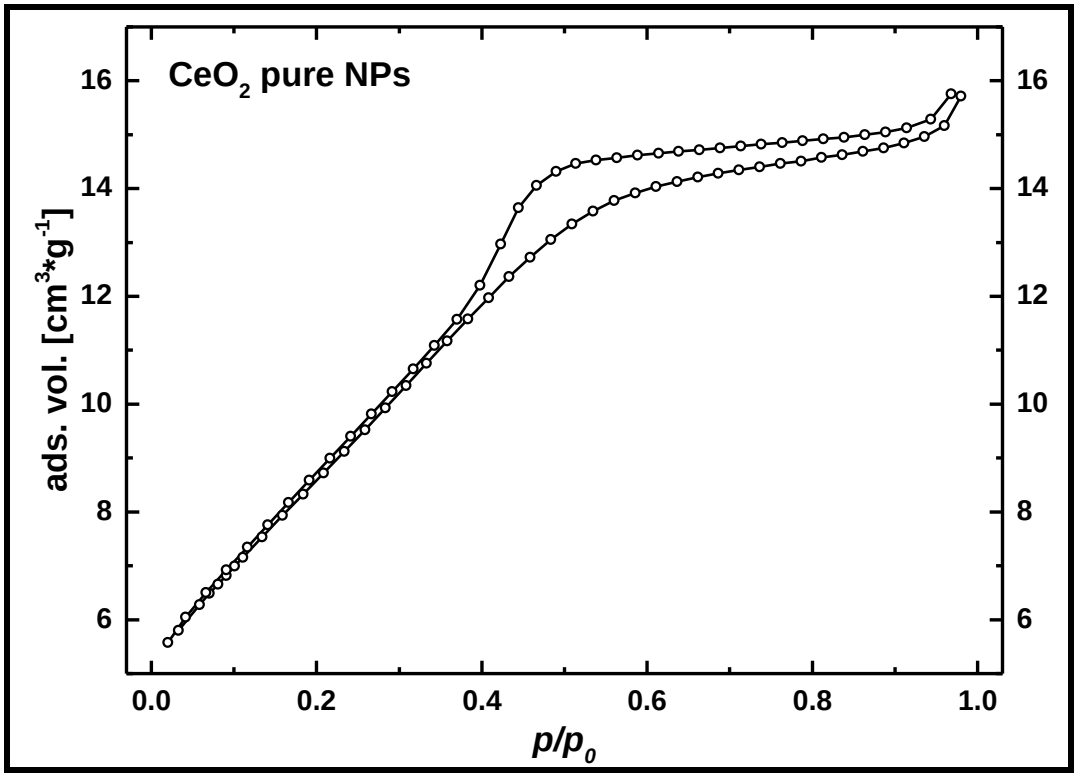

Figure 6-43: N_2-Physisorption isotherm of pure CeO_2 nanoparticles (see table 3-7, sample 5).

6.3.6 Nitrogen physisorption isotherms of tin oxide materials

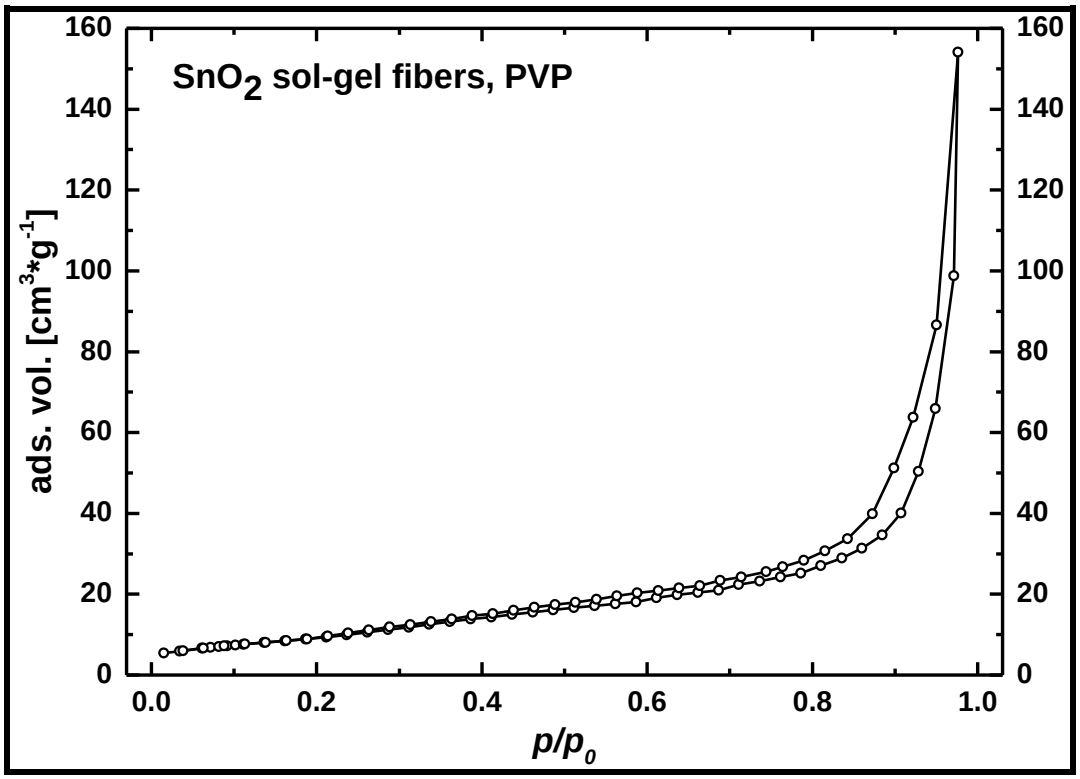

Figure 6-44: N_2-Physisorption isotherm of SnO_2 sol-gel fibers spun with PVP (see table 3-10, sample 1).

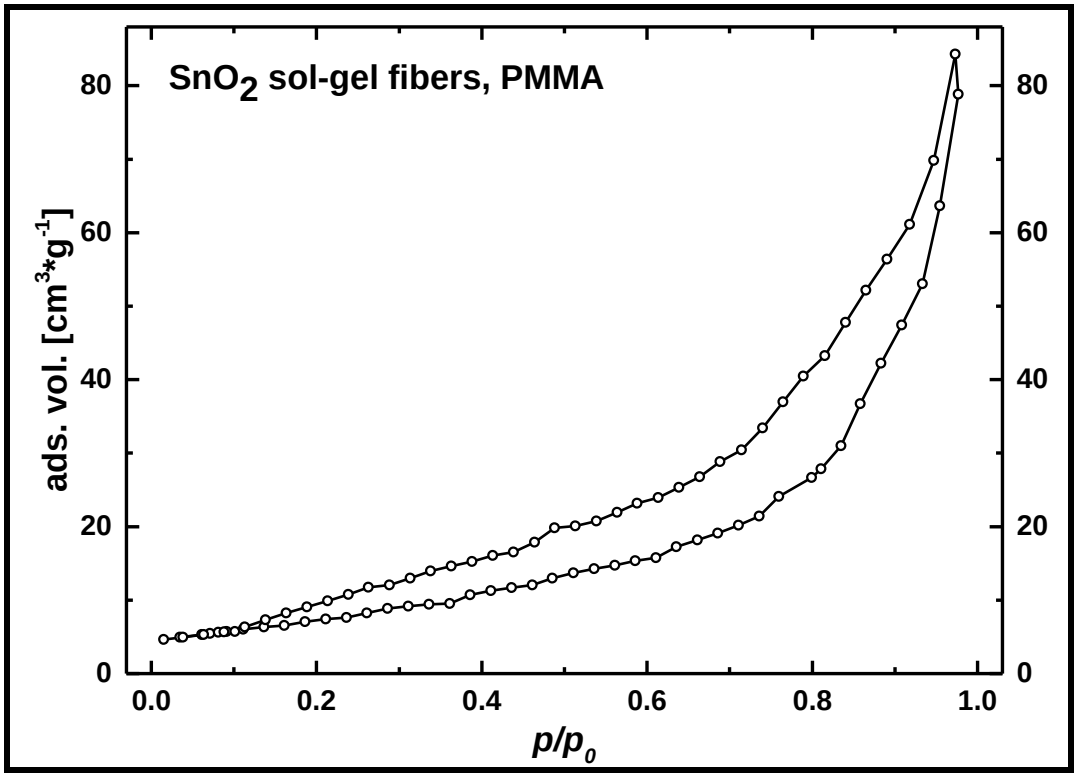

Figure 6-45: N_2-Physisorption isotherm of SnO_2 sol-gel fibers spun with PMMA (see table 3-10, sample 2).

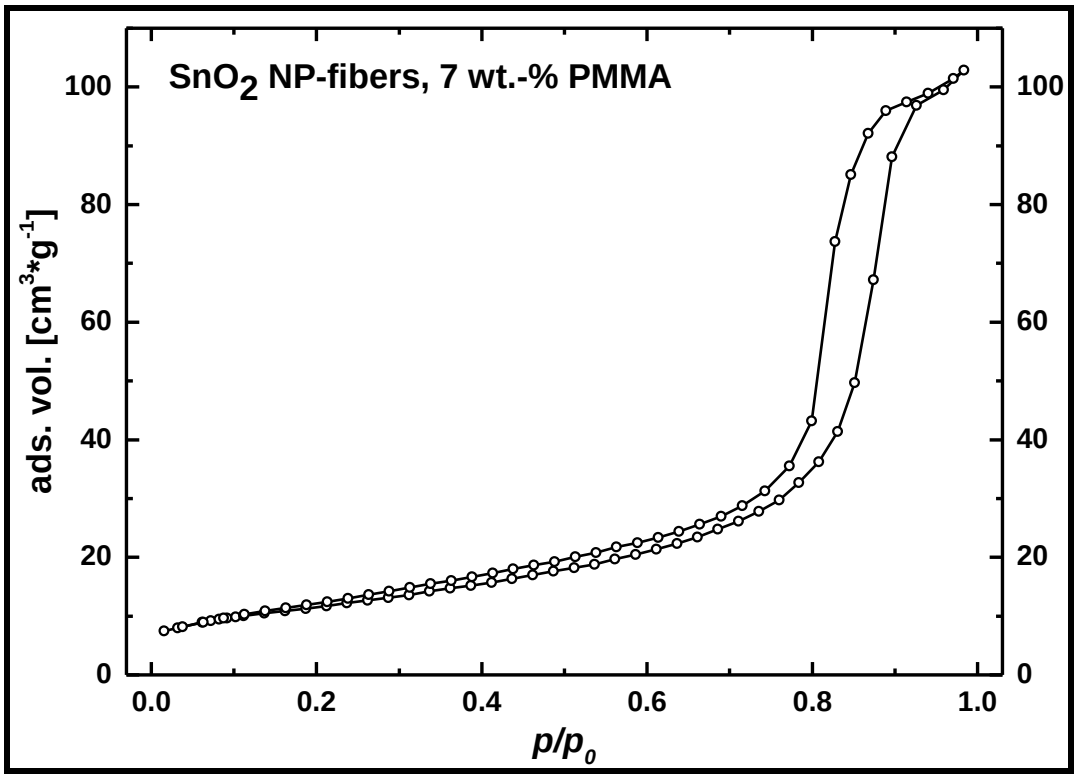

Figure 6-46: N_2-Physisorption isotherm of SnO_2 NP-fibers spun with 7 wt.-% PMMA (see table 3-10, sample 3).

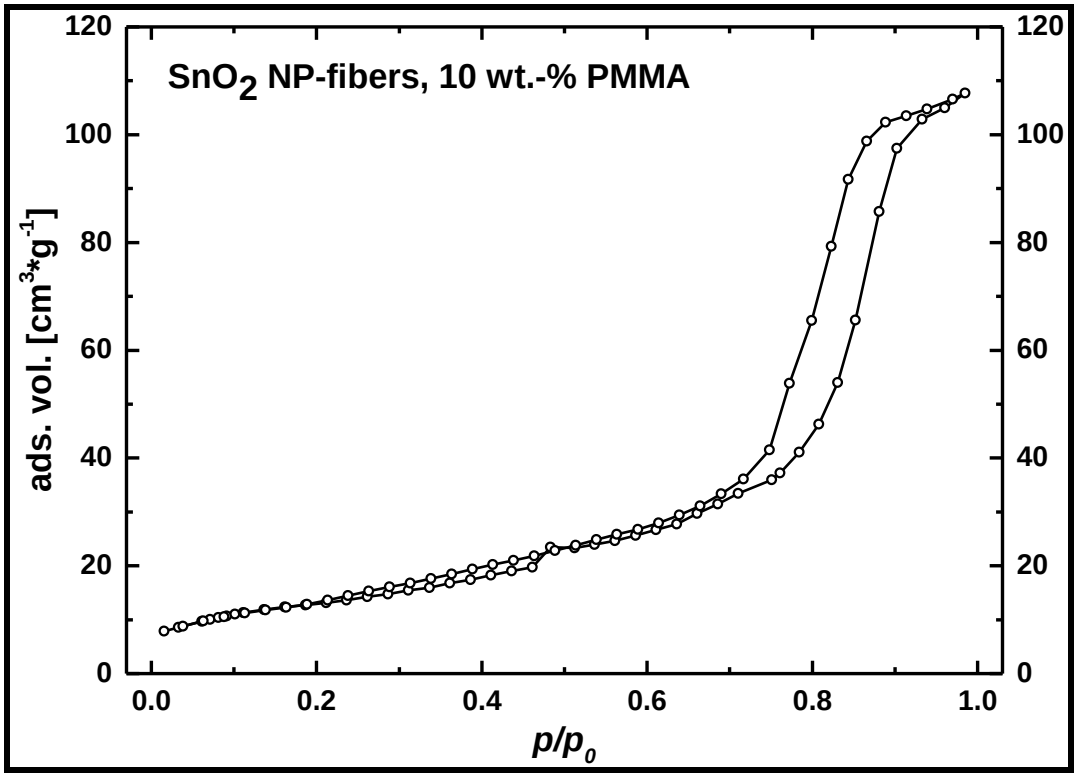

Figure 6-47: N_2-Physisorption isotherm of SnO_2 NP-fibers spun with 10 wt.-% PMMA (see table 3-10, sample 4).

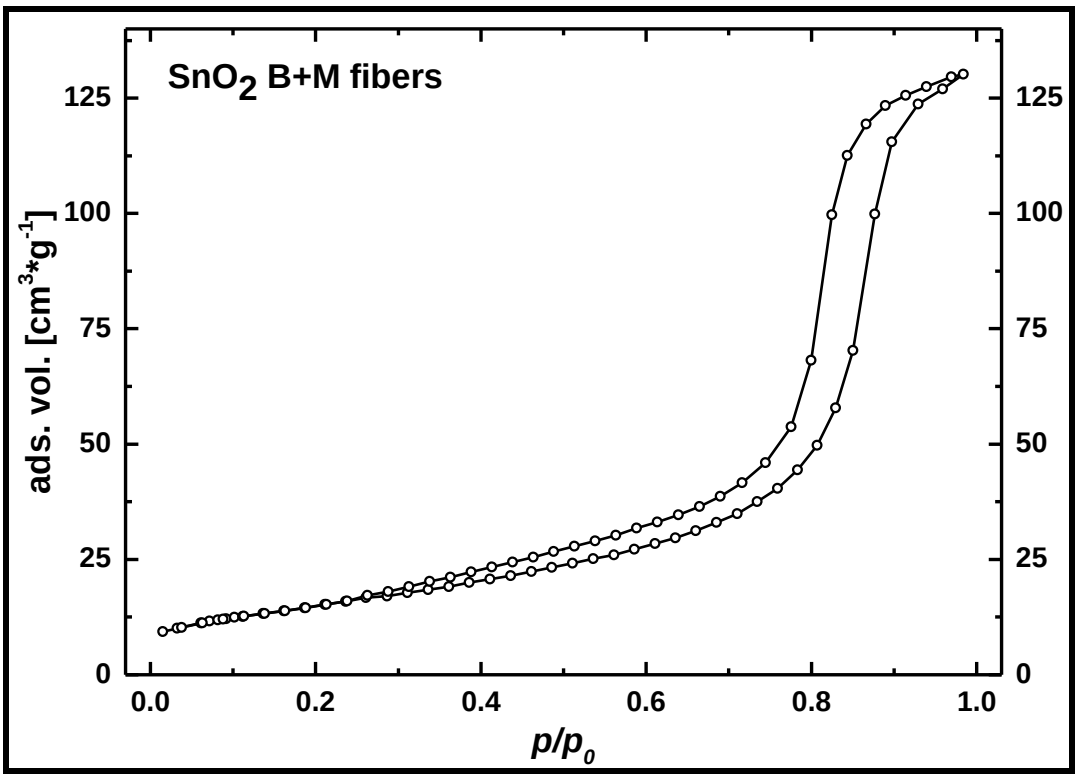

Figure 6-48: N_2-Physisorption isotherm of SnO_2 B+M-fibers (see table 3-10, sample 5).

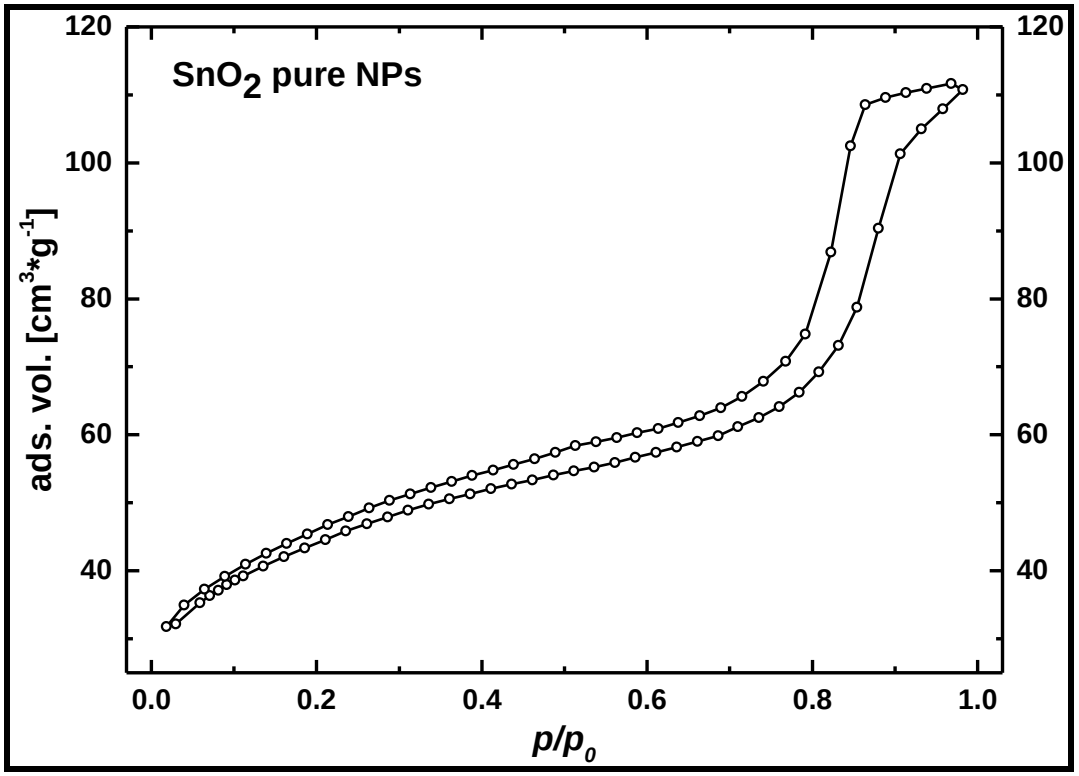

Figure 6-49: N_2-Physisorption isotherm of pure SnO_2 nanoparticles (see table 3-10, sample 6).

6.4 References

[1] C. Wessel, *Diploma Thesis, Philipps-University Marburg* **2009**.

[2] J. M. Szeifert, D. Fattakhova-Rohlfing, D. Georgiadou, V. Kalousek, J. Rathouský, D. Kuang, S. Wenger, S. M. Zakeeruddin, M. Grätzel, T. Bein, *Chem. Mater.* **2009**, *21*, 1260–1265.

[3] B.-L. Su, C. Sanchez, X.-Y. Yang, *Hierarchically Structured Porous Materials*, Wiley-VCH, Weinheim, **2012**.

[4] P. Gibson, H. Schreuder-Gibson, D. Rivin, *Colloids and Surfaces A: Physicochem. and Eng. Asp.* **2001**, *187-188*, 469–481.

[5] J. Jortner, C. N. R. Rao, *Pure Appl. Chem.* **2002**, *74*, 1491–1506.

[6] Y. Wan, D. Zhao, *Chem. Rev.* **2007**, *107*, 2821–2860.

[7] G. Wilde, *Nanostructured Materials*, Elsevier, Amsterdam, **2008**.

[8] L. J. Guo, *Adv. Mater.* **2007**, *19*, 495–513.

[9] Y. Xia, G. M. Whitesides, *Angew. Chemie Int. Ed.* **1998**, *37*, 550–575.

[10] R. Garcia, R. V Martinez, J. Martinez, *Chem. Soc. Rev.* **2006**, *35*, 29–38.

[11] P. Mendes, J. Preece, *Curr. Opin. Colloid Interface Sci.* **2004**, *9*, 236–248.

[12] K. W. Kolasinski, *Curr. Opin. Solid State Mater. Sci.* **2005**, *9*, 73–83.

[13] C. J. Brinker, Y. Lu, A. Sellinger, H. Fan, *Adv. Mater.* **1999**, *11*, 579–585.

[14] D. Grosso, F. Cagnol, G. J. de A. A. Soler-Illia, E. L. Crepaldi, H. Amenitsch, A. Brunet-Bruneau, A. Bourgeois, C. Sanchez, *Adv. Funct. Mater.* **2004**, *14*, 309–322.

[15] T. Brezesinski, M. Groenewolt, A. Gibaud, N. Pinna, M. Antonietti, B. Smarsly, *Adv. Mater.* **2006**, *18*, 2260–2263.

[16] K. S. W. Sing, D. H. Everett, R. A. W. Haul, L. Moscou, R. A. Pierotti, J. Rouquérol, T. Siemieniewska, *Pure Appl. Chem.* **1985**, *57*, 603–619.

[17] F. Schüth, K. S. W. Sing, J. Weitkamp, Eds., in *Handbook of Porous Solids*, Wiley-VCH, Weinheim, **2002**, pp. 535–666.

[18] W. Stöber, A. Fink, E. Bohn, *J. Colloid Interface Sci.* **1968**, *26*, 62–69.

[19] A.-H. Lu, F. Schüth, *Adv. Mater.* **2006**, *18*, 1793–1805.

[20] M. E. Davis, R. F. Lobo, *Chem. Mater.* **1992**, *4*, 756–768.

[21] C. R. Martin, *Chem. Mater.* **1996**, *8*, 1739–1746.

[22] E. Ortel, A. Fischer, L. Chuenchom, J. Polte, F. Emmerling, B. Smarsly, R. Kraehnert, *Small* **2012**, *8*, 298–309.

[23] S. Altmaier, *Ph. D. Thesis, University Hannover* **2003**.

[24] M. Schröder, S. Sallard, M. Böhm, M. Einert, C. Suchomski, B. M. Smarsly, S. Mutisya, M. F. Bertino, *Small* **2014**, *10*, 1566–1574.

[25] K. Landfester, M. Willert, M. Antonietti, *Macromolecules* **2000**, *33*, 2370–2376.

[26] O. Sel, D. Kuang, M. Thommes, B. Smarsly, *Langmuir* **2006**, *22*, 2311–2322.

[27] O. Sel, S. Sallard, T. Brezesinski, J. Rathouský, D. R. Dunphy, A. Collord, B. M. Smarsly, *Adv. Funct. Mater.* **2007**, *17*, 3241–3250.

[28] J. W. Cahn, *J. Chem. Phys.* **1965**, *42*, 93–99.

[29] J. W. Cahn, J. E. Hilliard, *J. Chem. Phys.* **1958**, *28*, 258–267.

[30] I. Steinbach, *Annu. Rev. Mater. Res.* **2013**, *43*, 89–107.

[31] M. Tang, A. Karma, *Phys. Rev. Lett.* **2012**, *108*, 265701.

[32] H. P. Fischer, P. Maass, W. Dieterich, *Europhys. Lett.* **1998**, *42*, 49–54.

[33] M. Haataja, J. Mahon, N. Provatas, F. Léonard, *Appl. Phys. Lett.* **2005**, *87*, 251901.

[34] M. K. Miller, J. M. Hyde, M. G. Hetherington, A. Cerezo, G. D. W. Smith, C. M. Elliott, *Acta Met. Mater.* **1995**, *43*, 3385–3401.

[35] J. M. Hyde, M. K. Miller, M. G. Hetherington, A. Cerezo, G. D. W. Smith, C. M. Elliott, *Acta Met. Mater.* **1995**, *43*, 3403–3413.

[36] J. M. Hyde, M. K. Miller, M. G. Hetherington, A. Cerezo, G. D. W. Smith, C. M. Elliott, *Acta Met. Mater.* **1995**, *43*, 3415–3426.

[37] C. Domb, J. L. Lebowitz, Eds., *Phase Transitions and Critical Phenomena*, Academic Press Inc., London, **1983**.

[38] R. Mori, M. Takahashi, T. Yoko, *Mater. Res. Bull.* **2004**, *39*, 2137–2143.

[39] R. Mori, M. Takahashi, T. Yoko, *J. Mater. Res.* **2006**, *21*, 270–275.

[40] H. Jinnai, Y. Nishikawa, T. Koga, T. Hashimoto, *Macromolecules* **1995**, *28*, 4782–4784.

[41] H. Jinnai, Y. Nishikawa, H. Morimoto, T. Koga, T. Hashimoto, *Langmuir* **2000**, *16*, 4380–4393.

[42] H. Jinnai, T. Koga, Y. Nishikawa, T. Hashimoto, S. Hyde, *Phys. Rev. Lett.* **1997**, *78*, 2248–2251.

[43] K. Nakanishi, *J. Porous Mater.* **1997**, *4*, 67–112.

[44] J. Konishi, K. Fujita, K. Nakanishi, K. Hirao, *Chem. Mater.* **2006**, *18*, 864–866.

[45] R. Takahashi, S. Sato, T. Sodesawa, T. Azuma, *J. Sol-Gel Sci. Technol.* **2004**, *31*, 373–376.

[46] T. Hara, *Ph. D. Thesis, Justus-Liebig-University Giessen* **2012**.

[47] M. Motokawa, H. Kobayashi, N. Ishizuka, H. Minakuchi, K. Nakanishi, H. Jinnai, K. Hosoya, T. Ikegami, N. Tanaka, *J. Chromatogr. A* **2002**, *961*, 53–63.

[48] K. Nakanishi, N. Tanaka, *Acc. Chem. Res.* **2007**, *40*, 863–873.

[49] W. C. K. Poon, M. D. Haw, *Adv. Colloid Interface Sci.* **1997**, *73*, 71–126.

[50] R. Jullien, M. Kolb, R. Botet, *J. Phys. Lettres* **1984**, *45*, 211–216.

[51] G. Wedler, *Lehrbuch Der Physikalischen Chemie*, Wiley-VCH, Weinheim, **2004**.

[52] H.-D. Dörfler, *Grenzflächen Und Kolloid-Disperse Systeme*, Springer Verlag, Berlin, **2002**.

[53] D. Crespy, K. Friedemann, A.-M. Popa, *Macromol. Rapid Commun.* **2012**, *33*, 1978–1995.

[54] A. Formhals, *Verfahren Und Vorrichtung Zur Herstellung von Kuenstlichen Fasern, German Patent 584801*, **1929**.

[55] A. Formhals, *Process and Apparatus for Preparing Artificial Threads, U.S. Patent 1975504*, **1930**.

[56] J. F. Cooley, *Apparatus for Electrically Dispersing Fluids, U.S. Patent 692631*, **1899**.

[57] G. Taylor, *Proc. R. Soc. London. A. Math. Phys. Sci.* **1964**, *280*, 383–397.

[58] G. Taylor, *Proc. R. Soc. London. A. Math. Phys. Sci.* **1966**, *291*, 145–158.

[59] G. Taylor, *Proc. R. Soc. London. A. Math. Phys. Sci.* **1969**, *313*, 453–475.

[60] D. H. Reneker, A. L. Yarin, *Polymer (Guildf).* **2008**, *49*, 2387–2425.

[61] A. L. Yarin, W. Kataphinan, D. H. Reneker, *J. Appl. Phys.* **2005**, *98*, 064501.

[62] H. Fong, I. Chun, D. . Reneker, *Polymer (Guildf).* **1999**, *40*, 4585–4592.

[63] D. Li, Y. Xia, *Adv. Mater.* **2004**, *16*, 1151–1170.

[64] A. Greiner, J. H. Wendorff, *Angew. Chemie Int. Ed.* **2007**, *46*, 5670–5703.

[65] R. Ramaseshan, S. Sundarrajan, R. Jose, S. Ramakrishna, *J. Appl. Phys.* **2007**, *102*, 111101.

[66] S. Ramakrishna, K. Fujihara, W.-E. Teo, T.-C. Lim, Z. Ma, *An Introduction to Electrospinning and Nanofibers*, World Scientific Publishing Co. Pte. Ltd., Singapore, **2005**.

[67] D. Li, J. T. McCann, Y. Xia, M. Marquez, *J. Am. Ceram. Soc.* **2006**, *89*, 1861–1869.

[68] W.-E. Teo, R. Inai, S. Ramakrishna, *Sci. Technol. Adv. Mater.* **2011**, *12*, 013002.

[69] W. Salalha, J. Kuhn, Y. Dror, E. Zussman, *Nanotechnology* **2006**, *17*, 4675–4681.

[70] Z.-M. Huang, Y.-Z. Zhang, M. Kotaki, S. Ramakrishna, *Compos. Sci. Technol.* **2003**, *63*, 2223–2253.

[71] M. Niederberger, G. Garnweitner, *Chem. A Eur. J.* **2006**, *12*, 7282–7302.

[72] C. Grote, T. A. Cheema, G. Garnweitner, *Langmuir* **2012**, *28*, 14395–14404.

[73] H. Kamiya, M. Iijima, *Sci. Technol. Adv. Mater.* **2010**, *11*, 044304.

[74] G. Garnweitner, in *Polym. Aging, Stab. Amphiphilic Block Copolym.* (Eds.: L. Segewicz, M. Petrowsky), Nova Science Pub. Inc., New York, **2010**, pp. 173–195.

[75] C. Wessel, R. Ostermann, R. Dersch, B. M. Smarsly, *J. Phys. Chem. C* **2011**, 362–372.

[76] M. von Bistram, *Ph. D. Thesis, Philipps-University Marburg* **2007**.

[77] C.-D. Kohl, T. Wagner, *Gas Sensing Fundamentals*, Springer Verlag, Berlin, **2014**.

[78] S. Patil, *Doped Tin Oxide Gas Sensors*, Lap Lambert Academic Publishing, OmniScriptum GmbH & Co. KG, Saarbrücken, **2013**.

[79] P. Hartmann, D. Lee, B. M. Smarsly, J. Janek, **2010**, *4*, 3147–3154.

[80] J. Hennemann, T. Sauerwald, C.-D. Kohl, T. Wagner, M. Bognitzki, A. Greiner, *Phys. Status Solidi A* **2012**, *209*, 911–916.

[81] S. Madhugiri, B. Sun, P. G. Smirniotis, J. P. Ferraris, K. J. Balkus, *Microporous Mesoporous Mater.* **2004**, *69*, 77–83.

[82] L. Guo, J. Bai, C. Li, Q. Meng, H. Liang, W. Sun, H. Li, H. Liu, *Appl. Surf. Sci.* **2013**, *283*, 107–114.

[83] H. Jia, G. Zhu, B. Vugrinovich, W. Kataphinan, D. H. Reneker, P. Wang, *Biotechnol. Prog.* **2002**, *18*, 1027–1032.

[84] C. H. Kanzler, S. Urban, K. Zalewska-Wierzbicka, F. Hess, S. F. Rohrlack, C. Wessel, R. Ostermann, J. P. Hofmann, B. M. Smarsly, H. Over, *ChemCatChem* **2013**, *5*, 2621–2626.

[85] S. Urban, N. Tarabanko, C. H. Kanzler, K. Zalewska-Wierzbicka, R. Ellinghaus, S. F. Rohrlack, L. Chen, P. J. Klar, B. M. Smarsly, H. Over, *Catal. Letters* **2013**, *143*, 1362–1367.

[86] "Elmarco Nano For Life," can be found under www.elmarco.com, **accessed 26. November 2015**.

[87] "IME Technologies," can be found under www.imetechnologies.nl, **accessed 26. November 2015**.

[88] C. J. Luo, S. D. Stoyanov, E. Stride, E. Pelan, M. Edirisinghe, *Chem. Soc. Rev.* **2012**, *41*, 4708–35.

[89] R. Ostermann, *Ph. D. Thesis, Justus-Liebig-University Giessen* **2010**.

[90] Hessischen Ministeriums für Wirtschaft, Energie, Verkehr und Landesentwicklung "Safety of Nanostructures," can be found under www.nano-sicherheit.de, **accessed 26. November 2015**.

[91] M. Kanehata, B. Ding, S. Shiratori, *Nanotechnology* **2007**, *18*, 315602.

[92] C. Wessel, L. Zhao, S. Urban, R. Ostermann, I. Djerdj, B. M. Smarsly, L. Chen, Y.-S. Hu, S. Sallard, *Chemistry* **2011**, *17*, 775–9.

[93] N. Horzum, R. Muñoz-Espí, G. Glasser, M. M. Demir, K. Landfester, D. Crespy, *Appl. Mater. Interfaces* **2012**, 6338–6345.

[94] P. Dayal, J. Liu, S. Kumar, T. Kyu, *Macromolecules* **2007**, *40*, 7689–7694.

[95] P. Dayal, T. Kyu, *J. Appl. Phys.* **2006**, *100*, 043512.

[96] A. J. Guenthner, S. Khombhongse, W. Liu, P. Dayal, D. H. Reneker, T. Kyu, *Macromol. Theory Simulations* **2006**, *15*, 87–93.

[97] Y. Zhang, J. Yang, Q. Li, X. Cao, *J. Cryst. Growth* **2007**, *308*, 180–184.

[98] Z. Wang, X. Liu, M. Lv, P. Chai, Y. Liu, J. Meng, *J. Phys. Chem. B* **2008**, *112*, 11292–11297.

[99] M. Macías, A. Chacko, J. P. Ferraris, K. J. Balkus, *Microporous Mesoporous Mater.* **2005**, *86*, 1–13.

[100] S. Zhan, D. Chen, X. Jiao, C. Tao, *J. Phys. Chem. B* **2006**, *110*, 11199–11204.

[101] H. He, J. Wang, X. Li, X. Zhang, W. Weng, G. Han, *Mater. Lett.* **2013**, *94*, 100–103.

[102] J. Saha, G. De, *Chem. Commun.* **2013**, *49*, 6322–6324.

[103] M. Bognitzki, T. Frese, M. Steinhart, A. Greiner, J. H. Wendorff, A. Schaper, M. Hellwig, *Polym. Eng. Sci.* **2001**, *41*, 982–989.

[104] C.-L. Pai, M. C. Boyce, G. C. Rutledge, *Macromolecules* **2009**, *42*, 2102–2114.

[105] C. L. Casper, J. S. Stephens, N. G. Tassi, D. B. Chase, J. F. Rabolt, *Macromolecules* **2004**, *37*, 573–578.

[106] J. T. McCann, M. Marquez, Y. Xia, *J. Am. Chem. Soc.* **2006**, *128*, 1436–1437.

[107] S. Megelski, J. S. Stephens, D. B. Chase, J. F. Rabolt, *Macromolecules* **2002**, *35*, 8456–8466.

[108] M. Bognitzki, W. Czado, T. Frese, A. Schaper, M. Hellwig, M. Steinhart, A. Greiner, J. H. Wendorff, *Adv. Mater.* **2001**, *13*, 70–72.

[109] D. Li, Y. Xia, *Nano Lett.* **2003**, *3*, 555–560.

[110] H. Matsuyama, M. Teramoto, R. Nakatani, T. Maki, *J. Appl. Polym. Sci.* **1999**, *74*, 171–178.

[111] C. Gao, A. Li, L. Feng, X. Yi, J. Shen, *Polym. Int.* **2000**, *49*, 323–328.

[112] D. Grosso, F. Babonneau, P.-A. Albouy, H. Amenitsch, A. R. Balkenende, A. Brunet-Bruneau, J. Rivory, *Chem. Mater.* **2002**, *14*, 931–939.

[113] D. A. Doshi, A. Gibaud, N. Liu, D. Sturmayr, A. P. Malanoski, D. R. Dunphy, H. Chen, S. Narayanan, A. Macphee, J. Wang, et al., *J. Phys. Chem. B* **2003**, *107*, 7683–7688.

[114] B. Smarsly, M. Antonietti, *Eur. J. Inorg. Chem.* **2006**, *2006*, 1111–1119.

[115] Y.-J. Cheng, J. S. Gutmann, *J. Am. Chem. Soc.* **2006**, *128*, 4658–4674.

[116] D. H. Reneker, A. L. Yarin, H. Fong, S. Koombhongse, *J. Appl. Phys.* **2000**, *87*, 4531–4547.

[117] P. Dayal, T. Kyu, *Phys. Fluids* **2007**, *19*, 107106.

[118] K. Binder, *J. Non-Equilib. Thermodyn.* **1998**, *23*, 1–44.

[119] X. Wang, N. Mashita, *Polymer* **2004**, *45*, 2711–2719.

[120] E. V. Albano, K. Binder, D. W. Heermann, W. Paul, *Physica A* **1992**, *183*, 130–147.

[121] M. Thommes, K. A. Cychosz, *Adsorption* **2014**, *20*, 233–250.

[122] M. Thommes, in *Nanoporous Mater. Sci. Eng.* (Eds.: G.Q. Lu, X.S. Zhao), Imperial College Press, London, **2004**, pp. 317–364.

[123] D. Stoeckel, C. Ku, K. Hormann, A. Ho, B. M. Smarsly, U. Tallarek, *Langmuir* **2014**, *30*, 9022–9027.

[124] J. Zečević, K. P. de Jong, P. E. de Jongh, *Curr. Opin. Solid State Mater. Sci.* **2013**, *17*, 115–125.

[125] Quantachrome Instruments, *Manual Autosorb iQ ASiQwin Gas Sorption System* **2013**.

[126] L. G. Gurvich, *J. Russ. Phys. Chim.* **1915**, *47*, 805.

[127] J. Landers, G. Y. Gor, A. V. Neimark, *Colloids Surfaces A Physicochem. Eng. Asp.* **2013**, *437*, 3–32.

[128] A. F. Hollemann, E. Wiberg, *Lehrbuch Der Anorganischen Chemie*, Walter De Gruyter Verlag, Berlin, **1995**.

[129] P. Behrens, *Angew. Chemie Int. Ed.* **1996**, *35*, 515–518.

[130] C. Shao, H. Guan, Y. Liu, J. Gong, N. Yu, X. Yang, *J. Cryst. Growth* **2004**, *267*, 380–384.

[131] X. Yang, C. Shao, Y. Liu, R. Mu, H. Guan, *Thin Solid Films* **2005**, *478*, 228–231.

[132] Y. Wang, M. Aponte, N. Leon, I. Ramos, R. Furlan, S. Evoy, J. J. Santiago-Avilés, *Semicond. Sci. Technol.* **2004**, *19*, 1057–1060.

[133] C. Shao, H.-Y. Kim, J. Gong, B. Ding, D.-R. Lee, S.-J. Park, *Mater. Lett.* **2003**, *57*, 1579–1584.

[134] S. Choi, S. G. Lee, S. S. Im, S. H. Kim, Y. L. Joo, *J. Mater. Sci. Lett.* **2003**, *22*, 891–893.

[135] A. C. Patel, S. Li, J.-M. Yuan, Y. Wei, *Nano Lett.* **2006**, *6*, 1042–1046.

[136] B. Ding, H. Kim, C. Kim, M. Khil, S. Park, *Nanotechnology* **2003**, *14*, 532–537.

[137] A. C. Patel, S. Li, C. Wang, W. Zhang, Y. Wei, *Chem. Mater.* **2007**, *19*, 1231–1238.

[138] S. Zhan, D. Chen, X. Jiao, Y. Song, *Chem. Commun.* **2007**, *1*, 2043–2045.

[139] J.-M. Lim, J. H. Moon, G.-R. Yi, C.-J. Heo, S.-M. Yang, *Langmuir* **2006**, *22*, 3445–3449.

[140] R. Furlan, E. W. Simões, M. L. P. da Silva, I. Ramos, E. Fachini, *Polymer* **2007**, *48*, 5107–5115.

[141] K. Friedemann, T. Corrales, M. Kappl, K. Landfester, D. Crespy, *Small* **2012**, *8*, 144–153.

[142] W. Shi, W. Lu, L. Jiang, *J. Colloid Interface Sci.* **2009**, *340*, 291–297.

[143] Dupont, "Ludox® -- Technical Literature," can be found under http://nathan.instras.com/documentDB/paper-190.pdf, **accessed 26. November 2015**.

[144] ccc-group, "Ludox products," can be found under http://www.ccc-group.com/chemicals/products, **accessed 26. November 2015**.

[145] S. Mascotto, D. Wallacher, A. Kuschel, S. Polarz, G. A. Zickler, A. Timmann, B. M. Smarsly, *Langmuir* **2010**, *26*, 6583–6592.

[146] S. Mascotto, D. Wallacher, A. Brandt, T. Hauss, M. Thommes, G. A. Zickler, S. S. Funari, A. Timmann, B. M. Smarsly, *Langmuir* **2009**, *25*, 12670–12681.

[147] B. Smarsly, A. Gibaud, W. Ruland, D. Sturmayr, C. J. Brinker, *Langmuir* **2005**, *21*, 3858–3866.

[148] B. Smarsly, G. Xomeritakis, K. Yu, N. Liu, H. Fan, R. A. Assink, C. A. Drewien, W. Ruland, C. J. Brinker, *Langmuir* **2003**, *19*, 7295–7301.

[149] B. Smarsly, S. Polarz, M. Antonietti, *J. Phys. Chem. C* **2001**, *105*, 10473–10483.

[150] C. Sanchez, G. J. de A. A. Soler-Illia, F. Ribot, D. Grosso, *Comptes Rendus Chim.* **2003**, *6*, 1131–1151.

[151] N. K. Raman, M. T. Anderson, C. J. Brinker, *Chem. Mater.* **1996**, *8*, 1682–1701.

[152] D. R. Lide, *CRC Press Handbook of Chemistry and Physics*, CRC Press LLC, New York, **2004**.

[153] N. Jing, M. Wang, J. Kameoka, *J. Photopolym. Sci. Technol.* **2005**, *18*, 503–506.

[154] E. Davies, A. Lowe, M. Sterns, K. Fujihara, S. Ramakrishna, *J. Am. Ceram. Soc.* **2008**, *91*, 1115–1120.

[155] D. Qin, A. Gu, G. Liang, L. Yuan, *RSC Adv.* **2012**, *2*, 1364–1372.

[156] H. B. Zhang, M. J. Edirisinghe, *J. Am. Ceram. Soc.* **2006**, *89*, 1870–1875.

[157] M. Möller, *Master Thesis, Justus-Liebig-University Giessen* **2012**.

[158] T. Chraska, A. H. King, C. C. Berndt, *Mater. Sci. Eng. A* **2000**, *286*, 169–178.

[159] R. C. Garvie, M. F. Goss, *J. Mater. Sci.* **1986**, *21*, 1253–1257.

[160] Y. Zhang, J. Li, Q. Li, L. Zhu, X. Liu, X. Zhong, J. Meng, X. Cao, *J. Colloid Interface Sci.* **2007**, *307*, 567–571.

[161] Q. Cui, X. Dong, J. Wang, M. Li, *J. Rare Earths* **2008**, *26*, 664–669.

[162] A.-M. Azad, T. Matthews, J. Swary, *Mater. Sci. Eng. B* **2005**, *123*, 252–258.

[163] Y. O. D. Ceo, E. Fibers, A. K. Alves, F. A. Berutti, F. Clemens, T. Graule, C. P. Bergmann, **2009**, *21*, 200–204.

[164] A. Trovarelli, P. Fornasiero, *Catalysis by Ceria and Related Materials*, Imperial College Press, London, **2002**.

[165] A. P. Amrute, C. Mondelli, M. Moser, G. Novell-Leruth, N. López, D. Rosenthal, R. Farra, M. E. Schuster, D. Teschner, T. Schmidt, et al., *J. Catal.* **2012**, *286*, 287–297.

[166] A. P. Amrute, C. Mondelli, M. A. G. Hevia, P. Javier, **2011**, 583–590.

[167] M. Moser, C. Mondelli, T. Schmidt, F. Girgsdies, M. E. Schuster, R. Farra, L. Szentmiklósi, D. Teschner, J. Pérez-Ramírez, *Appl. Catal. B Environ.* **2013**, *132-133*, 123–131.

[168] M. P. Yeste, J. C. Hernández-Garrido, D. C. Arias, G. Blanco, J. M. Rodríguez-Izquierdo, J. M. Pintado, S. Bernal, J. a. Pérez-Omil, J. J. Calvino, *J. Mater. Chem. A* **2013**, *1*, 4836–4844.

[169] M. S. Hegde, G. Madras, K. C. Patil, *Acc. Chem. Res.* **2009**, *42*, 704–712.

[170] H. Deacon, *Manufacture of Chlorine, U.S. Patent No. 85, 370*, **1868**.

[171] "Annual HCl output," can be found under www.eurochlor.org, **accessed 26. November 2015**.

[172] H. Y. Pan, R. G. Minet, S. W. Benson, T. T. Tsotsis, *Ind. Eng. Chem. Res.* **1994**, *33*, 2996–3003.

[173] J. Pérez-Ramírez, C. Mondelli, T. Schmidt, O. F.-K. Schlüter, A. Wolf, L. Mleczko, T. Dreier, *Energy Environ. Sci.* **2011**, *4*, 4786–4799.

[174] R. Farra, M. Eichelbaum, R. Schlögl, L. Szentmiklósi, T. Schmidt, A. P. Amrute, C. Mondelli, J. Pérez-Ramírez, D. Teschner, *J. Catal.* **2013**, *297*, 119–127.

[175] D. Li, Y. Wang, Y. Xia, *Nano Lett.* **2003**, *3*, 1167–1171.

[176] J.-K. Choi, I.-S. Hwang, S.-J. Kim, J.-S. Park, S.-S. Park, U. Jeong, Y. C. Kang, J.-H. Lee, *Sensors Actuators B Chem.* **2010**, *150*, 191–199.

[177] A. Yang, X. Tao, R. Wang, S. Lee, C. Surya, *Appl. Phys. Lett.* **2007**, *91*, 133110.

[178] R. Luoh, H. T. Hahn, *Compos. Sci. Technol.* **2006**, *66*, 2436–2441.

[179] L. Liu, T. Zhang, L. Wang, S. Li, *Mater. Lett.* **2009**, *63*, 2041–2043.

[180] Y. Zhang, X. He, J. Li, Z. Miao, F. Huang, *Sensors Actuators B Chem.* **2008**, *132*, 67–73.

[181] X. Song, Q. Qi, T. Zhang, C. Wang, *Sensors Actuators B Chem.* **2009**, *138*, 368–373.

[182] H. Bisht, H.-T. Eun, A. Mehrtens, M. A. Aegerter, *Thin Solid Films* **1999**, *351*, 109–114.

[183] T. von Graberg, *Ph. D. Thesis, Justus-Liebig-University Giessen* **2012**.

[184] R. Ostermann, R. Zieba, M. Rudolph, D. Schlettwein, B. M. Smarsly, *Chem. Commun.* **2011**, *47*, 12119–12121.

[185] W. Pan, X. He, Y. Chen, *Optoelectron. Adv. Mater. - Rapid Commun.* **2010**, *4*, 390–394.

[186] M. M. Munir, F. Iskandar, K. M. Yun, K. Okuyama, M. Abdullah, *Nanotechnology* **2008**, *19*, 145603.

[187] "Indium Prices," can be found under http://www.metalprices.com/pubcharts/Public/Indium_Price_Charts.asp, **accessed 26. November 2015**.

[188] K. Faber, *State Exam. Thesis, Justus-Liebig-University Giessen* **2011**.

[189] "Properties of PMMA," can be found under http://www.sigmaaldrich.com/catalog/product/aldrich/445746?lang=de&region=DE, **accessed 26. November 2015**.

[190] "Properties of PEO," can be found under http://www.sigmaaldrich.com/catalog/product/aldrich/182001?lang=de&region=DE, **accessed 26. November 2015**.

[191] J. A. Shetter, *J. Polym. Sci. Part B Polym. Lett.* **1963**, *1*, 209–213.

[192] N. Pinna, M. Antonietti, M. Niederberger, *Colloids Surfaces A Physicochem. Eng. Asp.* **2004**, *250*, 211–213.

[193] N. Pinna, G. Garnweitner, M. Antonietti, M. Niederberger, *Adv. Mater.* **2004**, *16*, 2196–2200.

[194] N. Pinna, G. Neri, M. Antonietti, M. Niederberger, *Angew. Chemie Int. Ed.* **2004**, *43*, 4345–4349.

[195] M. Niederberger, N. Pinna, J. Polleux, M. Antonietti, *Angew. Chemie Int. Ed.* **2004**, *43*, 2270–2273.

[196] M. Niederberger, G. Garnweitner, N. Pinna, M. Antonietti, *J. Am. Chem. Soc.* **2004**, *126*, 9120–9126.

[197] S. Koombhongse, W. Liu, D. H. Reneker, *J. Polym. Sci. Part B Polym. Phys.* **2001**, *39*, 2598–2606.

[198] M. Möller, N. Tarabanko, C. Wessel, R. Ellinghaus, H. Over, B. M. Smarsly, *Submitt. to J. Mater. Chem.* **2015**.

[199] M. Möller, H. Over, B. Smarsly, N. Tarabanko, S. Urban, *Catal. Today* **2015**, *253*, 207–218.

[200] S. Tripatanasuwan, Z. Zhong, D. H. Reneker, *Polymer* **2007**, *48*, 5742–5746.

[201] C. Helbig, *Ph. D. Thesis, University Augsburg* **2008**.

[202] L. B. McCusker, R. B. Von Dreele, D. E. Cox, D. Louër, P. Scardi, *J. Appl. Crystallogr.* **1999**, *32*, 36–50.

6.5 Acknowledgements

„Ich denke mal, wir sollten alle danach streben, irgendetwas zu hinterlassen,… irgendetwas…“[37]

The thesis on hand is what I leave after my academic education: A “doctor philosophicus“ thesis with approximately 230 pages summarizing my scientific research results acquired during the past six years of my doctorate at the Justus-Liebig university in Gießen. Accordingly, the thesis fulfills the standard to contain “a progress of scientific knowledge on the basis of single-handed research”.[38] Nevertheless, this thesis would not be the same without help of numerous people who all contributed to the success of my research in their individual manner. Consequently, I gratefully have to acknowledge:

- All my “helping hands” in the labs having done great jobs during their duration of study in our work group: Marcus Einert, Kristin Faber, Ralph (bomb man) Henning, Nils Hildebrandt, Maren Möller, Daniela Schön, Falko Schulze, Antonio Susanna, and Pascal Vöpel;
- My supervisor Prof. B. M. Smarsly for several interesting projects, helpful discussions and the freedom to follow own interests;
- Prof. H. Over for reviewing this thesis;
- The staff of our institutes mechanical and electronics workshops, especially Harry Heidt, Gerd Pfeiffer, Harald Weigand and Kurt Bürger helping with the construction of our electrospinning equipment. Without them not a single fiber of this thesis would exist;
- All my office mates for discussions, kicker matches, lab work in 0815 and tolerating me despite of bike and “music”: Kristin Faber, Till von Graberg, Takeshi Hara, Jan Heatge, Julia Migenda, Rainer Ostermann, and Daniela Stöckel;
- Till von Graberg, Roland Marschall, Christian Pszolla, Gwyneth Schulz, Christoph Seitz, Daniela Stöckel, and Pascal Vöpel for careful proofreading finding numerous of my deficiencies;
- Björn Luerßen, Rainer Ostermann, and Pascal Vöpel for their assistance with graphics;
- Christoph Seitz for help with Rietveld refinement analyses;
- The answer to all: “42”, being present also in this thesis;
- All members of the Smarsly group for a joyful time in Gießen;
- All other people not mentioned above, mea culpa I forgot you.

Finally, I have to acknowledge my parents for three decades of exciting life leading to successes like this thesis.

[37] English translation: “I believe, everybody should aspire to leave something,… anything…” (Stephan Weidner, 03. March 2001, Böhse Onkelz 20th anniversary concert, Frankfurt (Main), announcement to: „Ich“)

[38] Adapted from the promotions regulations of the Justus-Liebig University Gießen; original citation in German: „(Darüber hinaus hat die Dissertation den folgenden Ansprüchen zu genügen: Sie muss) einen Fortschritt der wissenschaftlichen Erkenntnis aufgrund selbständiger Forschung bringen.“